

RD-A158 188

COUPLED RADIATION TRANSPORT/THERMAL ANALYSIS OF THE
RADIATION SHIELD FOR A.. (U) AIR FORCE INST OF TECH
WRIGHT-PATTERSON AFB OH W J BARATTINO JUL 85

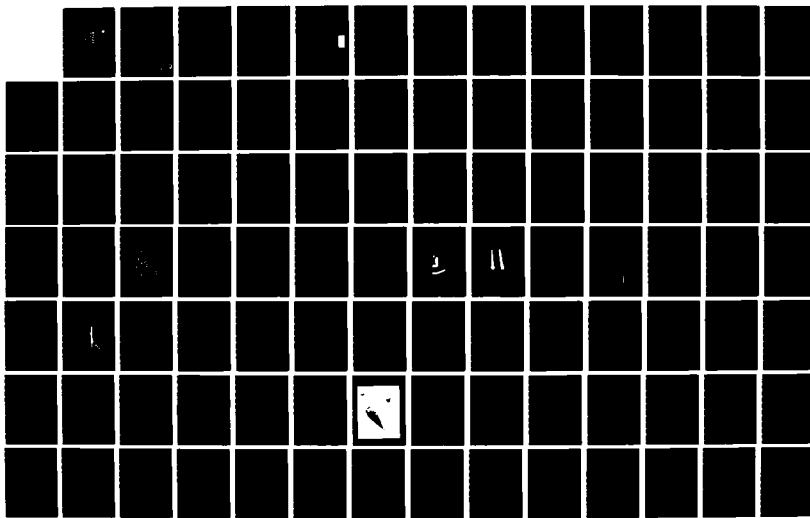
1/4

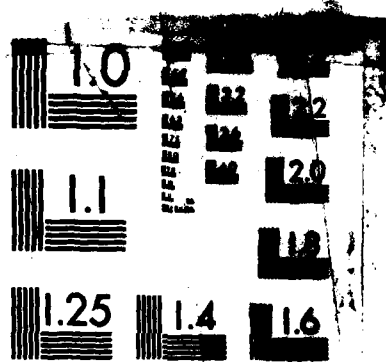
UNCLASSIFIED

AFIT/CI/NR-85-53D

F/G 18/6

NL





MICROCOPY RESOLUTION TEST CHART
NATIONAL BUREAU OF STANDARDS-1963-A

AD-A158 180

(1)

COUPLED RADIATION TRANSPORT/THERMAL ANALYSIS OF THE
RADIATION SHIELD FOR A SPACE NUCLEAR REACTOR

BY

WILLIAM JOHN BARATTINO

B.S. Applied Mechanics, The United States Military Academy, 1975

M.S. Mechanical Engineering, The George Washington University, 1979

M.B.A. Business Administration, New Mexico Highlands University, 1982

DISSERTATION

Submitted in Partial Fulfillment of the
Requirements for the Degree of

Doctor of Philosophy in Nuclear Engineering

The University of New Mexico
Albuquerque, New Mexico

July, 1985

MS FILE COPY

This document has been approved
for public release and sale; its
distribution is unlimited.



~~UNCLASS~~

SECURITY CLASSIFICATION OF THIS PAGE (When Data Entered)

| REPORT DOCUMENTATION PAGE | | READ INSTRUCTIONS BEFORE COMPLETING FORM | | | | | | | | | | |
|--|---|--|---------------|--|--------------|-------------------------------------|--------------|--------------------------|-------------|--------------------------|---------------|--|
| 1. REPORT NUMBER AFIT/CI/NR 85- 53D | 2. GOVT ACCESSION NO. <i>AD-A158 180</i> | 3. RECIPIENT'S CATALOG NUMBER | | | | | | | | | | |
| 4. TITLE (and Subtitle) Coupled Radiation Transport/Thermal Analysis of the Radiation Shield for a Space Nuclear Reactor | 5. TYPE OF REPORT & PERIOD COVERED THESIS/DISSERTATION | | | | | | | | | | | |
| 7. AUTHOR(s) William John Barattino | 6. PERFORMING ORG. REPORT NUMBER | | | | | | | | | | | |
| 9. PERFORMING ORGANIZATION NAME AND ADDRESS AFIT STUDENT AT: The University of New Mexico | 10. PROGRAM ELEMENT, PROJECT, TASK AREA & WORK UNIT NUMBERS | | | | | | | | | | | |
| 11. CONTROLLING OFFICE NAME AND ADDRESS AFIT/NR WPAFB OH 45433 | 12. REPORT DATE <i>July 1985</i> | | | | | | | | | | | |
| 14. MONITORING AGENCY NAME & ADDRESS(if different from Controlling Office) | 13. NUMBER OF PAGES 332 | | | | | | | | | | | |
| | 15. SECURITY CLASS. (of this report) UNCLASS | | | | | | | | | | | |
| | 15a. DECLASSIFICATION/DOWNGRADING SCHEDULE | | | | | | | | | | | |
| 16. DISTRIBUTION STATEMENT (of this Report) APPROVED FOR PUBLIC RELEASE; DISTRIBUTION UNLIMITED | | | | | | | | | | | | |
| 17. DISTRIBUTION STATEMENT (of the abstract entered in Block 20, if different from Report) | | | | | | | | | | | | |
| 18. SUPPLEMENTARY NOTES APPROVED FOR PUBLIC RELEASE: IAW AFR 190-1 <i>Lynn Dolan, LYNN E. WOLAVER Dean for Research and Professional Development SAX 1481 AFIT, Wright-Patterson AFB OH</i> | | | | | | | | | | | | |
| 19. KEY WORDS (Continue on reverse side if necessary and identify by block number) | | | | | | | | | | | | |
| <table border="1"> <tr> <td>Accession No.</td> <td></td> </tr> <tr> <td>NTIS GRAQ1</td> <td><input checked="" type="checkbox"/></td> </tr> <tr> <td>DTIC TAB</td> <td><input type="checkbox"/></td> </tr> <tr> <td>Unannounced</td> <td><input type="checkbox"/></td> </tr> <tr> <td>Justification</td> <td></td> </tr> </table> | | | Accession No. | | NTIS GRAQ1 | <input checked="" type="checkbox"/> | DTIC TAB | <input type="checkbox"/> | Unannounced | <input type="checkbox"/> | Justification | |
| Accession No. | | | | | | | | | | | | |
| NTIS GRAQ1 | <input checked="" type="checkbox"/> | | | | | | | | | | | |
| DTIC TAB | <input type="checkbox"/> | | | | | | | | | | | |
| Unannounced | <input type="checkbox"/> | | | | | | | | | | | |
| Justification | | | | | | | | | | | | |
| 20. ABSTRACT (Continue on reverse side if necessary and identify by block number) | | | | | | | | | | | | |
| <table border="1"> <tr> <td>By</td> <td></td> </tr> <tr> <td>Distribution</td> <td></td> </tr> <tr> <td>Availability</td> <td></td> </tr> <tr> <td>Dist</td> <td>Spec</td> </tr> </table> | | | By | | Distribution | | Availability | | Dist | Spec | | |
| By | | | | | | | | | | | | |
| Distribution | | | | | | | | | | | | |
| Availability | | | | | | | | | | | | |
| Dist | Spec | | | | | | | | | | | |
| <p>ATTACHED</p> <div style="text-align: center;">  <i>A1</i> </div> | | | | | | | | | | | | |

DD FORM 1 JAN 73 1473 EDITION OF 1 NOV 65 IS OBSOLETE

~~UNCLASS~~

AFIT RESEARCH ASSESSMENT

The purpose of this questionnaire is to ascertain the value and/or contribution of research accomplished by students or faculty of the Air Force Institute of Technology (AFIT). It would be greatly appreciated if you would complete the following questionnaire and return it to:

AFIT/NR
Wright-Patterson AFB OH 45433

RESEARCH TITLE: Coupled Radiation Transport/Thermal Analysis of the Radiation Shield for a Space Nuclear Reactor

AUTHOR: William John Barattino

RESEARCH ASSESSMENT QUESTIONS:

1. Did this research contribute to a current Air Force project?

a. YES b. NO

2. Do you believe this research topic is significant enough that it would have been researched (or contracted) by your organization or another agency if AFIT had not?

a. YES b. NO

3. The benefits of AFIT research can often be expressed by the equivalent value that your agency achieved/received by virtue of AFIT performing the research. Can you estimate what this research would have cost if it had been accomplished under contract or if it had been done in-house in terms of manpower and/or dollars?

a. MAN-YEARS _____ b. \$ _____

4. Often it is not possible to attach equivalent dollar values to research, although the results of the research may, in fact, be important. Whether or not you were able to establish an equivalent value for this research (3. above), what is your estimate of its significance?

a. HIGHLY SIGNIFICANT b. SIGNIFICANT c. SLIGHTLY SIGNIFICANT d. OF NO SIGNIFICANCE

5. AFIT welcomes any further comments you may have on the above questions, or any additional details concerning the current application, future potential, or other value of this research. Please use the bottom part of this questionnaire for your statement(s).

| | | |
|------|-------|----------|
| NAME | GRADE | POSITION |
|------|-------|----------|

| | |
|--------------|----------|
| ORGANIZATION | LOCATION |
|--------------|----------|

STATEMENT(s):

FOLD DOWN ON OUTSIDE - SEAL WITH TAPE

AFIT/NR
WRIGHT-PATTERSON AFB OH 45433
OFFICIAL BUSINESS
PENALTY FOR PRIVATE USE. \$300



NO POSTAGE
NECESSARY
IF MAILED
IN THE
UNITED STATES

BUSINESS REPLY MAIL

FIRST CLASS PERMIT NO. 72226 WASHINGTON D.C.

POSTAGE WILL BE PAID BY ADDRESSEE

AFIT/ DAA

Wright-Patterson AFB OH 45433



FOLD IN

William John Barattino
Candidate

Chemical and Nuclear Engineering
Department

This dissertation is approved, and it is acceptable in quality
and form for publication on microfilm:

Approved by the Dissertation Committee:

Mohamed El-Tayeb, Chairperson

Patrick J. McDaniel

Howard D. Schreyer

Norman F. Goldstein

Raymond J. Poggenpohl

James T. Lee Jr.

Accepted:

Dean, Graduate School

Date

Title of Dissertation: Coupled Radiation Transport/Thermal Analysis
of the Radiation Shield for a Space Nuclear Reactor

Performed by: William John Barattino
Captain, USAF

Degree Awarded: July, 1985

University: The University of New Mexico

Number of pages of dissertation: 332

Degree Awarded: Doctor of Philosophy in Nuclear Engineering

ABSTRACT

A coupled radiation transport-heat transfer-stress analysis of the radiation shield for an SP-100 reactor was performed using a numerical code developed at the University of New Mexico and Sandia National Laboratory. For a fast reactor operating at 1.66 MW_{th}, the energy deposited and resulting temperature distribution was determined for a shield consisting of tungsten and lithium hydride pressed into a stainless steel honeycomb matrix. While temperature feedback was shown to have a minor effect on energy deposition, the shielding configuration was found to have a major influence in meeting thermal requirements of the lithium hydride. It was shown that a shield optimized for radiation protection will fail because of melting. However, with minor modifications in the shield layering and material selection, the thermal integrity of the shield can be preserved. A shield design of graphite, depleted lithium hydride, tungsten, and natural lithium hydride was shown to satisfy neutron and gamma fluence requirements, maximum temperature limits, and minimize cracking in the LiH portion of the shield.

ACKNOWLEDGEMENTS

I'd like to take this opportunity to express my heartfelt thanks to particular individuals who assisted in making this research project a success. Dr. Mohamed S. El-Genk, my principal advisor, was a constant source of guidance and inspiration throughout my studies and research. In addition to his piercing review of the reasonableness of my results, his expertise in thermal sciences proved to be of invaluable assistance. Dr. Patrick J. McDaniel served as my primary counselor for numerical modelling, and his radiation transport code was a critical tool in generating these results. His insight into the relationship of physical and mathematical sciences served as constant goal to which I continue to aspire.

My thanks also goes to the remaining members of my committee. Each individual was selected because of their nationally recognized expertise in a given area, an expertise which I readily utilized and grew from. Specifically, these individuals include Dr. James Lee of the U.S. Air Force; and Dr. Norman Roderick, Dr. Howard Schreyer, and Dr. Roy Johnson of the University of New Mexico.

Several organizations require my thanks, as well. The Air Force Institute of Technology served as my sponsoring organization and was supportive of my course of studies and area of research. The U.S. Department of Energy and Sandia National Laboratory deserve my thanks for making their excellent research facilities accessible for my use. I am grateful to the other faculty members of the Nuclear Engineering

Department at UNM for sharing their expertise during my course of studies. Janice Johnston and Linda Todd of The New Mexico Engineering Research Institute also receives my thanks for their support in the preparation of this report.

Finally, my most appreciative thanks goes to my wife, Karen, for her unending support throughout the duration of my studies. Her silent endurement of the many lonely hours while I slaved away in front of a computer terminal, served as a major source of encouragement in never having to "slow down" my research activities.

There are many others deserving of my appreciation. To those of you in this group, I offer a sincere thank you.

Coupled Radiation Transport/Thermal Analysis of the
Radiation Shield for a Space Nuclear Reactor

WILLIAM J. BARATTINO

B.S. Applied Mechanics, The United States Military Academy, 1975

M.S. Mechanical Engineering, The George Washington University, 1979

M.B.A. Business Administration, New Mexico Highlands University, 1982

Ph.D. Nuclear Engineering, The University of New Mexico, 1985

The renewed interest of conducting operations in space has given rise to re-establishment of space reactor systems development. The current SP-100 program is focussing on design of a 100 kW_e nuclear reactor for space application. This research project investigated the coupling between radiation transport, energy deposition, and temperature distribution for a variety of space reactor shield configurations. The basic shield design consisted of tungsten [W], and natural lithium hydride either cast or pressed into a stainless steel matrix [LiH(Nat)].

For a nuclear reactor operating at a power level of $1.66 \text{ MW}_{\text{th}}$, temperature feedback effects on energy deposition in the shield were examined for a shield consisting of 4 cm of W, followed by 71 cm of LiH(Nat). Using the free gas differential scattering kernel, the temperature dependent thermal neutron cross sections (including upscatter) were generated for the non-Maxwellian neutron distribution in LiH(Nat). The calculations showed that the total energy deposited in the shield decreased by only 2.5% when temperature dependent number

densities and thermal neutron cross sections were included in the analysis. Considering the temperature effects only on the number densities, while neglecting temperature effects on the thermal neutron cross sections, resulted in a decrease of 5.9% in total energy deposition throughout the shield. The maximum change in temperature was about 1.5%, which leads to the conclusion that temperature feedback effects on energy deposition in the shield are not significant for SP-100 power levels.

The effects of shield configuration on energy deposition were shown to be a critical design consideration. Layered shields consisting of depleted lithium hydride [LiH(Depl)] followed by LiH(Nat) were compared with all natural LiH shields, with W either at the front of the shield or moved 13.4 cm into the shield. The movement of W into the shield was made to reduce the generation of secondary gammas. The impact on temperature distribution of LiH(Depl) was much greater for the configuration of W moved into the shield. With the substitution of LiH(Nat) with LiH(Depl) over part of the shield, the maximum LiH temperature was reduced from 772 K to 680 K when W was placed at the front of the shield, and reduced from 1074 K to 714 K with the W located 13.4 cm into the shield. The significant difference was mainly due to the relative contribution of the highly thermally conductive W to heat removal from the hot portion of the shield to the radiative outer surface.

With these results, a final design modification of the SP-100 shield was made to include a 2 cm graphite disk at the front of the shield. This passively cooled graphite, LiH(Depl), W, LiH(Nat) shield maintained a temperature profile below the 680 K upper temperature

limit of LiH throughout the entire shield. An analysis of the thermal stresses in the shield was made with the LiH and graphite modelled as bilinear, orthotropic materials, and W as an isotropic material. Calculations showed extremely large tensile stresses at the outer radial surface of the shield when this surface was free to expand. When this surface was pinned (corresponding to perfect contact between the LiH and its outer casing), the stress distribution throughout the shield was predominantly compressive. These results showed the importance of limiting the movement of the LiH at the outer radial surface, to prevent excessive tensile cracking.

The results of this research show that a shield optimized for radiation protection may fail due to thermal melting. Hence, thermal design considerations must be given the same priority as radiation protection for a shield using LiH at the power levels of the SP-100 reactor system.

- Bilinear, Orthotropic Material
- Composite Cylinders Model
- Energy Deposition
- Finite Element Method
- Free Gas Scattering Kernel
- Galerkin Projection
- Newton-Raphson Iteration
- Radiative Heat Transfer
- Radiation Transport
- Reactor Shielding
- Space Reactor

I. TABLE OF CONTENTS

| | |
|---|----|
| 1.0 INTRODUCTION..... | 1 |
| 2.0 HISTORICAL OVERVIEW..... | 6 |
| 2.1 Review of Previous Shield Designs for Space Reactors..... | 8 |
| 2.1.1 SNAP 10A Shield..... | 9 |
| 2.1.2 SNAP 8 Reactor Shield..... | 11 |
| 2.1.3 Thermionic Reactor Shield..... | 11 |
| 2.1.4 NASA-Lewis Shield Design..... | 13 |
| 2.1.5 ORNL Shield Design..... | 16 |
| 2.1.6 SP-100 Reactor Shield Design..... | 19 |
| 2.2 Shield Thermal Analysis..... | 22 |
| 2.2.1 Lithium Hydride Shield..... | 24 |
| 2.2.2 Fabrication of LiH Shield..... | 30 |
| 2.2.3 Emissivity Coating..... | 32 |
| 2.2.4 Summary of Previous Space Shielding Research..... | 34 |
| 2.3 Developments in Numerical Methods..... | 36 |
| 3.0 THEORETICAL BACKGROUND FOR ANALYSIS OF RADIATION SHIELD..... | 39 |
| 3.1 Research Overview..... | 39 |
| 3.2 Method of Weighted Residuals..... | 45 |
| 3.2.1 Finite Element Theory..... | 46 |
| 3.2.2 Shape Functions..... | 49 |
| 3.2.2.1 3 Node Triangular Elements..... | 50 |
| 3.2.2.2 4 Node Quadrilateral Elements..... | 51 |
| 3.3 Block 1: Radiation Transport Theory..... | 53 |
| 3.3.1 Derivation of System of Equations for Determining Coupled Neutron and Gamma Fluxes..... | 54 |
| 3.3.2 Generation of Heating Rate From Flux and Heating Kerma..... | 58 |
| 3.3.3 Temperature Feedback Effects on Energy Deposition..... | 61 |
| 3.3.3.1. Temperature Feedback in a Maxwell Boltzmann Medium (M-B)..... | 61 |
| 3.3.3.2. Temperature Feedback in a Non- Maxwell Boltzmann Medium..... | 65 |

| | |
|-----------------------|--|
| $F_{i \rightarrow j}$ | View factor of surface i to surface j |
| F_n | Component of fluence at back surface exiting shield (NVT or RAD) |
| f_s | Surface or traction forces |
| G_{ij} | Shear modulus of elasticity (N/cm^2) |
| $H(r), q'''$ | Volumetric heating rate as function of position (W/cm^3) |
| $h(T)$ | Convection coefficient as function of temperature ($W/cm^2\text{-K}$) |
| H_Y | Heating due to gamma interactions (kW) |
| H_n | Heating due to neutron interactions (kW) |
| H_{tot}, HR | Total heating rate (kW) |
| H_{tot}^D | Total energy deposited using elevated temperature number densities only (kW) |
| H_{tot}^{RT} | Total energy deposited using room temperature properties (kW) |
| H_{tot}^T | Total energy deposited including temperature effects on number densities and cross sections (kW) |
| J | Neutron or gamma current (n or $\gamma/cm^2\text{-sec}$) |
| k | Boltzmanns constant (J/K) |
| $K_j(E)$ | Neutron kerma factor for j^{th} nuclide as function of energy |
| K_{Yj} | Gamma kerma factor for j^{th} nuclide as function of energy |
| k_r | Thermal conductivity in radial direction ($W/cm\text{-k}$) |
| k_z | Thermal conductivity in axial direction ($W/cm\text{-k}$) |
| z | Surface length between two boundary nodes (cm) |
| LiH(Dep1) | Depleted lithium hydride (a/o 100 Li-7) |
| LiH(Nat) | Natural lithium hydride (a/o 7.42 Li-6) |
| m | Mass |
| mfp | Mean free path (cm) |

IV. NOMENCLATURE

| | |
|----------------|--|
| A | Atomic mass |
| C_{∞} | Material Matrix |
| c | Volume fraction |
| D, S | Compliance matrix |
| $D(E)$ | Diffusion coefficient (cm) |
| D_b | Diameter of back of shield (cm) |
| E | Energy (ev) (Section 3.3) |
| E_c | Young's modulus in compression (N/cm^2) |
| E_{cp} | Energy released in a charged particle reaction |
| E_d | Energy released due to radioactive decay |
| E_g | "g th " Energy group (ev) |
| E_{fi} | Young's modulus of elasticity in i axis direction (N/cm^2) |
| \bar{E}_{ij} | Energy released during i th reaction for j th nuclide |
| E_{LE}^i | Local energy deposited from i th reaction |
| E_n | Energy carried away by neutron undergoing either elastic or inelastic scattering |
| erf | Error function |
| E_T | Young's modulus in tension (N/cm^2) |
| E_{th} | Thermal energy threshold |
| f_B | Body forces |
| f_c | Fraction of gamma energy locally converted to heat |
| F_{DP} | Fluence at dose place (NVT or RAD) |
| F^i | Concentrated forces |
| FEM | Finite element method |

LIST OF TABLES (CONCLUDED)

| <u>Table</u> | | <u>Page</u> |
|--------------|---|-------------|
| 6.1-1 | Smallest Mean Free Path for Neutron and Gamma Interactions for Variations in Nitrogen 14 Nuclide Density..... | 265 |
| 6.1-2 | Sensitivity of Convergence on Number Density of Nitrogen-14 Used to Model Vacuum..... | 269 |
| 6.2-1 | Qualitative Effects on Relaxation Parameters with Changes in Key Variables..... | 282 |
| 7.1-1 | Summary of Varying W-LiH Configurations for SP-100 Reactor Operating at 1.66 MW _{th} | 306 |

LIST OF TABLES (CONTINUED)

| <u>Table</u> | | <u>Page</u> |
|--------------|--|-------------|
| 4.2-6 | Upscatter Cross Sections for a LiH(Nat) Medium at Elevated Temperature Using Free Gas Scattering Kernel..... | 185 |
| 4.2-7 | Energy Deposited in a W-LiH(Nat) Shield Using Room Temperature Material and Nuclear Properties..... | 186 |
| 4.2-8 | Energy Deposited in a W-LiH(Nat) Shield With Temperature Feedback Effects Included In Cross Sections Using Free Gas Scattering Kernel..... | 187 |
| 4.2-9 | Effects of Elevated Temperature on Energy Deposition for W-LiH(Nat) Shield..... | 188 |
| 4.2-10 | Fluxes, Heating Kermas and Energy Deposition for Neutrons in LiH(Nat) Portion of a W-LiH(Nat) Shield..... | 192 |
| 4.2-11 | Results of Temperature on Energy Deposition for a W-LiH(Nat) Shield..... | 194 |
| 5.1-1 | Shield Configurations Used in Analysis of Layering Effects on Radiation Transport-Temperature Distribution..... | 198 |
| 5.2-1 | Energy Deposition Throughout a Shield Consisting of W-LiH(Depl)-LiH(Nat) for an SP-100 Reactor Operating at 1.66 MW _{th} | 213 |
| 5.2-2 | Energy Deposition Throughout a Shield Consisting of LiH(Nat)-W-LiH(Nat) for an SP-100 Reactor Operating at 1.66 MW _{th} | 214 |
| 5.2-3 | Energy Deposition Throughout a Shield Consisting of LiH(Depl)-W-LiH(Nat) for an SP-100 Reactor Operating at 1.66 MW _{th} | 215 |
| 5.2-4 | Material Properties for SP-100 Shield as Function of Temperature..... | 240 |
| 5.2-5 | Material Properties of Homogenized LiH-SS Honeycomb Matrix (99.5% LiH) Used in SHLDSTR Analysis..... | 242 |
| 5.3-1 | Uncertainty Estimates for Major Variables Involved in This Research..... | 255 |

III. LIST OF TABLES (CONTINUED)

| <u>Table</u> | <u>Page</u> |
|---|-------------|
| 3.5-7a Effect of Temperature on Isotropic Properties of LiH-SS Matrix with $v_{LiH} = 0.3$ | 123 |
| 3.5-7b Effect of Temperature on Isotropic Properties of an LiH-SS Matrix with $v_{LiH} = 0.2$ | 123 |
| 3.5-8 Effect of Uncertainties in LiH Elastic Moduli at 600 K of an LiH-SS Matrix with $v_{LiH} = 0.3$ | 124 |
| 3.5-9 Effect of Uncertainties in v_{LiH} at 600 K for an LiH-SS Matrix with $E_{LiH} = 2.1$ GPa..... | 125 |
| 3.5-10 CCM Results for an LiH-SS Matrix at 600 K with an LiH Volume fraction of 99%..... | 130 |
| 3.5-11 Mapping of Material Properties from Local Cartesian to Global Cylindrical Coordinates..... | 131 |
| 3.5-12 Test Case Input Data..... | 146 |
| 4.1-1 Volume Fractions Used In Neutronic Analysis..... | 151 |
| 4.1-2a Neutron Energy Group Data for 38 Group Library..... | 152 |
| 4.1-2b Photon Energy Group Data for 38 Group Library..... | 152 |
| 4.1-3a Neutron Energy Group Data for 59 Group Library..... | 153 |
| 4.1-3b Photon Energy Group Data for 59 Group Library..... | 154 |
| 4.2-1 Principal Nuclides Found in Neutron Attenuation Portion of an SP-100 Type Reactor Shield..... | 159 |
| 4.2-2 Major Contributions to Energy Deposition in an LiH(Nat) Shield..... | 161 |
| 4.2-3 Energy Deposited in a W-LiH(Nat) Shield With and Without MB Temperature Feedback Included in Absorption Cross Sections..... | 167 |
| 4.2-4 Reaction Rates for W-LiH(Nat) Shield With and Without Temperature Feedback..... | 168 |
| 4.2-5 Comparison of Differences in Collapsed Group Absorption Cross Section of LiH(Nat) Based on Free Gas Scattering Kernel and Maxwell Boltzmann Model at Elevated Temperatures..... | 182 |

III. LIST OF TABLES

| <u>Table</u> | | <u>Page</u> |
|--------------|---|-------------|
| 2.1-1 | Summary of Radiation Shield Designs for Space..... | 7 |
| 2.1-2 | Dose Criteria for SNAP 10A for Five Year Lifetime..... | 9 |
| 2.1-3 | Materials Considered for Gamma Attenuation Shield Design of the 5 kW _e Thermionic Reactor System..... | 14 |
| 2.1-4 | HPR Radiation Shield Characteristics..... | 22 |
| 2.2-1 | Observations on the Interaction of Lithium-Lithium Hydride at 600, 900, and 1200°F for 500, 1000, 2000, 4000 hours..... | 31 |
| 3.1-1 | Description of Major Programs Used in Analysis of the SP-100 Radiation Shield..... | 41 |
| 3.3-1 | Identification of Coefficients for Equation 3.3-15 for Various Neutron Reactions..... | 61 |
| 3.3-2 | Effect on Absorption Cross Section of Increasing Temperature Above 293 K Reference Temperature..... | 63 |
| 3.3-3 | Inverse Moderating Ratio's, Γ , for Selected Hydrides at Room Temperature and 700 K..... | 66 |
| 3.5-1 | LiH and Al Properties Used in Composite Cylinders Model Analysis..... | 110 |
| 3.5-2a | Effect of Temperature on Isotropic Properties of LiH-Al Matrix with $v_{LiH} = 0.3$ | 111 |
| 3.5-2b | Effect of Temperature on Isotropic Properties of LiH-Al Matrix with $v_{LiH} = 0.2$ | 111 |
| 3.5-3 | Effect of Uncertainties in LiH Elastic Moduli at 600 K for an LiH-Al Matrix with $v_{LiH} = 0.3$ | 112 |
| 3.5-4 | Effect of Uncertainties in v_{LiH} at 600 K for an LiH-Al Matrix with $E_{LiH} = 2.1$ GPa..... | 113 |
| 3.5-5 | CCM Results for an LiH-Al Matrix at 600 K with an LiH Volume fraction of 99%..... | 120 |
| 3.5-6 | LiH and SS Properties Used in Composite Cylinders Model Analysis..... | 122 |

LIST OF FIGURES (CONCLUDED)

| <u>Figure</u> | <u>Page</u> |
|--|-------------|
| 6.2-1 Comparison of FEM with Exact Solution for $q''' = 0.0072 \text{ W/cm}^3$ | 270 |
| 6.2-2 Oscillatory Behavior of Surface Temperature for $q''' = 0.072 \text{ W/cm}^3$ | 272 |
| 6.2-3 Oscillatory Behavior of Surface Temperature for $q''' = 0.72 \text{ W/cm}^3$ | 273 |
| 6.2-4 Effects of Varying Internal Heat Generation on Critical and Optimal Relaxation Parameters..... | 276 |
| 6.2-5 Effects of Initial Value of Radiative Heat Transfer Coefficient on Critical and Optimal Relaxation Parameters..... | 279 |
| 6.2-6 Effects of Varying Surface Emissivity on Critical and Optimal Relaxation Parameters..... | 279 |
| 6.2-7 Effects of Thermal Conductivity on Critical and Optimal Relaxation Parameters..... | 280 |
| 6.2-8 Effects of Varying Ambient Temperature on Critical and Optimal Relaxation Parameters..... | 280 |
| 6.2-9 Effects of Varying Shield Thickness on Critical and Optimal Relaxation Parameters..... | 281 |
| 6.2-10 Effects of Varying Inner Radius on Critical and Optimal Relaxation Parameters..... | 281 |
| 6.2-11 Results of Worst Case Run..... | 284 |
| 6.2-12 Convergence Criteria for Dampening of Oscillatory Behavior..... | 287 |
| 6.3-1 Full and Modified Newton-Raphson Iteration Methods..... | 299 |
| 6.3-2 Resultant Stress State for Bilinear, Orthotropic Material Using Full Newton- Raphson Iteration..... | 302 |
| 6.3-3 Resultant Stress State for Bilinear, Orthotropic Material using Modified Newton-Raphson Iteration..... | 302 |

LIST OF FIGURES (CONTINUED)

| <u>Figure</u> | | <u>Page</u> |
|---------------|--|-------------|
| 5.2-6 | Axial Temperatures in a Shield Comprised of LiH(Nat)-W-LiH(Nat) for Selected Radial Positions..... | 229 |
| 5.2-7 | 7 Year Fluences of SP-100 Reactor at 25 m Dose Plane with LiH(Depl)-W-LiH(Nat) and Graphite-LiH(Depl)-W-LiH(Nat) Shields..... | 232 |
| 5.2-8 | Temperature Distribution of a Graphite-LiH(Depl)-W-LiH(Nat) Shield for an SP-100 Reactor Operating at 1.66 MW _{th} | 234 |
| 5.2-9 | Sensitivity of Maximum Temperature with Variations in the Ambient Temperature, Emissivity, and View Factor for a Graphite-LiH(Depl)-W-LiH(Nat) Shield..... | 235 |
| 5.2-10 | Sensitivity of Minimum Temperature with Variations in Ambient Temperature, Emissivity and View Factor for a Graphite-LiH(Depl)-W-LiH(Nat) Shield..... | 236 |
| 5.2-11 | Displacement Conditions for SP-100 Shield for Stress Analysis..... | 241 |
| 5.2-12 | Regions of Concern of the Optimized Shield from Stress Analysis with Outer Radial Surface Free to Expand..... | 243 |
| 5.2-13 | Regions of Concern of the Optimized Shield from Stress Analysis with Outer Radial Surface Pinned..... | 244 |
| 5.2-14 | Temperature Distribution of a Graphite-LiH(Depl)-W-LiH(Nat) Shield [View from Front Surface]..... | 246 |
| 5.3-1 | Change in Energy Deposited with Mesh Spacing for LiH(Depl)-W-LiH(Nat) Shield from FEMP2D..... | 251 |
| 5.3-2 | Uncertainty in Energy Deposited with Mesh Spacing for LiH(Depl)-W-LiH(Nat) Shield from FEMP2D..... | 253 |
| 5.3-3 | Difference Between Energy Deposited and Energy Radiated for LiH(Depl)-W-LiH(Nat) Shield with Mesh Interval from Temperature Analysis..... | 260 |
| 6.1-1 | Regions of Vacuum Modelled In Radiation Transport Analysis..... | 264 |

LIST OF FIGURES (CONTINUED)

| <u>Figure</u> | <u>Page</u> |
|--|-------------|
| 4.2-9 Effect of Temperature on Cross Sections of LiH(Nat) Using Free Gas Scattering Kernel for Energy Range of 1.855 ev to 0.411 ev..... | 178 |
| 4.2-10 Effect of Temperature on Cross Sections of LiH(Nat) Using Free Gas Scattering Kernel for Energy Range of 0.411 ev to 0.1113 ev..... | 179 |
| 4.2-11 Effect of Temperature on Cross Sections of LiH(Nat) Using Free Gas Scattering Kernel for Energy Range of 0.1113 ev to 0.00001 ev..... | 180 |
| 4.2-12 Results of Temperature Feedback Effects on Energy Deposition in a W-LiH(Nat) Shield..... | 195 |
| 5.1-1 Example of Collapse of 2-D to 1-D Densities for P_N Transport Calculation..... | 200 |
| 5.1-2 Shield Geometry Modelled in 1-D Fluence Calculations..... | 201 |
| 5.1-3 Geometric Relationship of Sources Exiting Back of Radiation Shield to Point of Maximum Dosage on 25 m Dose Plane..... | 203 |
| 5.1-4 7 Year NVT Fluences of SP-100 Reactor at 25 meter Dose Plane for Several W-LiH Configurations..... | 207 |
| 5.1-5 7 Year Gamma Fluences of SP-100 Reactor at 25 meter Dose Plane for Several W-LiH Configurations..... | 208 |
| 5.2-1 Temperature Distribution in a W-LiH(Nat) Shield for a Fast Reactor Operating at 1.66 MW _{th} | 220 |
| 5.2-2 Temperature Distribution in a W-LiH(Depl)-LiH(Nat) Shield for a Fast Reactor Operating at 1.66 MW _{th} | 221 |
| 5.2-3 Temperature Distribution of a LiH(Nat)-W-LiH(Nat) Shield for a Fast Reactor Operating at 1.66 MW _{th} | 222 |
| 5.2-4 Temperature Distribution of a LiH(Depl)-W-LiH(Nat) Shield for a Fast Reactor Operating at 1.66 MW _{th} | 223 |
| 5.2-5 Axial Temperatures in a Shield Comprised of W-LiH(Nat) for Selected Radial Positions..... | 228 |

LIST OF FIGURES (CONTINUED)

| <u>Figure</u> | | <u>Page</u> |
|---------------|--|-------------|
| 3.5-9 | Relationship of Composite Cylinders Axes (Local) to Axisymmetric Axes (Global) of the Reactor Shield..... | 132 |
| 3.5-10 | Bilinear Moduli of LiH at Elevated Temperature..... | 136 |
| 3.5-11 | Flowchart of Solution Method Used in Stress Code, SHLDSTR..... | 141 |
| 3.5-12a | Thermal Conditions for Stress Test Case (Plain Strain).... | 143 |
| 3.5-12b | Displacement Conditions for Stress Test Case (Plain Strain)..... | 143 |
| 3.5-13 | Numerical Mesh Used to Calculate FEM Stresses for Test Case..... | 146 |
| 3.5-14 | Comparison of Finite Element and Exact Solutions for Stresses Due to a Radial Temperature Distribution.... | 147 |
| 4.1-1 | Core and Shield Design Modelled in UNM Analysis..... | 150 |
| 4.1-2 | Neutron Leakage for the SP-100 Reactor..... | 156 |
| 4.2-1 | Absorption Cross Section for Li-6..... | 162 |
| 4.2-2 | Problem Setup for Temperature Feedback Analysis..... | 164 |
| 4.2-3 | Flowchart of Temperature Feedback Effects Calculation Methodology for Maxwell Boltzmann Flux Medium..... | 165 |
| 4.2-4 | Energy Deposited in Tungsten for W-LiH(Nat) Shield..... | 169 |
| 4.2-5 | Energy Deposited in Inner LiH Region for W-LiH(Nat) Shield..... | 170 |
| 4.2-6 | Energy Deposited in Outer LiH Region for W-LiH(Nat) Shield..... | 171 |
| 4.2-7 | Flowchart of Temperature Feedback Effects Calculation Methodology for a non-Maxwell Boltzmann Flux Medium..... | 172 |
| 4.2-8 | Flux and Source Over Thermal Energies For LiH(Nat) Temperature of 693.7 K..... | 173 |

LIST OF FIGURES (CONTINUED)

| <u>Figure</u> | | <u>Page</u> |
|---------------|---|-------------|
| 3.3-3 | Energy Transfer Function in a Monatomic Gas with A=16..... | 70 |
| 3.3-4 | Illustration of Collapse of Cross Sections from 7 Groups to 3 Groups..... | 75 |
| 3.4-1 | Temperature Model Overview..... | 78 |
| 3.4-2 | Unit Cell Used to Model Orthotropic Thermal Conductivities..... | 86 |
| 3.4-3 | Flowchart of Solution Method Used In Temperature Code, SHLDTEMP..... | 89 |
| 3.4-4 | Schematic of Heat Flow From a Single Finite Element Along a Heat Rejection Surface..... | 91 |
| 3.4-5 | Types of Surface Available for User Selection In Determining Final Heat Flow in SHLDTEMP..... | 93 |
| 3.4-6 | Comparison of FEM Solution Using SHLDTEMP with Exact Solution for 1-D, Slab Shield..... | 94 |
| 3.4-7 | Comparison of FEM with Exact Solution for 1-D Cylinder with Constant Internal Heating..... | 95 |
| 3.5-1 | Stress/Strain Model Overview..... | 97 |
| 3.5-2 | Unit Cell Used in Stress/Strain Analysis..... | 104 |
| 3.5-3 | Effect of Temperature on Isotropic Behavior of LiH-Al Shield with $\nu_{LiH} = 0.3$ | 115 |
| 3.5-4 | Effect of Temperature on Isotropic Behavior of LiH-Al Shield with $\nu_{LiH} = 0.2$ | 116 |
| 3.5-5 | Effect of Uncertainties in E_{LiH} at 600 K of an LiH-Al Matrix..... | 117 |
| 3.5-6 | Effect of Temperature on Isotropic Behavior of LiH-SS Shield with $\nu_{LiH} = 0.3$ | 126 |
| 3.5-7 | Effect of Temperature on Isotropic Behavior of LiH-SS Shield with $\nu_{LiH} = 0.2$ | 127 |
| 3.5-8 | Effect of Uncertainties in E_{LiH} at 600 K of an LiH-SS Matrix..... | 128 |

II. LIST OF FIGURES

| <u>Figure</u> | | <u>Page</u> |
|---------------|---|-------------|
| 1.1-1 | Effects of Varying Selected Angles and Lengths on the Shadow Shield Geometry..... | 3 |
| 2.1-1 | SNAP 10A Reactor and Subsystem Overview..... | 10 |
| 2.1-2 | SNAP 8 Reactor..... | 12 |
| 2.1-3 | ORNL Heat Pipe Reactor..... | 17 |
| 2.1-4 | Variations in W and LiH Shield Thicknesses for a Dose Constraint of 1.2 rem/hr (45.71 m dose plane) for the ORNL Heat Pipe Reactor Operating at 1700 kW _{th} | 18 |
| 2.1-5 | Reactor Shield Design for the Los Alamos Heat Pipe Space Nuclear Reactor (HPR)..... | 20 |
| 2.1-6 | Contours of Neutron Fluence Over 7 Years, 1.33 MW _{th} Power Level for Los Alamos HPR..... | 21 |
| 2.2-1 | Volume Expansion of LiH(Nat) as a Function of Neutron Fluence and Temperature..... | 25 |
| 2.2-2 | Principal Reactions in Irradiation Damage of Lithium Hydride Systems..... | 26 |
| 2.2-3 | Increase in Dose Rate After 10,000 Hours Due to Meteoroid Puncture of Shield Outer Casing with Variations in Casing Thickness and LiH Temperature..... | 28 |
| 2.2-4 | Compressive Creep of LiH..... | 33 |
| 3.0-1 | Summary Overview of Analysis of the Space Reactor Radiation Shield..... | 40 |
| 3.1-1 | Major Programs Used in UNM Radiation Shield Analysis Code..... | 42 |
| 3.1-2 | Artists Concept of SP-100 Reactor System..... | 44 |
| 3.2-1 | Bertrams Chart of Computational Methods..... | 47 |
| 3.2-2 | 3 Node, Axisymmetric Triangular Element..... | 50 |
| 3.2-3 | 4 Node, Axisymmetric Quadrilateral Element..... | 52 |
| 3.3-1 | Radiation Transport Model Overview..... | 55 |
| 3.3-2 | Energy Transfer Function in a Monatomic Gas with A=1..... | 70 |

I. TABLE OF CONTENTS (CONCLUDED)

| | |
|---|-----|
| 5.0 APPLICATION TO SP-100 SHIELD DESIGN..... | 197 |
| 5.1 Neutron and Gamma Fluences at 25 Meter Dose Plane..... | 198 |
| 5.2 Results of Shield Configuration Effects..... | 210 |
| 5.2.1 Energy Deposition Results..... | 211 |
| 5.2.2 Temperature Distribution Results..... | 218 |
| 5.2.3 Improved SP-100 Shield Design..... | 230 |
| 5.2.4 Stress Analysis Results..... | 237 |
| 5.3 Uncertainty Estimates..... | 248 |
| 6.0 NUMERICAL INSTABILITIES..... | 262 |
| 6.1 Numerical Instabilities Encountered During Radiation Transport..... | 263 |
| 6.2 Numerical Instabilities Encountered During Heat Transfer Analyses..... | 268 |
| 6.2.1 Test Case Results..... | 269 |
| 6.2.2 Theoretical Analysis of Thermal Instability..... | 285 |
| 6.2.2.1 Convergence Criteria Without Relaxation.... | 286 |
| 6.2.2.2 Convergence Criteria With Relaxation..... | 288 |
| 6.2.2.3 Determination of ω_{opt} | 290 |
| 6.2.3 Thermal Instability Summary..... | 297 |
| 6.3 Numerical Instabilities Encountered During Stress Analyses..... | 297 |
| 7.0 CONCLUSIONS..... | 303 |
| 8.0 AREAS FOR FUTURE WORK..... | 309 |
| APPENDICES | |
| Appendix 1: Analytic Solution for 1-D, W-LiH Slab Shield with Radiative Back Surface and Either Adrabatic or Isothermal Front Surface..... | 319 |
| Appendix 2: Analytic Solution for 1-D, W-LiH Cylinder Shield with Radiative Outer Surface and Constant Internal Heat Generation..... | 324 |
| REFERENCES..... | 327 |

I. TABLE OF CONTENTS (CONTINUED)

| | |
|---|------------|
| 3.3.3.3. Numerical Solution of the Non-Maxwellian Thermal Flux..... | 73 |
| 3.4 Block 2: Thermal Analysis Theory..... | 76 |
| 3.4.1 Derivation of System of Equations for Solving Nonlinear Temperature Distribution..... | 79 |
| 3.4.2 Principal Axes Thermal Conductivities..... | 85 |
| 3.4.3 Temperature Code, SHLDTEMP..... | 88 |
| 3.4.4 Validation of Temperature Code..... | 92 |
| 3.5 Block 3: Thermal Stress/Strain Theory..... | 96 |
| 3.5.1 Derivation of System of Equations for Determining Stresses/Strains..... | 100 |
| 3.5.2 Composite Cylinders Model (CCM)..... | 104 |
| 3.5.3 Application of CCM to LiH in Honeycomb Matrix..... | 108 |
| 3.5.3.1 CCM Results for an LiH-Al Honeycomb Matrix..... | 109 |
| 3.5.3.2 CCM Results for an LiH-SS Honeycomb Matrix..... | 121 |
| 3.5.4 Constitutive Equations for an Orthotropic Material..... | 129 |
| 3.5.4.1 Jones Constitutive Equations for Bilinear Material..... | 136 |
| 3.5.4.2 Idelsohn, et al. Constitutive Equations for Bilinear Material..... | 138 |
| 3.5.4.3 Constitutive Equations Used in This Research..... | 139 |
| 3.5.5 Stress Analysis Code, SHLDSTR..... | 140 |
| 3.5.6 Validation of Stress Code..... | 142 |
| 4.0 EFFECTS OF TEMPERATURE ON ENERGY DEPOSITION IN THE SHIELD..... | 148 |
| 4.1 SP-100 Reactor Design Concept..... | 148 |
| 4.2 Temperature Feedback Effects on Energy Deposition..... | 157 |
| 4.2.1 Temperature Feedback Problem Setup..... | 163 |
| 4.2.2 Temperature Effects on Energy Deposition in a M-B Medium..... | 163 |
| 4.2.3 Temperature Effects on Energy Deposition in a Non-M-B Medium..... | 176 |

| | |
|------------------------------|--|
| MG | Multi-group |
| n | Normal unit vector |
| NE | Total number of elements |
| N _i | Approximating or shape function for node i |
| N _j | Number density (Section 3.3.2) |
| N _b | Total number of neutrons in a Maxwellian distribution |
| P _n | Legendre polynomial of n-th order |
| Q | Energy deposition occurring from conversion of mass to energy |
| q | Surface heat flux (W/cm ²) |
| q ₀ | Internal heating at core-W interface (W/cm ³) |
| q _L | Internal heating at W-LiH interface (W/cm ³) |
| q _{net} | Resultant heat flow from vector addition of q _r and q _z (W/cm ²) |
| q _{out} | Projection of q _{net} normal to heat rejection surface (W/cm ²) |
| q _r | Heat flow in radial direction (W/cm ²) |
| q _z | Heat flow in axial direction (W/cm ²) |
| r | Radial position (cm) |
| ROM | Rule of Mixtures |
| R _r ^{UC} | Thermal resistance in radial direction for unit cell |
| R _z ^{UC} | Thermal resistance in axial direction for unit cell |
| S | Surface area (cm ²) |
| S(E) | Neutron or gamma source |
| SE | Number of surface elements |
| SS | Stainless steel |
| T | Temperature (K) |
| T(e) | Temperature of finite element (K) |
| T ₀ | Reference temperature, 20°C |

| | |
|---------------|---|
| T^S | Surface temperature (K) |
| T^P | Equivalent ambient temperature (K) $\sim \alpha q$ |
| ΔT | Increment Temperature (K) |
| U | Displacement (cm) |
| $u^{(e)}$ | Displacement of the element (cm) |
| U_f | Uncertainty of f^{th} variable (Section 4.3) |
| UCS | Ultimate compressive strength (N/cm^2) |
| UTS | Ultimate tensile strength (N/cm^2) |
| ΔU | Increment displacement (cm) |
| u^* | State variable (exact) |
| v | Test function |
| v | Neutron velocity (when used as $1/v$) |
| V | Volume (cm^3) |
| z | Axial position (cm) |
| z_b | Distance from axial mid-plane of core to shield back surface (cm) |
| α | Collision parameter = $(A - 1)^2/(A + 1)^2$ |
| α_T | Temperature coefficient of expansion ($\Delta L/L - K$) |
| α_T | Surface absorbtivity as function of temperature |
| γ | Gamma ray |
| Γ | 1/Moderating ratio = $\Sigma_a/\xi\Sigma_s$ |
| $\epsilon(T)$ | Surface emissivity as function of temperature |
| θ | Angular position (cylindrical coordinates) |
| $\kappa(T)$ | Linearized radiative heat transfer coefficient |
| λ | Fundamental system eigenvalue |
| λ | Lamé constant (Section 3.5) |
| ν | Poisson's ratio (Section 3.5) |

| | |
|------------------------------|---|
| ν | Average number of neutrons produced by a fission caused by neutrons of energy E (Section 3.3) |
| $\rho(T)$ | Material density as function of temperature (g/cm^3) |
| ξ | Average lethargy gain |
| σ | Stefan-Boltzmann constant ($\text{W}/\text{cm}^2 \cdot \text{K}^4$) |
| ϕ | Neutron or gamma flux (n or $\gamma/\text{cm}^2 \cdot \text{sec}$) |
| ω | Solid angle |
| ω_{crit} | Critical relaxation parameter |
| ω_{opt} | Optimum relaxation parameter |
| $\tilde{\psi}_i$ | Eigenvector of i^{th} iteration |
| Ω | Unit vector in direction of motion |
| Δ | Area of simplex element (cm^2) |
| $\% \Delta H_{\text{tot}}$ | % change in total energy deposited due to all temperature effects |
| $\% \Delta H_{\text{tot}}^D$ | % change in $\% \Delta H_{\text{tot}}$ due to temperature effects on number densities |
| $\% \Delta H_{\text{tot}}^N$ | % change in $\% \Delta H_{\text{tot}}$ due to temperature effects on thermal energy cross sections |
| Σ_a^{RT} | LiH(Nat) cross section at room temperature (cm^{-1}) |
| Σ_a^{FG} | LiH(Nat) cross section at elevated temperature using free gas scattering kernel (cm^{-1}) |
| Σ_a^{MB} | LiH(Nat) cross section at elevated temperature using MB model (cm^{-1}) |
| Σ_T | Total cross section (cm^{-1}) |
| Σ_s | Scattering cross section (cm^{-1}) |
| Σ_f | Free scattering cross section (without binding effects) (Section 3.3.3) |
| Σ_f | Fission cross section (cm^{-1}) |
| Σ_R | Removal cross section (cm^{-1}) |

| | |
|--------------------------------|---|
| $\Sigma_s(E' \rightarrow E)$, | Differential scattering cross section (cm^{-1}) |
| $\Sigma_s^{m>1}$ | |
| σ_{pe} | Photoelectric interaction cross section |
| σ_c | Compton scattering cross section |
| σ_{pp} | Pair production cross section |
| σ_a | Microscopic absorption cross section (barns) |
| σ_{ath} | Microscopic absorption cross section over thermal energy (barns) |
| σ_{ij} | Microscopic cross section of i^{th} reaction for j^{th} nuclide |
| σ_{yp} | Yield stress (N/cm^2) |
| σ_{uts} | Ultimate tensile stress (N/cm^2) |
| σ_{ucs} | Ultimate compressive stress (N/cm^2) |
| σ_{rr} | Radial stress (N/cm^2) |
| $\sigma_{\theta\theta}$ | Hoop stress (N/cm^2) |
| σ_{zz} | Axial stress (N/cm^2) |
| τ_{rz} | Shear stress (N/cm^2) |
| ϵ_{rr} | Radial strain |
| $\epsilon_{\theta\theta}$ | Hoop strain |
| ϵ_{zz} | Axial strain |
| γ_{rz} | Shear strain |

Subscript

| | |
|----------|------------------------------------|
| f | Fiber |
| i | Summation over local nodes |
| int | W-LiH interface |
| L | Lithium hydride |
| L6 | LiH(Nat) |
| L7 | LiH(Depl) |
| m | Matrix |
| n | Neutron |
| γ | Gamma |
| p,q | Principal material axis directions |
| W_0 | Core-W interface |
| W | Tungsten |

Superscript

| | |
|---------|------------------|
| i,m,l | Iteration number |
| s | Surface node |

1.0 INTRODUCTION

The renewed interest on the part of both the civilian and military sectors of our economy in conducting operations in space, is giving rise to re-establishment of space reactor systems development. In 1983, the organization of a tri-agency office comprised of the National Aeronautics and Space Agency (NASA), Department of Energy (DOE), and Department of Defense (DOD) personnel, and the recent Space Defense Initiatives Office (SDIO) are indications of the growing need within the United States for the development of space nuclear power systems.

The previous space reactor program, SNAP, was funded from the late 1950s through the early 1970s. During this period, numerous reactor system concepts were designed, built, and tested. Only one system, the SNAP-10A, was actually flown into space. Much knowledge gained from this program will assist in the development of new systems. At the time of the SNAP program closeout, extensive work had been performed and documented regarding the space reactor shield neutronic performance. Extensive experimental testing of candidate shielding materials was performed along with the application of numerous neutron transport codes¹ to insure that the dose requirements were met at the dose plane. However, as the operating power levels of the later systems reached the multi-kilowatt range, a number of issues regarding the thermal performance of the shield began to emerge. Unfortunately, SNAP program funding was cut-off before many of the questions pertinent to the shield thermal analyses were addressed [Keshishian et al., 1973].

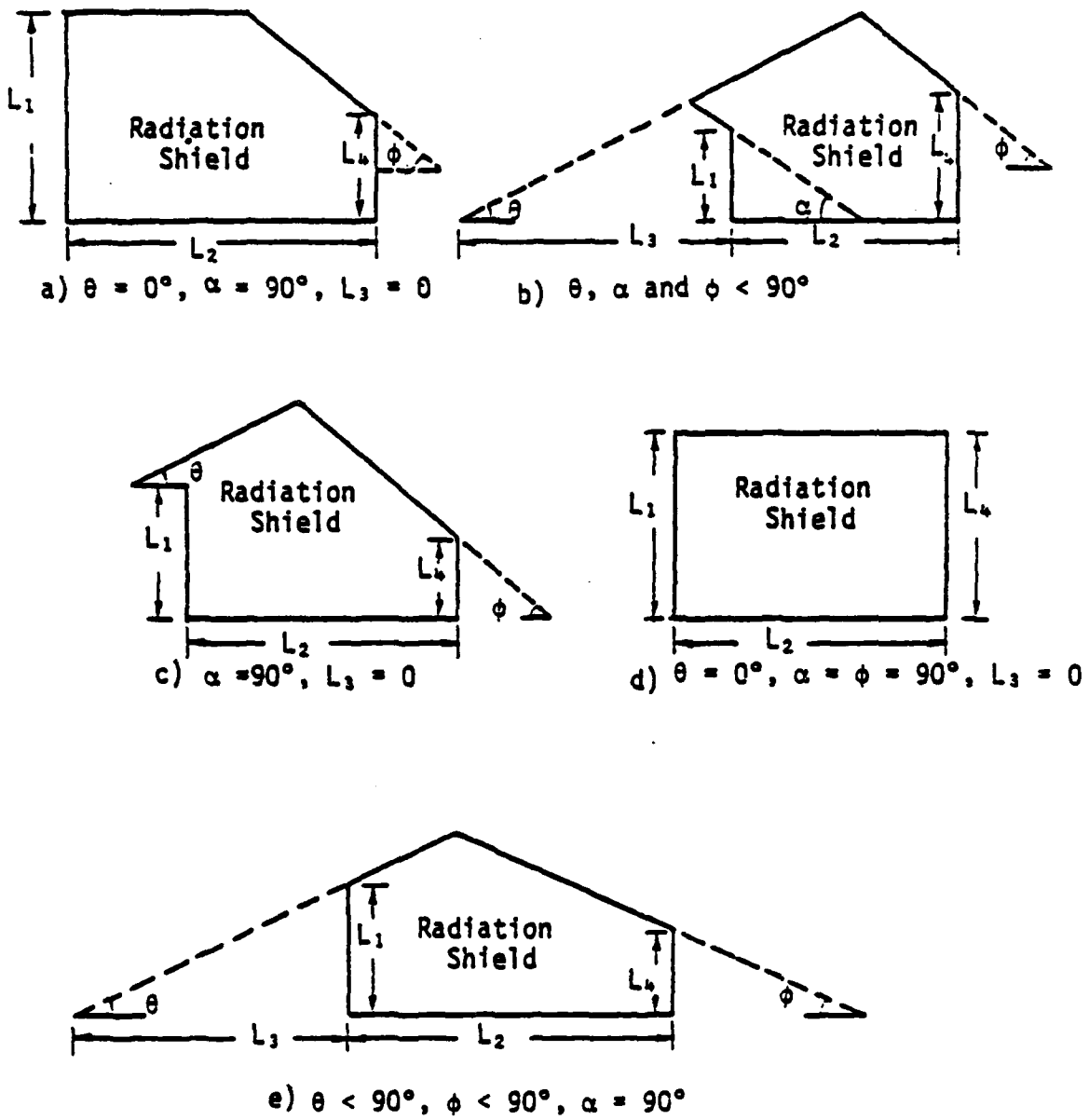
¹Based on Monte Carlo and Discrete Ordinates Methods

Based on neutronic analysis of the shield performance, the concept of shadow shields was developed to protect payloads from radiation exiting the core. While 4π shields were required for manned missions, the directional shielding protection provided by the shadow shield reduced neutron and gamma fluences to tolerable limits (within a given core angle), while minimizing the weight and volume of the shield.

Figure 1.1-1 shows how the shadow shield can assume different shapes by varying the key geometric parameters of the shield (angles σ , α , ϕ and lengths L_1 , L_2 , L_3 and L_4). Considering only the geometric complexities of the shield, one can readily understand why analytic solutions of a coupled radiation transport/thermal analysis of the space reactor shield cannot be obtained. The situation becomes even more difficult when the non-linear thermal boundary conditions and governing equations would have to be included, as well. It therefore is not surprising to learn how only extremely simplified coupled radiation transport/heat transfer/stress analysis calculations of the space reactor radiative shield were generated during the SNAP program.

In the ten years that have elapsed since the termination of the SNAP program, a number of advances have occurred in nuclear, thermal, and structural engineering communities. For instance, the rapid increases in digital computer capacities along with a more complete nuclear data base, allows for more accurate solutions of radiation transport codes in much less computing time than was possible in the 1960s. Computer application of numerical methods allows for the solution of temperature and thermal stress problems for more complex geometries than the engineer of the 1960s was able to perform.

Figure 1.1-1 Effects of Varying Selected Angles and Lengths on the Shadows Shield Geometry



The objectives of this research were to use the more advanced analytic tools available to the engineer of the 1980s to analyze the radiation transport, thermal and structural behavior of the shield as a function of shield geometry, operating conditions, and dose requirements. Specifically, this research accomplished the following goals:

A. Adapted a radiation transport code to determine the heating rates in a 3-D axisymmetric, layered radiation shield, with the capability of including temperature feedback effects on material and nuclear properties. Temperature dependent microscopic cross sections over thermal energies were generated using the free gas differential scattering kernel.

B. Developed an axisymmetric temperature distribution code for thermal analysis of the radiation shield. The finite element code was used in determining the temperature distribution throughout the shield during steady-state operation. The analysis included non-linear boundary conditions (due to thermal radiation at the outer surface of the shield), and temperature dependent thermal properties.

C. Developed an axisymmetric stress-strain code which was coupled with the thermal analysis code to determine the stresses and strains throughout the shield. The lithium hydride/stainless steel portion of the shield was modelled as a bilinear, elastic material with orthotropic properties. The stress analysis results were used to identify potential problem areas of the shield based on maintaining structural integrity during steady-state operation.

D. Subsequently, the coupled neutronics, temperature, and stress-strain code was applied to analyze the radiation shield of the SP-100

reactor. Specifically, this research studied the effects of temperature feedback on energy deposition in the non-Maxwellian LiH medium, and the effects of shield configuration on the temperature distribution. The results of this analysis were used to design a passively cooled shield for an SP-100 reactor which satisfied radiation protection, thermal, and structural requirements of the shield.

A review of past research regarding shielding analysis for space reactors and development of the finite element method are presented in Section 2. Section 3 provides the theoretical background essential to this research, as well as a discussion of the governing equations, methods of solution, and numerical techniques for the neutronics, temperature, and stress analyses calculations. The results of the SP-100 reactor shield analyses are presented in Sections 4 and 5. A discussion of the major numerical instabilities encountered in this research is presented in Section 6. The conclusions and recommendations for future work are contained in Sections 7 and 8, respectively.

2.0 HISTORICAL REVIEW

Because of renewed interest in conducting military and civilian operations in space, developing a large power source with high power density has re-emerged as a national priority. Within the federal government, organizational changes are occurring at this time to meet the national need for the development of space nuclear power systems.

Although high power density requirements (40 to 50 W/kg) can easily be accomplished by using nuclear power systems, such systems require an adequate radiation shield to attenuate core radiation to acceptable dose levels at the prescribed dose plane. At the time of the SNAP program closeout, extensive experimental testing of candidate shielding materials had been performed. This testing also investigated the application of numerous neutron transport codes to insure that the dose requirements were met at the dose plane. However, as the operating power levels reached the multi-kilowatt range, the need to study the thermal performance of the shield became apparent. Unfortunately, SNAP program funding was cut off before many significant questions concerning shield thermal analyses were answered.

Sections 2.1 and 2.2 discuss previous shielding work pertinent to space nuclear reactors; it focuses on neutronic analysis, thermal and stress analysis, and major issues regarding the performance of tungsten and lithium hydride shields. The discussion begins by reviewing previous shielding work for space reactors. The review is separated into the following areas: Space Shield Neutronics Analysis, Space Shield Thermal Analysis, and Lithium Hydride Shield. Experimental results of shields using lithium hydride for neutron attenuation are discussed in

TABLE 2.1-1
Summary of Radiation Shield Designs for Space

| Reactor | Power Level | Time Frame | Gamma | Neutron | Dosage Requirements | Status | Remarks |
|---|--|------------------------|-------------------------------|--|---|---------------|---|
| SNAP 10A [Scheaffer, 1973] | 0.5 kW _e | Early '60's | None | LiH | γ 's: 10^7 RAD @100 ft n's: 10^{12} nvt @100 ft and flown Over 1 year | Built, tested | Only U.S. reactor flown. Fast neutron flux higher than predicted due to scattering around shield |
| SNAP 50/SPUR [CNM-5869, 1964] | 300-1200 kW _e | 1964 | None | Li ⁷ H ment (one) LiH | Shadow shield: 5 m ² /hr 40 ³ 5×10^6 -- 10^3 nvt @ 12.8 m | Paper studies | For unmanned mission, preliminary design. Two region shield. |
| SNAP 8 [Masora, 1973] | 30-60 kW _e | 1960's- early '70's | N | LiH | | | Built development. Higher power level led to metal shields enrichment of Li-7 to reduce internal heating. |
| Advanced hydride/ 5 kW [Keshishian, 1973] | 5 kW | Early '70's | Borated Stainless Steel | LiH | γ 's: 10^6 rad @100 ft n's: 10^{12} nvt @100 ft Over 5 years | Paper studies | At program closeout, need for additional thermal analysis was documented. |
| Potassium heat pipe reactor [Engle, 1971] | 450 kW _e 1780 kWh | Early '70's | N | LiH | 3 mrem/hr @100 ft. Within shadow. 300 mrem/hr @100 ft. Outside shadow. | Paper studies | Shielding materials layered to optimize for weight, without consideration of varying thermal expansion coefficients. |
| 40-kW thermionic [Gulf GA, 1971] | 40 kW _e | Early '70's | N | LiH | Side shield: 100R/hr @ 30.5 m | Paper studies | Reactor designed for manner missions. Shield layered to minimize weight. |
| SP-100 reactor [JPL, 1982] | 100 kW _e (1.6 MW _{th}) | Early '80's | N | LiH | γ 's: 10^6 rad @25 m n's: 10^{12} @25 m Over 7 years | Paper studies | Consideration being given to the need for active cooling of shield. |

Legend: γ 's - Gamma absorbed dose
n's - Neutron fluence

a subsequent section. With the rapid advances in both the hardware and software necessary to perform computational analyses, the space reactor engineer has tools available to him that the SNAP engineers did not. Section 2.3 provides a brief review of developments in numerical analyses.

2.1 Review of Previous Shield Design for Space Reactors

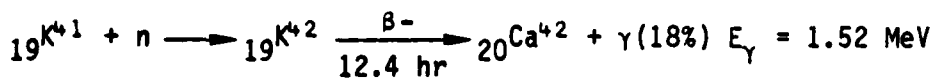
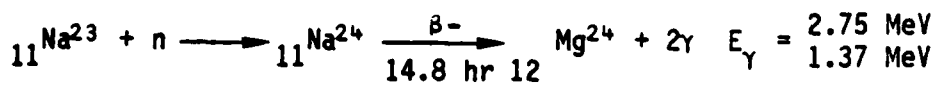
In the 1960s and early 1970s, much work was done on the development of radiation shields for space reactors. Table 2.1-1 is a composite picture of the major reactor shields developed during the SNAP program. Although other space reactors reached some level of design and testing, those listed in Table 2.1-1 represent the space reactors with the best documentation currently available. Tracing the development of space reactor shields shows the increasing sophistication of neutronic analysis and design, from the SNAP 10A shield that had no gamma attenuation to the potassium heat pipe reactor shield that is layered and optimized for weight [Engle et al., July 1971]. The table also implies the increasing concern with the need for thermal and structural analysis as the reactor power level increases [Keshshian et al., 1973].

The selection of radiation shielding materials is based on the shield's ability for attenuating core radiation to acceptable dose levels at the prescribed dose plane. The dose plane limits are functions of the mission for which the power is being supplied. For instance, the SNAP missions were primarily unmanned and, therefore, required only shadow shields. Table 2.1-2 lists the dose criteria specified for electrical component shielding in the SNAP 10A.

Table 2.1-2:
Dose Criteria for SNAP 10A for Five Year Lifetime
[Keshishian et al., 1973]

| <u>Radiation Source</u> | <u>Dose Limit (20 m from core center)</u> |
|--|---|
| Neutrons fluence ($E_n > 0.1$ MeV) | 10^{12} NVT |
| Gamma rays absorbed | 10^6 RAD |

2.1.1 SNAP 10A Shield. The SNAP 10A was a 0.5 kW_e reactor, thermoelectric system launched on April 3, 1965. Figure 2.1-1 is a schematic of the reactor system. Although expected to operate for at least 6 months, the reactor shut down after only 43 days of operation due to an apparent failure of a voltage regulator. Post-flight shield analysis revealed that the fast neutron flux densities were underestimated by a factor of 6.5 to 7.8, while the gamma fluxes were within 10 percent of pre-flight projections. On-board measurements were made with a Np-237 fission chamber for fast neutron fluxes, U-235 fission chambers (one cadmium wrapped) for thermal neutron fluxes, and a CO₂-filled ion chamber for gamma detection. Detectors were located at the SNAP-Agena mating plane in Figure 3.1-1. The higher than expected fast neutron fluxes were caused by the scattering from the control drums, and from the sides of the reactor; in addition, the NaK coolant piping came out from the core and curved around the shield. The use of NaK served as a source of secondary gammas by the following reactions:



code called "DEAF"; internal heating was not considered due to the low core operating power level (5 kW_e). Even at such low power level, it was concluded that "...passive control of shield temperature within a band smaller than 150°F is not considered a realistic objective" [Keshishian et al., 1975]. In addition to the induced thermal stresses in the radiation shield, the following areas were considered to require additional research:

- Refinement of the meteoroid equation to determine the probability of holes in the shield.
- Formulation of a model to describe the hydrogen migration in the shield as a function of both temperature and geometry.
- Determination of the temperature profile of the LiH shield under most probable (steady-state) operating conditions.
- Determination of the rate of plugging of punctures by LiH (assuming condensation at the hole) as a function of temperature and meteoride hole size.

The Keshishian, et al. work (1973) was the latest of the publications dealing specifically with space shielding.

Earlier works which included some thermal analysis of radiation shield are those of Beiriger (1968) and Thompson and Schwab (1969). Beiriger (1968) conducted a thermal analysis of Pb-W-LiH shield and a W-LiH shield, with the LiH separated by insulation for the Pb-W-LiH case. The steady state operating powers of the reactor were 600 and 1200 kW_{th} , and the heat generated in the shield was radiated to the reactor vessel (top and bottom at 978 K) and then to space (at 311 K). The emissivity of all radiating surfaces was 0.8. For the Pb-W-LiH

Table 2.1-4

HPR Radiation Shield Characteristics [JPL (1982)]

| | |
|----------------------------------|------------------|
| Neutron fluence | 10^{12} NVT |
| Gamma dose | 10^6 Rad/Si |
| Cone half-angle | 15 deg |
| Axial thickness | 0.80 m |
| Side length | 0.80 m |
| Maximum diameter | 1.05 m |
| Internal thermal power generated | to be determined |
| Component mass | |
| mass of LiH and container (kg) | 485 |
| Mass of tungsten (kg) | 305 |
| Total shield mass (kg) | 790 |

2.2 Space Shield Thermal Analysis

The area of thermal analysis of a space reactor's shield has not been covered extensively in the literature. Since the early 1970's, NASA funded research has focused on thermal analyses of heat shield performance upon reentry into the earth's atmosphere, with particular emphasis on the space shuttle.

Keshishian et al., in their work on the shield design of the ZrH₂ reactor, were concerned with the applied stresses on the W-LiH shield during lift-off. They were particularly concerned with the accompanying displacements in the shield and the effect on the structural support components and coolant pipes through the shield.

An area which remained unresolved at program closeout in 1973 was the determination of stresses induced in the shield outer casing, internal structure, and piping ducts. These stresses are caused by large differences in thermal expansion coefficients of LiH and stainless steel, particularly in the presence of thermal gradients during the shield casting cycle and during system transient and steady state operation. The shield temperatures were calculated using a computer

Figure 2.1-6 Contours of Neutron Fluence Over 7 Years,
1.33 MW_{th} Power Level for Los Alamos HPR

$$\phi_{out} = 5.03 \times 10^{12} \text{ n/cm}^2\text{-s}$$

nvt = 7-year Neutron Fluence at 1.33 MW_{th} Power Level

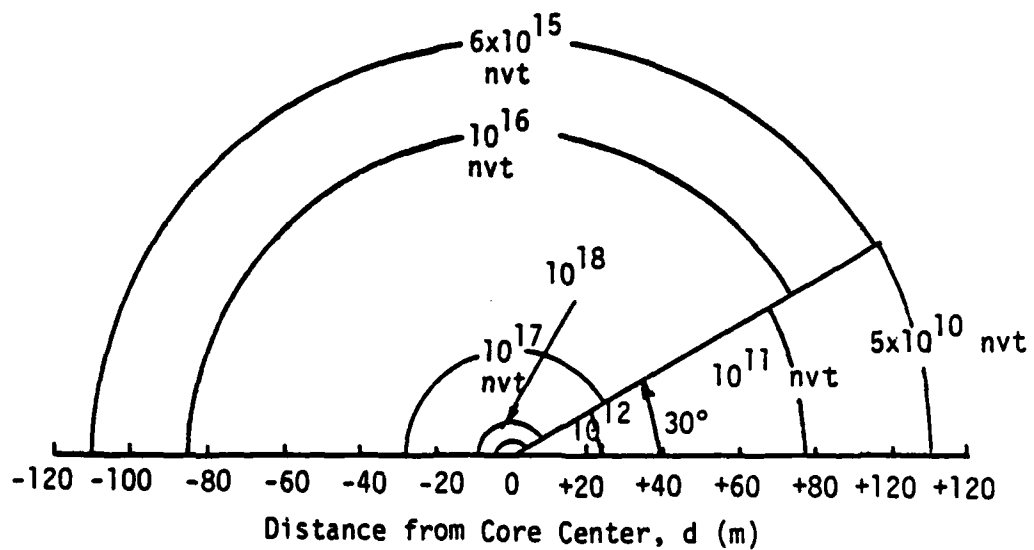
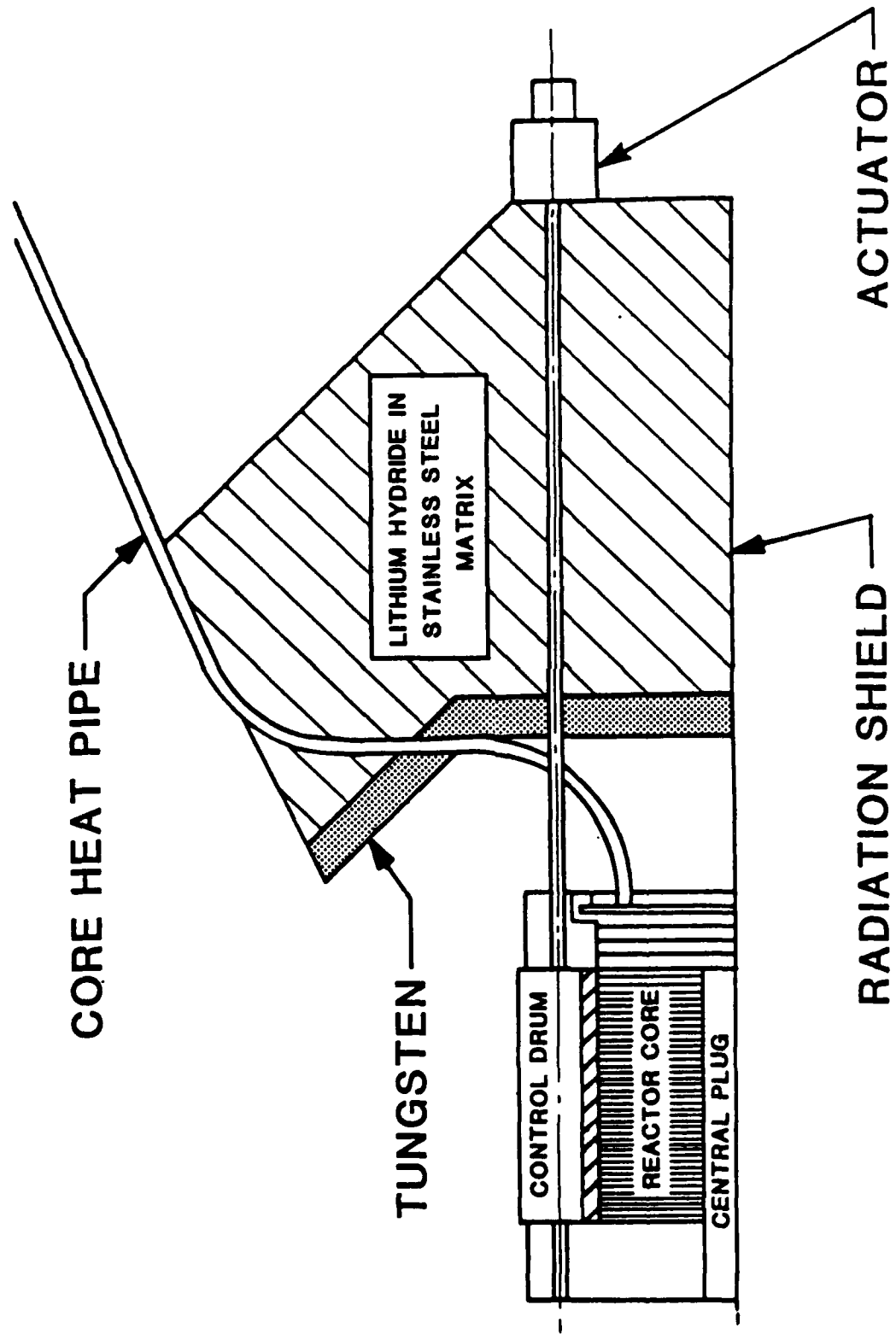


Figure 2.1-5 Reactor Shield Design for the Los Alamos Heat Pipe Space Nuclear Reactor (HPR)



interesting observation regarding the shield design of Figure 2.1-3 is that ~70.5 cm of LiH was required to adequately shield a crew from neutrons. As we shall soon see, about the same thickness was deemed necessary for electronic equipment protection for the SP-100 reactor.

2.1.6 SP-100 Reactor Shield Design. Figure 2.1-5 is a side view of the radiation shield for the Los Alamos heat pipe reactor (HPR) [LANL, 1982 and JPL, 1982]. Gamma attenuation was achieved with a layer of tungsten and neutron attenuation with lithium hydride shield. The characteristics of the shield (which are tentative at this stage) are included in Table 2.1-4.

Figure 2.1-6 is a plot of contours of neutron fluence over a seven-year lifetime for a $1.33 \text{ MW}_{\text{th}}$ average power level. The current SP-100 design calls for the reactor to operate at a slightly larger thermal output of 1.66 MW. From Figure 2.1-6, one can readily observe that the total neutron dose must be attenuated by five orders of magnitude in order to meet the dose plane requirement of $1 \times 10^{12} \text{ NVT}$ at 25 m. Using the Monte Carlo code (MCNP), LANL researchers have determined that 0.80 m of LiH are necessary to achieve the desired dose rate. The heat pipes, which transfer the reactor power to the thermo-electric conversion system, subtend part of the radiation shield as shown in Figure 2.1-5. This pathway through the shield is a source of concern from the standpoint of heat transfer from the heat pipe to the shield (somewhat offset with multi-foil insulation wrapped around the heat pipe), thermal expansion compatibility with shield materials, and radiation streaming through these ducts.

Figure 2.1-4 Variations in W and LiH Shield Thicknesses for a Dose Constraint of 1.2 rem/hr (45.71 m dose plane) for the ORNL Heat Pipe Reactor Operating at 1700 kW_{th}

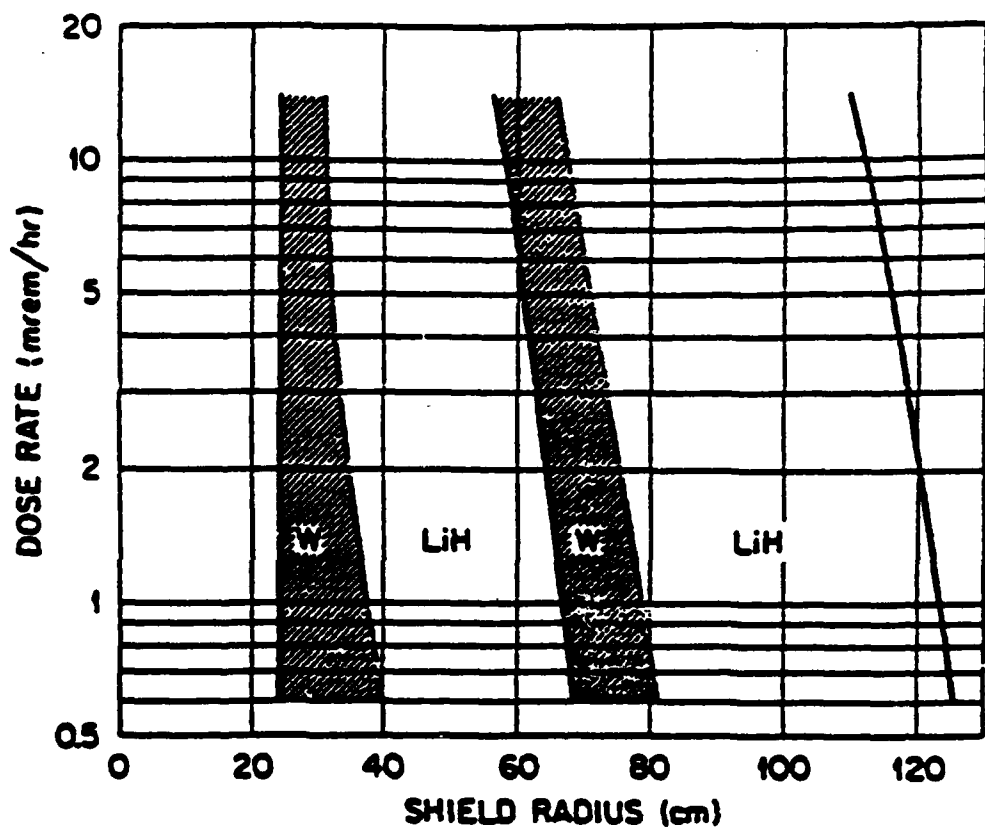
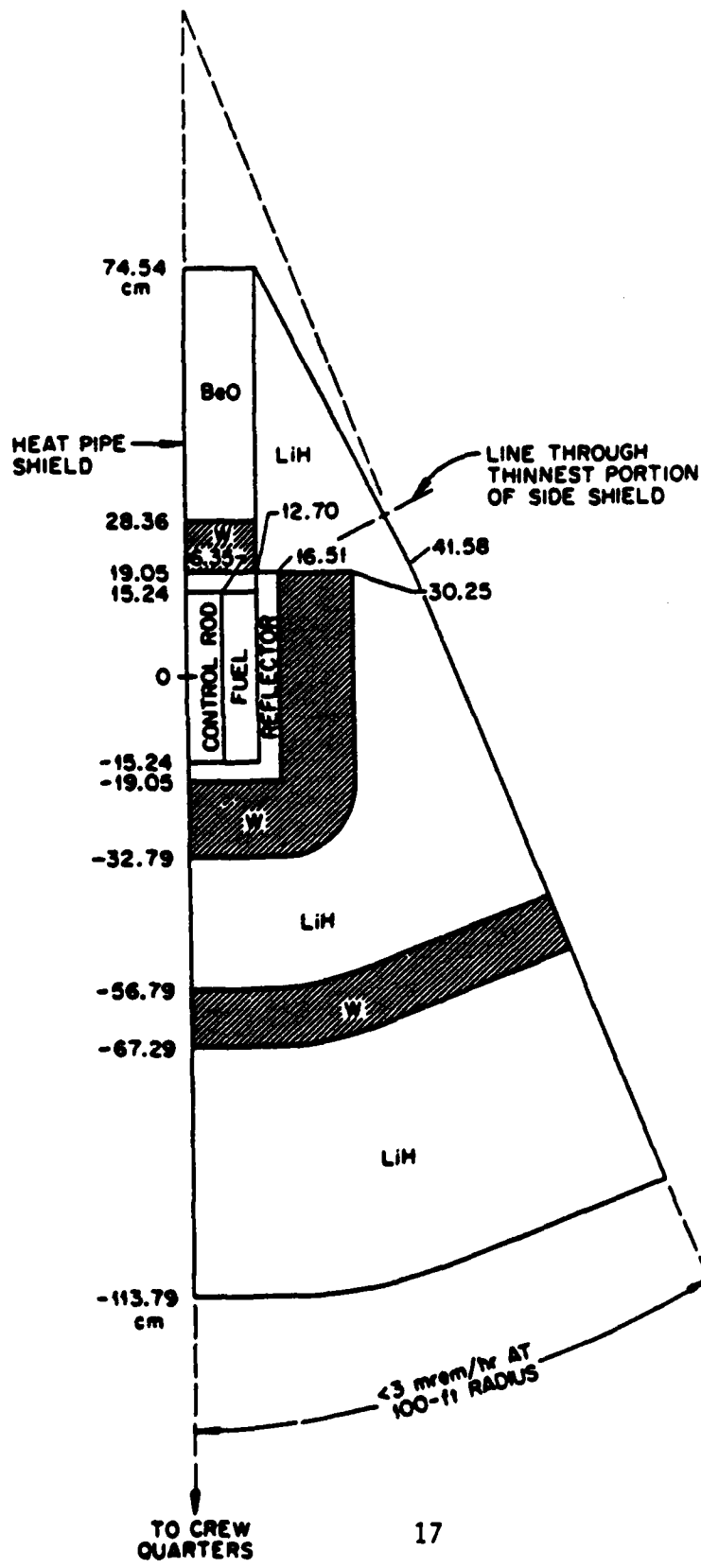


Figure 2.1-3 ORNL Heat Pipe Reactor



2.1.5 ORNL Shield Design. In 1971, ORNL published an optimized shield design for a stainless steel, potassium heat pipe reactor, fueled with uranium nitride fuel and operating at either 450 kW_{th} or 1780 kW_{th}. The reactor system of Figure 2.1-3 is for the 1780 kW_{th} design. The dose constraints were 3 mrem/hr within the shield shadow and 300 mrem/hr outside the shadow at 32.81 m radius [Engle et al., 1971]. The neutronic model used in the analysis was the ASOP code (ANISN Shield Optimization Program) using 1-D discrete ordinates transport theory and 3-D weight functions. The optimization technique calculated the dose rate for a given geometry and the first and second derivatives of the dose rate with a design variable (that is, weight) when the thickness of material was perturbed. The constraints were then the prescribed dose rate at the 32.81 m dose plane and a selected tolerable range of d(dose)/d(weight).

The heat pipes were assumed to protrude through the shield, as with the SP-100 reactor [LANL, 1982 and JPL, June 1982]. However, the ORNL approach considered that the temperature near the heat pipe would be above the LiH melting point (960 K) and BeO was used in this region instead. For a given dose rate (1.2 rem/hr at 45.71 m), the thickness of BeO required was 1.5 m, or 0.57 m thicker than the equivalent LiH thickness of 0.93 m. Results of required thicknesses of W and LiH, for an operating power level of 1780 kW_{th} are included in Figure 2.1-4. As shown in this figure, changing the dose rate requirement changes only the thicknesses of the first layers of W and LiH. The optimization of the material thickness in the shield for minimizing weight is based on the need to layer the gamma and neutron attenuating materials to minimize the effects of secondary gamma production on the dose plane. An

will differ for each reactor, the contribution of secondary gammas is worthy of note and must be considered in the thermal analysis of radiation shield. The neutronic analysis of the shield was performed using the following codes:

- GAM II and GATHER II programs from 26 group cross sections (P_3 approximation)
- ANISN program for radiation transport ($S_{16}-P_3$ approximation in 1-D)
- OPEX II for optimization of shield thickness

The effects on dose rates of perturbing the thickness of a given region of the shield was determined as:

$$D_i = C_i \exp(-\sum_j \mu_{ij} t_j),$$

$$D = \sum_i D_i,$$

where:

D_i = the i th component of the dose rate

D = the total absorbed dose rate

C_i = a constant determined from perturbing the thickness

μ_{ij} = the i th component attenuation of the j th region

t_j = the thickness of the j th region

The depleted uranium-LiH shield had a weight of 25,300 kg, and the W-LiH shield had a weight of 28,500 kg. However, these results may be misleading since using uranium near the reactor core is not desirable because excessive fissioning of uranium can cause an appreciable increase in heat generation and introduce intolerable swelling of the uranium shield [Kaszubinski, July 1968].

for a 2.2 MW_{th} reactor output. The analysis apparently was for a manned mission because the reference dose requirement was 2 mrem/hr at a distance 20 m from the core. (RBE = 7 for fast neutrons) [Lahti and Hermann, 1982].

Table 2.1-3:

Materials Considered for Gamma Attenuation Shield Design
of the 5 kW_e Thermionic Reactor System [Keshishian et al., 1973]

| | |
|--|---|
| 1. Lead | <u>Rejected</u> , because of its low melting point (600 K) |
| 2. Ta-W (10 wt%) | <u>Rejected</u> , because of the secondary gammas from Ta |
| 3. U-Mo (20 wt% U ²³⁵ and 80 wt% Mo) | Low weight, but was <u>rejected</u> because of its high internal heating and temperature instability. |
| 4. a. W alloy (95 wt% W) b. stainless steel, c. natural and enriched B ₄ C, and a borated stainless steel | <u>Evaluated</u> , based on 1-D calculations |

The contributions of radiation sources to the 2.0 mrem/hr dose rate were as follows: 15 percent from core neutrons, 1 percent from neutrons generated in depleted U, secondary gammas from reflector and shield accounted for 70 percent of dose for W and 55 percent of dose for U, remaining 15 percent of dose are from inelastic scatter gammas and fission gammas for U. Although the radiation source contributions

calculations showing less weight for the same gamma attenuation. However, this result apparently is the only time that tungsten did not emerge as the gamma attenuation material. Tungsten, although costly, is regarded as the most efficient (from a minimum-shield weight standpoint) material for gamma radiation attenuation.

Table 2.1-3 is a listing of the material considered for gamma attenuation in the 5 kW_e thermionic reactor.

The following codes were used in the analysis of the 5 kW_e reactor shield:

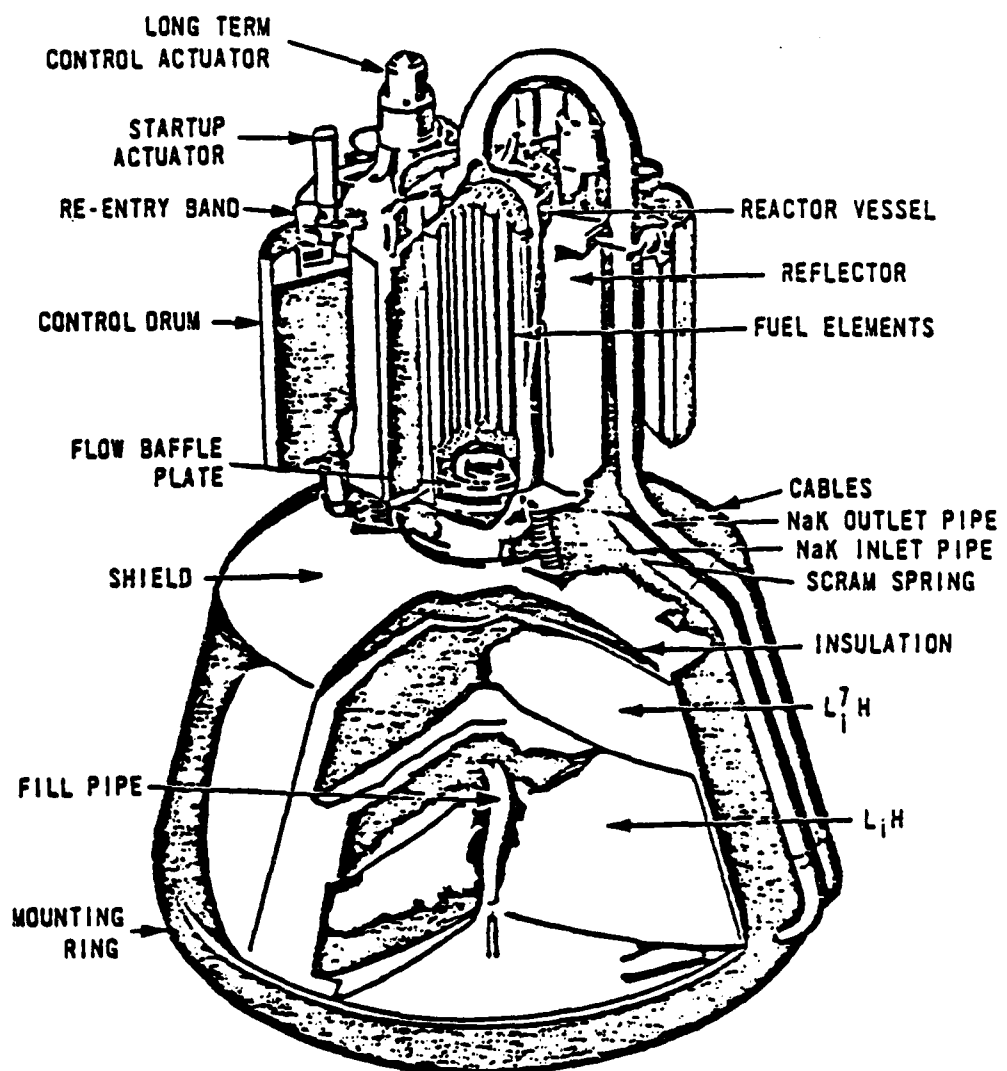
- 1D ANISN Transport Code,
- QAD for gamma fluxes,
- DOT/SPACETRAN Code, and
- DDM (DOT-DOMINO-MORSE) Code.

The learning point here is that no single neutronic code was used as an industry average and selection of a particular code generally depends on the application. Thermal analysis information of the shield was also reported and will be discussed in a later section.

The 40 kW_e thermionic power system [Gietzen et al., 1974] was designated to be launched by the space shuttle in two loads because of its large mass (12,000 kg); most of which was the shielding necessary for the manned space station. In a second design, the power system was designed to be tethered 2 miles away from the space station, reducing the shielding requirements and the total mass of the system by one-half.

2.1.4 NASA-Lewis Shield Design. In September 1969, NASA-LeRC published a comparison of tungsten-LiH and depleted uranium-LiH shields

Figure 2.1-2 SNAP 8 Reactor



Neutron attenuation for the SNAP 10A was accomplished using a lithium hydride shield. No gamma shielding material was included in the shield design because of the low power level of the core. [Schaeffer, 1973]

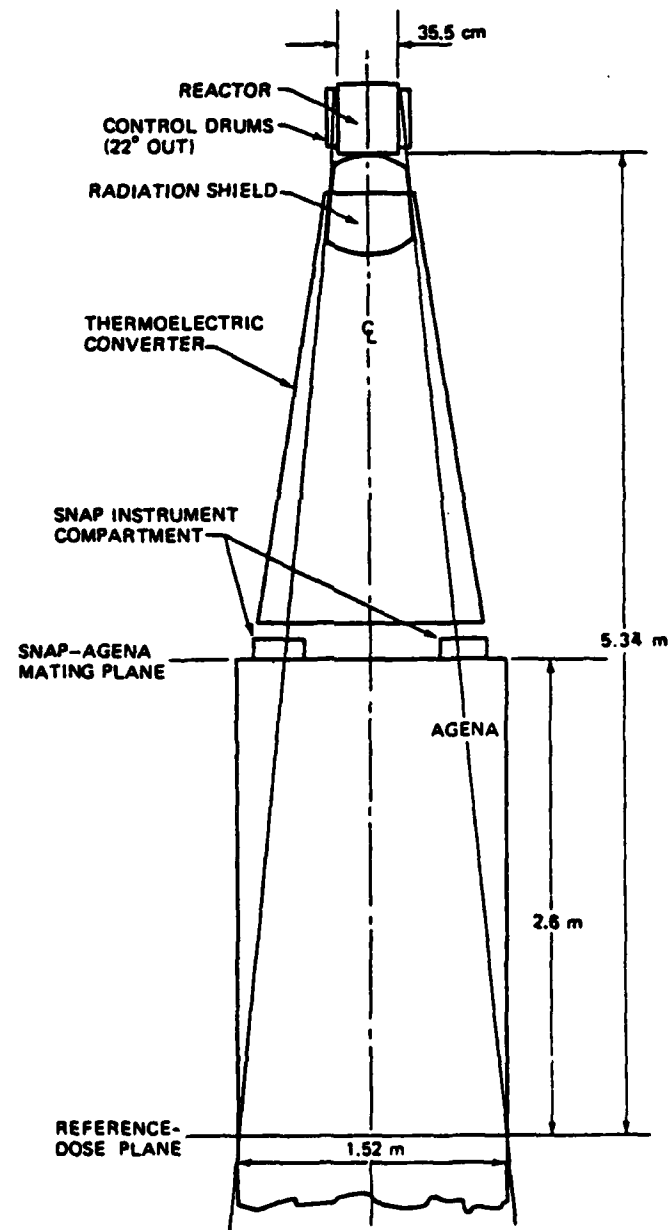
2.1.2 SNAP 8 Reactor Shield. The SNAP 8 reactor program began in the early 1960s and continued into the early 1970s. The reactor was intended to provide 30-60 kW_e of power for both manned and unmanned missions. The two SNAP 8 reactors that were built never got past the ground test stage. From Figure 2.1-2, the radiation shield consisted of tungsten for gamma radiation, and lithium hydride enriched to 99.99 wt.% Li-7 for fast neutrons. The enrichment of Li-7 (92.6 at% natural abundance) was done to reduce the internal heat generation within the shield caused by the (n, α) reaction within Li-6 (7.4 at% natural abundance) [Masora, 1973].

When the SNAP reactor developmental programs were stopped, unresolved concerns regarding the thermal and stress analysis as well as the prolonged performance of the radiation shield (for 3 to 7 years in space environment) remained.

2.1.3 Thermionic Reactor Shield. In the early 1970s, the use of in-core thermionic conversion for space was introduced. The Atomics International 5 kW_e thermionic reactor [Keshishian et al., 1971], as an auxiliary power supply of unmanned space applications, and the Gulf General Atomic design of 40 kW_e power system for a manned space laboratory [Gietzen et al., 1970] are two examples of such effort.

Shield design for the 5 kW_e thermionic reactor included borated stainless steel and lithium hydride. The selection of borated stainless steel over stainless steel and a tungsten alloy was based on 1-D

Figure 2.1-1 SNAP 10A Reactor and Subsystem Overview



shield, the maximum temperature of the LiH was 795 K at 600 kW_{th}, and 821 K at 200 kW_{th}. The W-LiH temperature analyses were not reported since the melting temperature of the LiH was exceeded. Unfortunately, details regarding how the temperature values were generated were not reported.

Thompson and Schwab (1969) examined the accuracy of several neutronic models in comparing the nuclear heating within the ZrH₂ reactor shield [Keshishian et al., 1973]. The results indicated that the QAD (point kernel) code and the ANISN code overestimated the heating in the shield due to primary and secondary gammas by a factor of 2, when compared to the DOT (discrete ordinates) code. This overestimation was corrected by "tuning down" the fluxes until agreement with DOT fluxes was reached. However, it was not clear how the DOT code results were calibrated to serve as the benchmark.

2.2.1 Lithium Hydride Shield. Lithium hydride, although brittle at elevated temperature, was recommended as the material for space power nuclear reactors because of its high hydrogen content, low weight density (0.72 gm/cm³), high melting point (960 K), relatively low dissociation pressure, very high effective neutron attenuation coefficient, and its ability to capture neutrons without releasing gamma rays. The major thermal concerns were the very low thermal conductivity and the need to maintain the temperature of lithium hydride between 600 and 680 K [Welch, 1967a].

The widely accepted temperature range of 600 K (620°F) to 680 K (769°F) for the LiH were based primarily on the data of Figures 2.2-1 and 2.2-3. From Figure 2.2-1, the volume expansion of LiH was projected to remain less than 6 percent for fast levels of 2×10^{20} NVT or

Figure 2.2-1 Volume Expansion of LiH(Nat) as a Function of Neutron Fluence and Temperature

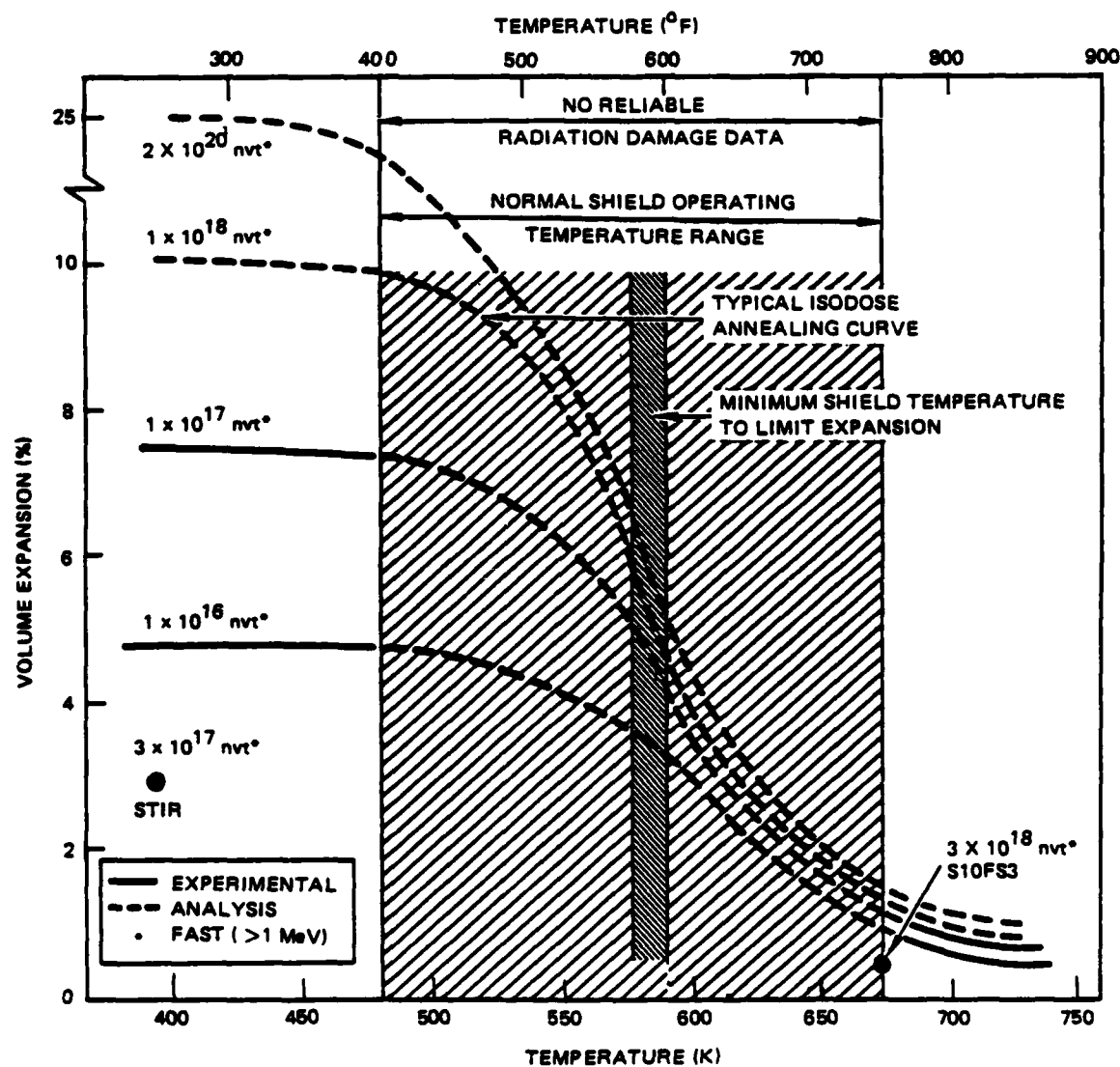
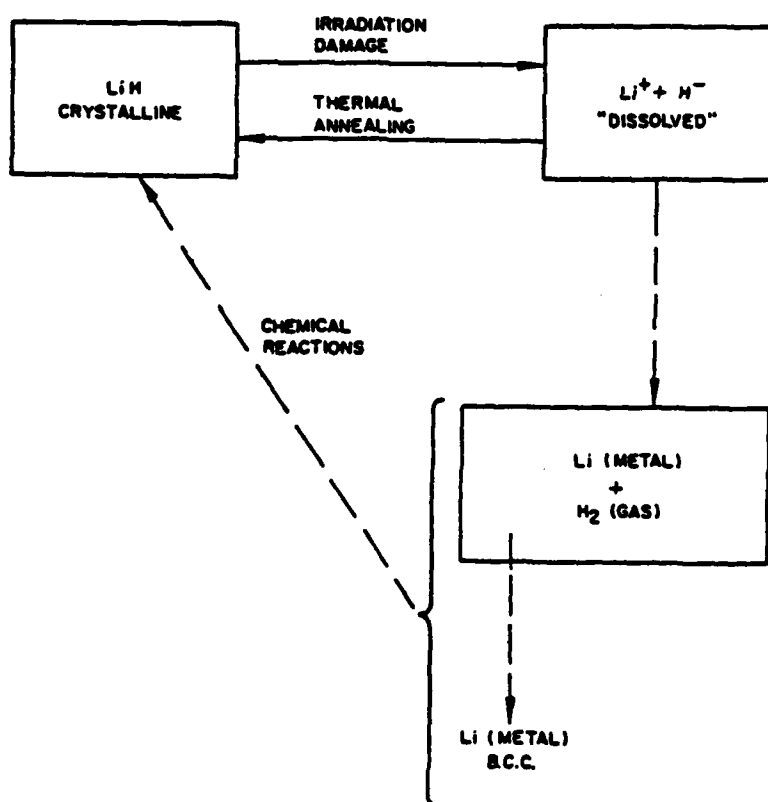


Figure 2.2-2 Principal Reactions in Irradiation Damage of Lithium Hydride Systems



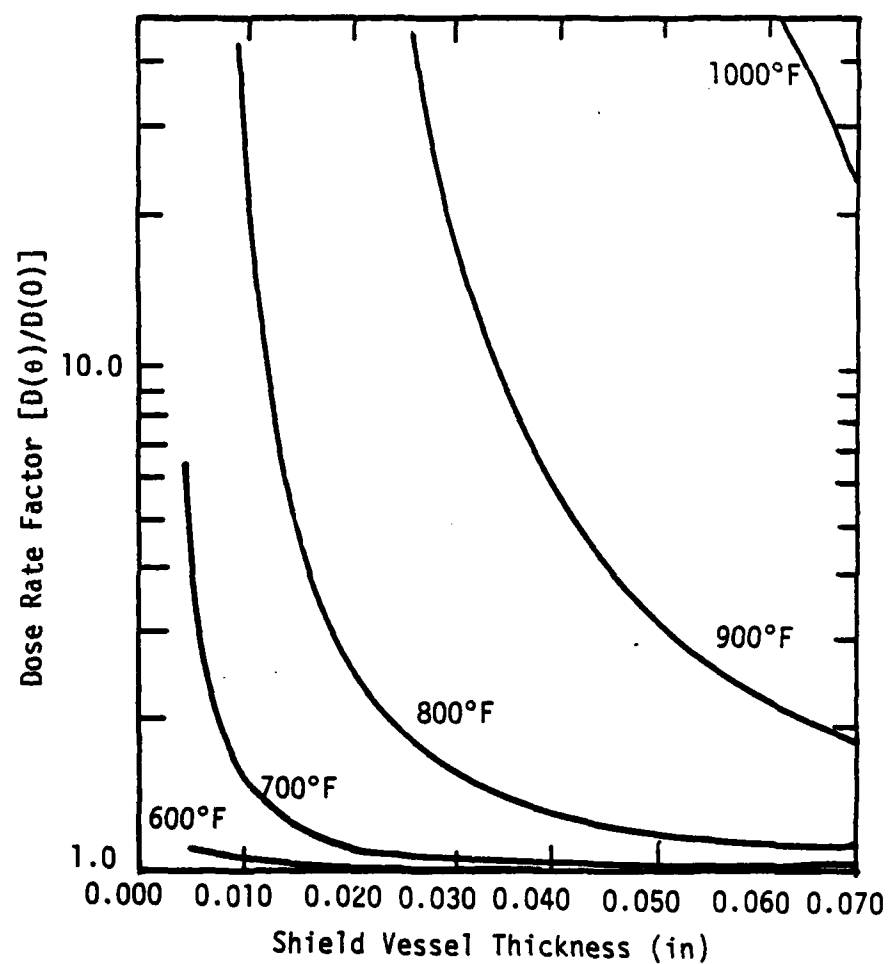
less at LiH temperatures of 600 K (620°F) or greater. Since cast or cold-pressed LiH is generally less than 94 percent of theoretical density, the volume expansion due to irradiation at temperatures in excess of 600 K could be handled without any structural damage.

Several theories were presented to account for the volume expansion as a function of neutron fluence and shield temperature. Willis of Atomics International proposed the explanation of Figure 2.2-2. [Welch, 1967c]. This argument was that the LiH crystal bonds were constantly being broken by the fast neutrons, resulting in lithium and hydrogen ions. The separate ions could either recombine to form LiH, or neutralize to separate lithium atoms and hydrogen gas. The reaction rate dictating which process dominated was strongly influenced by the system temperature. As the temperature increased, the thermal annealing reaction rate of the LiH recombination increased rapidly. Since a lithium metal atom occupies ~28 percent more volume than an LiH molecule, at lower temperatures the large volume expansion of Figure 2.2-1 might be expected.

However, the originator of Figure 2.2-1 points out that the data at temperatures above 470 K (and at lower temperatures for $NVT > 1 \times 10^{17}$) was not based on experimental findings and must be considered speculative [Welch, (1967c)]. Therefore, the lower bound of 600 K for LiH temperature might well have been overly conservative and an issue requiring further investigation.

Typical shield casing thickness designs (that is, Type 316 stainless steel) in the SNAP program were 0.15 to 0.25 cm (0.06 to 0.10 in). From Figure 2.1-3, one readily observes that for typical shield casing the dose rate should remain constant for temperatures below 680 K

Figure 2.2-3 Increase in Dose Rate After 10,000 Hours Due to Meteoroid Puncture of Shield Outer Casing with Variations in Casing Thickness and LiH Temperature



during prolonged exposure of 10,000 hours to meteoroid bombardment. (Dose rate increase is proportional to hydrogen loss through the puncture holes.) For a shield partitioned into several regions, this maximum temperature constraint would apply only to those regions subject to meteoroid impact. Thus, the inner regions of the LiH would not be subject to this constraint for a compartmentalized shield.

Based on these figures, many engineering issues were raised. The first was whether the dissociated hydrogen in the LiH would migrate quickly to the cooler regions because of the expected steep temperature gradients in the LiH, thus escaping faster than assumed in Figure 2.1-3. To answer this question, a slab of LiH 0.66 m thick was subjected to a temperature difference of 550 K (500°F) to 866 K (110°F) for periods of 1000 and 2000 h. The results showed that the maximum migration of hydrogen was 3.3 percent.¹ This value was probably too high because of leaks detected in the system; the migration occurring in the gas phase concomitantly increases with an increased surface area and path size. In turn, this increase is controlled by the rate of diffusion of H₂ to the surface of the LiH crystal.

The second issue was whether the interaction of molten LiH and stainless steel² would affect the H₂ diffusion rate through the stainless steel casing. The results of an experiment measuring this effect showed that the surface action of LiH and stainless steel did not have

¹ Maximum migration percentage determined from:
$$\% = \frac{(\text{Ave H content} - \text{Min H content})}{\text{Ave H content}}$$

² The later LiH shields were manufactured by casting molten LiH into a stainless steel matrix and heating that shield to 1200°F to outgas any LiOH impurities.

any impact on the H₂ diffusion rate. However, surfaces of LiH (both external boundaries and internal along cracks and crystal boundaries) will dehydride and metallic Li will form, while the LiH remains crystalline. The H₂ diffuses more slowly through the LiH crystal than through the capsule wall. The effects of hydrogen diffusion on the heat transfer properties and on the overall shielding performance were not reported.

2.2.2 Fabrication of LiH Shield. During the casting of the LiH into the stainless steel matrix, approximately 3 to 6 percent volume voids remained after solidification. The void problem was overcome by backfilling with metallic Li. This, in turn, reduced the number of cracks and added structural integrity during lift-off. (An unanticipated advantage of an increase of 15-30% in the bulk thermal conductivity of the Li-LiH shield was also realized.) There was concern that the Li would interact with LiH at operating temperatures. A summary of Li-LiH at various temperatures and periods of time is shown in Figure 2.2-4. At temperature near 588 K (600°F), very little interaction after 4000 h occurred; however above 810 K (1000°F) substantial interaction after 4000 h took place. Hence if a portion of the LiH shield is subjected to the higher temperatures over long periods, the effects on thermal and neutronic properties (as well as stresses due to volume increases) would have to be accounted for. Once normal operation of the reactor in space begins, some additional cracking of the LiH can be anticipated. These results imply that maintaining the shield above the Li melting point (453 K) may allow for self-sealing of cracks within the LiH by molten Li present in the shield. These findings also support justification of keeping the upper temperature

Table 2.1-1. Observations on the Interaction of Lithium, Lithium-Hydride at 600, 900, and 1200°F for 500, 1000, and 4000 hours [Welch, 1967c].

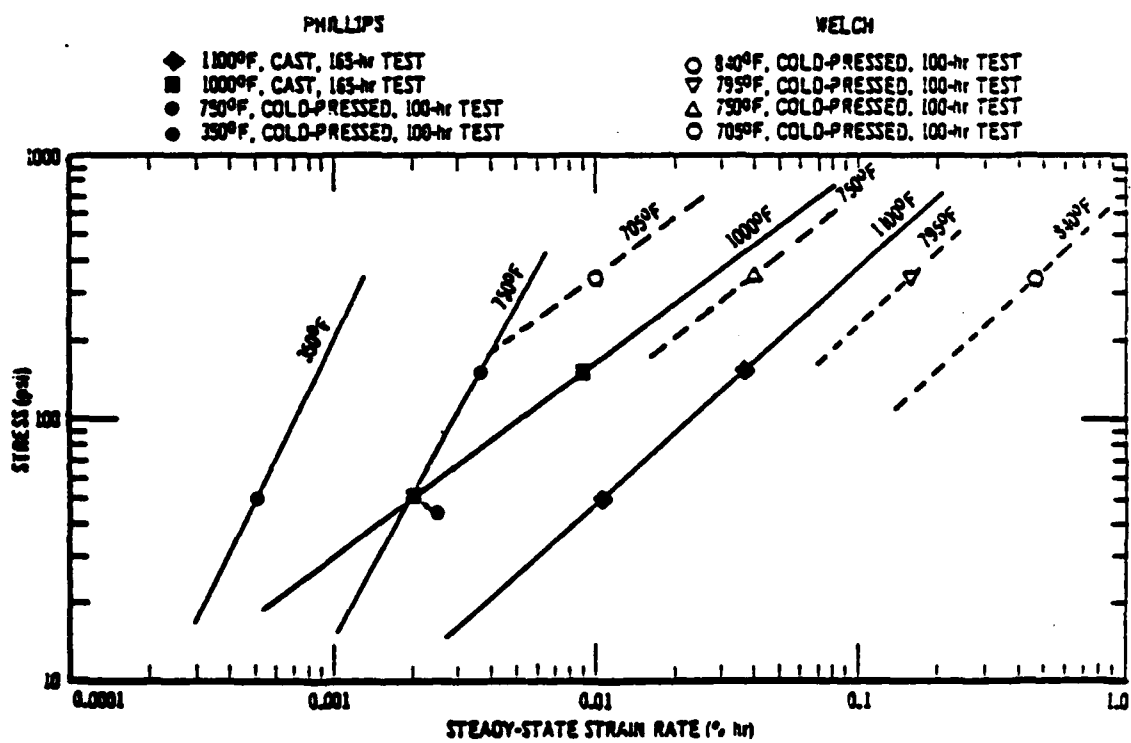
| Tempera-ture (K) | Time (hr) | 500 | 1000 | 2000 | 4000 |
|---------------------|--------------|---|---|--|---|
| 600°F (589 K) | | Li metal drained clean when capsule was inverted at 600°F. LiH appeared unchanged, although stuck to capsule. | Li metal drained from LiH sample. Apparently no change in the LiH pellet. | Li did not drain completely from LiH sample at 600°F. | Li did not drain completely from the LiH sample at 600°F. LiH crystals were observed in the Li at the bottom of the capsule. |
| 900°F (755 K) | | Li did not drain from LiH sample when inverted at 900°F. Surface of LiH appeared unchanged. | Same as 500-hr test, although capsule was kept inverted at 900°F for 3 days. | Capsule leaked air at pinchoff tube at edge of lower pinch. The walls of the capsule were coated with a 1/8-in thick layer of hard material. | Li did not drain completely at 900°F. Material at top and bottom both appeared metallic, but upper part had evidence of crystalline LiH. |
| 1200°F (922 K) | | The Li-LiH apparently interacted to form a liquid which flowed when the capsule was inverted and drained at 12°F. | The Li did not drain when inverted at 1200°F. LiH sample completely interacted, except for a small trace adhering to the capsule walls. | Only small flecks of LiH could be found in the Li matrix. Material did not drain at 1200°F. | Very small amount of liquid drained when inverted at 1200°F. Remainder of material appeared metallic with no evidence of crystalline LiH. |

limit of the LiH shield below 750 K. In general, one observes that cast LiH exhibits less creep under compressive loading than cold-pressed LiH. At 530 K, LiH behaves as a plastic; at 730 K, LiH becomes quite brittle. Some data regarding the compressive creep of LiH are shown in Figure 2.2-4. Cast LiH was considered better than cold-pressed LiH from both a thermal conductivity and time-dependent structural performance standpoint.

2.2.3 Emissivity Coating. To increase the emissivity of radiating surfaces, coatings are applied to the surface either before or after the casting process. A variety of coating materials and application methods was tested; after the tests, the coating was exposed to a vacuum (10^{-6} torr) at 800 K for 14 days to check for deterioration in emissivity. A second test was performed with the emissivity checked after the coating was subjected to hydrogen gas at 1300°F for five days. This test simulated the application of the coating prior to the LiH casting. Both chrome oxide and titanium dioxide retained high emissivities (0.87 to 0.90) in the vacuum, with the TiO_2 preferred if applied before casting, and the Cr_2O_3 preferred if applied after casting. However, a range of 0.85 to 0.90 for shield emissivities over the lifetime of the reactor system may not be reasonable because:

- a. One cannot necessarily extrapolate 5-14 days tests to the lifetime of the reactor (3-7 years).
- b. Testing has not been conducted to determine the stability of the coating in a high radiation field during prolonged operation.

Figure 2.2-4 Compressive Creep of LiH



In conclusion, many of the material properties of lithium hydride in a space shielding environment have been determined through experimental analysis. In particular, the interaction of lithium, lithium hydride and stainless steel at elevated temperatures had been examined closely. These results support previously stated requirements to maintain the maximum temperature of the LiH to the upper 600 K range.

2.2.4 Summary of Previous Space Shielding Research. Previous shielding work for space reactors was reviewed focusing on the areas of neutronic analysis, thermal, and stress analysis, and the performance of lithium hydride and tungsten shields. In the 1960s and early 1970s, much work was done on the development of radiation shields for space reactors. The major reactor shields were developed during the SNAP program. Tracing the development of space reactor shields, one observes the increasing sophistication of neutronic analysis and design from the SNAP 10A shield that had no gamma attenuation to the potassium heat pipe reactor shield that is layered and optimized for weight. There was an increasing concern with the need for thermal and structural analysis as the reactor power level increases.

Lithium hydride, although brittle at elevated temperature, had been recommended as the material for space power nuclear reactors because of its high hydrogen content, low weight density (0.72 gm/cc), high melting point (960 K), relatively low dissociation pressure, very high effective neutron attenuation coefficient, and its ability to capture neutrons without releasing gamma rays. The major thermal concerns were the very low thermal conductivity and the need to maintain the lithium hydride between temperature limits of 600 and 680 K during steady state operation. A minimum temperature of 600 K was recommended

to minimize radiolytically induced hydrogen dissociation from the Li metal, and the accompanying swelling of the shield. Above 600 K, the volume expansion of the LiH remained below 7 percent for a wide range of fast neutron fluences (10^{16} to 10^{20} NVT). Since the density of LiH after being cast into stainless steel matrix remains below 94 percent of theoretical density, this volume expansion does not cause structural deformation to the shield.

The upper operating temperature of LiH was limited to 680 K to reduce the effect of losing the dissociated hydrogen from the shield through the punctures caused by meteoroid impact. For typical shield outer casing thicknesses (0.06 to 0.10 in.), the dose rate at the dose plane would not change due to hydrogen loss after 10,000 hours if the LiH remained below 680 K.

Tungsten, although costly, was regarded as the most efficient (from a minimum-shield weight standpoint) material for gamma radiation attenuation. Depleted uranium's efficiency as a gamma attenuation material was similar to that of tungsten; yet it was much less expensive as tailing from fuel enrichment plants. However, using uranium near the reactor may not be desirable because excessive fissioning of uranium may cause an appreciable increase in heat generation and introduce intolerable swelling of the uranium shield.

The idea of crushing and pressing the tungsten and LiH into a single shielding material was explored briefly at the close of the SNAP program. While this first attempt produced a shield with significantly less structural strength of tungsten (and about half that of LiH), the idea of a composite shield remains virgin territory [Welch, 1967b].

The literature about the neutronic analysis of previous shield designs abounds. The evolution to weight optimized layered shields credits the advances in capabilities within the radiation transport community. However, a number of significant issues regarding thermal analysis of the shield remained at the time of the SNAP program close-out. Improvements in the skills and tools currently available to the nuclear and thermal sciences communities, allows for more efficient designs in subsystem such as the radiation shield. Advances such as more accurate cross section data, better numerical analysis methods, as well as increased capacities of digital computers encourage re-examination of designs completed before these tools were fully implemented.

Major unresolved thermal issues like the temperature range limitation of LiH, the need for active cooling of the shield, and the induced thermal stresses resulting in excessive cracking of the neutron shield are worthy of further study. Another major environmental change is the need for more stringent allowable dosages due to the increased sensitivity of modern electronics equipment. The off-the-shelf shield designs coupled with the increased limitations of allowable payloads of the space shuttle as the delivery system (in place of the rocket delivery systems), will not prove to be acceptable.

2.3 Developments in Numerical Methods. As the SNAP Program began winding down, there were concurrent (but unrelated) rapid increases in the capacities of digital computers and application of the finite element (FEM) method to engineering mathematics. The concept of representing a solution as a series of known functions and unknown coefficients can be traced as far back as the 19th century [Kantorovich and

[rylor, 1958]. Galerkin first introduced his method of weighted residuals in 1915, and the concept of finite elements can be seen in work of Sizens in 1924 [Finlayson and Scriven, 1966].

Courant is generally credited with the first formal presentation of the finite element method in his approximate solution to the St. Venant torsion problem in 1943 [Oden, 1972]. However, the world was preoccupied with a war at that time and his results went largely unnoticed. About ten years later, this method (which resembled a form of the Ritz method) began to gain notoriety in a series of papers by Argyris and collaborators dealing with linear, structural analysis [Huebner and Thornton, 1982].

During the 1960's, the finite element method (the term officially coined by Clough in 1960), gained widespread use within the structural engineering community. The first use of FEM to perform temperature and structural analysis of 3D, axisymmetric bodies was also recorded [Wilson, 1965]. However, the mathematics community did not seriously develop the theoretical foundation for this engineering technique until the 1970's [Huebner and Thornton, 1982]. During this decade, the radiation transport community began to apply the FEM in the spatially (and sometimes, without success, angular) discretization of the Boltzmann Transport Equation [Wills, 1984]. Researchers were pleased to learn that the ray effects associated with discrete ordinates solutions were not seen in the FEM derived fluxes.

Recent publications from England have shown the versatility of using higher order projected methods to solve the first order, transport equation [Fletcher, 1983]. Wills demonstrated the use of a combination of flux spatial discretization with Lagrangian polynomials

For the 3-node, triangular element, the shape function of Equation 3.2-7 takes the following form:

$$N_i(r, z) = \frac{1}{2\Delta} (a_i + b_i r + c_i z) \quad (3.2-8)$$

here:

i = local node number (1, 2, 3)

Δ = area of triangle

a_i, b_i, c_i = shape function coefficients
(based solely on nodal position coordinates)

An advantage of triangular elements lies in the simplicity of integrating the shape functions over area or length. Equations 3.2-9 and 3.2-10 provide the formulas necessary for obtaining closed form solutions for the integration of any power and combination of nodal shape functions [Huebner, 1982].

$$\int_A N_1^\alpha N_2^\beta N_3^\gamma dA = \frac{\alpha! \beta! \gamma!}{(\alpha + \beta + \gamma + 2)!} 2\Delta \quad (3.2-9)$$

$$\int_{\ell_{12}} N_1^\alpha N_2^\beta d\ell = \frac{\alpha! \beta! \ell_{12}}{(\alpha + \beta + 1)!} \quad (3.2-10)$$

where: No's are subscripts

N_1, N_2 , and N_3 are the shape functions for nodes of triangular element; α, β, γ are arbitrary constants; A represents integration over the element area; ℓ_{12} represents integration over a line segment of the element.

The use of Equation 3.2-10 comes into play when the boundary conditions are incorporated in the system of equations to be solved.

3.2.2.2 4 Node Quadrilateral Elements. Similar to the triangular element, the 4 node quadrilateral element is comprised of linear

solution of a 2nd order, elliptic equation with a weak, symmetric formulation, many researchers have shown that only C_0 continuity is required [Huebner, 1982]. This result means that linear shape functions are admissible for all phases of this research.

An enduring issue within all computational communities is the advantages (and disadvantages) of the trade-off regarding many linear elements versus fewer higher order elements. Since this issue is outside the scope of this research, a decision was made at the outset to use bilinear elements. The radiation transport code, FEMP2D, uses 4-node quadrilateral elements; the heat transfer code, SHLDTEMP, and the stress/strain code, SHLDSTR, use 3-node triangular elements. For this reason, elemental matrices are formulated directly in global coordinates, thus eliminating the need for use of a Jacobian transformation.

3.2.2.1 3 Node Triangular Elements. When formulating the algebraic system of equations for the temperature and stress analysis, triangular elements were used to discretize the shield. Figure 3.2-2 is a visualization of how a single triangular element approximates a 3-D axisymmetric body.

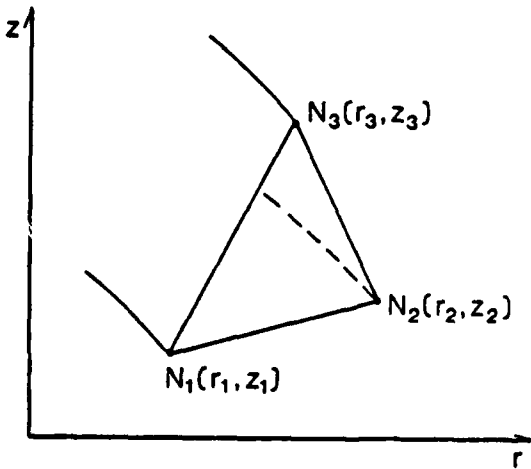


Figure 3.2-2: 3-Node Axisymmetric Triangular Element

series of symmetric equations, which are easily solved on a digital computer. Also, from an engineering standpoint, any problem for which the governing equation and boundary conditions are known can ultimately be formulated into a solvable system of algebraic equations using Galerkins method.

As shown in Equation 3.2-1, the state variable, u^* , can be expanded in terms of a series of unknowns, u_i , and approximating functions, N_i . In a similar manner, an elemental state variable can be defined as a finite series of unknown nodal values, or,

$$u^{(e)}(r, t) = \sum_{i=1}^N N_i(r, t) u_i(t) \quad (3.2-7)$$

where $u^{(e)}$ is the element state variable, N_i is the shape function, and u_i is the nodal state variable.

The control volume of interest can then be discretized into a number of elements, which are interconnected by continuity requirements at each node. The elemental state variable of Equation 3.2-7 is substituted as before, into Equation 3.2-6 to minimize the residual over the domain. The use of Equation 3.2-7 in the minimization of the spatially weighted residual is the basis of the finite element method. Of course, for a steady-state solution the time dependency of the nodal and element state variables vanish, and the resulting solution has a spatial dependency only.

3.2.2 Shape Functions. Focusing attention to the shape and test functions (which will be the same using Galerkins method), the type and order (if polynomial) of the function is directly related to the type of finite element used. The minimum order required for the element, in turn, is directly related to the order of the governing equation. For

where N_i are some arbitrary approximating functions. On the boundary, the conditions are:

$$u_s = f_s, \quad u_i = 0 \quad \text{on } S \quad (3.2-2)$$

where f_s is the prescribed boundary condition. Representing the governing equation as:

$$D[u(r, t)] - \frac{\partial u}{\partial t} (r, t) = 0 \quad t > 0 \quad (3.2-3)$$

where D is some differential operator which may include non-homogeneous terms, the problem can be reformulated with an approximate solution by substituting Equation 3.2-1 into Equation 3.2-3. This results in:

$$D[u^*] - \frac{\partial u^*}{\partial t} = R(u^*) \quad (3.2-4)$$

where $R(u^*)$ represents a residual resulting from the approximation to the exact solution, u .

The basic idea behind the Method of Weighted Residuals is simply to minimize this residual over the domain of the solution. This is accomplished by finding the value of u^* which minimizes the residual when spatially averaged over the volume against some weighting (test) function, v . The weighted residual to be minimized takes the form:

$$\int_V R(u^*)v \, dV = 0 \quad (3.2-5)$$

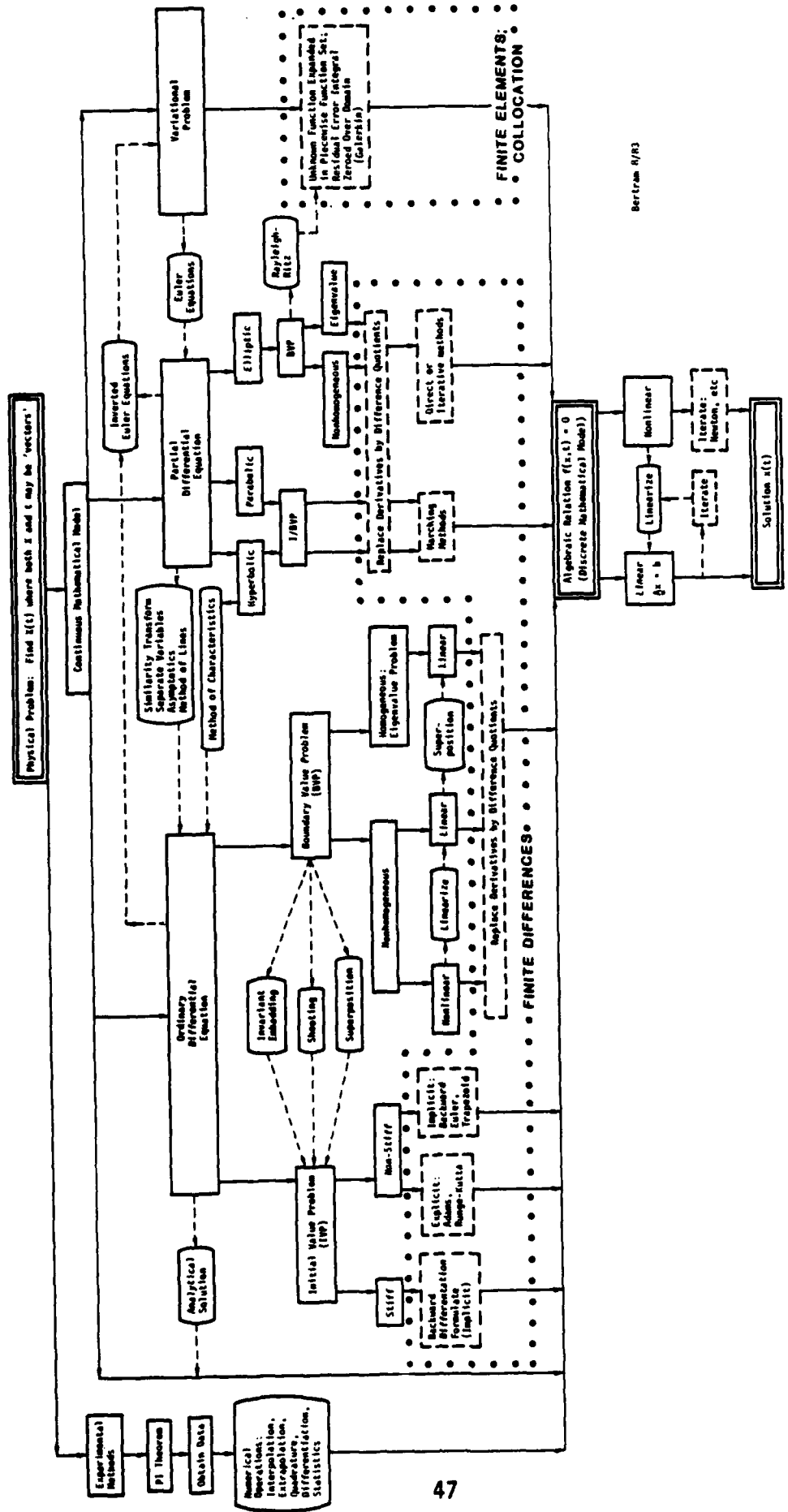
For an N degree of freedom problem, there will be N values of u^* and v . Thus, Equation (3.2-5) is recast in vector form as:

$$\int_V (R(u_j^*), v_i) \, dV = 0 \quad (3.2-6)$$

where $i, j = 1, 2, \dots, N$

In 1915, Galerkin presented his method of solution whereby the test function, v_i , and the spatial component of the trial function, N_j , were the same. The beauty of this approach is that it leads to a

Figure 5.4-1 Diagram of computer routes - page 4



methods (FEM) for the radiation transport, heat transfer, and stress/strain analyses, some background in FEM is required for a basic comprehension of the theory sections. Hence, a summary of FEM theory now follows.

3.2.1 Finite Element Theory. A brief discussion of numerical methods and, in particular, finite element methods (FEM) are in order at this stage. The accompanying text is intended only to highlight some FEM background pertinent to this research. The selection of FEM as the computational method used was based on the type of problem to be solved.

To gain some insight into this selection process, Bertram's Chart of Computational Methods of Figure 3.2-1 provides a useful tool in "weeding" through the various numerical options [Bertram, 1985]. The physical problem at hand includes the solution of non-linear, steady-state, coupled partial differential equations for an elliptic governing equation with specified boundary conditions. From Figure 3.2-1, the path toward setting up the system of algebraic equations moves down the right half of the figure, which calls for the use of the finite element method. Ultimately, the system of algebraic equations will be solved using either Gaussian elimination or iterative methods.

To get to the point where a system of equations are solved for the state variable (i.e., flux, temperature, or displacement), a widely used technique known as the Method of Weighted Residuals (Finlayson and Scriven, 1966) is often employed. In this method, the state variable u^* is expanded in a finite series of trial functions:

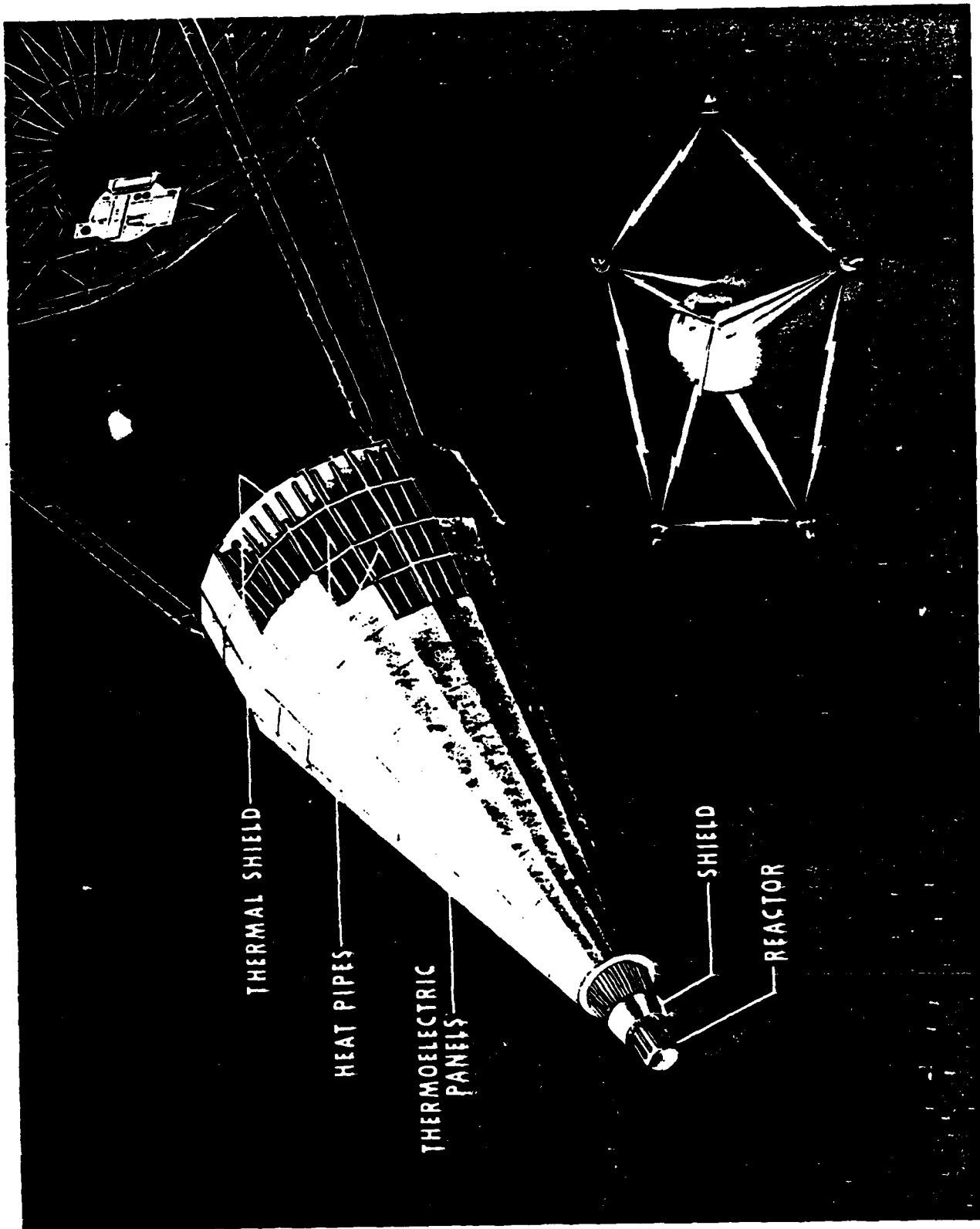
$$u^*(x, t) = u_s(x, t) + \sum_{i=1}^N N_i(x, t)u_i(t) \quad (3.2-1)$$

mesh of the radiation transport code was partitioned into the same number of regions, and the nuclide densities, heating kermas and cross sections for the thermal energy groups were corrected using the free gas model to account for temperature feedback. The radiation transport problem was re-run using the coarse mesh core/fine mesh shield to obtain new heating rates and to recalculate the temperature. This feedback loop was repeated until the temperature distribution stabilized. The final temperature distribution was then used to calculate the induced stresses/strains throughout the axisymmetric W-LiH shield. This portion of the code is referred to as SHLDSTR.

Sections 3.2 through 3.5 provide detailed discussions of the theory directly applicable to this research. The discussions include specific technical areas from radiation transport, heat transfer, and stress/strain analyses. As mentioned in this research overview, each of these technology areas required extensive use of numerical computations. In fact, this research project represents the first documented use of finite element methods for space reactor shielding computations. As each technology is discussed, the numerical method required for computer implementation is briefly presented, as well. For the student interested in an extensive theoretical development for each technical area, the references included in this report should serve as an excellent starting point.

3.2 Method of Weighted Residuals

To maintain a thread of continuity in the presentation of this theoretical background, numerical methods necessary to perform the computational analyses are presented along with the governing equations for each technical area. Since this research utilized finite element



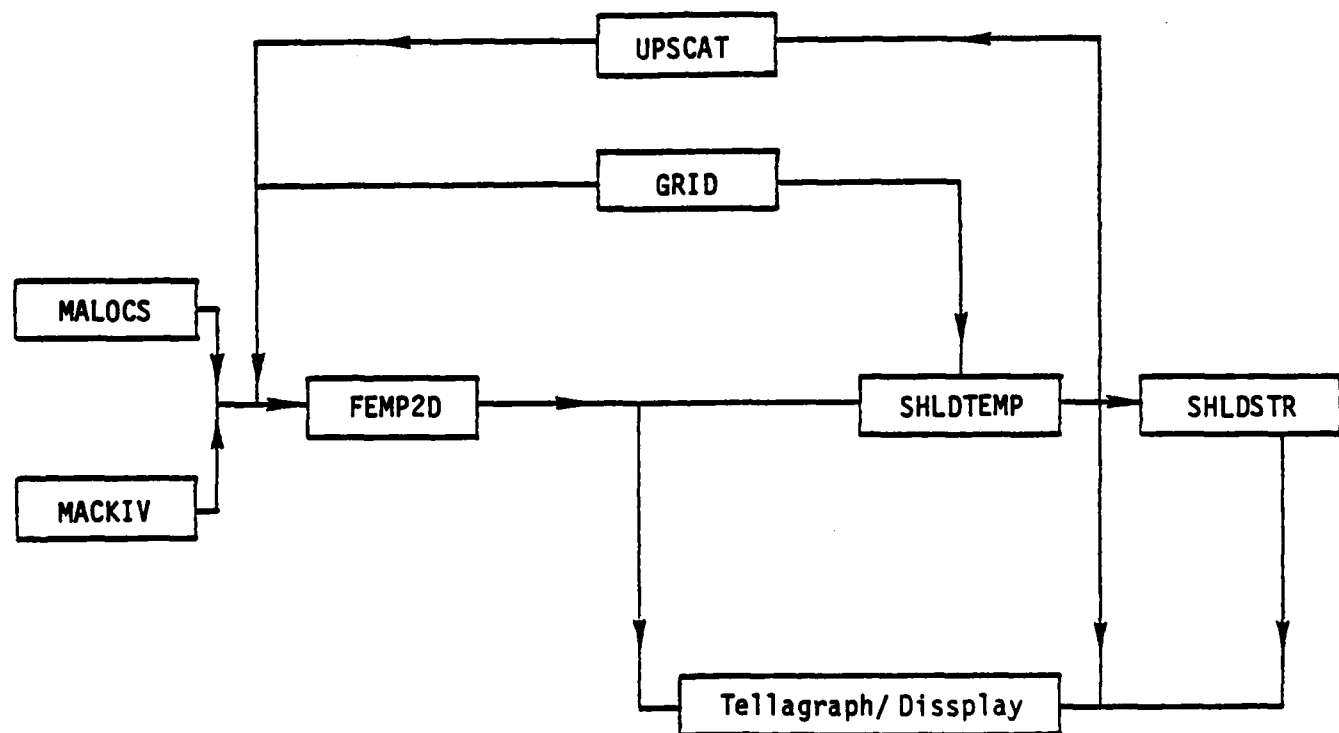
to be used as input for the shield calculation. The W-LiH shield was then modelled in the FEMP2D code, with a coarse mesh over the core and reflector (~3 cm), and a fine mesh throughout the shield (~1 cm) (referred to hereafter as coarse mesh core/fine mesh shield). The fine mesh converged fluxes for the core and reflector were used for a starting point; then the coarse mesh core/fine mesh shield was run to obtain the desired energy deposition values throughout the shield.

Figure 3.1-2 is an artists concept of the reactor in space analyzed in this research. The outer space environment, which is vacuum, was modelled into FEMP2D using an inert gas and a low nuclide density. The stability of the finite element solution was strongly influenced by the selection of the inert gas nuclide density. This stability condition is discussed in more detail in Section 5.1.

Nuclear cross sections used in the neutronics analysis were obtained from the BUGLE Cross Section Library, and collapsed to 38 energy groups (24 neutron and 14 gamma groups). Heating kermas (defined in section 3.3.2) for the shield were calculated with the code MACK-IV [Abdou et al., 1978], using ENDF/B cross section data. Because the triangular mesh used in the temperature and stress/strain calculations did not coincide with the quadrilateral mesh used in the radiation transport analysis, the nodal heating rate values from the 4-node elements were interpolated to the 3-node elements.

Heating rates were then input to the code, SHLDTEMP [Barattino, 1984], to calculate the nonlinear temperature distribution in the radiation shield. The shield was partitioned into smaller regions and an average temperature for the region was calculated. The quadrilateral

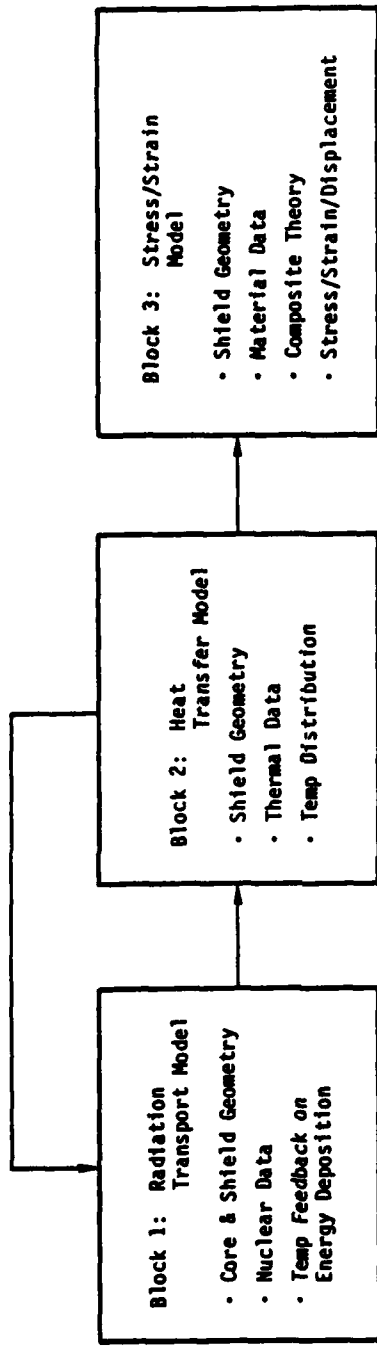
Figure 3.1-1. Major Programs Used in the UNM Radiation Shield Analysis Code.



**Table 3.1-1. Description of Major Programs Used in Analysis
of the SP-100 Radiation Shield**

| <u>Program</u> | <u>Developer</u> | <u>Purpose</u> |
|----------------|---|--|
| MALOCS | ORNL and P. McDaniel [McDaniel, 1984] | Collapses cross sections to a specified number over a flux weighting spectrum provided by the user |
| MACKIV | M. A. Abdou, Y. Gohar and R. P. Wright [Abdou et al., 1978] | Generates neutron and gamma heating kerma's for specified nuclides |
| FEMP2D | P. McDaniel [McDaniel, 1984] | Performs the criticality calculation using multi-group P_N approximation in R-Z, R-θ, or X-Y geometries (only P_1 approximation currently available) |
| SHLDTEMP | W. Barattino and M.S. El-Genk [Barattino, et al., 1984] | Calculates temperature distribution in R-Z or X-Y geometries using Newton-Raphson iteration. Handles radiative and convection boundaries, and temperature and spatially dependent thermal conductivities (only steady-state version currently available) |
| SHLDSTR | W. Barattino and M.S. El-Genk [Barattino, et al., 1984] | Calculates stresses, strains and displacements in R-Z (axisymmetric) or X-Y (plane stress or plane strain) geometries using modified Newton-Raphson iteration. Can handle linear or bi-linear elastic problems (only steady-state version currently available) |
| UPSCAT | W. Barattino and P. McDaniel [Barattino, et al., 1985] | Calculates the normalized flux distribution for thermal energies using free gas scattering kernel. Generates (absorption, differential, scattering, total scattering, and total cross sections.) |

Figure 3.0-1: Summary Overview of Analysis of the Space Reactor Radiation Shield



3.0 THEORETICAL BACKGROUND FOR ANALYSIS OF RADIATION SHIELD

Building on previous analysis and experimental work in the development of radiation shielding for space reactors, Figure 3.0-1 presents an overview of the interrelationship of major topics areas applied to this analysis of a space shield during steady state operation. From Figure 3.0-1 we observe that this research consisted of three distinct blocks: radiation transport, heat transfer, and stress-strain analyses. The coupling of the first two blocks to determine the importance of temperature feedback on energy deposition was a major uncertainty prior to this project. The theoretical structure for each technical areas appropriate to this research is included in Sections 3.3 through 3.5.

3.1 Research Overview

This research has focused on development of numerical tools to perform a coupled neutronics, thermal, and stress/strain analysis of radiation shield for space reactors [Bailey et al., 1984]. This section describes the codes; major components and their intrarelationship in analyzing a tungsten-lithium hydride shield for an SP-100 type reactor. Figure 3.2-1 is a flowchart of the implementation of the coupled neutronics, thermal and stress analysis codes, and Table 3.1-1 provides a brief description of the major programs identified in Figure 3.1-1.

The reactor shield analyzed was for a 1.66 MW_{th}, 93 percent enriched UO₂, liquid lithium cooled fast reactor. The reactor core and reflectors (see Figure 3.1-2) was modelled using a 2D finite element code, FEMP2D [McDaniel, 1984], and run over a fine mesh (~1 cm) as an eigenvalue problem. The neutron and gamma fluxes were stored on tape

and flux angular discretization with spherical harmonics to solve the second order, transport equation for a monoenergetic, steady-state problem [Wills, 1984].

The versatility of finite element methods is further explored with each passing day. Development of the method to fluid flow, and coupled fluid-flow and structural analysis are currently areas of intense interest within the FEM research community. As happened with linear analysis, the application of FEM based codes to non-linear problems (as in this research) is gaining more widespread use, despite a noticeable lag in a rigorous mathematical foundation (Hughes and Belyschko, 1984).

combinations of radial and axial shape functions. Figure 3.2-3 shows the quadrilateral element for an axisymmetric body.

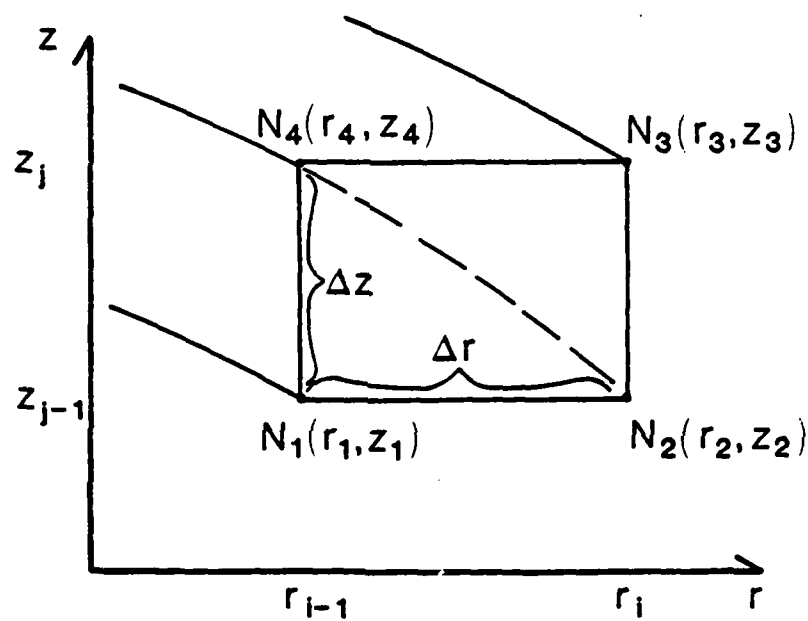


Figure 3.2-3: 4 Node Axisymmetric Quadrilateral Element

The shape functions for the quadrilateral element take the form:

$$\begin{aligned}
 N_1(r, z) &= \frac{1}{\Delta r \Delta z} (r_i - r)(z_j - z) \\
 N_2(r, z) &= \frac{1}{\Delta r \Delta z} (r - r_{i-1})(z_j - z) \\
 N_3(r, z) &= \frac{1}{\Delta r \Delta z} (r - r_{i-1})(z - z_{j-1}) \\
 N_4(r, z) &= \frac{1}{\Delta r \Delta z} (r_i - r)(z - z_{j-1})
 \end{aligned} \tag{3.2-11}$$

The shape functions of Equation 3.2-11 come into use in the formulation of the radiation transport equations to be solved for neutron and gamma fluxes.

Each of the theory sections that follow, utilize the basic concepts just presented. The governing equation will be cast as a Galerkin approximation, with a spatially weighted residual minimized over the domain. The shape functions used to carry out required integrations are those listed for the triangular and quadrilateral elements. The versatility of FEM to a broad range of technologies should become apparent in the ensuing sections.

3.3 Block 1: Radiation Transport Theory

The main objectives of this block were to:

- Perform a criticality calculation for steady-state operation of the SP-100 reactor
- Determine gamma and neutron fluxes throughout the radiation shield using P_1 theory in an R-Z geometry
- Generate heating rates throughout the shield
- Calculate neutron and gamma fluences at the 25 meter dose plane using transport theory for a 1-D equivalent geometry

The primary objective of performing radiation transport analysis was to obtain heating rates throughout the shield. The first three objectives were directly related toward this goal; whereas, the fluence calculations were necessary to compare radiation protection with thermal performance of a particular shield design. We specifically wanted to know whether a shield optimized for radiation protection would also

satisfy the thermal requirements imposed by use of lithium hydride for neutron attenuation. Figure 3.3-1 shows how these objectives tie together for the nuclear engineer.

The use of a P_1 approximation for the flux expansion in determining the energy deposited throughout the 3-D axisymmetric shield, was based on the best available radiation transport package adaptable to VAX 11/780 computer. However, for the deep penetration fluence calculations, an arbitrary order transport calculation was deemed necessary to accurately model the forward bias scattering of the neutrons [Bell and Glasstone, 1970]. For this reason, the 1-D transport version of the FEMP code was utilized. A comparison of energy deposition using P_1 and P_{15} approximations is discussed in the section on uncertainty analysis.

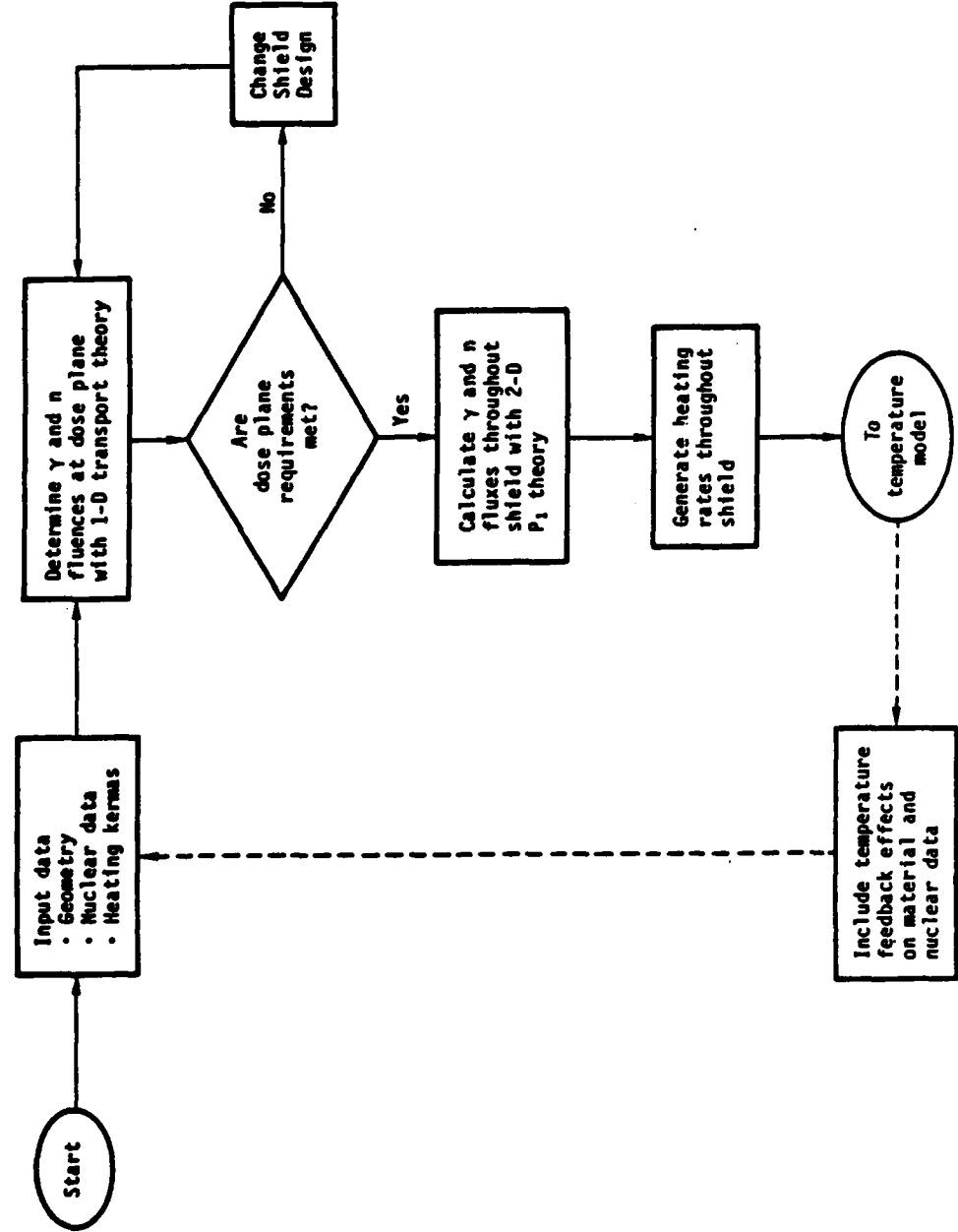
This section develops the theoretical background for the P_1 flux calculations in an R-Z geometry, identifies the equations used in determining heating rates, and presents the methods for determining the temperature feedback effects on energy deposition in both Maxwellian and non-Maxwellian flux mediums. An expression for calculating the 1-D neutron and gammas fluences at the dose plane is derived in Section 4.2.

3.3.1 Derivation of System of Equation for Determining Coupled Neutron and Gamma Fluxes. The radiation transport equation for steady-state operation takes the following form:

$$\begin{aligned} \nabla \cdot \nabla \phi(r, \Omega, E) + \Sigma_t(E) \phi(r, \Omega, E) \\ = \int_{4\pi} \int_E \Sigma_s(\Omega' + \Omega, E' + E) \phi(r, \Omega', E') d\Omega' dE' + S(r, \Omega, E) \end{aligned}$$

(3.3-1)

Figure 3.3-1. Radiation Transport Model Overview



To transform this integro-differential equation into a solvable form, the following assumptions are made [Duderstadt and Hamilton, 1976]:

- a. Flux can be expanded in Legendre polynomials, with only the first two terms of the expansion retained (P_1 approximation).
- b. The flux can be broken into energy and spatial components.
- c. Anisotropic downscatter is neglected.

With these assumptions, the transport equation can be reduced to a diffusion equation of the following form:

$$-\underline{D}(E)\nabla^2\phi(r, E) + \Sigma_t(E)\phi(r, E) = \int_E \Sigma_s(E' + E)\phi(r, E') dE' + S(r, E) \quad (3.3-2)$$

To discretize the diffusion equation into a system of algebraic equations that can be solved on a digital computer, a Galerkin formulation of the residual is established [Fletcher, 1983]:

$$\int_V [\underline{D}(E)\nabla^2\phi(r, E) - \Sigma_t(E)\phi(r, E) + \int_E \Sigma_s(E' + E)\phi(r, E') dE' + S(r, E)] dV = 0 \quad (3.3-3)$$

Expanding the flux in terms of nodal basis functions, inserting into Equation 3.3-3, and applying Gauss' Theorem for an axisymmetric geometry results in:

$$\begin{aligned} & \int_A (\underline{\phi}_k N_k) \cdot \underline{n} dA + \int_A (\underline{DN}_k, \underline{N}_j, \underline{r}\underline{\phi}_j) r dr dz + \int_A (\underline{DN}_k, \underline{z}\underline{N}_j, \underline{r}\underline{\phi}_j) r dr dz \\ & + \int_A (\Sigma_R \underline{N}_k \underline{N}_j \underline{\phi}_j) r dr dz = \frac{1}{\lambda} \int_A N_k \left(\sum_{i=1}^M v \underline{\Sigma}_{f_j}^i \underline{\phi}_j^i \right) r dr dz \\ & + \int_A (N_k \sum_{m=1}^{i-1} \Sigma_s^{m+1} \underline{N}_j^m \underline{\phi}_j^m) r dr dz \end{aligned} \quad (3.3-4)$$

where the differential scattering cross section, Σ_s^{m+1} , represents downscattering from energy group m to energy group i ; the fission

source term (r.h.s. of Equation 3.3-4) is summed over m energy groups in which fission occurs; and the superscripts on fission and down-scatter cross sections and fluxes refer to higher energy groups.

Also, the comma refers to "differential with respect to", and

$$J_i = \text{Neutron Current} = - D \frac{\partial \psi}{\partial r} = - D N_{i,n} \psi$$

λ = Fundamental System Eigenvalue

The energy dependence has been dropped from the variables to simplify notation. However, it should be understood that the multi-grouping approximation has been incorporated into these equations.

To gain a better understanding of how to solve these equations, Equation 3.3-4 can be written in matrix form as:

$$\underline{M} \underline{\psi} = \lambda^{-1} \underline{F} \underline{\psi} \quad (3.3-6)$$

where:

$$\begin{aligned} \underline{M} &= \int_A -DN_{i,n} N_k dr + \int_A DN_{k,m} N_j, r dr dz + \int_A DN_{k,z} N_j, r dr dz \\ &\quad + \int_A \sum_k N_k N_j r dr dz \end{aligned} \quad (3.3-7)$$

$$\underline{F} = \int_A N_k \sum_{i=1}^M v \sum_f f_j r dr dz + \int_A N_k \sum_{m=1}^{i-1} \sum_{s=j}^{m+i} N_s r dr dz \quad (3.3-8)$$

This system of equations can be solved iteratively using a power method (Wilkinson, 1965) to generate successive estimates for ψ and λ from:

$$\begin{aligned} \underline{\psi}_{i+1} &= \lambda_i^{-1} \underline{M}^{-1} \underline{F} \underline{\psi}_i \\ \lambda_{i+1} &= \lambda_i \frac{(\underline{F} \underline{\psi}_{i+1}, \underline{F} \underline{\psi}_{i+1})}{(\underline{F} \underline{\psi}_{i+1}, \underline{F} \underline{\psi}_i)} \end{aligned} \quad (3.3-9)$$

The exact form of each integral in Equations 3.3-7 and 3.3-8 is now dependent on the shape functions used to discretize the reactor system. The integration of each term becomes somewhat cumbersome. But to demonstrate how the type of element comes into play, the quadrilateral element shape functions of Equation 3.2-11 were substituted into the second term of Equation 3.3-8 and the integration carried out. The result is as follows:

$$\int_A D \tilde{B}_{k,r} \tilde{B}_{k,r} r dr dz$$

$$= D(r_1^2 - r_{1-1}^2) \frac{\Delta z}{2\Delta r^2} \begin{bmatrix} \frac{1}{3} & -\frac{1}{3} & \frac{1}{6} & -\frac{1}{6} \\ & \frac{1}{3} & \frac{1}{3} & -\frac{1}{6} \\ & & \frac{1}{3} & -\frac{1}{3} \\ & & & \frac{1}{3} \end{bmatrix}$$

Symmetric

(3.3-10)

Similarly, the remaining terms of Equations 3.3-7 and 3.3-8 would be evaluated, assembled, and solved with an iterative method scheme such as Equation 3.3-9. Of course, a complete system of equations must be solved for each energy group. The marching scheme continues until convergence tolerances for both ϕ and λ are reached. With a solution for both neutron and gamma fluxes, the energy deposition and heating rates throughout the shield can be determined when the fluxes are combined with the respective heating kerma. The appropriate theory for this calculation is presented in the next section.

3.3.2 Generation of Heating Rate From Flux and Heating Kerma.

With neutron and gamma fluxes calculated from the radiation transport

code, the volumetric heating rate throughout the shield is based on the sum of heating resulting from interactions with neutrons and gamma rays. The neutron heating is determined from [Abdou and Maynard, 1975]:

$$H(r) = c \int_E \phi(r, E) \sum_j N_j(r) \sigma_{ij}(E) E_{ij}(E) dE \quad \left[\frac{W}{cm^3} \right] \quad (3.3-11)$$

where:

$$c = 1.602 \times 10^{-19} \text{ J/eV}$$

The equation represents the reaction rate times the energy released per reaction for each nuclide j which undergoes reaction i . N_j refers to the number density of the j th nuclide throughout this section. The second part of Equation 3.3-11 is referred to as the microscopic kerma factor. Thus, the kerma factor for nuclide j can be represented as:

$$k_j(E) = \sum_i \sigma_{ij}(E) E_{ij}(E) \quad (3.3-12)$$

With the energy integration discretized by the multi-group approximation of diffusion theory as discussed previously, Equation 3.3-12 can be substituted into Equation 3.3-11 and rewritten as:

$$H(r) = \sum_{i=1}^{MG} \phi(r, E_i) \sum_j N_j(r) k_j(E_i) \quad (3.3-13)$$

This representation of the neutron heating rate thus lends itself to easy computational adaptation on a digital computer, once the neutron flux is determined from the radiation transport analysis.

In an analogous manner, the energy deposition due to gamma interaction can be determined with a gamma-ray kerma factor as [Abdou and Maynard, 1975]:

$$K_{Yj}(E) = E_Y \sigma_{pe_j}(E) + E_Y \sigma_{c_j}(E) + (E_Y - 1.02) \sigma_{pp_j}(E) \quad (3.3-14)$$

where the respective cross section for photoelectric, compton, and pair production interactions are used. (Notice that the rest mass energy of the electron--position pair is not available for energy deposition.) Equation 3.3-14 can then be used in Equation 3.3-13 to calculate the contribution of heating rates due to gamma interaction throughout the shield.

Returning to Equation 3.3-12, the energy deposition per neutron reaction must be determined in some manner for each nuclide. The principle reactions for energy deposition due to neutron interaction for the materials in a space reactor shield are elastic scattering, inelastic scattering, charged particle reactions, radiative capture, and radioactive decay. Of the total energy released per reaction, the local energy deposited at the point of interaction will be the kinetic energies of the recoil nucleus and charged particles emitted, and a fraction of the internal excitation energy converted into heat. A portion of the reaction energy will be carried away by gamma rays which then interact in accordance with Equation 3.3-14.

The local energy deposition can be written in a general form as:

$$E_{LE}^i = E - aE_n^i + bQ^i + c(f_c - 1)E_\lambda^i + dE_{cp}^i + eE_d^i \quad (3.3-15)$$

where i represents the particular reaction and the coefficients a-e identify the applicability of a given term for a given reaction. The terms of Equation 3.3-15 are identified in the nomenclature listing.

The boolean values for these coefficients are included in Table 3.3-1.

Table 3.3-1. Identification of Coefficients for Equation (3.3-15) for Various Neutron Reactions

| <u>Reaction</u> | <u>a</u> | <u>b</u> | <u>c</u> | <u>d</u> | <u>e</u> |
|----------------------------|----------|----------|----------|----------|----------|
| Elastic Scattering | 1 | 0 | 0 | 0 | 0 |
| Inelastic Scattering | 1 | 0 | 1 | 0 | 0 |
| Charged Particle Reactions | 0 | 1 | 1 | 1 | 1 |
| Radiative Capture | 0 | 1 | 1 | 0 | 1 |
| Radioactive Decay | 0 | 0 | 0 | 0 | 1 |

Analytic expressions for E_n , Q , E_λ , f_c , E_{cp} , and E_d are derived from nuclear physics based on conservation of mass, momentum, and energy principles. Abdou and Maynard (1975) present analytic expressions for each of these reaction parameters, which are the basis for the heating kermas generated in the code, MACK IV.

3.3.3 Temperature Feedback Effects on Energy Deposition. When the temperature of the shield is increased from ambient temperature to operating temperature, the effect on energy deposition must be considered in the shield where a substantial portion of the flux is thermalized. Besides the obvious changes in neutronic properties due to density decreases at elevated temperatures, the temperature rise will affect the low energy absorption cross-sections of 1/v nuclides.

3.3.3.1 Temperature Feedback in a Maxwell Boltzmann Medium. With a Maxwell Boltzmann (M-B) distribution for the thermal flux, the influence of temperature on the thermal neutron absorption cross section can be determined by averaging the microscopic group cross section with the M-B flux over all energy. Mathematically,

$$\sigma_{ath}(T) = \frac{\int_0^{\infty} \sigma_a(0.025\text{ev}) \phi_{MB}(E)dE}{\int_0^{\infty} \phi_{MB}(E)dE} \quad (3.3-16)$$

By definition [Glasstone and Sesonske, 1981],

$$\phi_{MB}(E) = \frac{2\pi n_0}{(\pi kT)^{3/2}} \left(\frac{2}{m}\right)^{1/2} E \exp\left(-\frac{E}{kT}\right) \quad (3.3-17)$$

Substitute Equation 3.3-17 into Equation 3.3-16:

$$\sigma_{a_{th}}(T) = \frac{\int_0^\infty \sigma_a(0.025\text{ev}) \frac{2\pi n_0}{(\pi kT)^{3/2}} \left(\frac{2}{m}\right)^{1/2} E \exp\left(-\frac{E}{kT}\right) dE}{\int_0^\infty \frac{2\pi n_0}{(\pi kT)^{3/2}} \left(\frac{2}{m}\right)^{1/2} E \exp\left(-\frac{E}{kT}\right) dE} \quad (3.3-18)$$

Carrying out the integration yields:

$$\sigma_{a_{th}}(T) = \frac{\sqrt{\pi}}{2} \left(\frac{T_0}{T}\right)^{1/2} \sigma_a(0.025\text{ev}) \quad (3.3-19)$$

where T_0 is the reference temperature in °K or °R for thermal cross section data, taken to be 20°C by convention.

The relative change in thermal absorption cross section at elevated temperatures for the reference temperature is obtained from Equation 3.3-19 as:

$$\Delta\sigma_{a_{th}}(T_0 + T) = \frac{\sigma_{a_{th}}(T) - \sigma_{a_{th}}(T_0)}{\sigma_{a_{th}}(T_0)} = 1 - \left(\frac{T_0}{T}\right)^{1/2} \quad (3.3-20)$$

In a similar manner, the relative change in thermal absorption cross section from a given temperature to a higher temperature is determined as:

$$\Delta\sigma_{a_{th}}(T_1 + T_2) = \frac{\sigma_{a_{th}}(T_1) - \sigma_{a_{th}}(T_2)}{\sigma_{a_{th}}(T_1)} = 1 - \left(\frac{T_1}{T_2}\right)^{1/2} \quad (3.3-21)$$

Table 3.3-2 shows the effect of temperature on thermal absorption cross section for several values of T using Equations 3.3-20 and 3.3-21.

Table 3.3-2: Effect on Absorption Cross Section of Increasing Temperature above 293 K Reference Temperature

| T[K] | $\Delta\sigma_{ath}(T_0 + T)$ | $\Delta\sigma_{ath}(T_1 + T_2)$ |
|------|-------------------------------|---------------------------------|
| 293. | 0.0 | |
| 400. | 0.144 | -0.144 |
| 500. | 0.234 | -0.106 |
| 600. | 0.301 | -0.087 |
| 700. | 0.353 | -0.074 |
| 800. | 0.395 | -0.065 |

From column 2 of Table 3.3-2, we observe that the microscopic thermal absorption cross section is reduced from its reference temperature value by 30-40% for the temperature range 600-800 K. From column 3 of Table 3.3-2 we see that the change in this cross section from one elevated temperature to the next, decreases with increasing temperature. In fact, over fairly large temperature changes (~ 100 K), the relative change in microscopic thermal absorption cross section is always less than 9% above 600 K. This observation leads to the conclusion that to include temperature feedback in the radiation transport evaluation of energy deposition for a shield operated in a 600-800 K temperature range, the numerical grid can be partitioned over a fairly broad geometric region and an average temperature used to include the temperature feedback effect on microscopic thermal absorption cross-section.

The temperature effect on the Maxwellian flux can be determined by integrating Equation 3.3-17 over the entire thermal energy range. This results in:

$$\phi_{th}(T) = \int_0^\infty \phi_{MB}(E, T) dE = \frac{2}{\sqrt{\pi}} \left(\frac{kT}{kT_0} \right)^{1/2} \phi_0 \quad (3.3-22)$$

where again, the subscript 0 refers to some reference datum (i.e., 20°C). The temperature effect on the energy deposition in a mixture

characterized by a M-B distribution can be quantified by insertion of Equations 3.3-12 and 3.3-22 into Equation 3.3-13. This leads to:

$$i_{th}(r) = \phi(r) \sum N_j(r) k_j(E_{th}) = \frac{2}{\sqrt{\pi}} \left(\frac{T}{T_0} \right)^{1/2} \phi_0 \sum N_j(r) \sigma_{ij}(E_{th}) E_{ij}(E_{th}) \quad (3.3-23)$$

When the dominant source of energy deposition is due to some absorption reaction (i.e., (n, α) reaction in Li-6), the absorption cross section of Equation 3.3-19, is inserted into Equation 3.3-23 resulting in:

$$\begin{aligned} H_{th}(r) &= \frac{2}{\sqrt{\pi}} \left(\frac{T}{T_0} \right)^{1/2} \phi_0 \sum N_j(r) \frac{\sqrt{\pi}}{2} \left(\frac{T_0}{T} \right)^{1/2} \sigma_a \sigma_{a_0} E_j(E_{th}) \\ &= \sum N_j(r) \phi_0 \sigma_a \sigma_{a_0} E_j(E_{th}) \end{aligned} \quad (3.3-24)$$

Equation 3.3-24 leads to the important conclusions that temperature will have no effect on energy deposition for a mixture in which the dominant energy release mechanism is an absorption reaction of a $1/v$ nuclide [Beckurts and Wirtz, 1964]. Since most nuclides exhibit $1/v$ behavior for absorption and even scattering cross sections at very low energies, there will be no temperature feedback effect on energy deposition for an infinite medium mixture. However, in a finite medium the effect of leakage must also be taken into account.

The Maxwellian distribution of Equation 3.3-17 was based on an infinite medium assumption. Therefore, it cannot be stated with certainty that absorption reaction rate is independent of temperature when leakage plays an important role. Several effects come into play here. Diffusion cooling will result in a softer spectrum as the higher energy neutrons will leak at a faster rate than the slower neutrons. However, in a hydrogenous medium these fast neutrons serve as the source for

ermal neutrons as they lose energy through elastic collisions. Additionally, thermal neutrons themselves have a diffusion length that ipetes with energy deposition mechanisms such as absorption reactions. Thus, even for a pure $1/v$ nuclide with a M-B distribution, the leakage effects make it unclear whether temperature will have much effect on energy deposition in a finite medium. To make this statement with certainty, the analysis must be performed for a given geometry and structure.

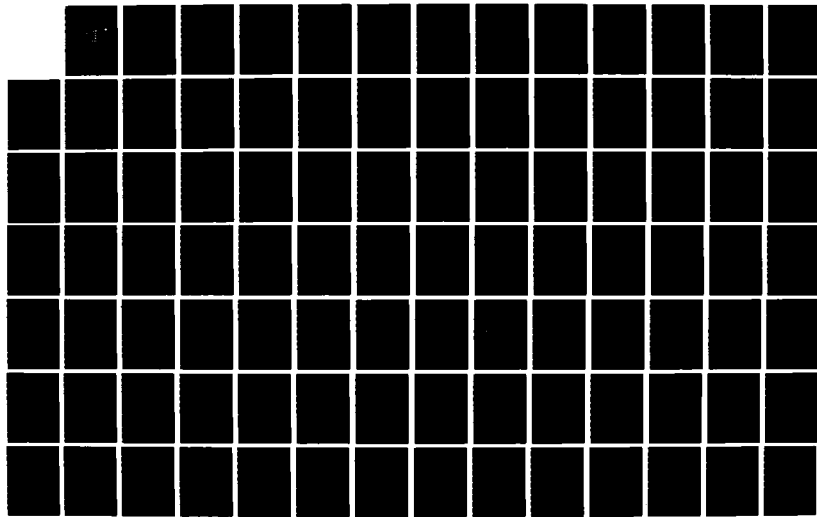
3.3.3.2. Temperature Feedback in a non-Maxwell Boltzmann Medium.
most "real-life" situations, the thermal flux distribution rarely displays a "pure" Maxwellian shape. The major causes of shifting from true M-B flux were briefly touched upon in the last section; namely, absorption, leakage, and neutron sources slowing down from epi-thermal energies [Duderstadt and Hamilton, 1976].

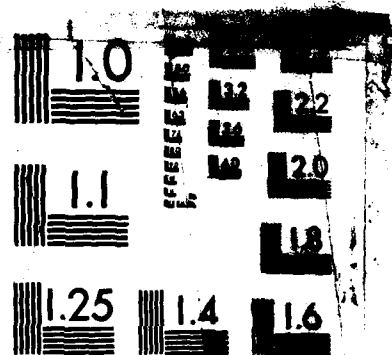
When the departure from a true M-B flux is not great, the effective neutron temperature model has successfully been used to model the actual flux shape in the infinite medium. As the departure becomes excessive, this model has been shown to breakdown. Also, at high energies, the model fails to display the $1/E$ behavior due to the slowing down spectrum. To quantify this departure, the inverse of the moderating ratio, Γ , was used, where:

$$\Gamma = \frac{1}{\text{Moderating Ratio}} = \frac{\sum_a (kT)}{\xi \sum_s} \quad (3.3-25)$$

The model was found to be inadequate for $\Gamma \gtrsim 0.1$ [Duderstadt and milton, 1976]. In Table 3.3-3, the inverse moderating ratio's are corded for several hydride materials at room temperature and at 0 K.

AD-A158 188 COUPLED RADIATION TRANSPORT/THERMAL ANALYSIS OF THE
RADIATION SHIELD FOR A. (U) AIR FORCE INST OF TECH 2/4
WRIGHT-PATTERSON AFB OH W J BARATTINO JUL 85
UNCLASSIFIED AFIT/CI/NR-85-53D F/G 18/6 NL





MICROCOPY RESOLUTION TEST CHART
NATIONAL BUREAU OF STANDARDS-1963-A

Table 3.3-3. Inverse Moderating Ratio's, Γ , for Selected Hydrides at Room Temperature and 700 K.

| <u>Hydride*</u> | <u>Room Temperature</u> | <u>700 K</u> |
|--------------------|-------------------------|--------------|
| LiH(Nat) | 3.52 | 2.28 |
| LiH(Dep1) | 0.0182 | 0.0118 |
| BeH ₂ | 0.0164 | 0.0106 |
| ZrH | 0.0195 | 0.0126 |
| TiH ₂ | 0.215 | 0.139 |
| YH _{1.89} | 0.0443 | 0.0286 |

*Cross section data obtained from [Mueller et al., 1968].

From the data of Table 3.3-3, one sees that natural lithium hydride is clearly non-Maxwellian. Titanium hydride could probably be modelled with the effective neutron temperature model at elevated temperature. The remaining hydrides (to include depleted LiH) should possess a M-B shape for the thermal flux.

The space reactor shield design includes LiH(Nat) for neutron attenuation. Because of the large deviation from a M-B flux due to the large thermal absorption cross section of Li-6, a more general method is needed which is different than either the M-B flux or the effective neutron temperature model to determine the temperature effect on energy deposition.

Returning to Equation 3.3-2, the P_1 equation for an infinite medium takes the form [Duderstadt and Hamilton, 1976]:

$$[\Sigma_a(E) + \Sigma_s(E)]\phi(E) = \int_E \Sigma_s(E' + E)\phi(E')dE' + S(E) \quad (3.3-26)$$

Employing a multi-group approximation and integrating over all thermal energy, results in:

$$\begin{aligned}
 E_{th} & \sum_{n=0}^{\infty} \left\{ \int_{E_{g+1}}^{E_g} [\Sigma_a(E) + \Sigma_s(E)] \phi(E) dE \right. \\
 & \quad \left. = \int_{E_{g+1}}^{E_g} \int_{E_{g+1}}^{E'} \Sigma_s(E' + E) \phi(E') dE' dE + \int_{E_{g+1}}^{E_g} S(E) dE \right\} \quad (3.3-27)
 \end{aligned}$$

where E_{th} represents the cut-off energy below which the thermal region begins.

Equation 3.3-27 can now be used to solve for the flux shape over all thermal energy. With the new flux shape, the multi-group, flux weighted cross sections can be recalculated at higher temperature and the energy deposition redetermined over all energy as discussed previously.

With this generalized approach, several subtleties must be included in the analysis. At low thermal energies, the neutron can gain energy in collisions with target nuclei. Consequently, upscatter cross sections must be included in the differential scattering term of Equation 3.3-27. Additionally, at these low energies, the effective cross sections increase due to the binding effects of the molecule. Physically, the neutron is moving at such low speed that its wavelength is generally several orders of magnitude larger than the radius of the target molecule. This means that the neutron interacts with the entire molecule rather than the individual atoms of the molecule [Williams, 1966]. Since the cross-section represents a probability of interaction, one would naturally expect the magnitude of this probability to increase at very low energies. The binding effects are particularly important for light nuclides and takes the form [Foderaro, 1971]:

$$\lim_{E \rightarrow 0} \sigma_{\text{bound}} = \sigma_{\text{free}} \left(\frac{A+1}{A} \right)^2 \quad (3.3-28)$$

From Equation 3.3-28, one can see that for hydrogen, the bound cross section can be as high as four times the free cross section as $E \rightarrow 0$. As A increases, the bound effect becomes less important. For example, for Li-6 the multiplier is 1.36, and for W-182 the multiplier is 1.01. Thus, binding effects on scattering are particularly important when the medium includes hydrogen at very low energies ($< 0.1\text{ev}$).

From quantum mechanics, the differential scattering kernel has been represented by the free gas model in which the target nuclei is treated as a monatomic gas. The following assumptions are made in deriving the free gas model [Williams, 1966]:

- A. No intermolecular forces
- B. No internal structure to the scatters
- C. No interference effects (neglect coherent scattering)
- D. Spin allowed
- E. Scattering occurs at equilibrium temperature, T , and possesses a Maxwellian velocity distribution in the absence of nonequilibrium effects

The differential scattering averaged over all angles takes the form:

$$\Sigma_s (E' + E) = \Sigma_f \frac{\theta^2}{2E'} \left\{ \begin{array}{l} \epsilon' - \epsilon \\ \epsilon' + \epsilon \end{array} \right\} \{ \text{erf}(\theta\sqrt{\epsilon'} - \lambda\sqrt{\epsilon}) + \text{erf}(\theta\sqrt{\epsilon'} + \lambda\sqrt{\epsilon}) \} \\ + \text{erf}(\theta\sqrt{\epsilon} - \lambda\sqrt{\epsilon'}) - \text{erf}(\theta\sqrt{\epsilon} + \lambda\sqrt{\epsilon'}) \quad (\epsilon' < \epsilon) \\ \left. \begin{array}{l} \epsilon' - \epsilon \\ \epsilon' + \epsilon \end{array} \right\} \{ \text{erf}(\theta\sqrt{\epsilon'} - \lambda\sqrt{\epsilon}) - \text{erf}(\theta\sqrt{\epsilon'} + \lambda\sqrt{\epsilon}) \} \\ + \text{erf}(\theta\sqrt{\epsilon} - \lambda\sqrt{\epsilon'}) + \text{erf}(\theta\sqrt{\epsilon} + \lambda\sqrt{\epsilon'}) \quad (\epsilon' > \epsilon) \end{array} \right. \quad (3.3-29)$$

where:

$$\epsilon = E/kT$$

$$\theta = (A+1)/2\sqrt{A}$$

$$\lambda = (A-1)/2\sqrt{A}$$

$$\Sigma_f = \Sigma_s(E') \quad \text{for } E' \gg kT$$

Unfortunately, the free gas model does not capture the complete binding effects of hydrogen at very low energy. However, as will be shown in the results section, the contribution to total energy deposition of neutron interactions below .1 ev is low enough so that this limitation of the free gas model has a minor effect on internal heating rates.

The condition of $\epsilon' < \epsilon$ represents a condition of neutron upscattering; whereas $\epsilon' > \epsilon$ represents a condition of downscattering. Figures 3.3-2 and 3.3-3 present a graphic portrayal of Equation 3.3-29 for hydrogen and oxygen. From classical physics, we know that maximum energy exchange occurs when the neutron strikes light nuclides. This physical reality is obvious when comparing the transfer probabilities of the light hydrogen with the heavier oxygen. From Figure 3.3-3 we also see why upscatter is not significant for heavier elements, even at low energies.

The scattering cross section at energy E' is defined as:

$$\Sigma_s(E') = \int_0^{\infty} \Sigma_s(E' + E) dE \quad (3.3-30)$$

Substituting Equation 3.3-29 into Equation 3.3-30 results in:

$$\Sigma_s(E') = \frac{\Sigma_f}{2 A \epsilon'} [(2A\epsilon' + 1) \operatorname{erf}(\sqrt{A}\epsilon') + \frac{2}{\sqrt{\pi}} \sqrt{A}\epsilon' e^{-A\epsilon'}] \quad (3.3-31)$$

Figure 3.3-2 Energy Transfer Function in a Monatomic Gas with $A=1$

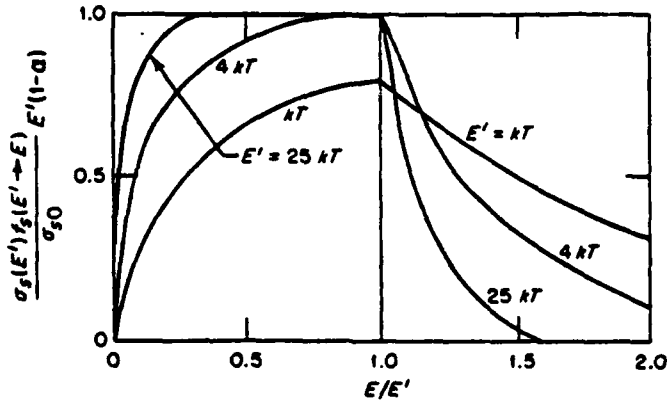
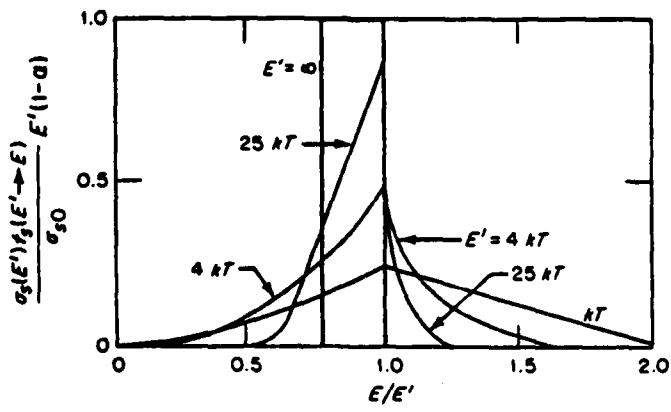


Figure 3.3-3 Energy Transfer Function in a Monatomic Gas with $A=16$



As with the scattering cross sections, the absorption cross section can be expressed in a closed form, analytic equation fitted to experimental data for each nuclide. For Li-6, the following expression can be derived from absorption cross section as:

$$\sigma_a = \exp(c_1 \ln E + c_2/E + c_3) \pm 0.0093\% \text{ barns}$$

for $10^{-5} < E < 10 \text{ ev}$ (3.3-32)

where:

$$c_1 = -5.000655 \times 10^{-1}$$

$$c_2 = 4.991685 \times 10^{-9}$$

$$c_3 = 5.002779$$

Similar expressions can be found for the absorption cross section of other nuclides.

The source term in Equation 3.3-27 represents neutrons arriving at a particular thermal energy level from epithermal energies. Above the thermal cut-off energy, the flux shape will be $1/E$ and a standard slowing down kernel can be used to represent differential scattering. Returning to Equation 3.3-29, the slowing down kernel is obtained by taking the limit of the downscattering term ($\epsilon' > \epsilon$) as $kT \rightarrow 0$.

This results in [Beckurts and Wirtz, 1964]:

$$\Sigma_s(E' + E) = \begin{cases} \frac{(A+1)^2}{4A} \frac{1}{E'} & \text{for } E_{th} < E < \frac{E_{th}}{\alpha} \\ 0 & \text{Otherwise} \end{cases} \quad (3.3-33)$$

The flux in the slowing down region is of the form:

$$\phi(E') = \frac{1}{\xi \Sigma_s(E') E'} \quad \text{for } E > E_{th} \quad (3.3-34)$$

The slowing down source term for thermal energies can then be represented as:

$$S(E) = \int_E^{E_{th}} \Sigma_s(E' + E)\phi(E')dE' \quad (3.3-35)$$

Substituting Equations 3.3-33 and 3.3-34 into Equation 3.3-35 results in:

$$S(E) = \int_{E_{th}}^{E/\alpha} \Sigma_s(E') \frac{(A+1)^2}{4A} \frac{1}{E'} \frac{1}{\xi \Sigma_s(E') E'} dE' \quad (3.3-36)$$

$$S(E) = \begin{cases} \frac{1}{(1-\alpha)\xi} \left[\frac{1}{E_{th}} - \frac{\alpha}{E} \right] & \text{for } E > \alpha E_{th} \\ 0 & \text{for } E < \alpha E_{th} \end{cases} \quad (3.3-37)$$

where:

$$\alpha = \left(\frac{A-1}{A+1} \right)^2$$

The source term of Equation 3.3-37 can be generalized to a mixture of nuclides by multiplying by the nuclide density and summing over all nuclides. This approach is valid from a physics standpoint since each neutron interacts with the atoms of the mixture separately, and from an engineering standpoint since we are interested in the thermal flux shape rather than magnitude. The source term for the mixture takes the form:

$$S_{mix}(E) = \sum_{i=1}^{\# \text{ nuclides}} N_i \cdot \begin{cases} \frac{1}{(1-\alpha_i)\xi} \left[\frac{1}{E_{th}} - \frac{\alpha_i}{E} \right] & \text{for } E > \alpha_i E_{th} \\ 0 & \text{for } E < \alpha_i E_{th} \end{cases} \quad (3.3-38)$$

The group source term is then:

$$S_{\text{mix}}(E_g) = \int_{E_{g+1}}^{E_g} S_{\text{mix}}(E) dE \quad (3.3-39)$$

Substituting Equation 3.3-38 into Equation 3.3-39 results in:

$$S_{\text{mix}}(E_g) = \sum_{i=1}^{\# \text{ nuclides}} N_i \cdot \begin{cases} \frac{1}{(1 - \alpha_i) \xi_i} \frac{\Delta E_g}{E_{\text{th}}} - \alpha_i \ln \left(\frac{E_g}{E_{g+1}} \right) & \text{for } E_{g+1} > \alpha_i E_{\text{th}} \\ 0 & \text{for } E_{g+1} < \alpha_i E_{\text{th}} \end{cases} \quad (3.3-40)$$

3.3.3.3 Numerical Solution of the Non-Maxwellian Thermal Flux. The non-MB thermal flux will be used as the weighting function for collapsing of the temperature dependent multi-group neutron cross sections into fewer neutron energy groups, to include the upscattering effects at low energy. The non-equilibrium flux can now be solved for by insertion of Equations 3.3-29, 3.3-31, and 3.3-40 into Equation 3.3-27, which can be rewritten in multigroup matrix form as:

$$\begin{aligned} (\Sigma_a^g(E) + \Sigma_s^g(E))\phi^g(E) &= S^g(E) \\ + \Sigma_s^g(E + E')\phi(E) + \sum_{E_{g-1}}^1 \Sigma_s^g(E' + E)\phi(E') &+ \sum_{E_{g+1}}^{E_{\text{th}}} \Sigma_s^g(E' + E)\phi(E') \end{aligned}$$

| | | |
|---------------------|-------------|-----------|
| In-group scatter | Downscatter | Upscatter |
|---------------------|-------------|-----------|

(3.3-41)

The differential scattering term has been subdivided into its three components; upscatter, downscatter, and in-group scatter. These differential scattering terms can be moved to the left hand side of Equation 3.3-41 for solution of the coupled group fluxes.

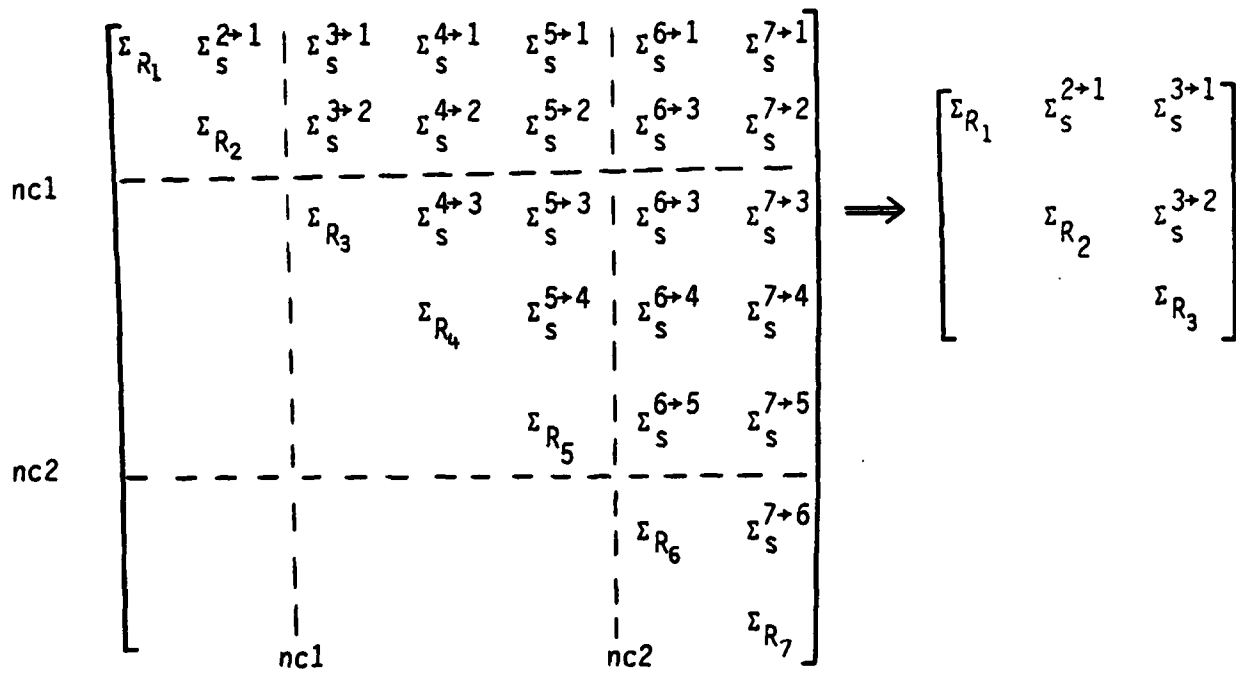
The system of equations to solve for the non-NB flux takes the

form:

$$\begin{bmatrix} \Sigma_R^1 & -\Sigma_S(E^2 + E^1) & -\Sigma_S(E^3 + E^1) & -\Sigma_S(E^4 + E^1) \\ -\Sigma_S(E^1 + E^2) & \Sigma_R^2 & -\Sigma_S(E^3 + E^2) & -\Sigma_S(E^4 + E^2) \\ -\Sigma_S(E^1 + E^3) & -\Sigma_S(E^2 + E^3) & \Sigma_R^3 & -\Sigma_S(E^4 + E^3) \\ -\Sigma_S(E^1 + E^4) & -\Sigma_S(E^2 + E^4) & -\Sigma_S(E^3 + E^4) & \end{bmatrix}$$

$$\begin{bmatrix} S^1 & S^2 & S^3 & S^4 \\ \phi^1 & \phi^2 & \phi^3 & \phi^4 \\ \vdots & \vdots & \vdots & \vdots \\ \phi^{th-1} & \phi^{th} & \phi^{th-1} & \phi^{th} \end{bmatrix} = \begin{bmatrix} \dots & \dots & \dots & \dots \\ \dots & \dots & \dots & \dots \\ -\Sigma_S(E^{\text{th}} + E^{\text{th}-1}) & -\Sigma_S(E^{\text{th}} + E^{\text{th}-1}) & \dots & \dots \\ -\Sigma_S(E^{(\text{th}-1)} + E^{\text{th}}) & \varepsilon_a^{\text{th}} & \dots & \dots \end{bmatrix}$$

(3.3-43)



| <u>Old</u> | <u>New</u> |
|------------|------------|
| 1, 2 | + 1 |
| 3, 4, 5 | + 2 |
| 6, 7 | + 3 |

$$\Sigma_{s_{\text{new}}}^{2-1} = \frac{(\Sigma_{s_{\text{old}}}^{3+1} + \Sigma_{s_{\text{old}}}^{3+2})\phi_3 + (\Sigma_{s_{\text{old}}}^{4+1} + \Sigma_{s_{\text{old}}}^{4+2})\phi_4 + (\Sigma_{s_{\text{old}}}^{5+1} + \Sigma_{s_{\text{old}}}^{5+2})\phi_5}{2\phi_3 + 2\phi_4 + 2\phi_5}$$

$$\Sigma_{s_{\text{new}}}^{3-1} = \frac{(\Sigma_{s_{\text{old}}}^{7+1} + \Sigma_{s_{\text{old}}}^{7+2})\phi_7 + (\Sigma_{s_{\text{old}}}^{6+1} + \Sigma_{s_{\text{old}}}^{6+2})\phi_6}{2\phi_7 + 2\phi_6}$$

$$\Sigma_{s_{\text{new}}}^{3-2} = \frac{(\Sigma_{s_{\text{old}}}^{7+3} + \Sigma_{s_{\text{old}}}^{7+4} + \Sigma_{s_{\text{old}}}^{7+5})\phi_7 + (\Sigma_{s_{\text{old}}}^{6+3} + \Sigma_{s_{\text{old}}}^{6+4} + \Sigma_{s_{\text{old}}}^{6+5})\phi_6}{3\phi_7 + 3\phi_6}$$

Figure 3.3-4. Illustration of Collapse of Cross Section from 7 Groups to 3 Groups

The upscatter cross sections represent the upper triangular off-diagonal elements, and the downscatter cross sections are included in the lower triangular off-diagonal elements. The in-group scattering term is a diagonal term, and become part of what is commonly referred to as the removal cross section. This is represented by:

$$\Sigma_R^g(E) = \Sigma_a^g(E) + \Sigma_s^g(E) - \Sigma_s^g(E \rightarrow E) \quad (3.3-42)$$

The highest energy group, E^1 , represents the first multigroup below the thermal energy threshold cut-off. The lowest energy group, E^{th} , represents the lowest group used in the analysis.

The thermal flux spectrum can now be used to collapse the large number of thermal group cross sections to the small number of multi-group cross sections used in the transport calculation, as discussed earlier. Figure 3.3-4 is an illustration of the collapse of the upscattering cross sections from seven neutron groups to three. The extension to a larger number of groups follows directly. Using the temperature corrected, non-M-B cross sections, the transport calculation can be re-run as before to determine any effects on the energy deposition in the shield.

3.4 Block 2: Thermal Analysis Theory

The main objectives of this block were to:

- a. Model the shield of the SP-100 reactor as an axisymmetric structure, with radiative heat transfer and adiabatic and/or isothermal boundary conditions.
- b. Using heating rates from the radiation transport calculation, determine the temperature distribution throughout the shield.

c. Develop an understanding of the coupling between radiation transport and heat transfer for the SP-100 reactor system.

Figure 3.4-1 is an overview of the temperature calculation model for the shield. The space reactor shield is a continuum medium with a radiative boundary condition at its outer radial surface. The front face of the shield (core side) and back face of the shield were thermally insulated with an adiabatic surface (i.e., thermal equilibrium with core, $q = 0$) [Barattino, 1985]. The governing equation for steady state operation was:

$$\nabla \cdot k(r,z,T) \nabla T(r,z) + q'''(r,z) = 0 \quad (3.4-1)$$

where:

$k(r, z, T)$ = Temperature and spatially dependent thermal conductivity

$T(r, z)$ = Steady state temperature as a function of position

$q'''(r,z)$ = Internal heat generation per unit volume due to gamma and neutron interaction

With boundary conditions:

a. For outer radial surface:

$$q \cdot n = \epsilon(T)\sigma F_{i+j}(\bar{T}^s - \bar{T}^\infty) = 0 \quad (3.4-2)$$

where:

q = Heat flux at surface

n = Normal unit vector at surface

$\epsilon(T)$ = Emissivity of the radiating surface

σ = Stefan-Boltzmann constant

F_{i+j} = View factor of surface with adjacent surfaces

T^s = Temperature of radiating surface

\bar{T}^∞ = Ambient temperature as a function of orbit

Figure 3.4-4 is a schematic of the energy balance calculation just described.

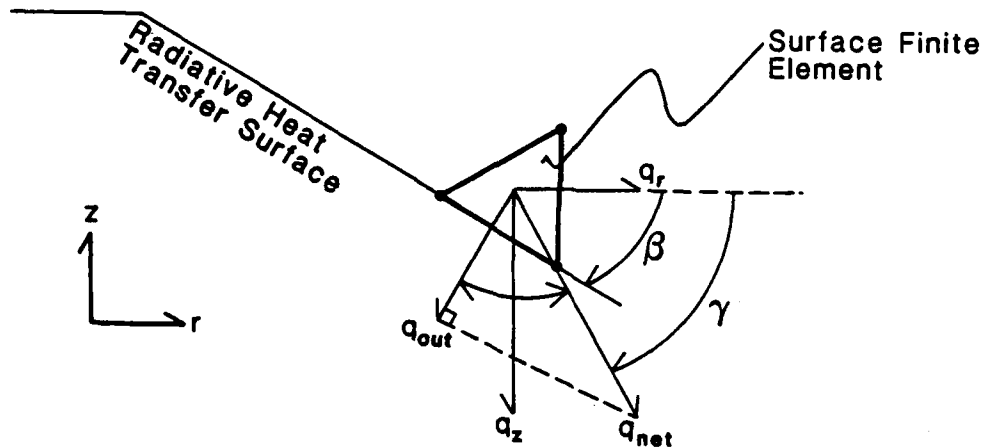


Figure 3.4-4: Schematic of Heat Flow From a Single Finite Element Along a Heat Rejection Surface

From this figure, the radial and axial heat flows from a single element are determined from:

$$q_r^{(e)} = -k_r T_{r,r}^{(e)} = -k_r N_{i,r} T_i \quad (3.4-31)$$

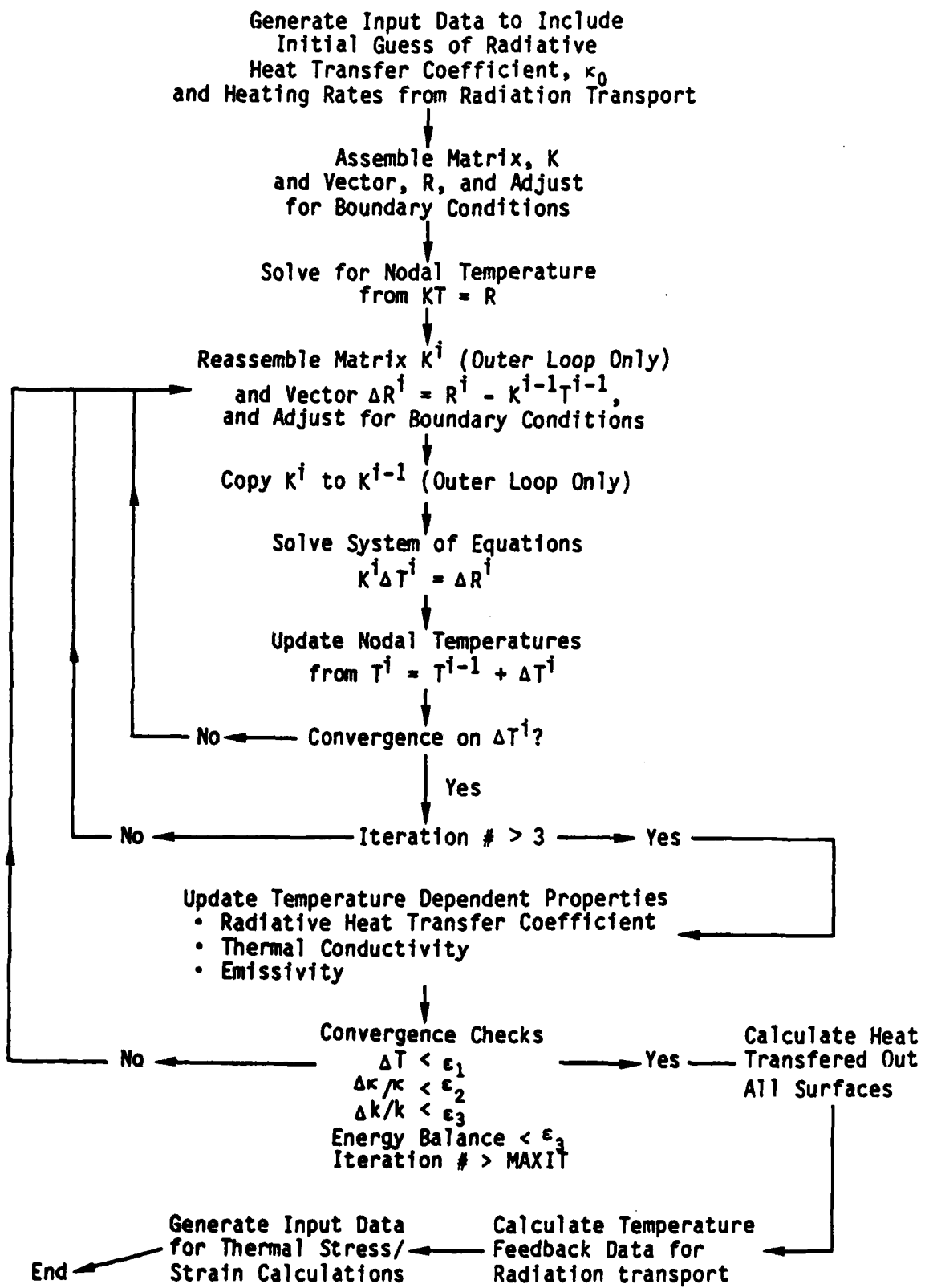
$$q_z^{(e)} = -k_z T_{z,z}^{(e)} = -k_z N_{i,z} T_i$$

The resultant heat flow is q_{net} , which has a vector projection γ degrees from the horizontal. The angle of the heat rejection surface is β degrees, which can be determined for the coordinates of the nodes on the surface. When $\gamma > \beta$, net heat flow out the surface occurs. The amount of heat leaving the surface, q_{out} , is the projection of q_{net} normal to the surface. The algorithm of Equation 3.4-32 shows how q_{out} is determined.

Use of this convergence check, in turn, requires some suitable method for determining λ_{\max} . Thus, when the spectral radius is very close to 1.0, the effective convergence criteria is reduced by its product with $(1 - \lambda_{\max})$. In SHLUTEMP, the user can specify tolerances on the maximum change in nodal temperatures from one iteration to the next, the relative change in radiative heat transfer coefficient, or the relative change in thermal conductivities. The radiative heat transfer coefficient can be quite limiting criterion for small ϵ as its value is proportional to T^3 . Of course, the final check to premature convergence (as well as accuracy of results) is the comparison of total energy deposited to energy transferred out, based on the final temperature distribution. The importance of convergence criteria for the nonlinear radiation heat transfer problem is further discussed in Section 5.2. As will be shown, energy balances over boundary elements proved to be the most critical convergence criterion.

With regard to the final energy balance, the net heat flux at each surface must be integrated over the surface area and summed over all surfaces for comparison with total energy deposition. This is accomplished in SHLUTEMP by determining the energy leaving each finite element along a given surface. The net heat flow vector is the vector sum of radial and axial heat flows from a single element. If this vector lies within the plane of heat rejection, then the component of the net heat flow vector normal to the heat rejection surface is the amount of energy exiting that particular segment of surface.

Figure 3.4-3: Flowchart of Solution Method Used in Temperature Code, SHLDTEMP



where c is the volume fraction of the fiber (or LiH). As with k_z , the radial thermal conductivity k_r , collapses to k_f as $c \rightarrow 1$.

3.4.3 Temperature Code, SHLDTEMP. Figure 3.4-3 flowcharts the solution method used in the temperature analysis code SHLDTEMP. With the system of assembled equations, the incremental nodal temperatures, ΔT , are solved for using either a direct elimination or iterative solver method. SHLDTEMP (and SHLDSTR) allows for solution of the equations with either an LDL^T Gaussian elimination routine (Bathe, 1982) or an iterative method using a preconditioned Jacobi method with conjugent gradient acceleration (Eisenstat, 1980).

The details of Figure 3.4-3 are self-explanatory with some exceptions. By keeping the thermal conductivity constant for the first 3 iterations, the temperature distribution has an opportunity to begin to stabilize. Allowing $k(T)$ to vary from the start can sometimes lead to a diverging system if the initial surface temperature swings are large. However, by the fourth iteration, the system no longer experiences extreme perturbations and convergence is more likely to be achieved.

The three convergence checks of Figure 3.4-3 represents a very conservative approach toward program termination. But with an incremental solution method, there is always a chance of premature convergence due to slowly varying changes in the unknown. This is particularly true for a system with a spectral radius, λ_{\max} , close to one. Some codes (particularly in radiation transport) overcome this false convergence with a convergence check of [Hageman and Young, 1981]:

$$\left(\frac{1}{1 - \lambda_{\max}} \right) \frac{\|\Delta X\|}{\|X\|} < \epsilon \quad (3.4-30)$$

where ϵ is some prescribed convergence tolerance.

To obtain thermal conductivity from thermal resistance:

$$k_z^{uc} = \frac{\Delta X_{uc}}{R_{uc} A_{uc}} \quad (3.4-26)$$

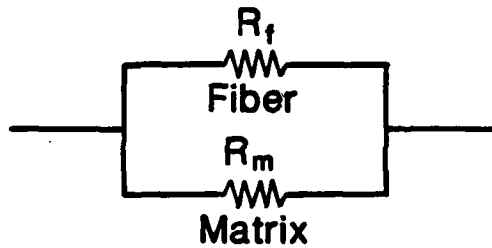
Substituting Equation 3.4-25 into Equation 3.4-26 results in:

$$k_z^{uc}(T) = \frac{2b\Delta x_m k_m^2(T) + b^2 k_m(T) k_f(T)}{2b\Delta x_m k_f(T) + b^2 k_m(T)} \quad (3.4-27)$$

With this result, we see that k_z reduces to k_f as $\Delta x_m \rightarrow 0$.

b. Radial Thermal Conductivity

The radial thermal conductivity is determined with the following thermal resistance model:



From this model, the radial thermal resistance for the unit cell (uc) is:

$$R_r^{uc} = \frac{R_f R_m}{R_f + R_m} \quad (3.4-28)$$

From Equation 3.4-28, the radial thermal conductivity for the unit cell is:

$$k_r^{uc}(T) = (1 - c)k_m(T) + ck_f(T) \quad (3.4-29)$$

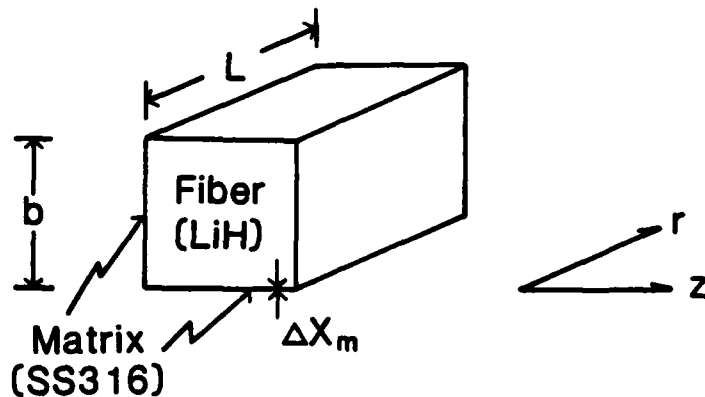
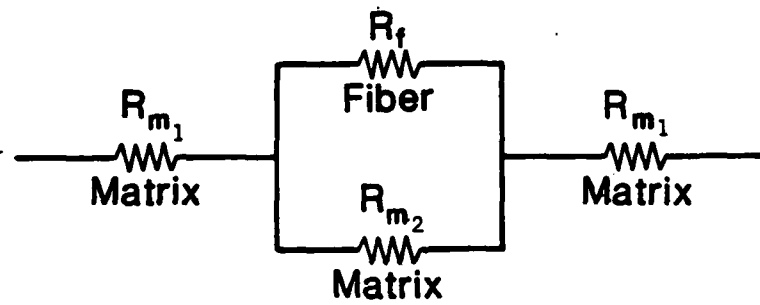


Figure 3.4-2: Unit Cell Used to Model Orthotropic Thermal Conductivities

a. Axial Thermal Conductivity

The axial thermal conductivity is determined with the following thermal resistance model:



From this model, the axial thermal resistance for the unit cell (uc) is:

$$R_z^{uc} = R_{m1} + \frac{1}{1/R_f + 1/R_{m2}} + R_{m1} \quad (3.4-24)$$

With $b - 2\Delta X_m \approx b$, Equation (3.4-24) simplifies to:

$$R_z^{uc} = \frac{2\Delta X_m}{bLk_m} + \frac{b}{L(2\Delta X_m k_m + k_f b)} \quad (3.4-25)$$

For surface elements the local node numbers 1 and 2 form the boundary nodes in Equations 3.4-22.

3.4.2 Principal Axis Thermal Conductivities. The algebraic set of equations used to solve for the temperature throughout the shield includes a tensor matrix to account for directionally dependent thermal conductivities. Tungsten, the gamma attenuation portion of the shield, is an isotropic material, thereby simplifying to $k_r(T) = k_z(T)$. However, the neutron attenuation material for the space reactor is currently envisioned to be comprised of lithium hydride either pressed (hot or cold) or cast into a thin foil honeycomb matrix, made of stainless steel. This material had been shown to have a minor directional dependence to the principal axis thermal conductivities [Welch, 1967a].

To maintain an axisymmetric shield, thermal resistance of the shield was modelled as shown in Figure 3.4-2. The LiH and honeycomb matrix were homogenized to a unit cell, with principal axes aligned with material axes.

All radial conduction paths were considered as parallel to the longitudinal axis of the honeycomb structure. The axial direction thermal resistance was based on the heat conduction path perpendicular to the honeycomb structure. The conductivity matrix was considered to be orthotropic, with no contribution of axial heat transfer to radial heat transfer and vice versa. In other words.

$$k(r,z,T) = \begin{bmatrix} k_r(T) & 0 \\ 0 & k_z(T) \end{bmatrix} \quad (3.4-23)$$

The values of k_r and k_z were based on the following thermal resistance models:

The contributions of K_s , $\tilde{R}_{q_{ext}}$, R_h , and R_k to the matrix and vector are included only for surface elements (SE) experiencing convection, radiative heat transfer, or an external heat flux. A final substitution to be made is to discretize the radius, r , within each integral by:

$$r = N_i r_i \quad (3.4-21)$$

The integrations can now be carried out using the shape functions for the 3 node triangular elements, presented in Equation 3.2-8. Carrying out these integrations, the elemental equations are:

$$\begin{aligned} K &= \frac{k_r}{12\Delta} (r_1 + r_2 + r_3) \begin{bmatrix} b_1^2 & b_1 b_2 & b_1 b_2 \\ b_2 b_1 & b_2^2 & b_2 b_3 \\ b_2 b_3 & b_3 b_2 & b_3^2 \end{bmatrix}_{\text{sym}} \\ &\quad + \frac{k_z}{12\Delta} (r_1 + r_2 + r_3) \begin{bmatrix} c_1^2 & c_1 c_2 & c_1 c_3 \\ c_2 c_1 & c_2^2 & c_2 c_3 \\ c_3 c_1 & c_3 c_2 & c_3^2 \end{bmatrix}_{\text{sym}} \\ K_s &= h(T^{s(i-1)}) \frac{\ell_{ij}}{12} \begin{bmatrix} 3r_1 + r_2 & r_1 + r_2 \\ r_1 + r_2 & r_1 + 3r_2 \end{bmatrix} \\ &\quad + \kappa (T^{s(i-1)}) \frac{\ell_{ij}}{12} \begin{bmatrix} 3r_1 + r_2 & r_1 + r_2 \\ r_1 + r_2 & r_1 + 3r_2 \end{bmatrix} \\ \tilde{R}_{q_{ext}} &= \frac{\Delta}{60} \begin{bmatrix} 6r_1 + 2r_2 + 2r_3 & 2r_1 + 2r_2 + r_3 & 2r_1 + r_2 + 2r_3 \\ \text{Sym} & 2r_1 + 6r_2 + 2r_3 & r_1 + 2r_2 + 2r_3 \\ & 2r_1 + 2r_2 + 6r_3 & \end{bmatrix} \{q_1^{(i)} \quad q_2^{(i)} \quad q_3^{(i)}\} \\ R_h &= h(T^{s(i-1)}) \frac{\ell_{ij}}{12} \begin{bmatrix} 3r_1 + r_2 & r_1 + r_2 \\ r_1 + 3r_2 & r_3 + 3r_2 \end{bmatrix} \left\{ T^\infty - T_1^{s(i-1)} \quad T^\infty - T_2^{s(i-1)} \right\} \\ R_k &= \kappa (T^{s(i-1)}) \frac{\ell_{ij}}{12} \begin{bmatrix} 3r_1 + r_2 & r_1 + r_2 \\ r_1 + r_2 & r_1 + 3r_2 \end{bmatrix} \left\{ T^\infty - T_1^{s(i-1)} \quad T^\infty - T_2^{s(i-1)} \right\} \end{aligned} \quad (3.4-22)$$

Substitution of Equation 3.4-18 into Equation 3.4-17 and this, in turn, into Equation 3.4-16 results in:

$$\begin{aligned}
 & \int_A k_r N_i, r N_j, r \Delta T_i^j r dr dz + \int_A k_z N_i, z N_j, z \Delta T_i^j r dr dz + \int_{\text{ext}} h(T) N_i N_j \Delta T_i^j r d\alpha \\
 & + \int_{\text{ext}} \kappa(T) N_i N_j \Delta T_i^j r d\alpha = \int_A N_i N_j q_i^{i-1} r dr dz + \int_{\text{ext}} N_i N_j q_i^{i-1} r d\alpha \\
 & + \int_{\text{ext}} h(T) N_i N_j (T_i^{\infty} - T_i^{s(i-1)}) r dr dz + \int_{\text{ext}} \kappa(T) N_i N_j (T_i^{\infty} - T_i^{s(i-1)}) r dr dz \\
 & - \int_A k_r N_i, r N_j, r T_i^{i-1} r dr dz - \int_A k_z N_i, z N_j, z T_i^{i-1} r dr dz
 \end{aligned} \tag{3.4-19}$$

This represents the system of equations for a single element. The total system of equations are assembled by simply summing over all elements. The final system to be solved can be expressed in matrix form as:

$$[K^i + K_s^i] \Delta T^i = R^i - K^{i-1} T^{i-1} \tag{3.4-20}$$

where:

$$K = \sum_{i=1}^{NE} \int_A (k_r N_i, r N_j, r + k_z N_i, z N_j, z) r dr dz$$

$$K_s = \sum_{i=1}^{SE} \int_{\text{ext}} (h(T) N_i N_j + \kappa(T) N_i N_j) r dr dz$$

$$R = R_q \dots + R_{q_{\text{ext}}} + R_h + R_k$$

$$R_q = \sum_{i=1}^{NE} \int_A N_i N_j q_i^{i-1} r dr dz$$

$$R_{q_{\text{ext}}} = \sum_{i=1}^{SE} \int_{\text{ext}} N_i N_j q_i^{i-1} r d\alpha$$

$$R_h = \sum_{i=1}^{SE} \int_{\text{ext}} h(T) N_i N_j (T_i^{\infty} - T_i^{s(i-1)}) r dr dz$$

$$R_k = \sum_{i=1}^{SE} \int_{\text{ext}} \kappa(T) N_i N_j (T_i^{\infty} - T_i^{s(i-1)}) r dr dz$$

A final substitution to made is based on an energy balance at the surface which requires that energy flux conducted to the surface equals the energy flux carried away by convection and radiation and energy flux deposited by external heat sources. Or,

$$-k_n T_{n,n} = q_{n,n} = h(T)(T^s - T^o) + \kappa(T)(T^s - T^o) - q_{ext} \quad (3.4-15)$$

The boundary condition of Equation 3.4-2 does not include the convection or external heat source terms, as they are not present in this analysis. Nevertheless, they are carried through in this derivation for the sake of completeness.

Substituting Equation 3.4-15 into Equation 3.4-14 and performing some algebra results in:

$$\int_V k_r T_r N_r dV + \int_V k_z T_z N_z dV = \int_V q''' N dV + \int_S q_{ext} N dS \\ + \int_S N h(T)(T^o - T^s) dS + \int_S N \kappa(T)(T^o - T^s) dS \quad (3.4-16)$$

As before, an elemental temperature is expended in terms of the shape functions and nodal unkowns as:

$$T^{(e)} = \sum_{i=1}^3 N_i T_i = N_i T_i \quad (3.4-17)$$

Indicial
Notation

where the expansion is defined in terms of 3 node, triangular elements. A further substitution is made for T_i by making a Newton-Raphson approximation for determining the nonlinear temperature in an incremental approach. Thus, the nodal temperature for the i th iteration is found from:

$$T_i^i = T_i^{i-1} + \Delta T_i^i \quad (3.4-18)$$

where the subscript i still represents the nodal value and the superscript i represents the iteration number.

$$\int_V \left[\frac{1}{r} ((k_r r N T_r)_r - k_r r T_r N_r) + \frac{1}{r} ((k_z r N T_z)_z - k_z r N_z T_z) + q''' N \right] dV = 0 \quad (3.4-9)$$

From Gauss' Theorem, for a general vector \mathbf{y} :

$$\int_V \text{div } \mathbf{y} dV = \int_S \mathbf{v}_n dS \quad (3.4-10)$$

where \mathbf{v}_n is the normal component of \mathbf{y} at the surface.

In cylindrical coordinates, the divergence of \mathbf{y} is:

$$\text{div } \mathbf{y} = \frac{1}{r} [(r v_r)_r + (r v_z)_z + v_{\theta,\theta}] \quad (3.4-11)$$

The axisymmetry of the problem requires that $v_{\theta,\theta} = 0$. From Fourier's law, we have:

$$q \cdot n_r = -k_r T_r \quad (3.4-12)$$

$$q \cdot n_z = -k_z T_z$$

where n_r and n_z are unit normals in the radial and axial directions.

The first and third terms of Equation 3.4-9 can be rewritten in terms of Equation 3.4-12, as:

$$\frac{1}{r} (k_r r N T_r)_r = -\frac{1}{r} (r N q \cdot n_r)_r \quad (3.4-13)$$

$$\frac{1}{r} (k_z r N T_z)_z = -\frac{1}{r} (r N q \cdot n_z)_z$$

Comparison of Equations 3.4-13 with Equation 3.4-11 shows that the volume integrals of the first and third terms of Equation 3.4-9 can be replaced by surface integrals, resulting in:

$$\int_S (q \cdot n_r) N dS + \int_S (q \cdot n_z) N dS + \int_V k_r T_r N_r dV + \int_V k_z T_z N_z dV + \int_V q''' N dV = 0 \quad (3.4-14)$$

was achieved in the same manner as the radiation transport (diffusion) equation. The residual of the governing equation was weighted with an arbitrary test function and integrated over the volume. The state variable, temperature, was expanded in terms of a linear set of basis functions. Using the same basis functions for the state variable and the test function, the Galerkin formulation for steady state heat conduction in cylindrical coordinates takes the form:

$$\int_V \left[\frac{1}{r} (r k_r T_{,r})_{,r} + \frac{1}{r} (r k_z T_{,z})_{,z} + q''' \right] N \, dV = 0 \quad (3.4-4)$$

In its current form, Equation 3.4-4 would produce a nonsymmetric matrix and the order of the basis functions would have to be at least quadratic to insure a continuous temperature distribution. However, with a slight amount of algebra, a weak, symmetric form can be derived which is more readily adaptable to digital computation. We begin by recalling the chain rule from calculus:

$$(rNT_{,r})_{,r} = rNT_{,rr} + NT_{,r} + rT_{,r}N_{,r} \quad (3.4-5)$$

Again from the chain rule:

$$N(rT_{,r})_{,r} = rNT_{,rr} + NT_{,r} \quad (3.4-6)$$

Comparing Equations 3.4-6 and 3.4-5 results in:

$$N(rT_{,r})_{,r} = (rNT_{,r})_{,r} - rT_{,r}N_{,r} \quad (3.4-7)$$

A similar application of the chain rule leads to:

$$N(rT_{,z})_{,z} = (rNT_{,z})_{,z} - rN_{,z}T_{,z} \quad (3.4-8)$$

Now assuming a weak dependence of k_r and k_z on r , Equations 3.4-7 and 3.4-8 can be substituted into Equation 3.4-4 resulting in:

D. For all other shield surfaces:

$$\mathbf{g} \cdot \mathbf{n} = 0 \quad (3.4-3)$$

The internal heat generation $q'''(r, z)$ was determined for each mesh point from radiation transport. Heating within the shield was due primarily to neutron scattering and absorption, and gamma attenuation. The equations for converting the respective neutron and gamma fluxes were included in the previous section.

With the internal heat generation within the shield determined, the temperature distribution can be calculated. The nonlinearity due to radiative cooling of the shield can be dealt with by linearizing the energy transfer at the cooling surface by:

$$\begin{aligned} g_r &= \sigma \epsilon F_{i+j} (\bar{I}^{s^4} - \bar{I}^{\infty^4}) \\ &= \sigma \epsilon F_{i+j} (\bar{I}^{s^2} + \bar{I}^{\infty^2})(\bar{I}^s + \bar{I}^{\infty})(\bar{I}^s - \bar{I}^{\infty}) = \xi(T)(\bar{I}^s - \bar{I}^{\infty}) \end{aligned} \quad (3.4-4)$$

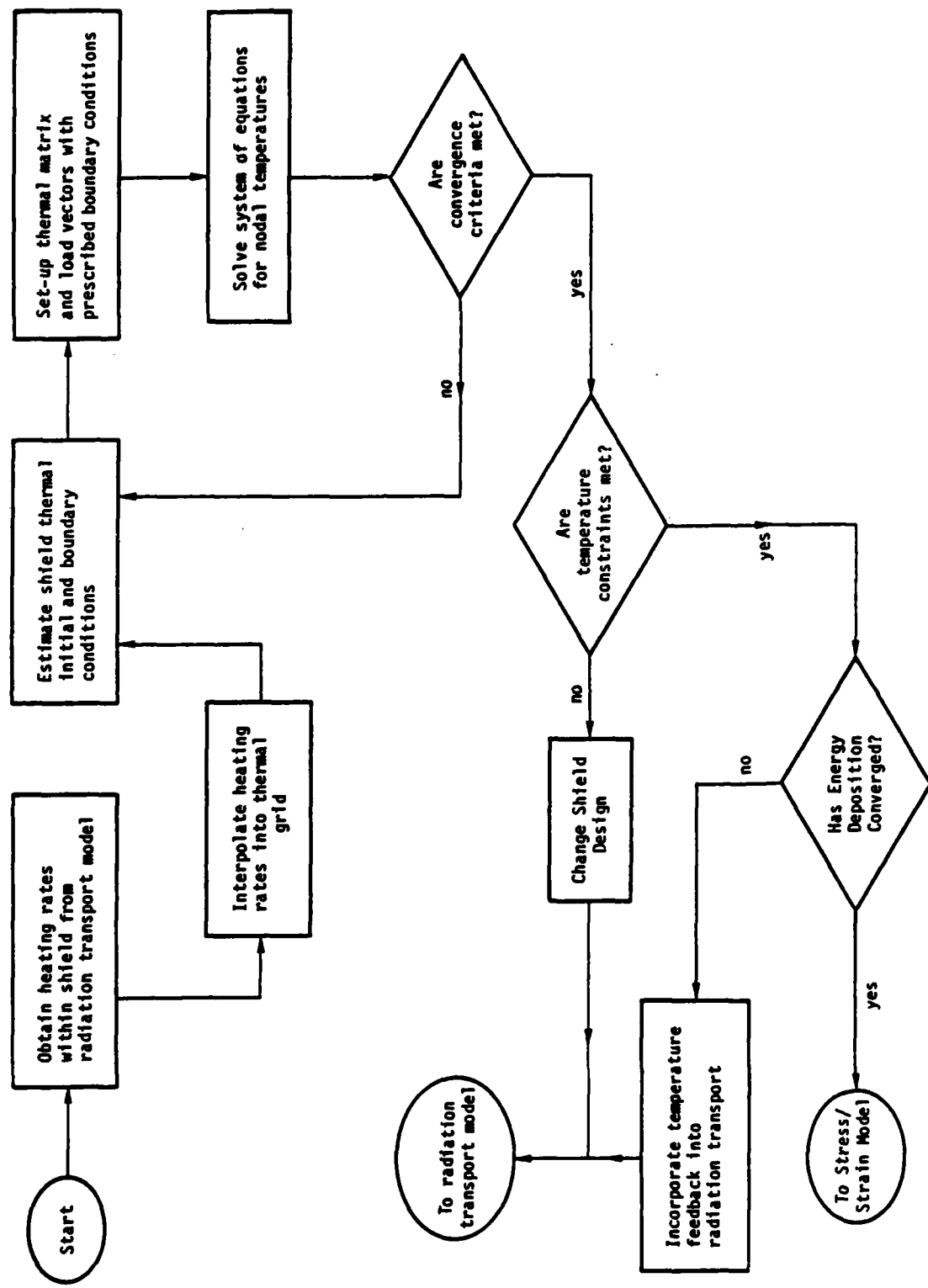
where:

$$\xi(T) = \sigma \epsilon F_{i+j} (\bar{I}^{s^2} + \bar{I}^{\infty^2})(\bar{I}^s + \bar{I}^{\infty})$$

A variety of numerical schemes have been employed to equate the radiated energy with the energy conducted to the surface through the shield in order to determine the temperature dependent radiation heat transfer coefficient, $\xi(T)$ [Bathe, 1982 and Huebner and Thornton, 1982]. Using this equivalent radiation coefficient, the temperature distribution can be iterated on until an energy balance equilibrium is achieved.

3.4.1 Derivation of System of Equations for Solving Nonlinear Temperature Distribution. The discretization of the heat conduction equation into a form that can be easily solved on a digital computer

Figure 3.4-1. Temperature Model Overview



If $-180 < \gamma < 0$ and $|\gamma| < 90 + |\beta|$ then

$$\alpha = 90 - (|\gamma| - \beta) \quad (3.4-32)$$

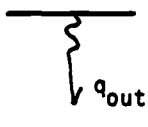
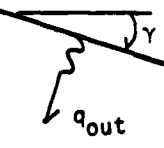
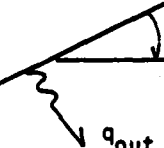
$$q_{out} = q_{net} \cdot \cos\alpha$$

The value of q_{out} is then summed as part of the total energy leaving that particular surface. Similar type algorithms are built into SHLDTEMP for other angled surfaces. All that is required of the user is to define the type of surface (see Figure 3.4.5) and the surface boundary condition (adiabatic, isothermal, radiative heat transfer, convective heat transfer) when the mesh is being generated. From this input, the necessary information to perform the heat transfer calculation is generated.

3.4.4 Validation of Temperature Code. To test the accuracy of the temperature code, SHLDTEMP, 1-D temperature distributions in both cartesian and cylindrical coordinates were determined using the Newton-Raphson method with simplex elements. The results were then compared with the exact solution. The test cases consisted of a W-LiH shield, internally heated by gamma radiation and neutrons, cooled by thermal radiation to space, and either insulated or isothermal at its front (slab) or inner surface (cylinder). Heating rates at the front surface of the shield were assumed uniform along the entire core-shield interface.

The governing equation for the temperature distribution in each region was a Poisson equation with constant thermal conductivities. For the slab shield, internal heating rates were exponentially attenuated by each region's respective neutron removal and gamma absorption cross sections. The exact analytical solutions for the slab are contained in Appendix 1. For the cylindrical shield, internal heating was

Figure 3.4-5 Types of Surface Available for User Selection
In Determining Final Heat Flow in SHLDTEMP

| Type # | Axes Frame | Geometric | Surface Descriptor | SP-100 Shield Location ¹ |
|--------|---|---|--------------------|-------------------------------------|
| 1 |  |  | | Inner Radial Front |
| 2 | " |  | | Outer Radial Front |
| 3 | " |  | | Outer Axial Front |
| 4 | " |  | | Outer Axial Back |
| 5 | " |  | | Radial Back |

¹Surface in SP100 Shield as Follows:

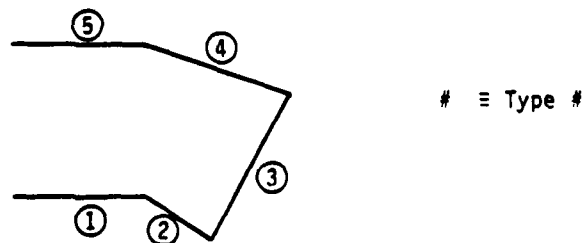


Figure 3.4-6 Comparison of FEM Solution Using SHIELD with Exact Solution for 1-D, Slab Shield

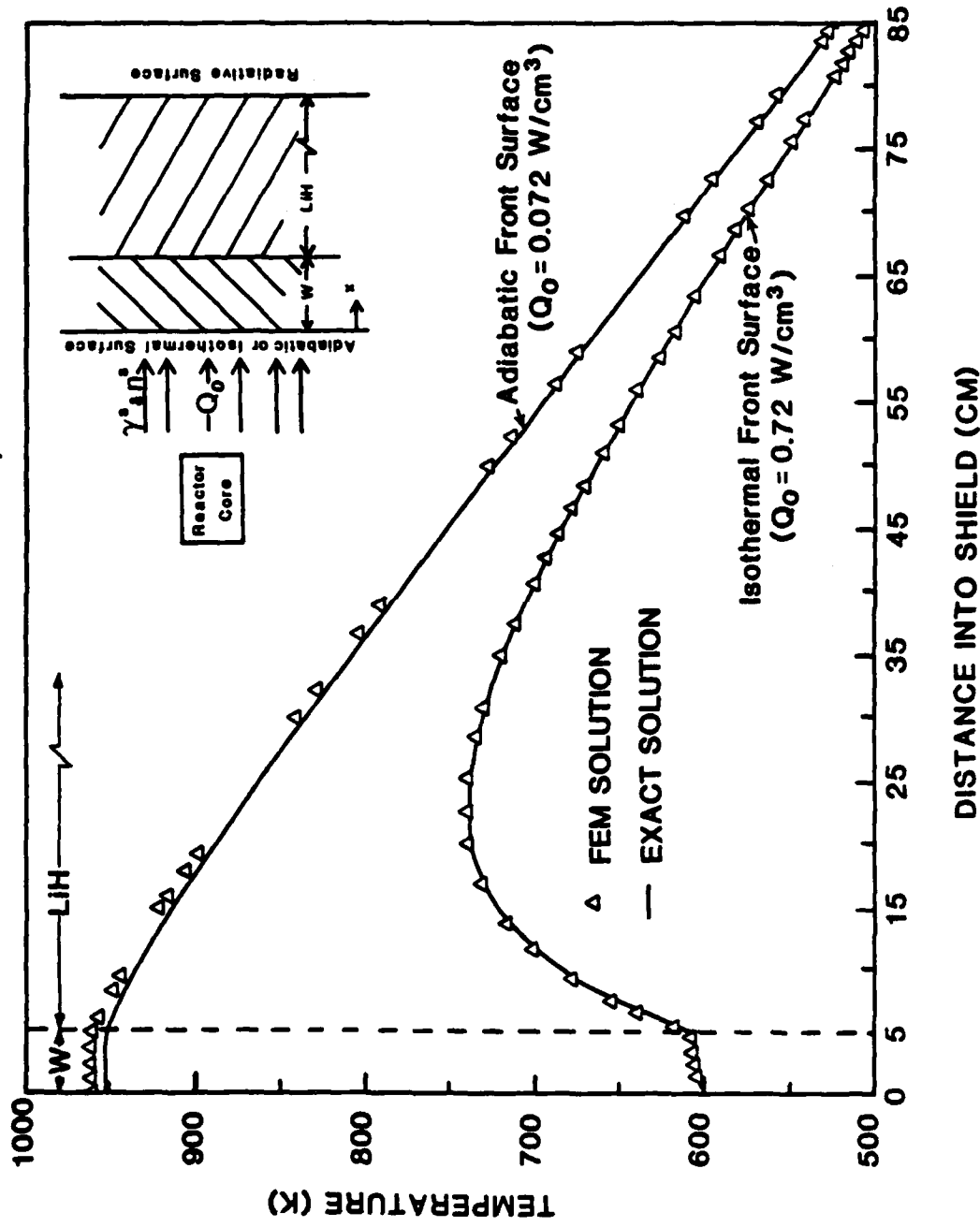
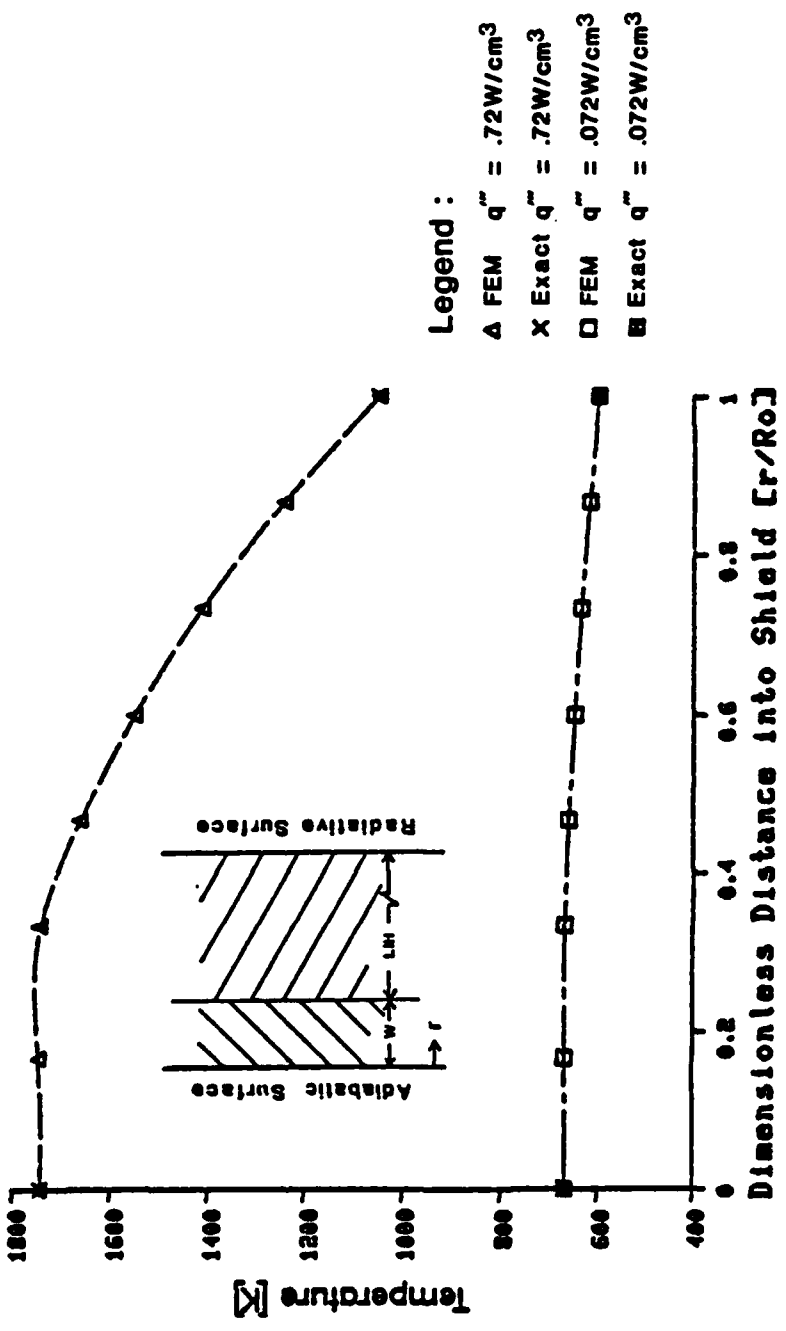


Figure 3.4-7 Comparison of FEM with Exact Solution for 1-D Cylinder with Constant Internal Heating



kept constant. The exact solution for the cylinder is included in Appendix 2. Figure 3.5-6 shows the 1-D slab results for both the adiabatic and isothermal front surface conditions. The excellent agreement between analytic and FEM solutions is readily apparent. The maximum difference between the two solutions was less than 0.1%. The input data from the test cases is included in Table A1 of Appendix 1. Figure 3.5-7 shows the 1-D, cylinder results for an adiabatic inner surface for two different heating values. Again, the agreement between exact and numerical solutions is excellent, differing by less than 0.1% at any given radial position.

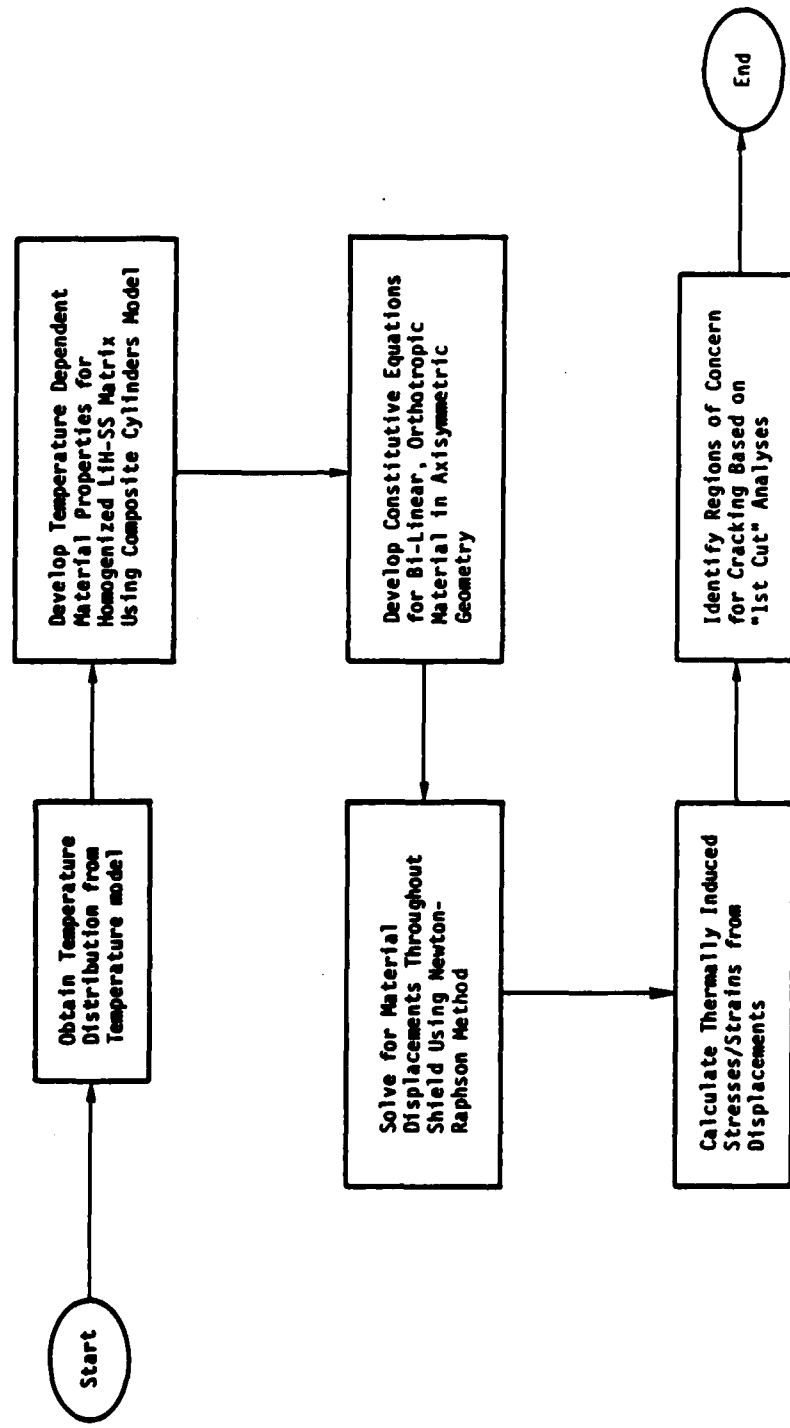
3.5 Block 3: Thermal Stress/Strain Theory. The main objectives of this block were to:

- a. Model the shield of the SP-100 reactor as an axisymmetric structure, with specified displacement conditions.
- b. Develop a finite element code for evaluating the steady-state stresses, strains, and displacements induced by the temperature gradient throughout the axisymmetric shield. Bilinear elasticity theory was used during this analysis.

Figure 3.5-1 is an overview of the stress/strain analysis model developed for the shield. Once the temperature distribution was known, the effects of temperature gradient on the strains and stresses were determined. To better understand the effect of temperature, the equilibrium equations for a 3-D body are [Rivello, 1969]:

$$(\lambda + G) \frac{\partial e}{\partial x_{11}} + G v^2 u_{11} - (3\lambda + 2G) \frac{\partial \alpha_T T}{\partial x_{11}} + X_{11} = 0 \quad (3.5-1)$$

Figure 3.5-1. Stress/Strain Model Overview.



where:

$$\lambda = \text{Lamé constant} = \frac{\nu E}{(1 + \nu)(1 - 2\nu)}$$

E = Young's modulus of elasticity

ν = Poisson's ratio

G = Shear modulus of elasticity

u_{ii} = Displacement in i axis direction

$\alpha_{T_{ii}}$ = Temperature coefficient of expansion in i axis direction

T = Temperature

x_{ii} = Surface force component in i axis direction

$e = \nabla \cdot u_{ii}$

x_{ij} = Position vector

One can readily see from Equation 3.5-1 that the temperature gradient (3rd term on left hand side of the equation) takes the form of a body force in its influence on the equilibrium of a continuum structure. Once the displacements (and strains) are known, the stresses are determined from:

$$\sigma_{ii} = \lambda e + 2G \epsilon_{ii} - (3\lambda + 2G) \alpha_{T_{ii}} T \quad (3.5-2)$$

$$\sigma_{ij} = G \epsilon_{ij} \quad (3.5-3)$$

where ϵ_{ii} are longitudinal strains and ϵ_{ij} are shearing strains.

The temperature of Equation 3.5-2 represents the local temperature rise at a point location above some reference datum.

The magnitude of the temperature gradient affects the thermal strains, and along with the temperature at that location, gives rise to local stresses. The flowchart of Figure 3.4-1 gives an overview of the displacement method in solving for the strains and stresses using finite element theory.

From previous experimental data during the SNAP program, tension cracking was encountered in the LiH in previous designs at the lower power levels. Welch (1967a and 1967c) has also reported the appearance of compressive creep in LiH at elevated temperatures. Such behavior was not unexpected since the material was mentioned at temperatures well above $0.5 \times T_{melt}$. At such high temperatures, a detailed stress analysis must account for the plastic behavior prior to fracture cracking in the LiH.

As if this geometric nonlinearity did not offer the computational analyst enough challenge, lithium hydride is a bilinear material, with different elastic moduli for compression and tension. Hence, even for small strain states, an incremental load approach is required to analyze the thermal stresses. The general approach adopted in this research was to initially consider the LiH-SS matrix in a 3-D coordinate systems, treating the LiH surrounded by SS as a composite material. Using composite cylinders models developed by Christensen and Hashin [Christensen, 1979] to analyze a unit cell, the principal axes material properties were calculated for the homogenized cell.

Compliance and stiffness moduli were then determined using bilinear elasticity theory as developed by Jones (1977) for orthotropic materials in a principal axes coordinate system. The calculation of the thermal stress/strains was completed using a modified Newton-Raphson iteration, with the spatial discretization modelled with the 3 node, bilinear shape functions for each element.

The system of equations to be solved for the material displacements using linear elastic theory will shortly be derived. As before,

a Galerkin formulation can be used to generate this system of equations. Such a derivation is included in the finite element text by Zienkiewicz and Morgan (1983). However, as a comparison with the previous derivations, the equations will be briefly outlined starting with a variational function. While the end result is the same, what becomes obvious is the somewhat "blind" reliance on the accuracy of the functional by the engineer in accurately representing the physical reality of the system to be analyzed. As with the question of linear versus higher order elements, this issue is well outside the scope of this research and left for others to address.

3.5.1 Derivation of System of Equations for Determining Stresses/Strains. The system of equations to be solved for the displacements of the shield are based on an equilibrium of forces during steady-state operation. Variational calculus is used to derive this system in axisymmetric cylindrical coordinates.

For a linear elastic continuous medium, the variational function is [Pian and Tong, 1969 and Bathe, 1982]:

$$\pi = \frac{1}{2} \int_V \epsilon^T C \epsilon dV - \int_V U^T f_B dV - \int_S U^T f_S dS - \sum_i U^T F^i \quad (3.5-4)$$

where:

ϵ = strain vector

C = Material matrix

U = Displacements

f_B = Body forces

f_S = Surface or traction forces

F^i = Concentrated forces

The virtual derivative of the functional is set equal to zero, resulting in:

$$\delta \pi = 0 = \int_V \delta \epsilon^T C \epsilon dV - \int_V \delta U^T f_B dV - \int_S \delta U^T f_S dS - \sum_i \delta U^T F^i$$

(3.5-5)

By discretizing Equation 3.5-5, a system of algebraic equations can be derived in terms of the unknown displacements at each node.

For each element, we have:

$$u^{(e)}(r,z) = \sum_{i=1}^n N_i(r,z) U_i = N_i U_i \quad \text{Indicial Notation}$$

where:

$u^{(e)}$ = Displacement of the element

N_i = Shape function for the i th node

U_i = Nodal displacement

n = Number of nodes for each element

From Equation 3.5-6, one can write the discretized strain equation as:

$$\epsilon^{(e)}(r,z) = \sum_{i=1}^n B_i(r,z) U_i = B_i U_i \quad \text{Indicial Notation}$$

where B_i is the strain-displacement operator for an axisymmetric geometry.

Substituting Equations 3.5-6 and 3.5-7 into Equation 3.5-5, we are left with:

$$\begin{aligned}
 \int_V B_i \delta U_i C B_j u_j dV &= \int_S N_i \delta U_i f_s dS \\
 + \int_V N_i \delta U_i f_B dV - \int_V B_i \delta U_i C \alpha_T T dV \\
 - \int_V B_i \delta U_i \sigma_I dV
 \end{aligned} \tag{3.5-8}$$

The last term on the right-hand side of Equation 3.5-8 is included to account for any initial stresses on the system other than thermal loading due to the temperature gradient. Since Equation 3.5-8 accounts for only a single element, the system of equations for the entire assemblage of elements must be included. Thus, the final system of algebraic equations to be solved becomes:

$$\begin{aligned}
 \sum_{e=1}^{NE} \delta U_i^t \int_V B_i C B_j U_j dV &= \sum_{e=1}^{NE} \delta U_i^t [\int_S N_i f_s dS + \int_V N_i f_B dV \\
 - \int_V B_i C \alpha_T T dV - \int_V B_i \sigma_I dV]
 \end{aligned} \tag{3.5-9}$$

Dividing out the δU_i from both sides, Equation 3.5-9 can be rewritten as:

$$\sum_z K_{ij} U_j = R_i \tag{3.5-10a}$$

and

$$R_i = R_s + R_B - R_I - R_T \tag{3.5-10b}$$

where:

$$\sum_z K_{ij} = \int_A B_i C B_j r dr dz$$

$$R_s = \int_z N_i f_s r dz$$

$$R_B = \int_A N_i f_B r dr dz$$

$$\underline{R}_I = \int_A B_i \sigma r dr dz$$

$$\underline{R}_T = \int_A B_i C_a T r dr dz$$

As with the temperature calculation, Equation 3.5-10 can be cast as a Newton Raphson iteration and solved as:

$$\underline{\underline{K}}^i \underline{\underline{\Delta U}}^i = \underline{\underline{R}}^i - \underline{\underline{K}}^{i-1} \underline{\underline{U}}^i \quad (3.5-11a)$$

from which the displacements are determined as:

$$\underline{\underline{U}}^i = \underline{\underline{U}}^{i-1} + \underline{\underline{\Delta U}}^i \quad (3.5-11b)$$

The use of Equation 3.5-11a allows for the solution of material nonlinear problems. It also means that the program used to solve the nonlinear temperature distribution, can be adapted to solve for the bilinear elastic or materially nonlinear stresses, as well.

During steady-state operation of the SP-100 reactor, the only loading on the shield is due to temperature effects, which are often viewed as initial body loads. This means that \underline{R}_T of Equation 3.5-10 is the only contribution to the right hand side of the equilibrium Equation 3.5-11.

The exact composition of \underline{N}_i , \underline{B}_i , and \underline{C} have yet to be defined. The discussion of the next section focuses on the material matrix, $\underline{\underline{C}}$, for the neutron attenuation portion of the shield. The SP-100 design calls for lithium hydride to be cast or cold-pressed into a honeycomb matrix, made of stainless steel. The LiH-honeycomb matrix must be "homogenized" in some manner for the numerical calculation of the stress/strain/displacements throughout the shield. The effective material properties of the homogenized matrix were developed using composite theory, which will be presented in the next section.

3.5.2 Composite Cylinders Model. At first appearance, the LiH honeycomb matrix shield appears to be highly anisotropic. The axis parallel to the honeycomb extends throughout the entire radial distance at a prescribed angle in the R-θ plane. This geometry accounts for a θ -dependence of material properties, thus requiring a full 3-D analysis (R-θ-Z). However, in the interest of simplifying the analyses, a single unit cell of the LiH-honeycomb matrix was evaluated to determine under what conditions orthotropic or even isotropic material properties could be used to calculate the thermal stress/strains throughout the shield.

The unit cell was idealized as shown in Figure 3.5-2.

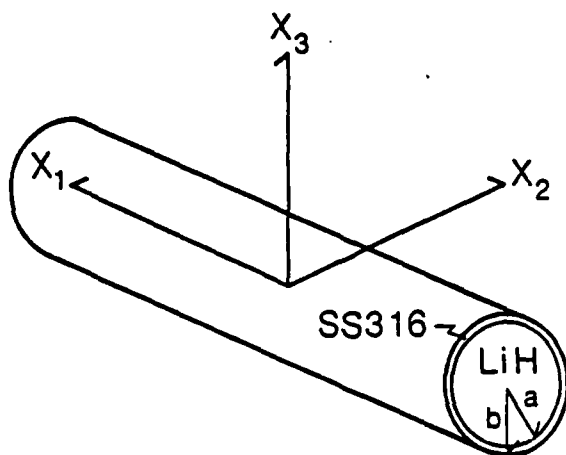


Figure 3.5-2. Unit Cell Used in Stress/Strain Analysis

The composite cylinders model used in composite theory was employed during this analysis in which the LiH was analogous to the fiber and the SS represented the matrix. The coordinate system of Figure 3.5-2 is employed such that the 2-3 plane corresponds to the r-θ (transverse) plane and the 1-axis is the same as the 3-axis of the unit cell. Because of the symmetry in the 2-3 plane, the material is transversely isotropic.

According to composite cylinders theory, the following displacement field was assumed [Christensen, 1979]:

$$\begin{aligned} u_{r_{\text{LiH}}} &= A r \\ u_{r_{\text{SS}}} &= B r + \frac{C}{r} \\ u_z &= \epsilon_z z \end{aligned} \quad (3.5-12)$$

Subject to the following boundary conditions:

$$\begin{aligned} u_{r_{\text{LiH}}} &= u_{r_{\text{SS}}} && \text{at } r = a \\ \sigma_{r_{\text{LiH}}} &= \sigma_{r_{\text{SS}}} && \text{at } r = a \\ \sigma_{r_{\text{SS}}} &= 0 && \text{at } r = b \end{aligned} \quad (3.5-13)$$

The first two boundary conditions of Equation 3.5-13 imply perfect contact between the LiH and SS during operation, which is quite reasonable based on experimental results during the SNAP program. The third boundary condition requires that the outer radial stress disappears from the unit cell. Since this outer surface is not free to expand due to the constraint of the adjacent unit cell (honeycomb matrix), this boundary condition represents an approximation to the real system.

effective shear modulus is 1.4% at $c = 0.99$ and independent of the Poisson's ratio difference. The error on the uniaxial moduli ranges from 0.7% (for $|v_{\text{LiH}} - v_{\text{Al}}| = 0.13$) to 1.1% (for $|v_{\text{LiH}} - v_{\text{Al}}| = 0.03$) at $c = 0.99$.

Thus, the treatment of an LiH-Al shield at temperatures near 600 K as an isotropic material, has been quantified using the cylindrical cylinders model. The isotropic approximation using ROM is quite reasonable for a wide range of elastic moduli of LiH, provided the difference in Poisson's ratio between the LiH and Al is small. As this difference increases to 0.08 (i.e., $v_{\text{LiH}} = 0.25$), the volume ratio of LiH must be greater than 0.98 to remain within a 10% error bound on all material properties.

The effect of the aluminum on the stiffness of the unit cell can be examined with CCM results. At elevated temperatures, neither LiH nor Al maintain very much stiffness (or strength). Hence, intuitively one would expect the material properties to be very close to those of LiH, as the volume fraction of LiH remains above 99%. Table 3.5-5 lists the moduli and Poisson's ratios for the fiber, matrix, and unit cell using CCM for two widely varying values of Poisson's ratio of LiH and a volume fraction of 99%. From this data, when the difference in Poisson's ratio between the fiber and matrix is minimal, the material properties of the unit cell are nearly those of the fiber at this high volume fraction. However, as the difference in Poisson's ratios widens, the directional dependence of properties begins to emerge, even for a fiber-matrix combination whose stiffness moduli are of the same order of magnitude. Of particular interest from Table 3.5-5 is the fact that when Poisson's ratio of the fiber is much less than that for

both temperatures [Lundberg, 1962], the value of $E_{600\text{ K}}^T = 2.1 \text{ GPa}$ was determined from:

$$E_{600\text{ K}}^T = E_{293\text{ K}}^T \times \frac{E_{600\text{ K}}^C}{E_{293\text{ K}}^C} \quad (3.5-27)$$

The possible error in using this correlation depends on the quality of the LiH samples used in the experiments. The room temperature density of the sample was recorded as 97% weight, minimum. Both the compression and tension test samples were cold pressed. However, there was no mention in these test results as to whether the LiH sample used in compression had been sintered as had the tension test sample.²

An even more basic reason that Equation 3.5-27 may not be accurate, is simply that such a ratio is not valid for a bilinear material. Hence, some sensitivity on E at elevated temperature is warranted. Figure 3.5-5 shows the effect of uncertainties in the elastic modulus of LiH at elevated temperature.

For a modulus of 2.1 GPa for LiH, the ratio of $E_{\text{Al}}/E_{\text{LiH}}$ is 4.0. As this ratio moves closer to 1.0 (corresponding to $E/E_0 = 3$ in figure 3.5-5), the material approaches isotropic over all range of LiH volume fraction, for small differences in Poisson's ratio.

Table 3.5-4 is an attempt to quantify the effect of uncertainties in Poisson's ratio at elevated temperature. For $c = 0.99$, the maximum error in an isotropic assumption ranges from 21.9% (for $|v_{\text{LiH}} - v_{\text{Al}}| = 0.13$) to 1.1% (for $|v_{\text{LiH}} - v_{\text{Al}}| = 0.03$). The error associated with

²however, the test engineer who conducted these experiments recently conveyed that all samples were sintered, to his recollection [Lundberg, 1984].

Figure 3.5-5 Effect of Uncertainties in E_{LH} at 600 K of an LiH-Al Matrix

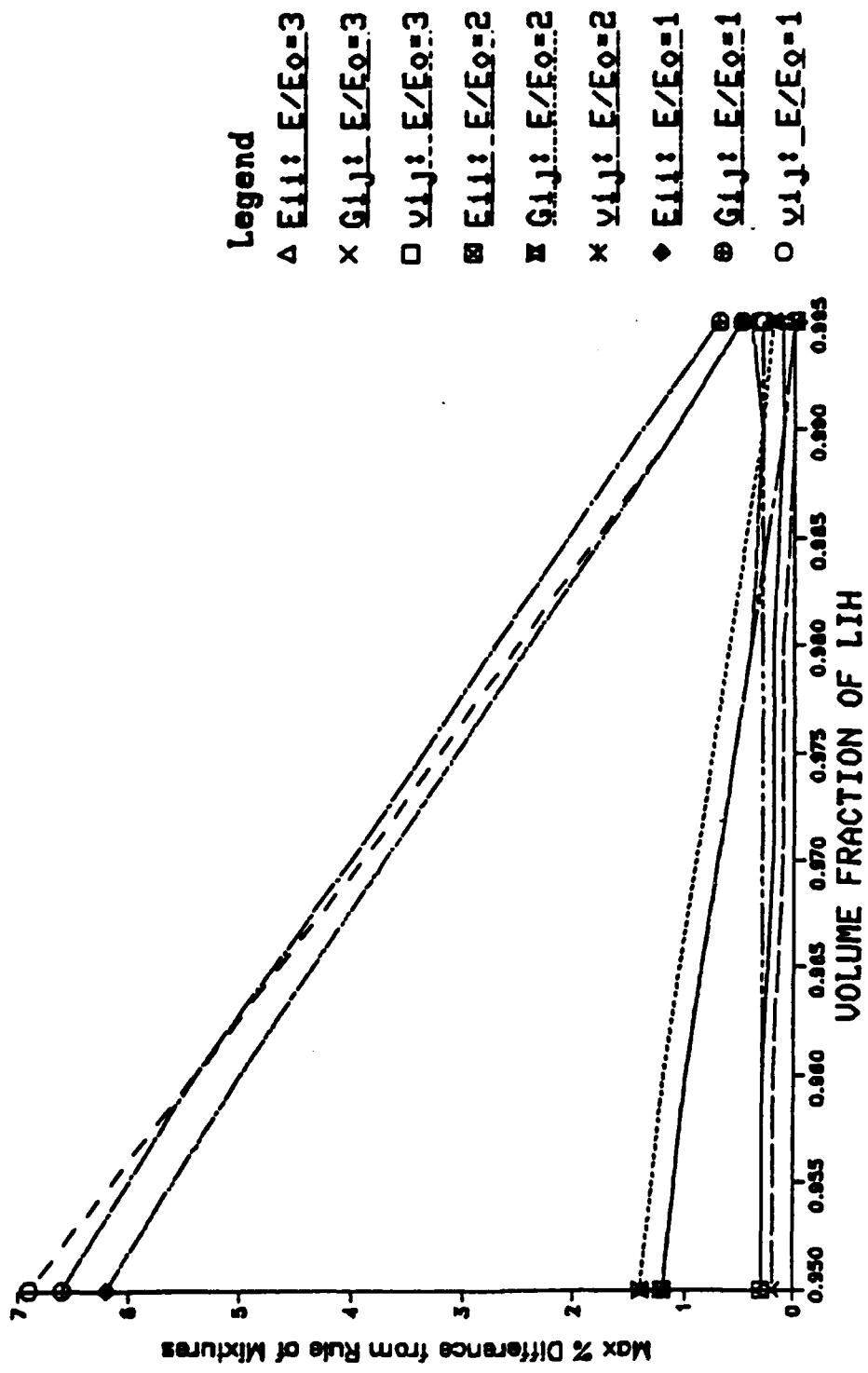


Figure 3.5-4 Effect of Temperature on Isotropic Behavior of LiH-Al Shield with $\nu_{\text{LiH}} = 0.2$

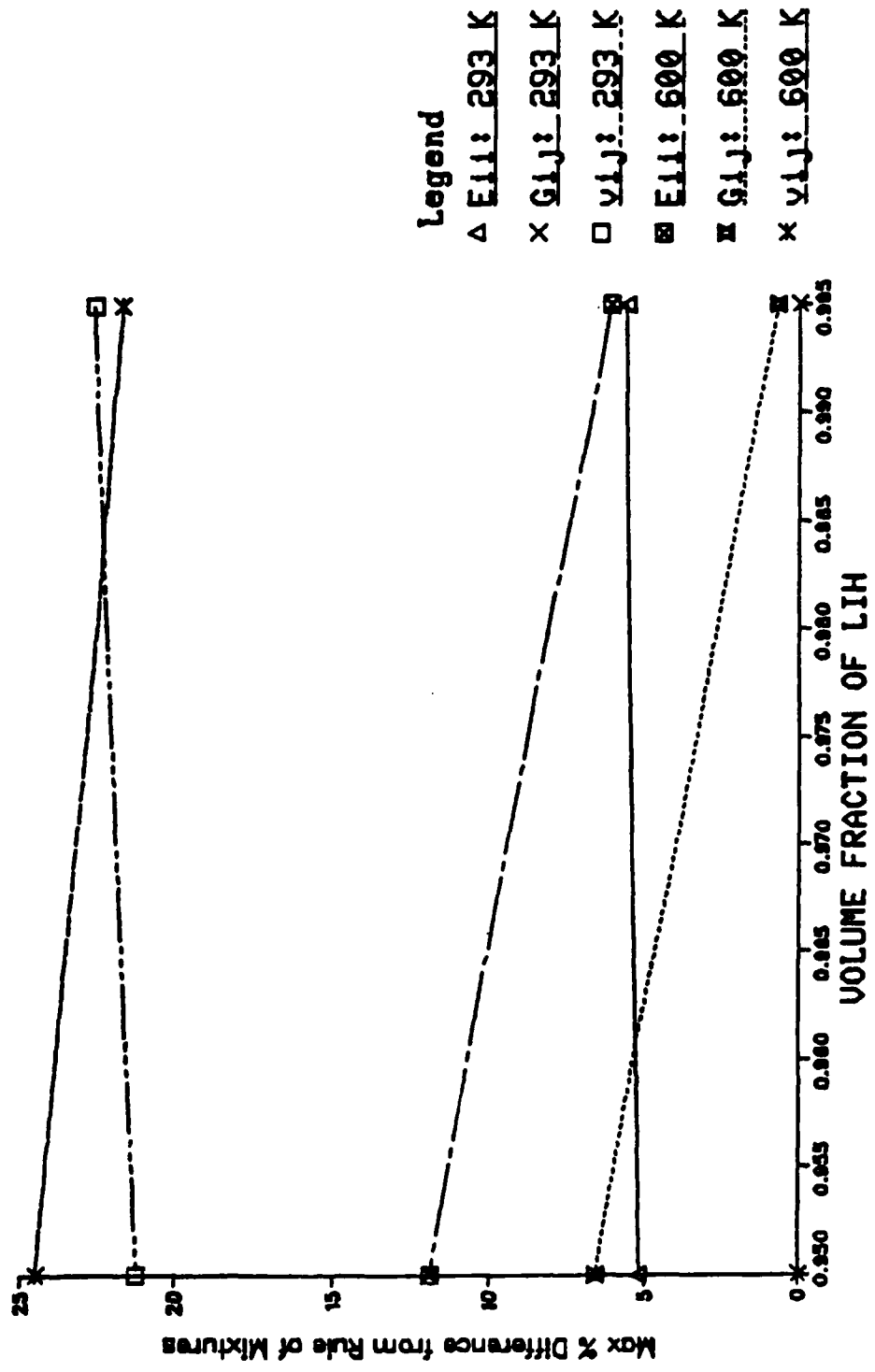
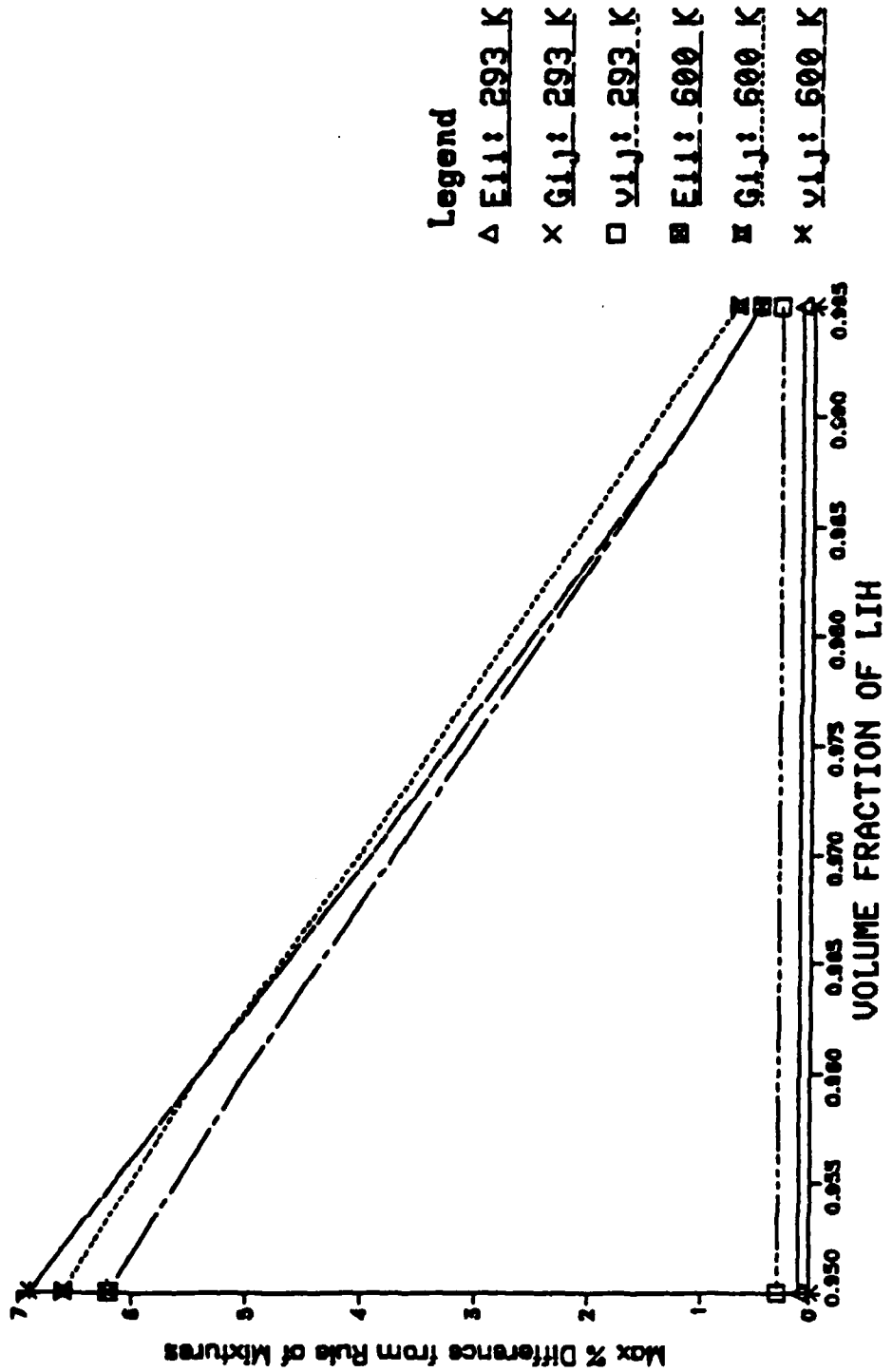


Figure 3.5-3 Effect of Temperature on Isotropic Behavior
of LiH-Al Shield with $v_{LiH} = 0.3$



While the material properties of aluminum are known with a fair degree of certainty even at elevated temperatures, this is not the case for LiH. Hence, some sensitivity analysis is necessary with respect to moduli and Poisson's ratio of the LiH. These sensitivity results are plotted in Figures 3.5-3 through 3.5-5.

From Figures 3.5-3 and 3.5-4, the effect of temperature on isotropicity is analyzed. For the case where Poisson's ratio is close for the two materials ($\nu_{\text{LiH}} = 0.3$, $\nu_{\text{Al}} = 0.33$), the fiber-matrix cell is essentially isotropic, and ROM is quite accurate for determining material properties for all volume fractions of LiH at room temperature. At elevated temperature (600 K), the isotropic approximation with ROM remains quite reasonable (< 7% error) down to 95% volume fraction. Based on past shield designs, the actual volume fraction of LiH should be above 99%, which results in a maximum error of 1.4% or less for the ROM approximation.

As the difference in Poisson's ratio increases between LiH and Al, (i.e., ν_{LiH} decreases), the error in ROM for the effective Poisson's ratio of the homogenized material increases significantly. For a volume fraction of 0.99, the error is 22.4% at room temperature and 21.9% at 600 K. The difficulty of predicting material behavior for composites is reflected by Figure 3.5-4 in observing that the ROM error increases with increasing LiH volume fraction at room temperature, and decreases with increasing LiH volume fraction at elevated temperature. This reversal is due to the relative differences in elastic moduli of LiH and Al at the two temperatures.

The tension modulus for LiH at high temperatures was not reported in any open literature. Since the compression moduli was available for

Table 3.5-4: Effect of Uncertainties in v_{LiH} at 600 K
for an LiH-Al Matrix with $E_{LiH} = 2.1$ GPa

| c | Maximum % Difference From ROM | | |
|-----------------|-------------------------------|----------|----------|
| | E_{ij} | G_{ij} | v_{ij} |
| $v_{LiH} = .20$ | | | |
| .995 | 6.1 | .7 | 21.6 |
| .99 | 6.7 | 1.4 | 21.9 |
| .98 | 8.1 | 2.7 | 22.4 |
| .97 | 9.4 | 4.1 | 23.1 |
| .96 | 10.7 | 5.4 | 23.8 |
| .95 | 11.9 | 6.6 | 24.5 |
| $v_{LiH} = .25$ | | | |
| .995 | 3.2 | .7 | 9.1 |
| .99 | 3.9 | 1.4 | 9.6 |
| .98 | 5.2 | 2.7 | 10.8 |
| .97 | 6.5 | 4.1 | 12.0 |
| .96 | 7.8 | 5.4 | 13.2 |
| .95 | 9.0 | 6.6 | 14.3 |
| $v_{LiH} = .30$ | | | |
| .995 | .5 | .7 | .5 |
| .99 | 1.1 | 1.4 | 1.1 |
| .98 | 2.4 | 2.7 | 2.5 |
| .97 | 3.7 | 4.0 | 3.9 |
| .96 | 5.0 | 5.4 | 5.4 |
| .95 | 6.2 | 6.6 | 6.9 |

Table 3.5-3: Effect of Uncertainties in LiH Elastic Moduli
at 600 K for an LiH-Al Matrix with $\nu_{LiH} = 0.3$
[$E_0 LiH = 2.1$ GPa]

| c | Maximum % Difference From ROM | | |
|-----------------------|-------------------------------|----------|------------|
| | E_{ij} | G_{ij} | ν_{ij} |
| $E_{LiH}/E_0 LiH = 3$ | | | |
| .995 | .1 | 0.0 | .3 |
| .99 | .1 | 0.0 | .3 |
| .98 | .2 | .1 | .3 |
| .97 | .2 | .1 | .3 |
| .96 | .3 | .2 | .3 |
| .95 | .3 | .2 | .3 |
| $E_{LiH}/E_0 LiH = 2$ | | | |
| .995 | 0.0 | .2 | .4 |
| .99 | .1 | .3 | .3 |
| .98 | .4 | .6 | .4 |
| .97 | .7 | .9 | .7 |
| .96 | 1.0 | 1.2 | 1.0 |
| .95 | 1.2 | 1.4 | 1.2 |
| $E_{LiH}/E_0 LiH = 1$ | | | |
| .995 | .5 | .7 | .5 |
| .99 | 1.1 | 1.4 | 1.1 |
| .98 | 2.4 | 2.7 | 2.5 |
| .97 | 3.7 | 4.0 | 3.9 |
| .96 | 5.0 | 5.4 | 5.4 |
| .95 | 6.2 | 6.6 | 6.9 |

Table 3.5-2a. Effect of Temperature on Isotropic Properties
of LiH-Al Matrix with $v_{LiH} = 0.3$

| <u>c</u> | Max % Difference from ROM | | | | | |
|----------|---------------------------|-----------------------|-----------------------|-----------------------|-----------------------|-----------------------|
| | T = Room Temp | | | T = 600 K | | |
| | <u>E₁₁</u> | <u>G_{1j}</u> | <u>v_{1j}</u> | <u>E₁₁</u> | <u>G_{1j}</u> | <u>v_{1j}</u> |
| .995 | .1 | 0.0 | .3 | .5 | .7 | .5 |
| .99 | .1 | 0.0 | .3 | 1.1 | 1.4 | 1.1 |
| .98 | .1 | 0.0 | .3 | 2.4 | 2.7 | 2.5 |
| .97 | .1 | 0.0 | .3 | 3.7 | 4.0 | 3.9 |
| .96 | .1 | 0.0 | .3 | 5.0 | 5.4 | 5.4 |
| .95 | .1 | 0.0 | .3 | 6.2 | 6.6 | 6.9 |

Table 3.5-2b. Effect of Temperature on Isotropic
Properties of LiH-Al Matrix with $v_{LiH} = 0.2$

| <u>c</u> | Max % Difference from ROM | | | | | |
|----------|---------------------------|-----------------------|-----------------------|-----------------------|-----------------------|-----------------------|
| | T = Room Temp | | | T = 600 K | | |
| | <u>E₁₁</u> | <u>G_{1j}</u> | <u>v_{1j}</u> | <u>E₁₁</u> | <u>G_{1j}</u> | <u>v_{1j}</u> |
| .995 | 5.6 | 0.0 | 22.5 | 6.1 | .7 | 21.6 |
| .99 | 5.6 | 0.0 | 22.4 | 6.7 | 1.4 | 21.9 |
| .98 | 5.5 | 0.0 | 22.1 | 8.1 | 2.7 | 22.4 |
| .97 | 5.4 | 0.0 | 21.8 | 9.4 | 4.1 | 23.1 |
| .96 | 5.3 | 0.0 | 21.5 | 10.7 | 5.4 | 23.8 |
| .95 | 5.2 | 0.0 | 21.2 | 11.9 | 6.6 | 24.5 |

Table 3.5-1. LiH and Al Properties Used in Composite Cylinders Model Analysis

Room Temperature, T = 293 K

LiH:

$$E = 72.4 \text{ GPa}$$

$$G = 27.8 \text{ GPa}$$

$$\nu = .3-.2$$

Aluminum 1100

$$E = 69.0 \text{ GPa}$$

$$G = 26.0 \text{ GPa}$$

$$\nu = .33$$

Elevated Temperature, T = 600 K

LiH:

$$E = 2.1 \text{ GPa}$$

$$G = .81 \text{ GPa}$$

$$\nu = .3 - .2$$

Aluminum

$$E = 8.4 \text{ GPa}$$

$$G = 3.2 \text{ GPa}$$

$$\nu = .33$$

and an LiH-Al honeycomb matrix, since both types of honeycomb structure were candidates for neutron attenuation in the SP-100 shield. The application of the composite cylinders model to this type of matrix serves several purposes. The first is to gain an appreciation for the effect of the matrix on the stiffness of this portion of the shield. Because the function of the matrix is to direct any cracking in the LiH away from the shielded payload, a matrix material that will provide this directional stiffness is required. A second use of CCM results is to gain an understanding as to the directional dependence of the material properties. The accuracy of isotropic versus orthotropic treatment of the structure affects the constitutive equations, and ultimately, the numerical modelling of the system for eventual calculation of the stresses and strains. The final use of CCM is to generate the material properties of the homogenized LiH-honeycomb matrix cell in the determination of the axisymmetric thermal stresses, strains, and displacements.

The results of applying the composite cylinders model to both a LiH-Al and an LiH-SS honeycomb matrix are presented in the next section.

3.5.3.1 CCM Results for an LiH-Al Honeycomb Matrix. Using CCM and the properties of LiH and aluminum as identified in Table 3.5-1, the results listed in Tables 3.5-2 through 3.5-4 were generated. These results are useful in evaluating the validity of treating the LiH-Al honeycomb matrix as isotropic, with material properties calculated using a rule of mixtures approximation (ROM).

where:

$$\begin{aligned}
 A = & 3c(1 - c)^2(\mu_f/\mu_m - 1)(\mu_f/\mu_m + n_f) \\
 & + (\mu_f/\mu_m n_m + n_f n_m - (\mu_f/\mu_m n_m - n_f)c^3) \\
 & \times (n_m c(\mu_f/\mu_m - 1) - (\mu_f/\mu_m n_m + 1))
 \end{aligned} \tag{3.5-24}$$

$$\begin{aligned}
 B = & -6c(1 - c)^2(\mu_f/\mu_m - 1)(\mu_f/\mu_m + n_f) \\
 & + ((\mu_f/\mu_m)n_m + (\mu_f/\mu_m - 1)c + 1)((n_m - 1)(\mu_f/\mu_m + n_f) \\
 & - 2c^3(\mu_f/\mu_m)n_m - n_f) + (n_m + 1)c(\mu_f/\mu_m - 1)(\mu_f/\mu_m + n_f) \\
 & + ((\mu_f/\mu_m n_m - n_f)c^3)
 \end{aligned} \tag{3.5-25}$$

$$\begin{aligned}
 C = & 3c(1 - c)^2(\mu_f/\mu_m - 1)(\mu_f/\mu_m + n_f) \\
 & + (\mu_f/\mu_m n_m + (\mu_f/\mu_m - 1)c + 1)(\mu_f/\mu_m + n_f + (\mu_f/\mu_m n_m - n_f)c^3)
 \end{aligned} \tag{3.5-26}$$

where:

$$n_f = 3 - 4 v_f$$

$$n_m = 3 - 4 v_m$$

A simple check on the accuracy of these rather tedious expressions is to examine the asymptotic behavior of each homogenized engineering parameter as the volume ratio of the fiber approaches 1. Indeed, all values collapse to that of the fiber material (to include the transverse plane shear modulus). This result lends credence to Hashin's analysis that all expressions (with the exception of μ_{23}) are exact for small and large values of volume fraction, c .

3.5.3 Application of Composite Cylinders Model (CCM) to LiH in Honeycomb Matrix. The results of Equations 3.5-15 through 3.5-26 were used to determine the homogenized material properties of both an LiH-SS

$$E_{22} = \frac{4\mu_{23} K_{23}}{K_{23} + \mu_{23} + 4v_{12} \mu_{23} K_{23}/E_{11}} \quad (3.5-16)$$

$$v_{23} = \frac{K_{23} - \mu_{23} - 4v_{12} \mu_{23} K_{23}/E_{11}}{K_{23} + \mu_{23} + 4v_{12} \mu_{23} K_{23}/E_{11}} \quad (3.5-17)$$

$$v_{12} = (1 - c)v_m + cv_f + c(1 - c)(v_f - v_m) \cdot \frac{\left[\frac{\mu_m}{K_m + \frac{\mu_m}{3}} - \frac{\mu_m}{K_f + \frac{\mu_f}{3}} \right]}{\left[\frac{(1 - c)\mu_m}{K_f + \frac{\mu_f}{3}} + \frac{c\mu_m}{K_m + \frac{\mu_m}{3}} + 1 \right]} \quad (3.5-15)$$

$$K_{23} = K_m + \frac{\mu_m}{3} + \frac{c}{1/[K_f - K_m + \frac{1}{3}(\mu_f - \mu_m)] + (1 - c)/[K_m + \frac{4}{3}\mu_m]}$$

$$\mu_{12} = \mu_m \left[\frac{\mu_f(1 + c) + \mu_m(1 - c)}{\mu_f(1 - c) + \mu_m(1 + c)} \right] \quad (3.5-20)$$

and by symmetry:

$$\frac{v_{12}}{E_{11}} = \frac{v_{21}}{E_{22}} \quad (3.5-21)$$

from which:

$$v_{21} = v_{12} \frac{E_{22}}{E_{11}} \quad (3.5-22)$$

The only remaining unknown is the transverse plane shear modulus, μ_{23} . While an exact solution to μ_{23} has not been found, Christensen and Lo (1979) proposed the following solution for determining μ_{23} :

$$A \left(\frac{\mu_{23}}{\mu_m} \right)^2 + B \left(\frac{\mu_{23}}{\mu_m} \right) + C = 0 \quad (3.5-23)$$

However, the thermal conductivity of the stainless steel matrix will be ~4 times greater than the LiH filler, resulting in a significantly smaller temperature gradient in the matrix. Thus, the stresses induced by the temperature gradient at the outer radius of the unit cell will be an order of magnitude less than in the filler material and the boundary condition of Equation 3.5-13c is a valid approximation to the physical reality.

The compliance matrix for the cartesian coordinate system of Figure 3.5-2 takes the following form:

$$[S_{ij}] = \begin{bmatrix} 1/E_{11} & -v_{21}/E_{22} & -v_{21}/E_{22} & 0 & 0 & 0 \\ -v_{12}/E_{11} & 1/E_{22} & -v_{32}/E_{22} & 0 & 0 & 0 \\ -v_{12}/E_{11} & -v_{23}/E_{22} & 1/E_{22} & 0 & 0 & 0 \\ 0 & 0 & 0 & \frac{1}{2\mu_{23}} & 0 & 0 \\ 0 & 0 & 0 & 0 & \frac{1}{2\mu_{23}} & 0 \\ 0 & 0 & 0 & 0 & 0 & \frac{1}{2\mu_{12}} \end{bmatrix} \quad (3.5-14)$$

From continuum mechanics arguments, it can be shown that

$S_{ij} = S_{ji}$. This results in six unknowns in the compliance matrix to be determined; E_{11} , E_{22} , v_{12} , v_{23} , μ_{12} , and μ_{23} . Hashin showed the following expressions to be exact [Christensen, 1979]:

$$E_{11} = cE_f + (1 - c)E_m + \frac{\frac{4c(1 - c)}{} (v_f - v_m)^2 \mu_m}{\frac{(1 - c) \mu_m}{K_f + \mu_f/3} + \frac{c \mu_m}{K_m + \mu_m/3} + 1} \quad (3.5-15)$$

Table 3.5-5: CCM Results for an LiH-Al Matrix at 600 K
with an LiH Volume Fraction of 99% (All Moduli in GPa)

| | LiH | Al | Unit Cell |
|-----------------|------|------|-----------|
| E_{rr} | 2.1 | 8.4 | 2.16 |
| E_{zz} | 2.1 | 8.4 | 2.16 |
| $G_{r\sigma}$ | 0.81 | 3.2 | 0.83 |
| G_{zr} | 0.81 | 3.2 | 0.83 |
| ν_{rz} | 0.30 | 0.33 | 0.30 |
| ν_{zr} | 0.30 | 0.33 | 0.30 |
| $\nu_{r\sigma}$ | 0.30 | 0.33 | 0.30 |
| | | | |
| E_{rr} | 2.1 | 8.4 | 2.03 |
| E_{zz} | 2.1 | 8.4 | 2.17 |
| $G_{r\sigma}$ | 0.81 | 3.2 | 0.82 |
| G_{zr} | 0.81 | 3.2 | 0.83 |
| ν_{rz} | 0.20 | 0.33 | 0.19 |
| ν_{zr} | 0.20 | 0.33 | 0.20 |
| $\nu_{r\sigma}$ | 0.20 | 0.33 | 0.23 |

the matrix, the transverse plane stiffness modulus of the unit cell is less than both the fiber and matrix. The transverse plane of the unit cell corresponds to the axial direction of the core-shield system (in the direction of the payload). Hence, for a given temperature distribution and thermal strain, the lower transverse plane stiffness modulus results in lower stresses in this direction. This is precisely the desired effect of the honeycomb matrix; that is, to minimize cracking in the payload direction.

3.5.3.2 Composite Cylinder Model Results for an LiH-SS Honeycomb Matrix. Analogous to the analysis of the LiH-Al matrix, the CCM was used to evaluate the unit cell material properties of an LiH-SS matrix. The results are presented for a matrix at room temperature and at 600 K. The properties of LiH and SS used are identified in Table 3.5-6. Tables 3.5-7 through 3.5-9 provide sensitivity analyses in examining the validity of treating the LiH-SS matrix as an isotropic structure. This data is also presented in graphical form in Figures 3.5-6 through 3.5-8.

From Tables 3.5-7a and 3.5-7b, the treatment of the LiH-SS matrix as an isotropic material is quite reasonable (~1% error) at room temperature, provided the value of ν_{LiH} is very close to that of stainless steel. At room temperature, as the difference in Poisson ratios between the two materials increases, the error in the isotropic approximation increases to unacceptable levels for the unit cell Poisson's ratio.

At 600 K, the isotropic approximation is seen to be highly inaccurate for any volume fraction or Poisson's ratio of LiH. The material

TABLE 3.5-6: LiH and SS Properties Used in Composite Cylinders Model Analysis

Room Temperature, T = 293 K

LiH:

$$E = 72.4 \text{ GPa}$$

$$G = 27.8 \text{ GPa}$$

$$\nu = 0.30-0.20$$

Stainless Steel - 316

$$E = 190.0 \text{ GPa}$$

$$G = 73.0 \text{ GPa}$$

$$\nu = 0.305$$

Elevated Temperature, T = 600 K

LiH:

$$E = 2.1 \text{ GPa}$$

$$G = 0.81 \text{ GPa}$$

$$\nu = 0.30$$

Stainless Steel - 316

$$E = 175.0 \text{ GPa}$$

$$G = 67.3 \text{ GPa}$$

$$\nu = 0.305$$

TABLE 3.5-7a: Effect of Temperature on Isotropic Properties of an LiH-SS Matrix with $v_{LiH} = 0.3$

| Max % Difference from ROM | | | | | | |
|---------------------------|-----------------------|-----------------------|-----------------------|-----------------------|-----------------------|-----------------------|
| T = Room Temp | | | | T = 600 K | | |
| <u>c</u> | <u>E_{ii}</u> | <u>G_{ij}</u> | <u>v_{ij}</u> | <u>E_{ii}</u> | <u>G_{ij}</u> | <u>v_{ij}</u> |
| .995 | .4 | .3 | .7 | 23.4 | 25.9 | 32.8 |
| .99 | .7 | .6 | 1.1 | 45.2 | 51.1 | 69.2 |
| .98 | 1.3 | 1.3 | 1.8 | 84.5 | 99.3 | 146.3 |
| .97 | 1.9 | 1.9 | 2.6 | 119.9 | 145.0 | 225.5 |
| .96 | 2.4 | 2.5 | 3.3 | 152.2 | 188.4 | 305.0 |
| .95 | 3.0 | 3.1 | 4.0 | 182.2 | 229.8 | 383.2 |

TABLE 3.5-7b: Effect of Temperature on Isotropic Properties of an LiH-SS Matrix with $v_{LiH} = 0.2$

| Max % Difference from ROM | | | | | | |
|---------------------------|-----------------------|-----------------------|-----------------------|-----------------------|-----------------------|-----------------------|
| T=Room Temp | | | | T=600 K | | |
| <u>c</u> | <u>E_{ii}</u> | <u>G_{ij}</u> | <u>v_{ij}</u> | <u>E_{ii}</u> | <u>G_{ij}</u> | <u>v_{ij}</u> |
| 0.995 | 6.0 | 0.3 | 27.7 | 30.4 | 26.0 | 54.0 |
| 0.99 | 6.3 | 0.6 | 22.7 | 53.1 | 51.6 | 93.0 |
| 0.98 | 6.9 | 1.3 | 22.8 | 93.3 | 100.6 | 177.4 |
| 0.97 | 7.4 | 1.9 | 22.9 | 128.9 | 147.0 | 263.7 |
| 0.96 | 8.0 | 2.5 | 23.0 | 161.3 | 191.3 | 349.1 |
| 0.95 | 8.5 | 3.1 | 23.1 | 191.3 | 233.4 | 432.2 |

Table 3.5-8: Effect of Uncertainties in LiH Elastic Moduli at 600 K of an LiH-SS Matrix with $v_{LiH} = 0.3$
 $[E_{0LiH} = 2.1 \text{ GPa}]$

| c | Maximum % Difference From ROM | | |
|--------------------------|-------------------------------|----------------------------|----------------------------|
| | <u>E_{ij}</u> | <u>G_{ij}</u> | <u>v_{ij}</u> |
| $E_{LiH}/E_{0LiH} = 3.0$ | | | |
| 0.995 | 7.8 | 8.3 | 10.4 |
| 0.99 | 15.2 | 16.2 | 21.0 |
| 0.98 | 29.3 | 32.4 | 42.9 |
| 0.97 | 42.5 | 47.8 | 65.4 |
| 0.96 | 54.9 | 62.6 | 88.0 |
| 0.95 | 66.5 | 76.8 | 110.6 |
| $E_{LiH}/E_{0LiH} = 2.0$ | | | |
| 0.995 | 11.5 | 12.6 | 15.2 |
| 0.99 | 22.7 | 25.1 | 31.8 |
| 0.98 | 43.6 | 49.3 | 66.7 |
| 0.97 | 62.9 | 72.5 | 102.6 |
| 0.96 | 80.7 | 94.6 | 138.9 |
| 0.95 | 97.3 | 115.8 | 174.9 |
| $E_{LiH}/E_{0LiH} = 1.0$ | | | |
| 0.995 | 23.4 | 25.9 | 32.8 |
| 0.99 | 45.2 | 51.1 | 69.2 |
| 0.98 | 84.5 | 99.3 | 146.3 |
| 0.97 | 119.9 | 145.0 | 225.5 |
| 0.96 | 152.2 | 188.4 | 305.0 |
| 0.95 | 182.2 | 229.8 | 383.2 |

Table 3.5-9: Effect of Uncertainties in v_{L1H} at 600 K for an L1H-SS Matrix with $E_{L1H} = 2.1$ GPa.

| <u>c</u> | Maximum % Difference From ROM | | |
|-----------------|-------------------------------|-----------------------|-----------------------|
| | <u>E_{ij}</u> | <u>G_{ij}</u> | <u>v_{ij}</u> |
| $v_{L1H} = .2$ | | | |
| 0.995 | 30.4 | 26.0 | 54.0 |
| 0.99 | 53.1 | 51.6 | 93.0 |
| 0.98 | 93.3 | 100.6 | 177.4 |
| 0.97 | 128.9 | 147.0 | 263.7 |
| 0.96 | 161.3 | 191.3 | 349.1 |
| $v_{L1H} = .25$ | | | |
| 0.995 | 27.0 | 26.0 | 41.8 |
| 0.99 | 49.3 | 51.3 | 79.5 |
| 0.98 | 89.3 | 100.0 | 160.4 |
| 0.97 | 124.9 | 146.1 | 243.6 |
| 0.96 | 157.3 | 190.0 | 326.5 |
| 0.95 | 187.3 | 231.7 | 407.6 |
| $v_{L1H} = .3$ | | | |
| 0.995 | 23.4 | 25.9 | 32.8 |
| 0.99 | 45.2 | 51.1 | 69.2 |
| 0.98 | 84.5 | 99.3 | 146.3 |
| 0.97 | 119.9 | 145.0 | 225.5 |
| 0.96 | 152.2 | 188.4 | 305.0 |
| 0.95 | 182.2 | 229.8 | 383.2 |

Figure 3.5-6 Effect of Temperature on Isotropic Behavior of LiH-SS Shield with $v_{LiH} = 0.3$

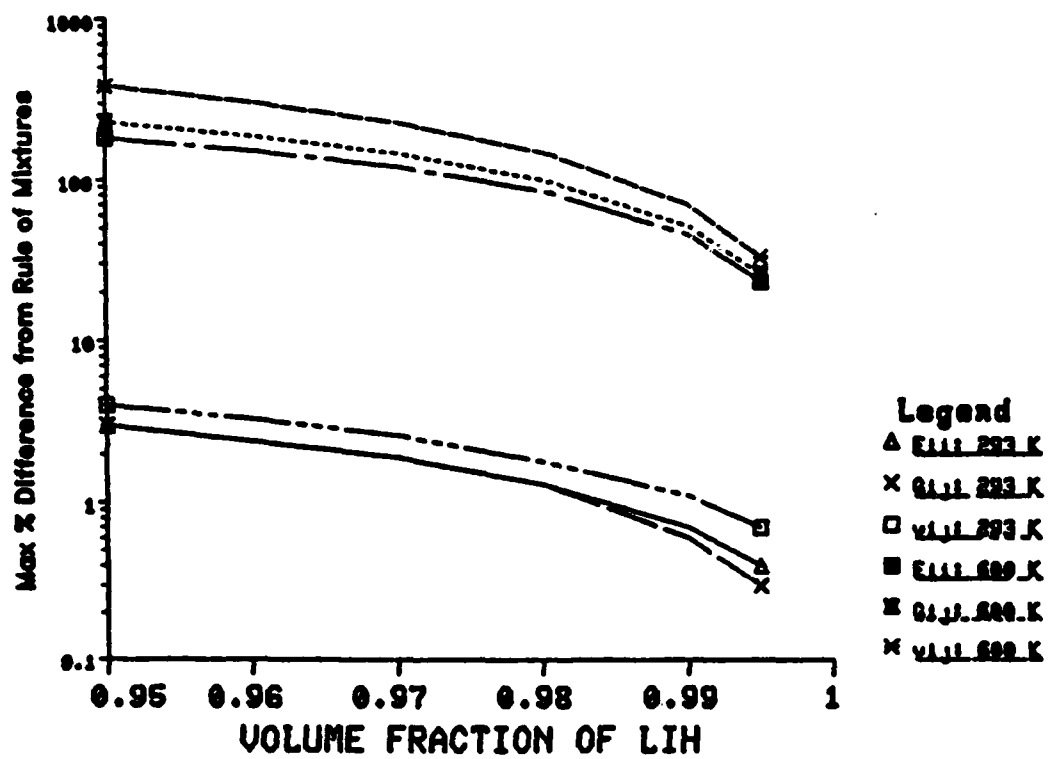


Figure 3.5-7 Effect of Temperature on Isotropic Behavior of LiH-SS Shield with $v_{LiH} = 0.2$

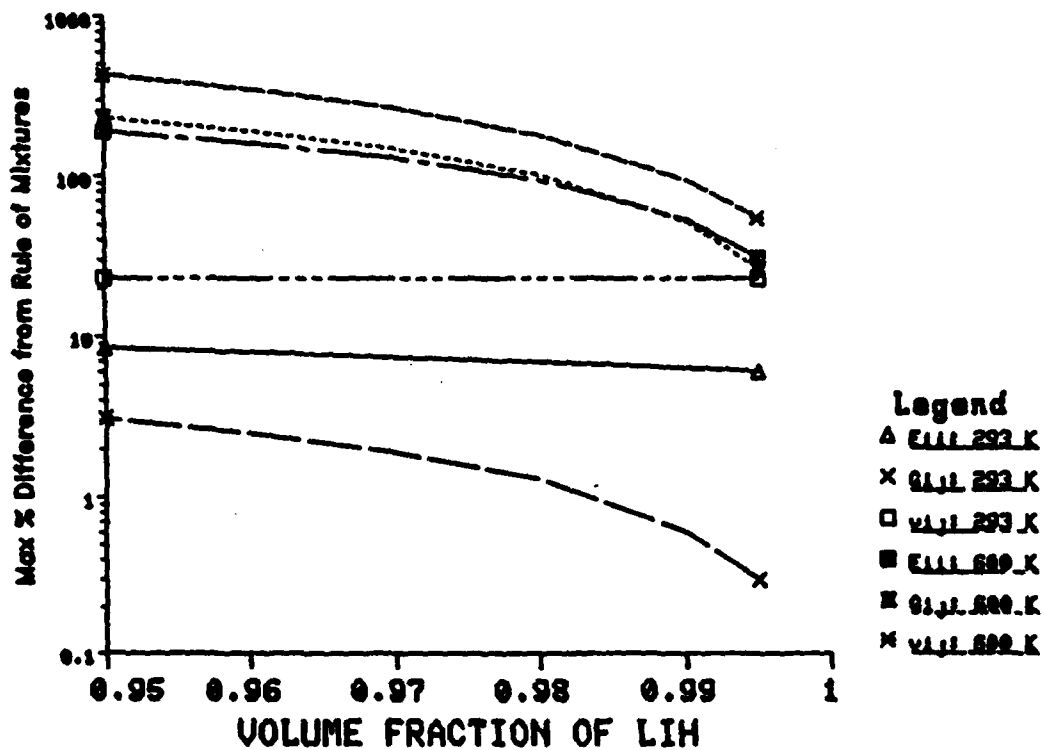
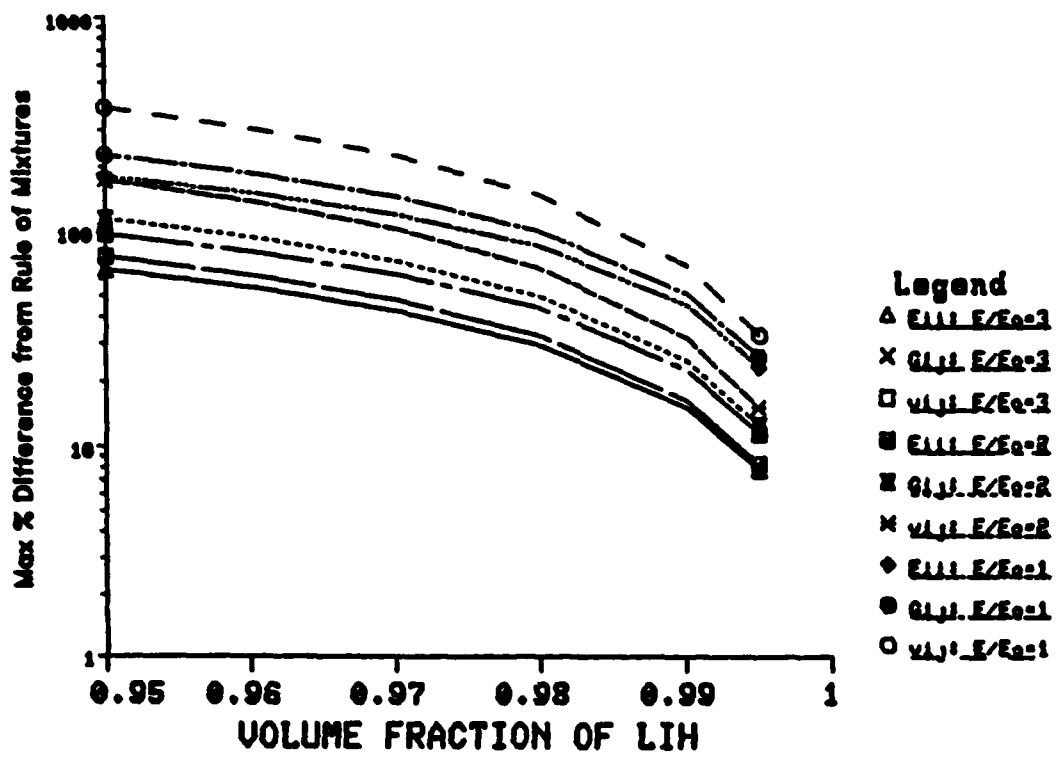


Figure 3.5-8 Effect of Uncertainties in E_{LiH} at 600 K of an LiH-SS Matrix



properties are highly directionally dependent and an orthotropic compliance matrix is required in the stress-strain analysis. The basis for this directional dependence is included in Table 3.5-10, which lists the CCM results for the LiH-SS matrix at 600 K for a 99% volume fraction of LiH.

The discussion of the LiH-Al matrix regarding the effect of a smaller modulus in the $r-\sigma$ plane than the axial plane is even more pertinent for the LiH-SS matrix. From the engineering standpoint that a low radial moduli is desirable to minimize neutron streaming to the payload, the lower LiH Poisson's ratio of Table 3.5-10 yields excellent results. This conclusion is obtained from the following data: for $v_{LiH} = 0.3$, the ratio of $E_{rr}/E_{zz} = .69$; and for $v_{LiH} = 0.2$, the ratio of $E_{rr}/E_{zz} = 0.65$. Table 3.5-10 data also shows that the 1% of stainless steel increases the effective unit cell stiffness by 19% in the $r-\sigma$ plane and 83% in the axial plane. (as defined by the coordinate system of Figure 3.5-2).

Thus, the use of CCM theory for the LiH-SS matrix has shown that the structure is highly anisotropic at elevated temperature and such material behavior must be included in the constitutive equations. The stiffness modulus of the unit cell will be significantly increased with only 1% of stainless steel, particularly in the cell axial directional (corresponding to the radial plane in the actual reactor shield geometry).

3.5.4 Constitutive Equations for an Orthotropic Material. As shown using CCM theory, the "homogenized" LiH-Al matrix may be considered isotropic for some conditions; whereas, the LiH-SS matrix must be treated orthotropically for all volume fractions and temperatures.

TABLE 3.5-10: CCM Results for an LiH-SS Matrix at 600 K with an LiH Volume Fraction of 99% (All Moduli in GPa)

| | LiH | SS | Unit Cell |
|---------------|------|-------|-----------|
| E_{rr} | 2.10 | 175.0 | 2.64 |
| E_{zz} | 2.10 | 175.0 | 3.83 |
| $G_{r\sigma}$ | 0.81 | 67.3 | 0.98 |
| G_{zr} | 0.81 | 67.3 | 1.15 |
| v_{rz} | 0.30 | 0.305 | 0.207 |
| v_{zr} | 0.30 | 0.305 | 0.301 |
| $v_{r\sigma}$ | 0.30 | 0.305 | 0.351 |
| | | | |
| E_{rr} | 2.10 | 175.0 | 2.50 |
| E_{zz} | 2.10 | 175.0 | 3.84 |
| $G_{r\sigma}$ | 2.10 | 67.3 | 0.97 |
| G_{zr} | 0.81 | 67.3 | 1.15 |
| v_{rz} | 0.20 | 0.305 | 0.15 |
| v_{zr} | 0.20 | 0.305 | 0.23 |
| $v_{r\sigma}$ | 0.20 | 0.305 | 0.29 |

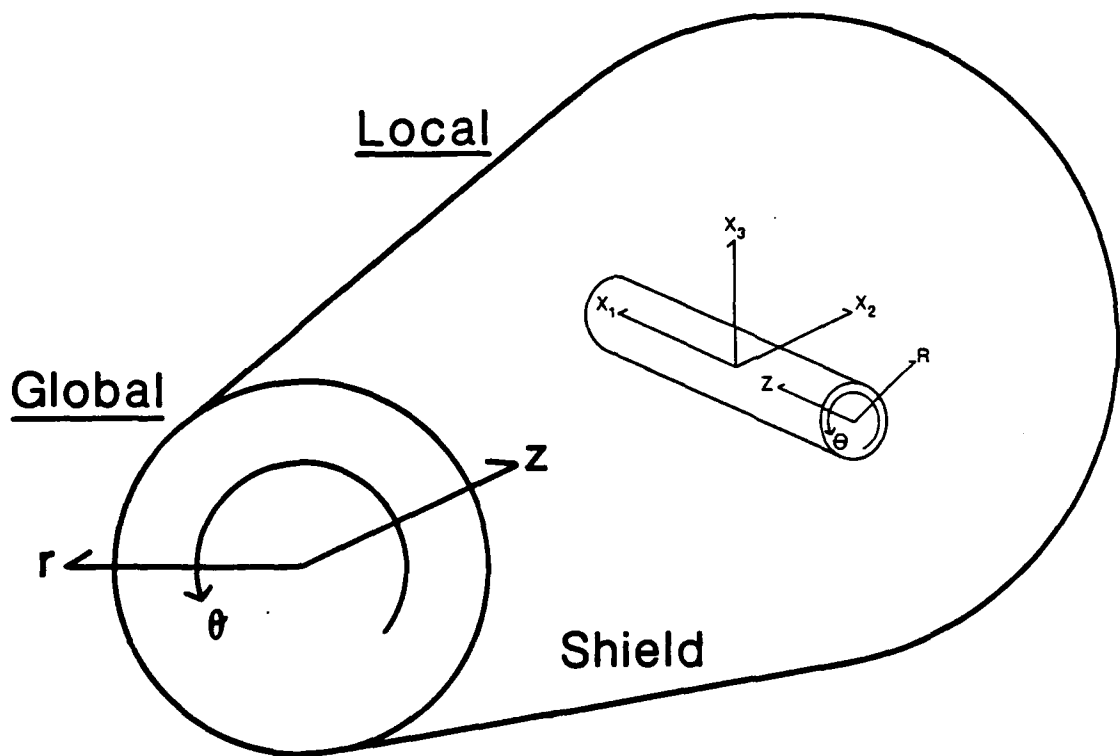
Therefore, any numerical codes developed in this research must be capable of handling the more general orthotropic case in an axisymmetric geometry.

Before presenting the constitutive equations for the axisymmetric material, it may be helpful to show how the cartesian coordinate system of composite cylinders model relates to the cylindrical coordinate system represented in the constitutive equations. The relationship for a single LiH-Honeycomb matrix unit cell is shown in Figure 3.5-9. The actual material properties mapping from the local cartesian to the global cylindrical systems are included in Table 3.5-11. When two properties were combined in transforming from local cylindrical to global cylindrical, the mean value was used. (This actually turned out to be a minor assumption, as the two values to be combined differed only in the 3rd significant number. This was true for both the Poisson's ratios and the shear moduli of Table 3.5-11.)

TABLE 3.5-11: Mapping of Material Properties from Local Cartesian to Global Cylindrical Coordinates

| <u>Local Cartesian</u> | <u>Local Cylindrical</u> | <u>Global Cylindrical</u> |
|----------------------------|------------------------------|-------------------------------|
| E_{11} | E_{ZZ} | E_{rr} |
| E_{22} | E_{RR} | E_{zz} |
| ν_{21} | ν_{RZ} | ν_{zr} |
| ν_{12} | ν_{ZR} | ν_{rz} |
| ν_{23} | $\nu_{R\theta}$ | |
| G_{23} | $G_{R\theta}$ | |
| G_{12} | G_{ZR} | G_{zr} |

Figure 3.5-9: Relationship of Composite Cylinders Axes (Local) to Axisymmetric Axes of the Reactor System (Global)



| <u>Local Cartesian</u> | <u>Local Cylindrical</u> | <u>Global Cylindrical</u> |
|----------------------------|------------------------------|-------------------------------|
|----------------------------|------------------------------|-------------------------------|

$$\begin{array}{ccc}
 x_3 & \longrightarrow & r \\
 x_2 & \nearrow & \sigma \\
 x_1 & \longrightarrow & z \\
 & & \longrightarrow R
 \end{array}$$

The constitutive equations for an axisymmetric material take the following matrix form:

$$\underline{\epsilon} = \underline{\underline{C}} \underline{\sigma}$$

or,

$$\begin{Bmatrix} \epsilon_{rr} \\ \epsilon_{\sigma\sigma} \\ \epsilon_{zz} \\ \epsilon_{rz} \end{Bmatrix} = \begin{bmatrix} 1/E_{rr} & -v_{\sigma r}/E_{\sigma\sigma} & -v_{zr}/E_{zz} & 0 \\ -v_{r\sigma}/E_{rr} & 1/E_{\sigma\sigma} & -v_{z\sigma}/E_{zz} & 0 \\ -v_{rz}/E_{rr} & -v_{\sigma z}/E_{\sigma\sigma} & 1/E_{zz} & 0 \\ 0 & 0 & 0 & 1/G_{rz} \end{bmatrix} \begin{Bmatrix} \sigma_{rr} \\ \sigma_{\sigma\sigma} \\ \sigma_{zz} \\ \tau_{rz} \end{Bmatrix} \quad (3.5-28)$$

Because the strain energy must be positive definite (which implies that a potential function exists), the compliances and stiffnesses must be symmetric. The requirement, along with the assumption of a transversely isotropic media, lead to the following relations:

$$v_{zr} = v_{z\sigma}$$

$$v_{rz} = v_{\sigma z}$$

$$v_{r\sigma} = v_{\sigma r}$$

$$E_{rr} = E_{\sigma\sigma}$$

$$\frac{v_{zr}}{E_{zz}} = \frac{v_{rz}}{E_{rr}} = \frac{v_{\sigma z}}{E_{rr}}$$

Figure 3.5-14 Comparison of Finite Element and Exact Solutions for Stresses Due to a Radial Temperature Distribution

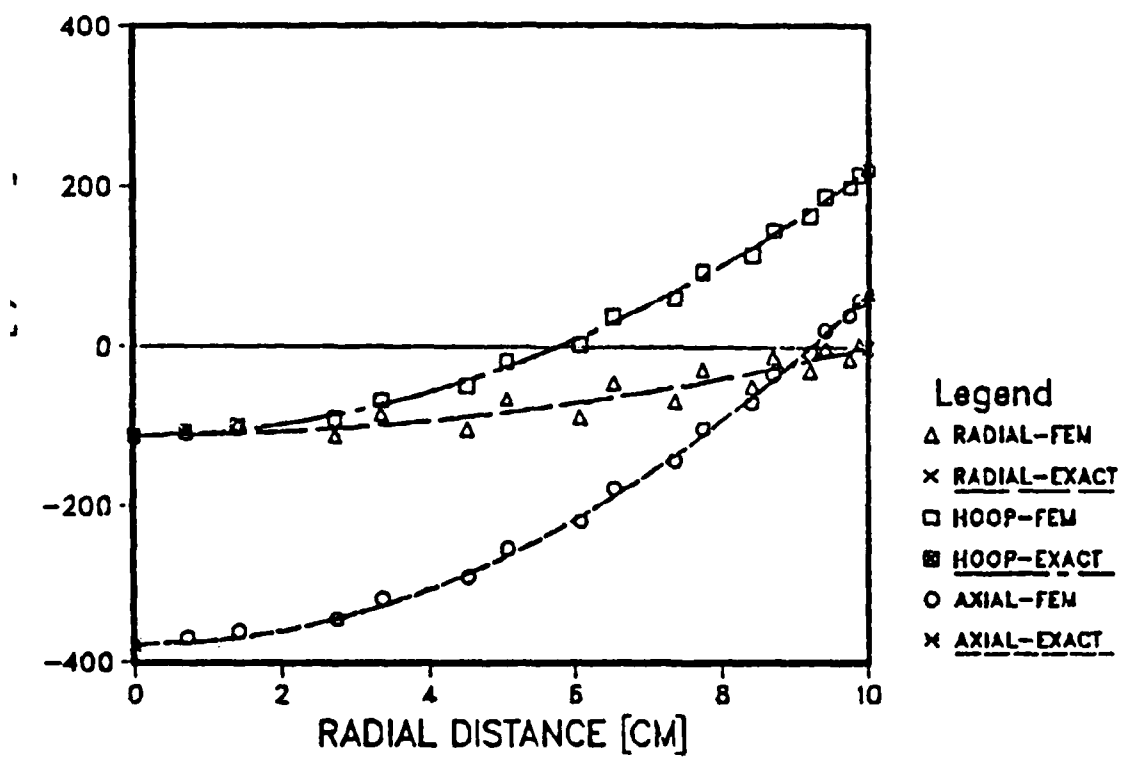
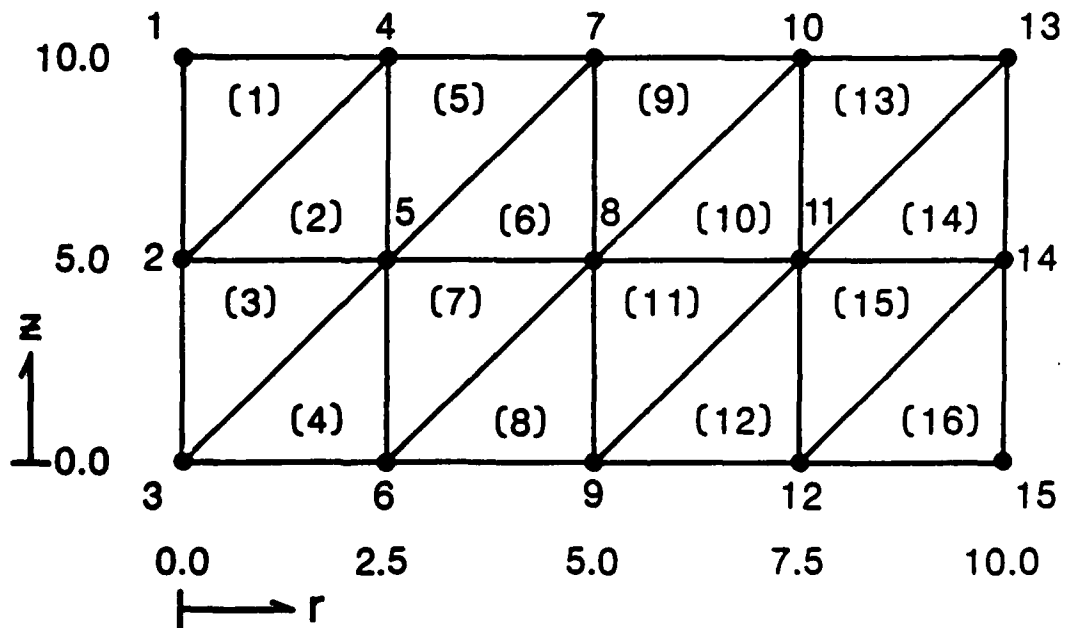


Table 3.5-12: Test Case Input Data

| | |
|--------------------------|--|
| Elastic Modulus | 4.1368×10^5 N/cm ² |
| Coefficient of Expansion | 3.0×10^{-6} cm/cm-K |
| Poisson's Ratio | 0.3 |
| Radius of Cylinder | 10.0 cm |
| Internal Heat Generation | 0.5 W/cm ³ |
| Thermal Conductivity | 0.05 W/cm-K |

Figure 3.5-13 Numerical Mesh Used to Calculate FEM Stresses for Test Case



The temperature solution from Equation 3.5-45 is:

$$T(r) = T_0 + \frac{q''' a^2}{4k} \left(1 - \frac{r^2}{a^2} \right) \quad (3.5-46)$$

Substituting Equation 3.5-46 into Equations 3.5-41 and 3.5-42, which are then substituted into Equations 3.5-38, 3.5-39, and 3.5-40, results in the following solutions for thermal stresses:

$$\sigma_{rr} = \frac{Ea}{(1-\nu)} \frac{q''' a^2}{16k} \left(\frac{r^2}{a^2} - 1 \right) \quad (3.5-48)$$

$$\sigma_{\theta\theta} = \frac{Ea}{(1-\nu)} \frac{q''' a^2}{16k} \left(\frac{3r^2}{a^2} - 1 \right) \quad (3.5-48)$$

$$\sigma_{zz} = \frac{Ea q''' a^2}{(1-\nu) 8k} \left(2 - \frac{r^2}{a^2} - (2-\nu) \right) \quad (3.5-49)$$

The numerical mesh of Figure 3.5-13 was used in SHLDSTR to compare the exact solution with the approximate solution. The simple mesh consisted of 15 nodes and 16 elements. The mesh was not optimized for minimum bandwidth or star clustering of elements to reduce the stiffness associated with triangular elements.

The input data of Table 3.5-12 was used for the comparison. The results of the FEM and exact solutions are included in Figure 3.5-14. The numerical results plotted are the stresses for the elements of figure 3.5-13 which straddle the geometric centerline ($z = 5.0$ cm). This accounts for the alternating high-low numerical values when compared with the exact solution curve. The excellent agreement between the numerical and exact solutions for this simple mesh, shows why FEM codes have gained such widespread use in numerical computations.

surface and completely restrained for axial movement. All material properties are constant and the cylinder is isotropic.

Starting with the constitutive equations for a 3-D, axisymmetric body, the following relationships can be derived for stresses in the solid cylinder:

$$\sigma_{rr} = \frac{E\alpha'}{2} (\bar{T} - \bar{T}_f) \quad (3.5-38)$$

$$\sigma_{\theta\theta} = E\alpha' (T(r)) \frac{E\alpha'}{2} (\bar{T} - \bar{T}_f) \quad (3.5-39)$$

$$\sigma_{zz} = \frac{E\alpha}{1-\nu} (\nu \bar{T} - T(r)) \quad (3.5-40)$$

where:

$$\bar{T} = \frac{2}{\pi^2} \int_0^a T(r) r dr \quad (3.5-41)$$

$$\bar{T}_f = \frac{2}{\pi^2} \int_0^r T(r) r dr \quad (3.5-42)$$

$$E' = \frac{E}{1-\nu^2} \quad (3.5-43)$$

$$\alpha' = (1+\nu) \alpha \quad (3.5-44)$$

The governing equation and boundary conditions for the temperature distribution is:

$$\frac{1}{r} \frac{d}{dr} (rk \frac{dT}{dr}) + q''' = 0 \quad (3.5-45)$$

Subject to:

a. $T = T_f$ at $r = 0$

b. $T = T_0$ at $r = a$

Figure 3.5-12a Thermal Conditions for Stress Test Case (Plain Strain)

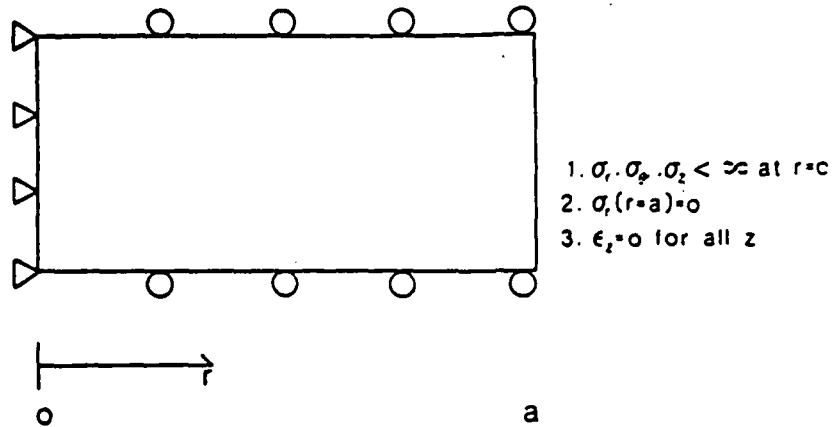
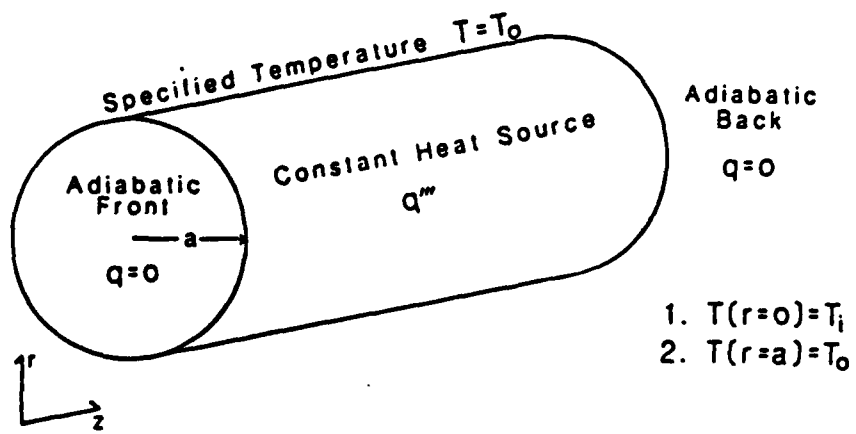


Figure 3.5-12b Displacement Conditions for Stress Test Case (Plain Strain)



Two types of convergence checks are employed in SHLDSTR. The inner loop convergence criteria is a check on the incremental displacements calculated with the N-R iteration and takes the form:

$$\frac{\|(\Delta \tilde{U}, \Delta \tilde{U})\|_2}{\|(\tilde{U}, \tilde{U})\|_2} < \epsilon_1 \quad (3.5-36)$$

According to many respected researchers, convergence based on displacement criteria is preferable to an energy convergence criteria for the N-R iteration (Bergan and Clough, 1972). Although in this research, it was generally observed that for a well-behaved solution, displacement and energy convergence accompanied each other.

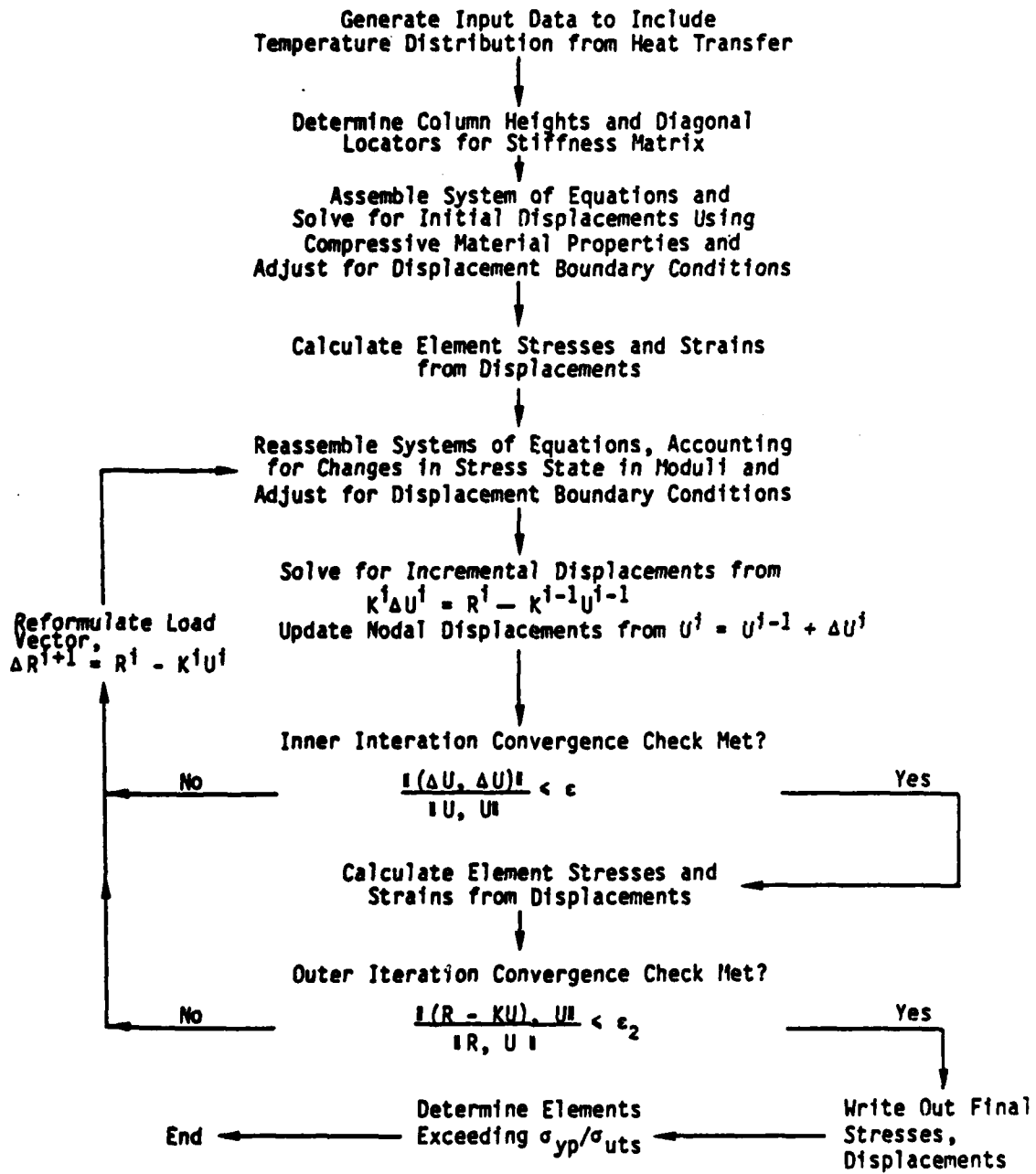
The outer loop convergence criteria was based on an energy balance, and takes the form:

$$\frac{\|(\tilde{R} - \tilde{K} \tilde{U}), \tilde{U}\|_2}{\|(\tilde{R}, \tilde{U})\|_2} \quad (3.5-37)$$

The energy convergence criteria is a scalar measure of the work done by residual forces to work done by applied forces (Cook, 1981). While convergence according to this equilibrium check does not insure accuracy of the solution (Noble, 1969), the combination of convergence over displacement and energy balance provides a stronger basis for confidence in the results (Bathe, 1982).

3.5.6 Validation of Stress Code. The accuracy of the stress code, SHLDSTR, was analyzed by comparison of the numerical stresses with an exact solution. The problem setup of Figures 3.5-12a and b were used as the test case, consisting of a solid cylinder with insulated ends, a constant internal heat source, and heat flow in the radial direction. The cylinder is free to expand at its outer radial

Figure 3.5-11: Flowchart of Solution Method Used in Stress Code, SHLDSTR



3.5.5 Stress Analysis Code, SHLDSTR. The temperature code, SHLUTEMP, was adapted to calculate the 3-D, axisymmetric stresses, strains, and displacements for the bilinear, orthotropic shield. The resulting stress code, SHLDSTR, uses the same 3 node triangular elements, Newton-Raphson iteration, and a choice of an LDL^T Direct Solver or the Pre-conditioned Point Jacobi Method with Conjugent Gradient Acceleration to solve the system of equations for nodal displacements.

Figure 3.5-11 is a flowchart describing the solution method currently coded in SHLDSTR. The stress code differs from the temperature code in several aspects. For stability reasons described in Section 6.3, the solution method in SHLDSTR allows for the option of either a full or modified Newton-Raphson iteration. The user can specify the maximum number of inner iterations allowed before the stiffness matrix is updated to account for any elements changing their stress state (compressive to tensile, or visa versa).

With two degree of freedom per node, the matrix for the system of equations is twice the size for the stress problem than the temperature problem (for the same mesh). Due to the size of the problem, the matrix was too large to be assembled in-core on the VAX 11/780. For this reason, the matrix entries are located directly into a vector, with the diagonal element locators in a separate vector. This assemblage procedure resulted in approximately two orders of magnitude savings in required storage ($\sim 10^4$ vs $\sim 10^6$) for a 1500 degree of freedom problem. With the more efficient assemblage, an in-core assemblage and solution was possible.

3.5.4.3 Constitutive Equations Used in This Research. For this first cut at the thermal stresses in the LiH-honeycomb matrix, the approaches used by Jones and Idelsohn, et al. were combined in formulation of the material matrix. Jones' weighting functions for off-diagonal elements based on principal material axis stresses were used directly in the formulation of the material matrix for an axisymmetric LiH-honeycomb matrix (homogenized using composite cylinders model theory). Using the following axes reference frame:

Subscript 1 = R axis

2 = σ axis

3 = Z axis

the material matrix elements assume the following form:

$$c_{ij}^t \quad \text{if } \sigma_{11} > 0, \sigma_{22} > 0, \sigma_{33} > 0$$

$$c_{ij} = \begin{cases} c_{ij}^t & \text{if } \sigma_{11} < 0, \sigma_{22} < 0, \sigma_{33} < 0 \\ c_{ij}^c & \text{if } \sigma_{11} > 0 \end{cases}$$

$$c_{ii} = \begin{cases} c_{ii}^t & \text{if } \sigma_{ii} > 0 \\ c_{ii}^c & \text{if } \sigma_{ii} < 0 \end{cases}$$

$$c_{ji} = c_{ij} = \begin{cases} k_{ji} c_{ji}^t + l_{ji} c_{ji}^c & \text{if } \sigma_{ii} > 0, \sigma_{jj} < 0 \\ k_{ji} c_{ji}^c + l_{ji} c_{ji}^t & \text{if } \sigma_{ii} < 0, \sigma_{jj} > 0 \end{cases}$$

where:

$$\begin{aligned} k_{ji} &= \frac{|\sigma_{ii}|}{|\sigma_{ii}| + |\sigma_{jj}|} \\ l_{ji} &= \frac{|\sigma_{jj}|}{|\sigma_{ii}| + |\sigma_{jj}|} \end{aligned} \tag{3.5-35}$$

3.5.4.2 Idelsohn, et al. Constitutive Equations for Bilinear Material.

Material. Idelsohn, et al., (1982) recently proposed another criterion for maintaining symmetry in the bilinear material matrix, while working in principal stress axes. They identified different weighting factors which operate on the off-diagonal elements of the material matrix directly, instead of the compliance matrix as Jones presented. The material matrix now takes the form:

$$C_{ij}^t \text{ if } \sigma_{11} > 0, \sigma_{22} > 0, \sigma_{33} > 0 \\ C_{ij} = \begin{cases} C_{ii}^c & \text{if } \sigma_{11} < 0, \sigma_{22} < 0, \sigma_{33} < 0 \\ C_{jj}^t & \text{if } \sigma_{ii} > 0 \end{cases} \quad (3.5-34)$$

$$C_{ii} = \begin{cases} C_{jj}^c & \text{if } \sigma_{ii} < 0 \\ \alpha_{ji} C_{ji}^t + \beta_{ji} C_{ji}^c & \text{if } \sigma_{ii} > 0, \sigma_{jj} < 0 \\ C_{ji} = C_{ij} = \begin{cases} \alpha_{ji} C_{ji}^c + \beta_{ji} C_{ji}^t & \text{if } \sigma_{ii} < 0, \sigma_{jj} > 0 \end{cases} \end{cases}$$

where α_{ji} and β_{ji} assume values based on the particular material type and geometry. The subscripts i and j refer to a material axis and do not imply a summation.

Furthermore, they assume that the shear moduli in orthotropic directions are the same for tension and compression. Unfortunately, unless experimental data is available to determine the values of α_{ji} and β_{ji} , any values used will be completely arbitrary. Therefore, Jones approach of weighting coefficients for off-diagonal elements based on the calculated stresses in principal material axis directions appears more valid for an unknown material.

The compliances of Equation 3.5-32 were assigned the following weights:

$$\text{if } \sigma_p > 0 \text{ and } \sigma_q > 0: S_{ij}^{pq} = S_{ijt}^{pq} \quad (3.5-33)$$

$$\text{if } \sigma_p < 0 \text{ and } \sigma_q < 0: S_{ij}^{pq} = S_{ijc}^{pq}$$

$$\begin{aligned} \text{if } \sigma_p > 0 \text{ and } \sigma_q < 0: \quad S_{11}^{pq} &= S_{11t}^{pq} \\ S_{12}^{pq} &= k_p S_{12t}^{pq} + k_q S_{12c}^{pq} \\ S_{22}^{pq} &= S_{22c}^{pq} \\ S_{61}^{pq} &= S_{61t}^{pq} \\ S_{62}^{pq} &= S_{62c}^{pq} \end{aligned}$$

$$\begin{aligned} \text{if } \sigma_p < 0 \text{ and } \sigma_q > 0: \quad S_{11}^{pq} &= S_{11c}^{pq} \\ S_{12}^{pq} &= k_p S_{12c}^{pq} + k_q S_{12t}^{pq} \\ S_{22}^{pq} &= S_{22t}^{pq} \\ S_{61}^{pq} &= S_{61c}^{pq} \\ S_{62}^{pq} &= S_{62t}^{pq} \end{aligned}$$

where:

$$k_p = \frac{|\sigma_p|}{|\sigma_p| + |\sigma_q|}$$

$$k_q = \frac{|\sigma_q|}{|\sigma_p| + |\sigma_q|}$$

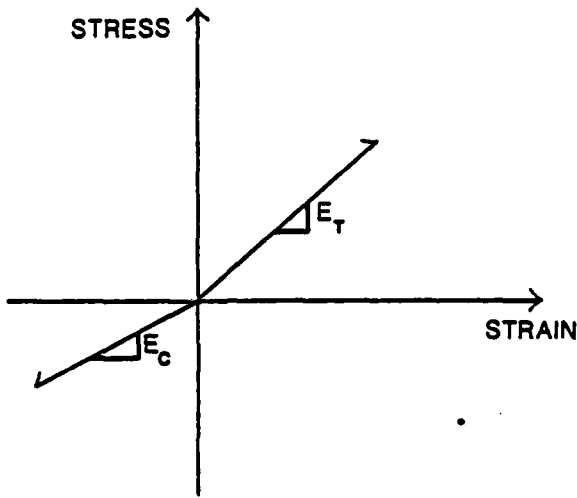


FIGURE 3.5-10: Bilinear LiH at 600 K

matrix for plane stress, working in principal material axes.

Idelsohn et al. (1982) presented a different criterion for generating the off-diagonal elements of the material matrix, working in principal stress components. In this research, Jones and Idelsohn's treatment of the constitutive equations were extended to an axisymmetric, orthotropic structure to model the LiH-honeycomb matrix portion of shield.

3.5.4.1 Jones Constitutive Equations for Bilinear Material. As with the thermal conductivities, the assumption was made that the global axes of the shield ($r-z$ axes) coincide with the principal axes, as well. Jones proposed the following stress-strain relations for bilinear, orthotropic materials in principal material coordinates under plane stress:

$$\begin{aligned}\epsilon_p &= S_{11}^{pq} \sigma_p + S_{12}^{pq} \sigma_q \\ \epsilon_q &= S_{12}^{pq} \sigma_p + S_{22}^{pq} \sigma_q \\ \gamma_{pq} &= S_{61}^{pq} \sigma_p + S_{62}^{pq} \sigma_q\end{aligned}\tag{3.5-32}$$

Where,

$$D = \frac{E_{zz}}{(1+v_{rz})(1-v_{rz}-2nv_{zr}^2)} \begin{bmatrix} n(1-nv_{zr}^2) & n(v_{rz}+nv_{zr}^2) & nv_{zr}(1+v_{rz}) & 0 \\ n(v_{rz}+nv_{zr}^2) & n(1-nv_{zr}^2) & nv_{zr}(1+v_{rz}) & 0 \\ nv_{zr}(1+v_{rz}) & nv_{zr}(1+v_{rz}) & (1-v_{rz}^2) & 0 \\ 0 & 0 & 0 & \frac{m(1+v_{rz})}{(1-v_{rz}-2nv_{zr}^2)} \end{bmatrix} \quad (3.5-31)$$

At this point, another difficulty in the constitutive equations must be addressed: specifically, the bi-modularity of elastic moduli for LiH. The difference between the tensile and compressive moduli was shown with Equation 3.5-27. At elevated temperature, there will be some dissociation of Li and H. Because the melting point of Li is only 450 K and the shield will operate well above this temperature, there will be some liquid lithium throughout the LiH which causes different stiffness for tension and compression. Because of this difference in moduli, the symmetry of Equations 3.5-29 and 3.5-31 will not be preserved. Thus, the approximations of bilinear elasticity theory must be used. Figure 3.5-10 is a stress-strain curve for the bilinear LiH with different tension and compression moduli at 600 K.

Ambartsumyan was the first credited with addressing the constitutive equation dilemma of bilinear theory for isotropic materials [Idelsohn, et al., 1982]. However, his results did not preserve symmetry in the material matrix. Jones (1977) further developed the theory preserving symmetry for both an isotropic and orthotropic material

However, $v_{zr} \neq v_{rz}$

Equations 3.5-28 may now be rewritten:

$$\begin{Bmatrix} \epsilon_{rr} \\ \epsilon_{\sigma\sigma} \\ \epsilon_{zz} \\ \gamma_{rz} \end{Bmatrix} = \begin{bmatrix} 1/E_{rr} & -v_{\sigma r}/E_{rr} & -v_{zr}/E_{zz} & 0 \\ -v_{\sigma r}/E_{rr} & 1/E_{\sigma\sigma} & -v_{zr}/E_{zz} & 0 \\ -v_{zr}/E_{zz} & -v_{zr}/E_{zz} & 1/E_{zz} & 0 \\ 0 & 0 & 0 & 1/G_{rz} \end{bmatrix} \begin{Bmatrix} \sigma_{rr} \\ \sigma_{\sigma\sigma} \\ \sigma_{zz} \\ \tau_{rz} \end{Bmatrix} \quad (3.5-29)$$

Defining,

$$n = E_{rr}/E_{zz} \text{ and } m = G_{rz}/E_{zz}$$

Equation 3.5-29 can be inverted to determine the stresses as a function of the strains. This results in,

$$\underline{\underline{\sigma}} = \underline{\underline{C}}^{-1} \underline{\underline{\epsilon}}$$

or,

$$\begin{Bmatrix} \sigma_{rr} \\ \sigma_{\sigma\sigma} \\ \sigma_{zz} \\ \tau_{rz} \end{Bmatrix} = \begin{bmatrix} & & & \\ & & & \\ & D & & \\ & & & \end{bmatrix} \begin{Bmatrix} \epsilon_{rr} \\ \epsilon_{\sigma\sigma} \\ \epsilon_{zz} \\ \gamma_{rz} \end{Bmatrix} \quad (3.5-30)$$

4.0 EFFECT OF TEMPERATURE ON ENERGY DEPOSITION IN THE SHIELD

The theory of the previous section was utilized in the analyses of radiation shields for the SP-100 space reactor. The results of this research are broken into two major focus areas:

- a. The effects of temperature feedback on energy deposition due to changes in nuclear properties.
- b. The effects of shield configuration on temperature distribution due to the coupling of radiation transport with thermal transport.

The second focus area, shield configuration effects on temperature, is the ultimate goal for a thermal analysis of the radiation shield. The significant findings of this focus area will be presented in Section 5.0. However, before accepting temperature distributions as final, the first major focus area must be analyzed in detail. Should temperature have a significant effect on energy deposition in the shield, then the difficult task of including temperature feedback effects must be included in the analysis each time the shield configuration or boundary conditions of the shield are slightly modified. On the other hand, should the energy deposition-temperature feedback coupling prove to be weak, then the computational requirements of the thermal analysis of the shield are greatly simplified. The effects of temperature on energy deposition in an SP-100 reactor shield will now be discussed.

4.1 SP-100 Reactor Design Concept. Before presenting these results, the reactor concept for which the shield was designed, shall be discussed.

The SP-100 reactor design concept considered in this analysis was a fast reactor fueled with 93% enriched UO_2 and coupled to thermoelectrics for converting thermal energy to electric energy [General Electric Company, 1983]. Control of the reactor core was provided by $\text{B}_4\text{C}/\text{BeO}$ drums external to the reactor and contained in the radial reflector.³ An inner annulus, filled with BeO during operation, was included in the design. Heat removal from the core was accomplished via liquid lithium pumped through the core to a heat exchanger external to the core-shield system. As discussed previously, the radiation transport portion of this analysis was performed in two parts. First the core was modelled with a fine grid to solve for the fundamental mode eigenvalue. The neutron and gamma fluxes were read onto tape and used as input for the determination of fluxes throughout the shield.

The basic reactor and shield model used in the present analysis is included in Figure 4.1-1. The volume fractions for each region of the system during steady-state operation are included in Table 4.1-1. Number densities were calculated with these volume fractions and physical densities at elevated temperatures.

All results generated during this research were based on either 59 group or 38 group BUGLE cross section libraries in AMPX format [ORNL, 1976]. The 59 group set, consisting of 41 neutron groups and 18 gamma groups, was used in the 1-D fluence calculations. The 38 group library, consisting of 24 neutron groups and 14 gamma groups, was used for all 3-D, axisymmetric analyses for energy deposition in the shield. All cross sections are based on ENDF/V data. Tables 4.1-2 and 4.1-3 list the range for both sets of cross sections.

³ More recent reactor designs include control rods in the core.

Figure 4.1-1 Core and Shield Design Modelled in UNM Analysis

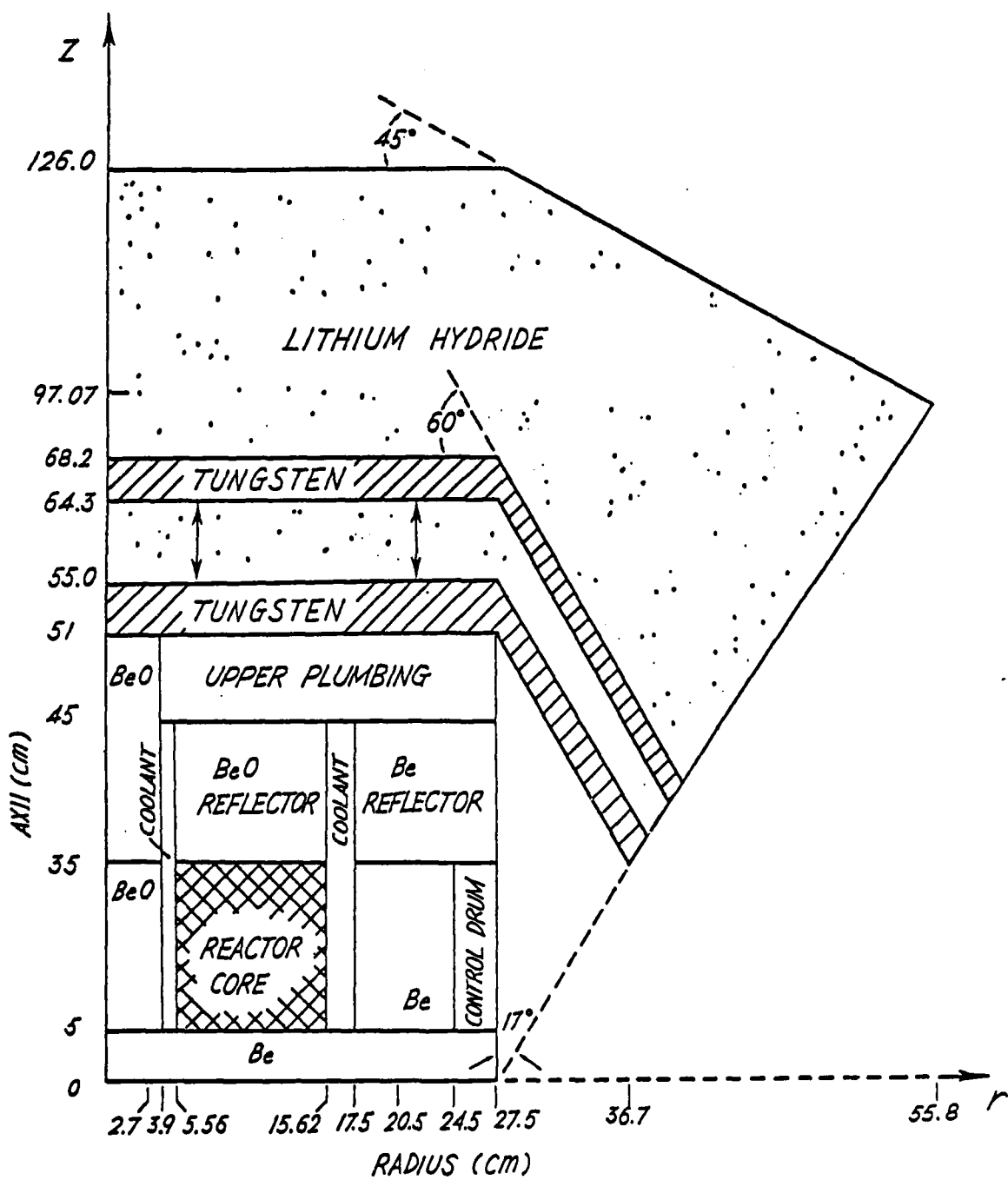


Table 4.1-1: Volume Fractions Used in Neutronic Analysis

| Mixture | UO ₂ | Li | Nb-Zr-C | Mo | Be0 | B ₄ C | Be | H ₂ O | W | LiH | SS |
|---------------------------------------|-----------------|-------|---------|-------|-------|------------------|-------|------------------|-----|------|-----|
| Core (c) | .6259 | .2040 | .1701 | --- | --- | --- | --- | --- | --- | --- | --- |
| Axial Reflector (AR) | --- | .2040 | .1701 | --- | .6259 | --- | --- | --- | --- | --- | --- |
| Inner Reflector (IR) | --- | --- | .1000 | --- | .9000 | --- | --- | --- | --- | --- | --- |
| Inner Structure/ Coolant (ISC) | --- | .6089 | .2364 | .1044 | --- | --- | --- | --- | --- | --- | --- |
| Outer Structure/ Coolant (OSC) | --- | .6182 | .2700 | .1118 | --- | --- | --- | --- | --- | --- | --- |
| Control Drum (CD) | --- | --- | --- | .0462 | --- | --- | .1846 | .7792 | --- | --- | --- |
| Upper Radial Corner Reflector (CR) | --- | --- | .1000 | --- | --- | --- | .9000 | --- | --- | --- | --- |
| Upper Plumbing (UP) | --- | .4000 | .6000 | --- | --- | --- | --- | --- | --- | --- | --- |
| Tungsten Shield (W) | --- | --- | --- | --- | --- | --- | --- | --- | 1.0 | --- | --- |
| LiH Shield (LiH) | --- | --- | --- | --- | --- | --- | --- | --- | --- | .995 | .05 |

Table 4.1-2a: Neutron Energy Group Data for 38 Group Library

| GRP | E _{MIN} | E _{MAX} | AVE E | DEL E | U MAX | U MIN | U AVE | DEL U | ECU AVE | GRP VEL | CHI | |
|-----|------------------|------------------|------------|------------|-------------|------------|-------------|------------|------------|------------|------------|------------|
| 1 | 1.7310E+07 | 1.8000E+07 | 1.3665E+07 | 7.3390E+06 | -3.4935E+01 | 0.0000E+00 | -2.7493E+01 | 5.4905E+01 | 1.3164E+01 | 5.0404E+01 | 0.9012E+01 | |
| 2 | 1.8000E+07 | 7.4000E+06 | 8.7040E+06 | 2.5192E+06 | 0.0000E+00 | 3.0002E+01 | 1.5001E+01 | 3.0002E+01 | 8.4070E+00 | 4.0002E+00 | 0.0022E+00 | |
| 3 | 7.4000E+06 | 4.9500E+06 | 4.1855E+06 | 2.4430E+06 | 3.0001E+01 | 1.0017E+01 | 5.0010E+01 | 4.0015E+01 | 6.4004E+00 | 3.2026E+00 | 0.0437E+00 | |
| 4 | 4.9500E+06 | 3.0110E+06 | 3.0110E+06 | 1.9540E+06 | 7.0011E+01 | 2.0003E+00 | 1.0000E+00 | 5.0002E+00 | 5.0014E+01 | 3.0004E+00 | 2.3660E+00 | |
| 5 | 3.0110E+06 | 1.6310E+06 | 2.3120E+06 | 1.3580E+06 | 1.2003E+00 | 1.0000E+00 | 2.0004E+00 | 2.0004E+00 | 5.0002E+00 | 5.0002E+00 | 2.0703E+00 | |
| 6 | 1.6310E+06 | 1.0000E+06 | 1.3225E+06 | 6.5100E+05 | 1.0000E+00 | 2.0004E+00 | 2.0004E+00 | 5.0002E+00 | 5.0005E+01 | 2.2310E+00 | 2.2770E+00 | |
| 7 | 1.0000E+06 | 7.4210E+05 | 8.7235E+05 | 2.5930E+05 | 2.3000E+00 | 2.0000E+00 | 2.6000E+00 | 2.6000E+00 | 2.6593E+00 | 2.2870E+00 | 1.7705E+00 | |
| 8 | 7.4210E+05 | 4.9770E+05 | 6.2052E+05 | 2.4490E+05 | 2.6000E+00 | 2.6000E+00 | 2.6000E+00 | 2.6000E+00 | 2.6001E+00 | 6.4264E+00 | 1.2923E+00 | |
| 9 | 4.9770E+05 | 3.0770E+05 | 1.8310E+05 | 2.4051E+05 | 3.1450E+05 | 3.0000E+00 | 4.0000E+00 | 3.0000E+00 | 3.5002E+00 | 4.0002E+00 | 7.4652E+00 | |
| 10 | 1.8310E+05 | 1.1100E+05 | 1.4769E+05 | 7.2100E+04 | 4.0003E+00 | 4.5000E+00 | 5.5000E+00 | 6.2504E+00 | 5.0050E+01 | 1.2556E+01 | 5.3336E+00 | |
| 11 | 1.1100E+05 | 4.0000E+04 | 7.5910E+04 | 7.0100E+04 | 4.5000E+00 | 5.5000E+00 | 6.0005E+00 | 9.9338E+01 | 3.0100E+00 | 6.7346E+01 | 0.0124E+00 | |
| 12 | 4.0000E+04 | 2.4170E+04 | 3.2515E+04 | 1.4490E+04 | 5.5002E+00 | 6.0023E+00 | 6.7627E+00 | 5.5004E+01 | 3.1424E+01 | 2.6666E+01 | 0.0020E+01 | |
| 13 | 2.4170E+04 | 1.5030E+04 | 1.9600E+04 | 9.1400E+03 | 6.0252E+00 | 6.5003E+00 | 6.2628E+00 | 4.7506E+01 | 1.1060E+01 | 1.3209E+01 | 0.0006E+01 | |
| 14 | 1.5030E+04 | 7.1010E+03 | 1.1066E+04 | 7.9299E+03 | 6.5003E+00 | 7.2591E+00 | 6.8752E+00 | 7.4901E+01 | 1.3331E+01 | 1.1424E+01 | 0.0005E+01 | |
| 15 | 7.1010E+03 | 3.3540E+03 | 5.2221E+03 | 3.7470E+03 | 7.2501E+00 | 8.0002E+00 | 7.6251E+00 | 7.5000E+01 | 4.8802E+01 | 9.1202E+01 | 0.0000E+01 | |
| 16 | 3.3540E+03 | 1.5800E+03 | 2.4650E+03 | 1.7700E+03 | 8.0002E+00 | 8.7504E+00 | 9.3753E+00 | 7.5020E+01 | 6.2049E+03 | 6.4001E+07 | 0.0000E+01 | |
| 17 | 1.5800E+03 | 4.5400E+02 | 1.0190E+03 | 1.1300E+03 | 8.7504E+00 | 1.0000E+01 | 1.2752E+00 | 1.2496E+00 | 8.8022E+02 | 6.5191E+01 | 0.0000E+01 | |
| 18 | 4.5400E+02 | 1.0210E+02 | 2.7705E+02 | 3.5227E+02 | 1.0000E+01 | 1.2500E+01 | 1.0750E+01 | 1.5000E+00 | 2.1445E+02 | 2.0316E+07 | 0.0000E+01 | |
| 19 | 1.0130E+02 | 3.7200E+01 | 6.4040E+01 | 6.4040E+01 | 1.1500E+01 | 1.2000E+01 | 1.2000E+01 | 1.0000E+00 | 1.0000E+01 | 1.0000E+01 | 0.0000E+01 | |
| 20 | 3.7200E+01 | 1.0610E+01 | 2.3935E+01 | 2.6559E+01 | 1.2500E+01 | 1.3751E+01 | 1.3125E+01 | 1.2500E+01 | 1.2595E+01 | 6.2133E+01 | 0.0000E+01 | |
| 21 | 1.0610E+01 | 1.8550E+00 | 6.2635E+00 | 8.8150E+00 | 1.3751E+01 | 1.5500E+01 | 1.4625E+01 | 1.4946E+00 | 1.4448E+00 | 2.948E+00 | 0.0000E+01 | |
| 22 | 1.8550E+00 | 4.1300E+01 | 1.1344E+00 | 1.4411E+00 | 1.5500E+01 | 1.7000E+01 | 1.4250E+01 | 1.5000E+00 | 8.7423E+01 | 1.3025E+00 | 0.0000E+01 | |
| 23 | 4.1300E+01 | 9.9400E+01 | 2.5649E+01 | 3.1394E+01 | 1.7000E+01 | 1.8421E+01 | 1.7711E+01 | 1.2006E+00 | 6.0334E+01 | 6.2157E+05 | 0.0000E+01 | |
| 24 | 9.9400E+01 | 1.0000E+02 | 9.9999E+02 | 1.0000E+02 | 1.0000E+02 | 1.0422E+01 | 2.7633E+01 | 2.7026E+01 | 2.7026E+01 | 9.2102E+00 | 9.9995E+04 | 0.0000E+01 |

Table 4.1-2b: Photon Energy Group Data for 38 Group Library

| GRP | E _{MIN} | E _{MAX} | AVE E | CELE E | U MAX | U MIN | AVF U | DEL U | ECU AVE | GRP VEL | CHI |
|-----|------------------|------------------|------------|------------|-------------|------------|-------------|------------|------------|------------|------------|
| 1 | 1.4000E+07 | 1.0000E+07 | 1.2000E+07 | 4.0000E+06 | -3.3637E+01 | 0.0000E+00 | -1.6825E+01 | 3.3647E+01 | 1.3032E+07 | 3.0000E+10 | 0.0000E+10 |
| 2 | 1.0000E+07 | 8.0000E+06 | 8.0000E+06 | 2.0000E+06 | 0.0000E+00 | 2.2314E+01 | 1.1157E+01 | 2.2314E+01 | 6.9445E+01 | 3.0000E+10 | 0.0000E+10 |
| 3 | 8.0000E+06 | 6.0000E+06 | 7.0000E+06 | 2.0000E+06 | 5.0000E+01 | 5.2314E+01 | 5.1033E+01 | 5.0000E+01 | 6.9282E+01 | 3.0000E+10 | 0.0000E+10 |
| 4 | 6.0000E+06 | 4.0000E+06 | 5.0000E+06 | 2.0000E+06 | 5.0000E+01 | 5.1203E+01 | 5.1203E+01 | 5.0000E+01 | 4.8990E+01 | 3.0000E+10 | 0.0000E+10 |
| 5 | 4.0000E+06 | 3.0000E+06 | 3.5000E+06 | 1.0000E+06 | 9.1529E+01 | 1.2000E+00 | 1.0600E+00 | 2.0768E+01 | 3.4441E+01 | 3.0000E+10 | 0.0000E+10 |
| 6 | 3.0000E+06 | 2.0000E+06 | 2.7000E+06 | 1.0000E+06 | 1.2640E+00 | 1.6094E+00 | 1.4061E+00 | 4.0547E+01 | 2.4495E+01 | 3.0000E+10 | 0.0000E+10 |
| 7 | 2.0000E+06 | 1.5000E+06 | 1.7500E+06 | 5.0000E+05 | 1.6094E+00 | 1.8971E+00 | 1.7531E+00 | 2.0768E+01 | 1.7321E+01 | 3.0000E+10 | 0.0000E+10 |
| 8 | 1.5000E+06 | 1.0000E+06 | 1.2500E+06 | 5.0000E+05 | 1.8971E+00 | 2.3034E+00 | 2.0939E+00 | 4.0547E+01 | 1.2247E+01 | 3.0000E+10 | 0.0000E+10 |
| 9 | 1.0000E+06 | 7.0000E+05 | 8.5000E+05 | 3.0000E+05 | 2.3026E+00 | 2.6593E+00 | 2.4909E+00 | 3.5467E+01 | 0.3666E+05 | 3.0000E+10 | 0.0000E+10 |
| 10 | 7.0000E+05 | 4.0000E+05 | 5.5000E+05 | 3.0000E+05 | 2.6593E+00 | 3.2199E+00 | 2.4939E+00 | 5.5362E+01 | 5.2915E+05 | 3.0000E+10 | 0.0000E+10 |
| 11 | 4.0000E+05 | 2.0000E+05 | 3.0000E+05 | 2.0000E+05 | 3.2199E+00 | 3.9120E+00 | 3.5655E+00 | 6.9315E+01 | 2.0284E+05 | 3.0000E+10 | 0.0000E+10 |
| 12 | 2.0000E+05 | 1.0000E+05 | 1.5000E+05 | 1.0000E+05 | 3.9120E+00 | 4.6032E+00 | 4.2588E+00 | 6.9315E+01 | 1.4142E+05 | 3.0000E+10 | 0.0000E+10 |
| 13 | 1.0000E+05 | 6.0000E+04 | 8.0000E+04 | 4.0000E+04 | 4.6032E+00 | 5.1160E+00 | 4.8500E+00 | 5.1043E+01 | 7.7460E+04 | 3.0000E+10 | 0.0000E+10 |
| 14 | 6.0000E+04 | 1.0000E+04 | 2.5000E+04 | 5.0000E+04 | 5.1160E+00 | 6.9078E+00 | 6.0119E+00 | 1.7918E+01 | 2.4495E+04 | 3.0000E+10 | 0.0000E+10 |

Table 4.1-3a: Neutron Energy Group Data for 59 Group Library

| GRP | EN(MV) | AVG E | DELT E | U MAX | U MIN | U AVG | DEL U |
|-----|-----------|-----------|-----------|------------|------------|------------|-----------|
| 1 | 1.733E+01 | 1.516E+01 | 1.166E+00 | -5.695E-01 | -3.995E-01 | -4.199E-01 | 5.510E+00 |
| 2 | 1.419E+01 | 1.221E+01 | 8.320E+00 | -1.980E+00 | -1.966E+00 | -2.769E+00 | 5.508E+00 |
| 3 | 1.221E+01 | 1.165E+01 | 7.116E+00 | -1.974E+00 | -1.967E+00 | -2.749E+00 | 5.314E+00 |
| 4 | 1.088E+01 | 8.467E+00 | 9.303E+00 | 1.393E+00 | 9.000E+00 | 1.590E+00 | 4.632E+00 |
| 5 | 8.467E+00 | 6.607E+00 | 6.695E+00 | 1.500E+00 | 1.501E+00 | 1.500E+00 | 6.000E+00 |
| 6 | 7.468E+00 | 6.736E+00 | 1.347E+00 | 2.000E+00 | 5.660E+00 | 1.502E+00 | 3.918E+00 |
| 7 | 6.865E+00 | 4.945E+00 | 1.000E+00 | 5.000E+00 | 5.000E+00 | 6.102E+00 | 6.693E+00 |
| 8 | 4.965E+00 | 3.678E+00 | 4.321E+00 | 7.001E+00 | 1.600E+00 | 6.001E+00 | 2.524E+00 |
| 9 | 3.678E+00 | 3.011E+00 | 3.345E+00 | 6.470E+00 | 1.000E+00 | 1.200E+00 | 2.000E+00 |
| 10 | 3.011E+00 | 2.725E+00 | 2.860E+00 | 2.000E+00 | 1.300E+00 | 1.350E+00 | 2.000E+00 |
| 11 | 2.725E+00 | 2.231E+00 | 2.470E+00 | 4.940E+00 | 1.300E+00 | 1.500E+00 | 2.400E+00 |
| 12 | 2.231E+00 | 1.928E+00 | 2.075E+00 | 3.110E+00 | 1.500E+00 | 1.650E+00 | 2.455E+00 |
| 13 | 1.928E+00 | 1.653E+00 | 1.706E+00 | 2.670E+00 | 1.650E+00 | 1.650E+00 | 2.000E+00 |
| 14 | 1.653E+00 | 1.353E+00 | 1.500E+00 | 3.000E+00 | 1.000E+00 | 1.500E+00 | 2.000E+00 |
| 15 | 1.353E+00 | 1.020E+00 | 1.177E+00 | 3.510E+00 | 2.000E+00 | 2.150E+00 | 3.000E+00 |
| 16 | 1.020E+00 | 8.208E+00 | 1.114E+00 | 1.812E+00 | 2.300E+00 | 2.800E+00 | 3.000E+00 |
| 17 | 8.208E+00 | 7.427E+00 | 7.817E+00 | 7.010E+00 | 2.500E+00 | 2.550E+00 | 2.550E+00 |
| 18 | 7.427E+00 | 6.081E+00 | 6.754E+00 | 7.400E+00 | 2.400E+00 | 2.700E+00 | 2.700E+00 |
| 19 | 6.081E+00 | 4.978E+00 | 5.229E+00 | 1.103E+00 | 2.000E+00 | 2.000E+00 | 2.000E+00 |
| 20 | 4.978E+00 | 3.688E+00 | 4.333E+00 | 1.290E+00 | 3.000E+00 | 3.000E+00 | 3.000E+00 |
| 21 | 3.688E+00 | 2.972E+00 | 3.338E+00 | 7.160E+00 | 3.300E+00 | 3.515E+00 | 3.800E+00 |
| 22 | 2.972E+00 | 1.831E+00 | 2.461E+00 | 3.141E+00 | 3.515E+00 | 4.000E+00 | 4.300E+00 |
| 23 | 1.831E+00 | 1.103E+00 | 1.470E+00 | 7.210E+00 | 4.000E+00 | 4.500E+00 | 4.750E+00 |
| 24 | 1.103E+00 | 4.606E+00 | 7.014E+00 | 4.500E+00 | 5.000E+00 | 5.000E+00 | 5.000E+00 |
| 25 | 4.086E+00 | 2.417E+00 | 3.251E+00 | 1.669E+00 | 1.500E+00 | 1.625E+00 | 1.700E+00 |
| 26 | 2.417E+00 | 2.017E+00 | 2.302E+00 | 4.000E+00 | 6.000E+00 | 6.250E+00 | 6.500E+00 |
| 27 | 2.017E+00 | 1.503E+00 | 1.845E+00 | 6.848E+00 | 4.125E+00 | 6.900E+00 | 7.000E+00 |
| 28 | 1.503E+00 | 7.101E+00 | 1.104E+00 | 7.929E+00 | 4.500E+00 | 7.250E+00 | 7.400E+00 |
| 29 | 7.101E+00 | 3.354E+00 | 5.227E+00 | 7.250E+00 | 8.000E+00 | 8.750E+00 | 9.250E+00 |
| 30 | 3.354E+00 | 1.586E+00 | 2.669E+00 | 1.770E+00 | 8.000E+00 | 8.750E+00 | 9.250E+00 |
| 31 | 1.586E+00 | 4.546E+00 | 1.019E+00 | 1.300E+00 | 1.750E+00 | 1.900E+00 | 2.000E+00 |
| 32 | 4.546E+00 | 2.144E+00 | 3.342E+00 | 2.396E+00 | 1.000E+00 | 1.075E+00 | 1.075E+00 |
| 33 | 2.144E+00 | 1.013E+00 | 1.578E+00 | 1.131E+00 | 1.075E+00 | 1.150E+00 | 1.150E+00 |
| 34 | 1.013E+00 | 3.726E+00 | 6.928E+00 | 6.404E+00 | 1.150E+00 | 1.250E+00 | 1.200E+00 |
| 35 | 3.726E+00 | 1.067E+00 | 2.394E+00 | 2.659E+00 | 1.250E+00 | 1.375E+00 | 1.325E+00 |
| 36 | 1.067E+00 | 5.063E+00 | 7.856E+00 | 5.627E+00 | 1.375E+00 | 1.450E+00 | 1.425E+00 |
| 37 | 5.063E+00 | 1.043E+00 | 1.490E+00 | 3.100E+00 | 1.450E+00 | 1.500E+00 | 1.500E+00 |
| 38 | 1.043E+00 | 8.764E+00 | 1.365E+00 | 9.786E+00 | 1.550E+00 | 1.250E+00 | 1.275E+00 |
| 39 | 8.764E+00 | 4.139E+00 | 6.455E+00 | 4.625E+00 | 1.625E+00 | 1.700E+00 | 1.625E+00 |
| 40 | 4.139E+00 | 9.990E+00 | 2.594E+00 | 3.139E+00 | 1.700E+00 | 1.842E+00 | 1.711E+00 |
| 41 | 9.990E+00 | 1.000E+00 | 5.000E+00 | 5.990E+00 | 1.990E+00 | 2.163E+00 | 2.102E+00 |

Table 4.1-3b: Photon Energy Group Data for 59 Group Library

| GRP | E BOUNDS | AVE E | DEL E | U SOUNDS | AVE U | DEL U | (CU AVE) | GRP VEL |
|-----|------------|------------|------------|------------------------|------------------------|-----------------------|------------|------------|
| 1 | 1.4000E+07 | 1.0000E+07 | 1.2000E+07 | 4.0000E+06 -3.3647E-01 | 0.0000E+00 -1.4024E-01 | 3.3647E+01 | 1.1032E+07 | 3.0000E+10 |
| 2 | 1.0000E+07 | 8.0000E+06 | 9.0000E+06 | 2.0000E+06 0.0000E+00 | 2.2314E+01 1.1157E+01 | 2.2314E+01 | 0.3043E+00 | 3.0000E+10 |
| 3 | 8.0000E+06 | 7.0000E+06 | 7.5000E+06 | 2.2314E+01 0.0000E+00 | 3.5667E+01 3.1093E+01 | 2.0591E+01 1.3353E+01 | 7.4033E+00 | 3.0000E+10 |
| 4 | 6.0000E+06 | 5.0000E+06 | 6.5000E+06 | 1.0000E+06 3.5667E+00 | 5.1093E+01 6.9313E+01 | 4.3375E+01 6.0119E+01 | 6.0077E+00 | 3.0000E+10 |
| 5 | 4.0000E+06 | 3.0000E+06 | 5.0000E+06 | 1.0000E+06 5.1093E+00 | 6.9313E+01 9.1629E+01 | 1.0232E+01 8.0472E+01 | 5.4772E+00 | 3.0000E+10 |
| 6 | 3.0000E+06 | 4.0000E+05 | 4.5000E+06 | 1.0000E+06 6.9313E+00 | 9.1629E+01 1.2040E+01 | 2.2314E+01 1.0444E+01 | 4.4721E+00 | 3.0000E+10 |
| 7 | 4.0000E+05 | 3.0000E+06 | 3.5000E+06 | 1.0000E+06 9.1629E+01 | 1.2040E+01 1.4661E+00 | 2.0168E+01 1.0661E+00 | 3.4444E+00 | 3.0000E+10 |
| 8 | 3.0000E+05 | 2.0000E+05 | 2.5000E+05 | 1.0000E+06 1.2040E+00 | 1.4661E+00 1.4094E+00 | 1.4094E+00 1.4094E+00 | 2.4925E+00 | 3.0000E+10 |
| 9 | 2.0000E+05 | 1.5000E+05 | 1.7500E+05 | 1.0000E+06 1.4094E+00 | 1.4094E+00 1.8971E+00 | 1.7533E+00 1.7533E+00 | 1.7721E+00 | 3.0000E+10 |
| 10 | 1.5000E+05 | 1.0000E+05 | 1.2500E+05 | 1.0000E+05 1.8971E+00 | 1.8971E+00 2.3026E+00 | 2.3026E+00 2.3026E+00 | 1.2247E+00 | 3.0000E+10 |
| 11 | 1.0000E+05 | 8.0000E+05 | 9.0000E+05 | 2.0000E+05 2.0000E+05 | 2.0000E+05 2.5257E+00 | 2.5257E+00 2.5257E+00 | 2.4142E+00 | 3.0000E+10 |
| 12 | 8.0000E+05 | 7.0000E+05 | 7.5000E+05 | 1.0000E+05 7.5000E+05 | 7.5000E+05 2.6593E+00 | 2.6593E+00 2.6593E+00 | 1.3353E+00 | 3.0000E+10 |
| 13 | 7.0000E+05 | 6.0000E+05 | 6.5000E+05 | 1.0000E+05 6.5000E+05 | 6.5000E+05 2.8134E+00 | 2.8134E+00 2.8134E+00 | 1.5615E+00 | 3.0000E+10 |
| 14 | 6.0000E+05 | 4.0000E+05 | 5.0000E+05 | 2.0000E+05 5.0000E+05 | 5.0000E+05 2.0134E+00 | 2.0134E+00 2.0134E+00 | 4.0547E+00 | 3.0000E+10 |
| 15 | 4.0000E+05 | 2.0000E+05 | 3.0000E+05 | 2.0000E+05 3.0000E+05 | 3.0000E+05 3.2109E+00 | 3.2109E+00 3.2109E+00 | 6.9315E+00 | 3.0000E+10 |
| 16 | 2.0000E+05 | 1.0000E+05 | 1.5000E+05 | 1.0000E+05 1.5000E+05 | 1.5000E+05 3.9120E+00 | 4.6052E+00 4.2584E+00 | 6.9315E+00 | 3.0000E+10 |
| 17 | 1.0000E+05 | 6.0000E+04 | 8.0000E+04 | 4.0000E+04 8.0000E+04 | 8.0000E+04 4.6052E+00 | 5.1160E+00 4.0466E+00 | 5.0003E+00 | 3.0000E+10 |
| 18 | 6.0000E+04 | 1.0000E+04 | 3.5000E+04 | 5.0000E+04 3.5000E+04 | 3.5000E+04 6.9078E+00 | 5.1160E+00 4.0119E+00 | 1.7916E+00 | 2.4495E+04 |

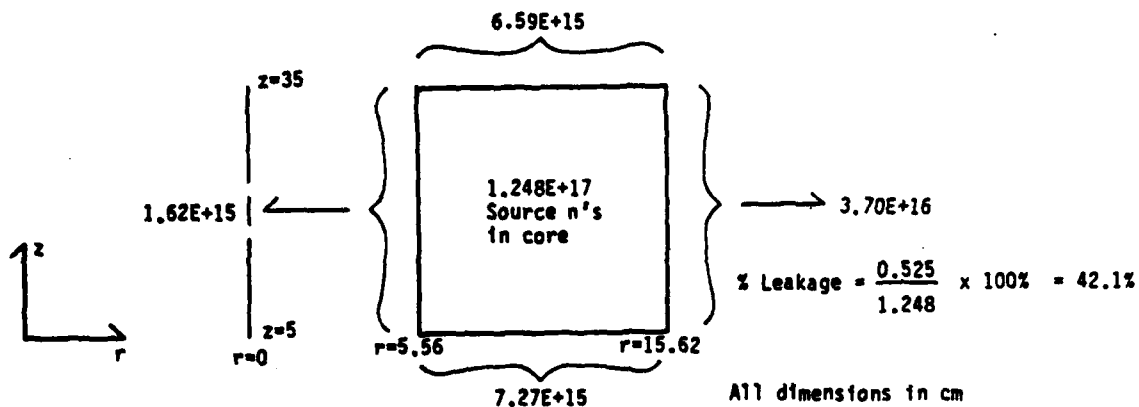
The initial fine mesh core eigenvalue calculation was made with a 36×51 node mesh. The average grid spacing in the core was $\sim .5$ cm (radial) by 1.0 cm (axial). The 38 group cross section library was generated by running the criticality problem with the 59 group cross section library, then using the flux spectrum from the core as a weighting function in collapsing the 59 group library to 38 groups. The same spectrum was used to collapse the BUGLE cross sections in MACK IV to 38 groups in generating the heating kermas. The 38 group library was then used in FEMP2D to calculate the heating rates throughout the shield.

The eigenvalue of the fine mesh core with reflectors was calculated as $\lambda = 1.031163$ using volume fractions as recorded in Table 4.1-1. Twelve outer iterations were required for a 10^{-4} error tolerance on the eigenvalue. The maximum number of inner iterations was 60 for a 10^{-6} error tolerance for each energy group. The system was well-conditioned as 53.2 was the largest condition number encountered during any iteration.

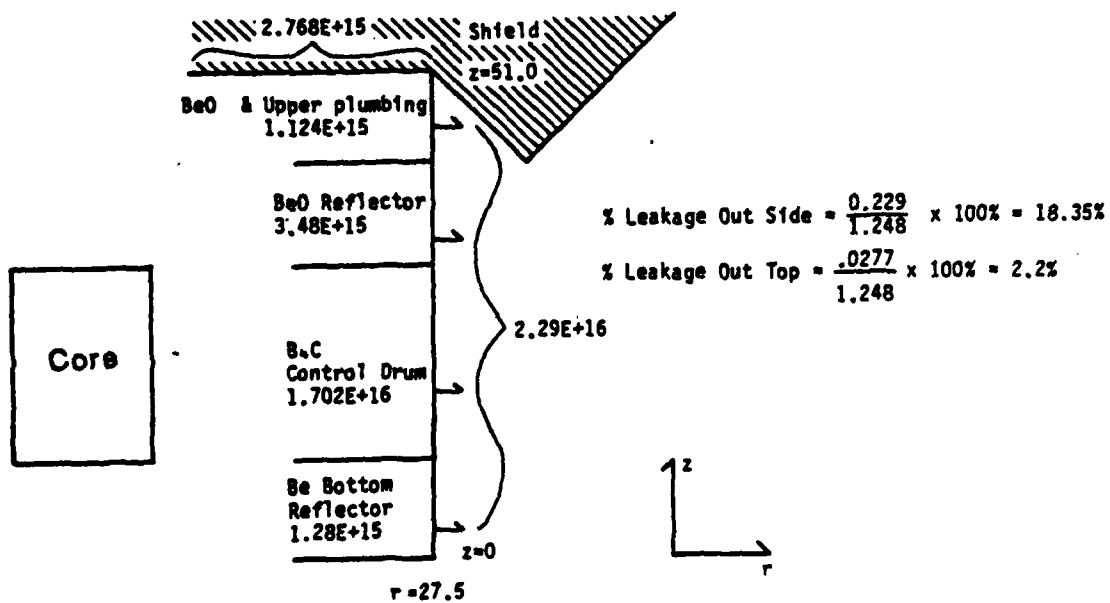
Figure 4.1-2 shows the neutron leakage from the core, and outer radial and axial surfaces of the reflectors. For an operating power level of $1.66 \text{ MW}_{\text{th}}$, there are 1.248×10^{17} source neutrons generated. Of this total, some 42.1% leak out of the core over a 4π geometric factor. About 18.4% of the total source neutrons leak out the outer radial surface, and 2.2% leak out the top axial reflector surface directly into the shield. As expected, the leakage flux spectrum is quite hard over these surfaces with almost 20% of the neutrons with 1 Mev or greater energies.

Figure 4.1-2 Neutron Leakage for the SP-100 Reactor

a. Core Leakage



b. Side Leakage



The results that follow were based on this reactor design, which is typical of the space based reactors currently on the drawing boards of SP-100 planners. Section 4.2 will discuss the importance of including temperature feedback effects in radiation transport calculations for determining the energy deposition throughout the shield. The feedback mechanisms specifically include the temperature effects on number densities and on the microscopic cross sections at thermal energies.

4.2 Temperature Feedback Effects on Energy Deposition. The effect of temperature on energy deposition in the radiation shield is an important design consideration. If the effect is significant, then the coupled radiation transport-temperature calculations must be recalculated each time any engineering parameter is changed. For example, if the ambient temperature of the space environment is varied, a new set of energy deposition values throughout the shield must be determined. With three to four hours of CPU time consumed on a VAX 11/780 for a one cycle of radiation transport-heat transfer calculations, a single set of heating rates can easily require 12 or more hours of CPU time.

On the other hand, if the temperature effect on energy deposition is only weakly coupled, the conditions of the shield analysis can be varied (i.e. ambient temperature or surface emissivity) and the same set of heating rates used again. Thus, from an economic as well as engineering viewpoint, the strength of the temperature-energy deposition coupling is a significant concern.

The discussion of section 3.3 provided the theoretical background for the results that are presented here. Basically, the temperature effects on energy deposition can be broken down into the following areas:

- Change in density of shielding materials
- Change in neutron absorption and total cross sections at low energies
- Inclusion of upscatter cross sections at low energies

As we recall, temperature has no effect in a medium characterized by a pure Maxwellian flux. Equation 3.3-24 showed that the decrease in absorption cross section is accompanied by the same increase in thermal flux, resulting in a constant reaction rate. Of course, this conclusion assumes that the change in number densities due to temperature increases has already been included in the reaction rate. For a non-Maxwellian medium, temperature effects are less obvious. The thermal cross sections must be calculated using free gas scattering kernel (or some other scattering kernel such as harmonic oscillator) to calculate the new thermal flux, which serves as the weighting function in the cross section collapse.

The principal nuclides of materials found in the neutron attenuation portion of an SP-100 type reactor shield are included in Table 4.2-1, along with each molecule's volume percentage, isotopic abundance, and $1/v$ cross section indicator.

From Table 4.2-1, several observations can be made. On a volume or atom percent basis, the LiH temperature effect behavior will dominate the shield as there are few stainless steel nuclides in the medium. When LiH is used which has been enriched to 100% Li-7 (referred to as LiH [Depl]), the flux shape will be Maxwellian and temperature will not have any appreciable effect on energy deposition (other than changes in nuclide densities).

Table 4.2-1. Principal Nuclides Found in Neutron Attenuation Portion of an SP-100 Type Reactor Shield

| <u>Nuclide</u> | <u>% Volume in Shield</u> | <u>Abundance of Isotope atom %</u> | <u>Abundance of Isotope in molecule, atom %</u> | <u>Absorption Cross section (barns) 1/v</u> | |
|------------------------|-------------------------------|--|---|---|-----|
| <u>LiH(Nat)</u> | 99.5 | | | | |
| ${}_1^{\text{H}}{}^1$ | | 100 | 50 | .332 | No |
| ${}_3^{\text{Li}}{}^7$ | | 7.4 | 3.7 | .045 | No |
| ${}_3^{\text{Li}}{}^6$ | | 92.6 | 46.3 | 945 | Yes |
| <u>LiH(Degl) (1)</u> | 99.5 | | | | |
| ${}_1^{\text{H}}{}^1$ | | 100 | 50 | .332 | No |
| ${}_3^{\text{Li}}{}^7$ | | 100 | 50 | .045 | No |
| <u>SS-316:</u> | 0.5 | | | | |
| Fe | | (2) | 62-69 | 2.55 | Yes |
| Cr | | (2) | 16-18 | 3.1 | Yes |
| Ni | | (2) | 10-14 | 4.6 | Yes |
| Mo | | (2) | 2-3 | <.3 | Yes |
| Mn | | (2) | 2 | 13.3 | Yes |
| Si | | (2) | 1 | .16 | Yes |

(1) Li enriched to 100% Li-7.

(2) Each element of SS-316 has a number of isotopes naturally occurring in nature.

For an LiH shield with naturally occurring LiH (referred to as LiH[Nat]), the presence of only 3.7% of Li-6 atoms will dominate the temperature response of the shield because of the large absorption cross section at thermal energy (945 barns at 0.025 ev). The microscopic absorption cross section of LiH at low energies is plotted in Figure 4.2-1. The major contribution of Li-6 to heat rate even with its low natural isotopic abundance of 7.4% can be easily demonstrated with a simple calculation. The heating rate (HR) can be expressed as:

$$HR \sim N\phi\bar{E}$$

which represents the reaction rate times the energy released per reaction. At thermal energies, the major interactions resulting in energy deposition in an LiH(Nat) shield are the (n,α) reaction in Li-6, radiative capture of Li-7 and the immediate decay to two alpha particles, and the radiative capture and elastic scattering of H. Assuming that all reaction energies are deposited at the point of interaction, the contributions of the respective reactions are included in Table 4.2-2.

The contribution to heating rate of elastic scattering is based on the assumption that the average neutron energy is 1 Mev and all this energy is deposited at one location. This is obviously an extremely conservative assumption. Nevertheless, from Table 4.2-2, one readily sees that the dominant contribution to energy deposition in an LiH(Nat) shield is the $\text{Li}^6(n,\alpha)\text{T}^3$ reaction.

On the basis of the previous discussion of this section, the temperature feedback on energy deposition was examined by investigating this effect in a W-LiH(Nat) shield of the SP-100 reactor. The 4 cm of

Table 4.2-2. Major Contributions to Energy
Deposition in an LiH (Nat) Shield

| Reaction | N^1 | σ (barns) | \bar{E}^2 (MeV) | HR | $\frac{HR}{HR_{Li-6}}$ |
|--------------------------------------|-------|---------------------|----------------------|-------------|------------------------|
| $Li^6(n, \alpha)T^3$ | 0.037 | 945 | 4.78 | 172 ϕ | 1.0 |
| $Li^7(n, \gamma)Li^8$ | .463 | .045 | 2.05 | 0.24 ϕ | 0.0014 |
| $Li^8 \xrightarrow{\beta^-} 2\alpha$ | | | 9.31 | | |
| $H(n, \gamma)H^2$ | .5 | .332 | 2.23 | 9 ϕ | 0.052 |
| Elastic Scatt | .5 | 18 | 1.0 | | |

¹ Number densities normalized to one

² Based on $\Delta E = \Delta mc^2$

RD-A158 180 COUPLED RADIATION TRANSPORT/ THERMAL ANALYSIS OF THE
RADIATION SHIELD FOR A. (U) AIR FORCE INST OF TECH
WRIGHT-PATTERSON AFB OH W J BARATTINO JUL 85

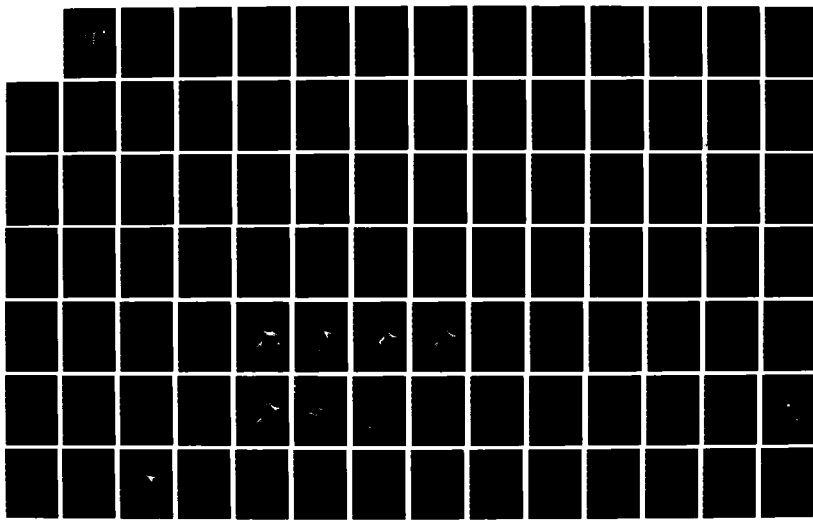
3/4

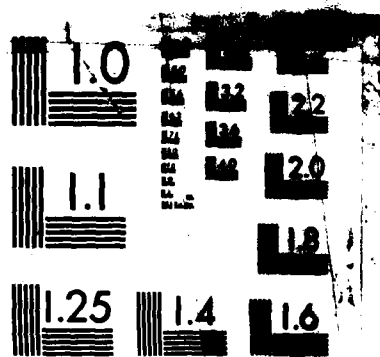
UNCLASSIFIED

AFIT/CI/NR-85-53D

F/G 18/6

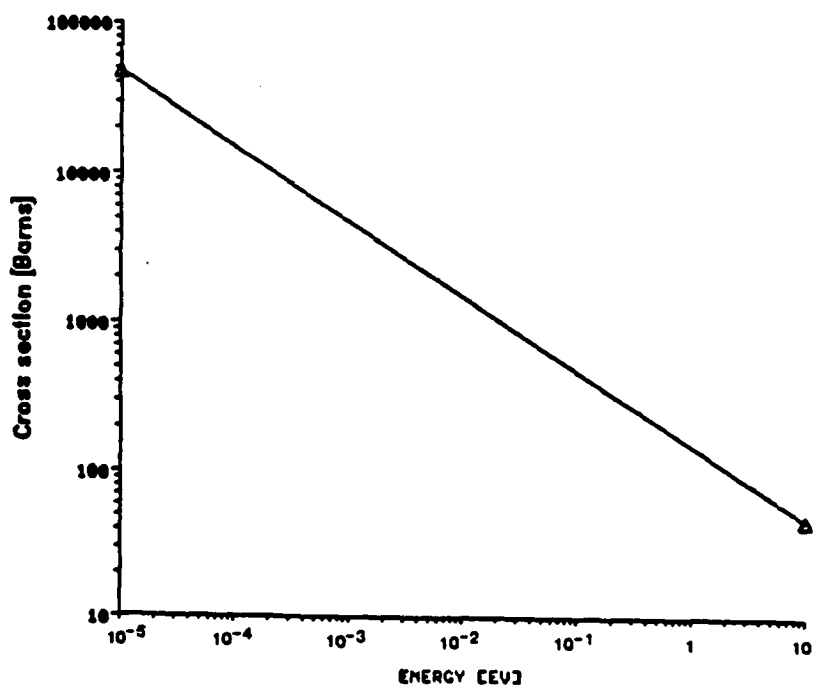
NL





MICROCOPY RESOLUTION TEST CHART
NATIONAL BUREAU OF STANDARDS-1963-A

Figure 4.2-1 Absorption Cross Section for Li-6



tungsten at the front of the shield will provide a "softening" effect on the hard neutron spectrum emerging from the core axial reflector. With natural LiH throughout the remainder of the shield, a wide temperature range could be anticipated within the shield. Thus, if an elevated or widely varying temperature distribution does influence the energy deposition in a highly absorbing, non-Maxwellian medium, this shield design would reflect such a feedback effect.

4.2.1 Temperature Feedback Problem Setup. Figure 4.2-2 sets up the problem analyzed to investigate the temperature effects on energy deposition in an SP-100 reactor radiation shield.

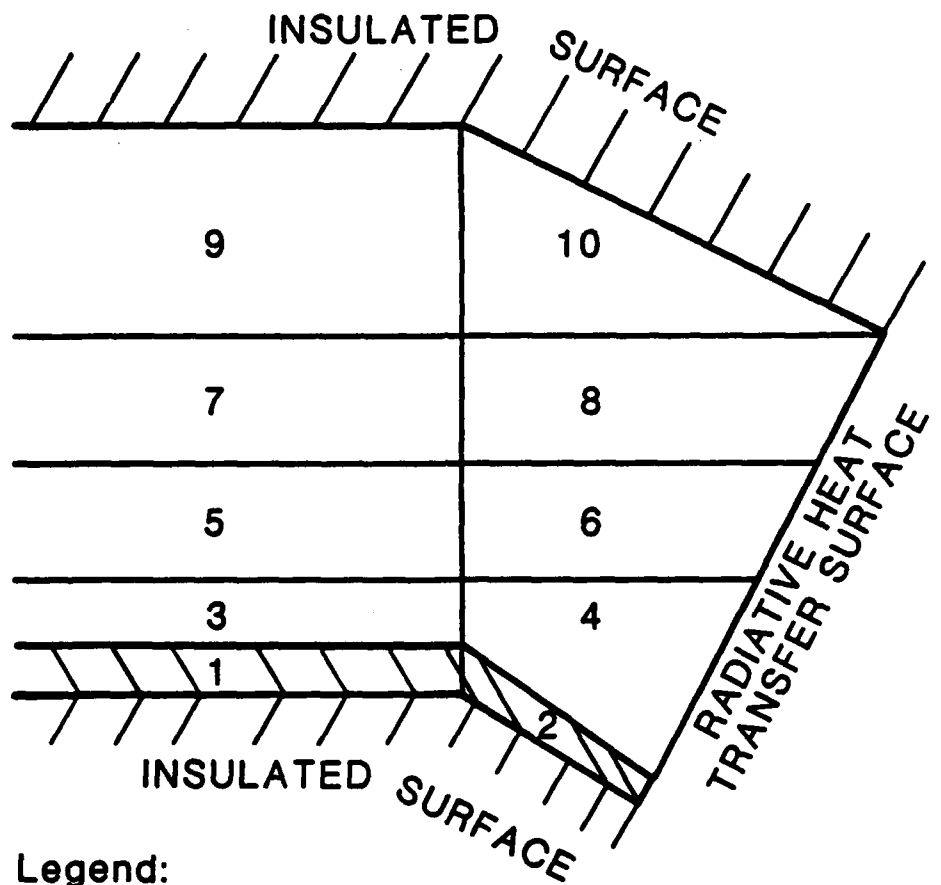
The dimensions of the shield were presented earlier in Figure 4.1-1. Regions 1 and 2 of Figure 4.2-2 were made of tungsten, and regions 3 through 10 were natural LiH , cold pressed in a stainless steel matrix.

4.2.2. Temperature Effects on Energy Deposition in a M-B Medium. As shown previously, the LiH(Nat) region is non-Maxwellian because of the heavy absorption of the Li-6. However, for the purpose of verifying the theoretical prediction that the reaction rate remains constant for a $1/v$ medium characterized by a M-B flux, the temperature feedback effects can be examined with this shield using M-B theory.

Figure 4.2-3 flowcharts the methodology used to examine the temperature feedback of the M-B medium. The results of this section will also be of interest for comparing how energy deposition in a non-M-B medium differs from the M-B medium.

For the M-B medium, the effects of temperature on energy deposition is defined as the change in heating rates throughout the shield

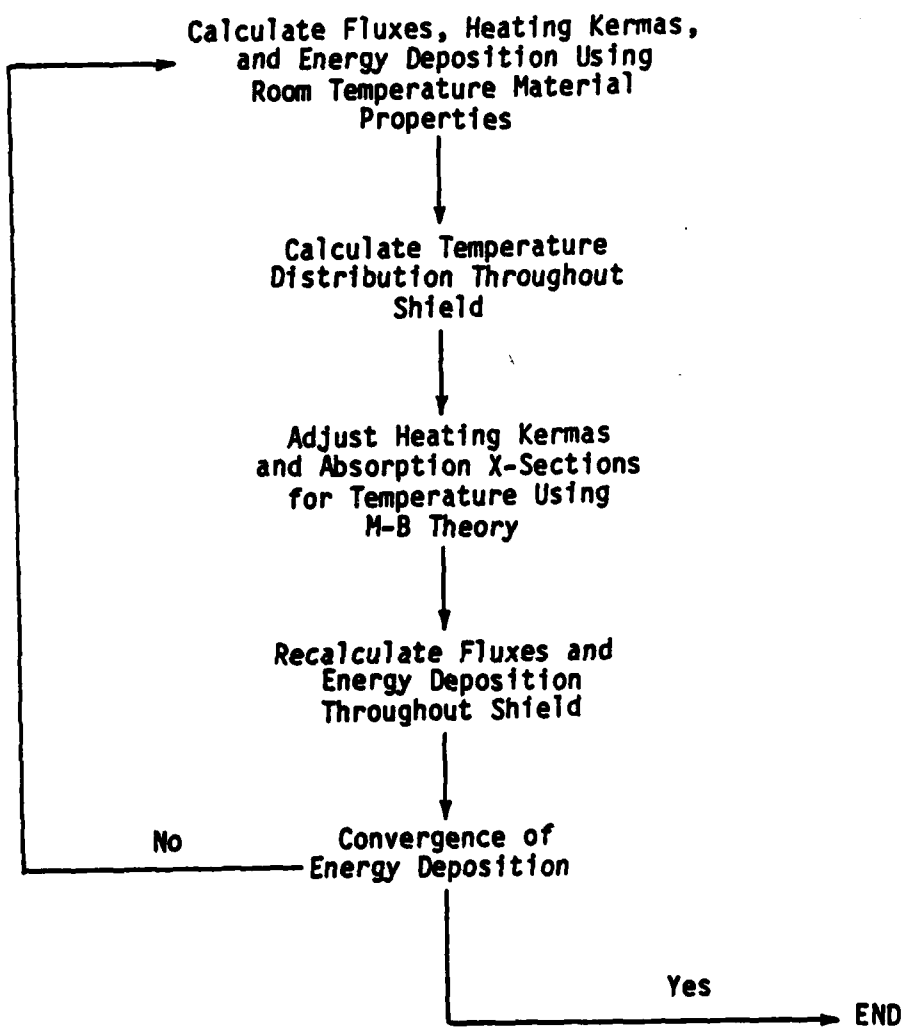
Figure 4.2-2 Problem Setup for Temperature Feedback Analysis



Legend:

| <u>Zones</u> | <u>Material</u> |
|--------------|-----------------|
| 1-2 | W |
| 3-10 | LiH |

Figure 4.2-3. Flowchart of Temperature Feedback Effects Calculation Methodology for a Maxwell Boltzmann Flux Medium



after accounting for material density changes due to elevated temperatures. This definition may be considered somewhat limiting since material density changes are indeed temperature related and, hence, should be included. However, a counter argument is that the elevated temperature properties can be pre-estimated and accounted for in the initial calculation. Without passing judgement on the wisdom of either school of thought, the cold start and elevated temperature differences will be included in the next section dealing with non-M-B mediums.

Therefore, using elevated temperature material properties the energy deposition can be compared with and without the temperature effects on absorption cross section as calculated with Equation 3.3-22 for an M-B medium. As we recall, this equation showed that the absorption cross section varied as $1/T$ for a $1/v$ nuclide characterized by an M-B flux. The results of applying this correction and utilizing the methodology of Figure 4.2-3 are included in Tables 4.2-3 and 4.2-4. The zones of these tables correspond to those included on Figure 4.2-2.

The energy deposition values of Table 4.2-3 did not change for the calculations with and without the temperature feedback effect on the thermal group absorption cross section. Of the 10 kW of heat deposited in the shield, slightly less than half (4.92 kW) was due to neutron interactions. And of this total, only 0.03 kW was attributable to neutron interactions in the tungsten. Over 63% of the total energy deposited occurred within the first 15 cm of the shield and over 55% of the heat generation due to neutron interactions occurred within this region, as well. Over the last 29 cm of the shield (of a total thickness of 75 cm), only 0.12 kW of neutron energy and 0.38 kW of gamma energy was deposited.

**Table 4.2-3. Energy Deposited in a W-LiH(Nat) Shield
With and Without MB Temperature Feedback
Included in Absorption Cross Sections
(Same for Both Cases)**

| Energy Deposited [kW] | | | | | | |
|-----------------------|----------|--------------|--------------|---------------|------------------|---------|
| Zone | Material | H_{γ} | H_n | H_{tot} | Summary | |
| <u>W:</u> | | | | | | |
| 1 | W | .738 | .025 | 1.763 | H_{γ} | = 3.175 |
| 2 | " | 1.437 | .013 | 1.450 | H_n | = .038 |
| 3 | LiH(Nat) | .110 | 1.211 | 1.321 | H_{tot} | = 3.213 |
| 4 | " | .318 | 1.482 | 1.800 | <u>LiH(Nat):</u> | |
| 5 | " | .128 | .046 | .174 | H_{γ} | = 1.751 |
| 6 | " | .329 | .888 | 1.217 | H_n | = 4.888 |
| 7 | " | .135 | .003 | .138 | H_{tot} | = 6.639 |
| 8 | " | .494 | 1.138 | 1.632 | | |
| 9 | " | .146 | .007 | .153 | | |
| 10 | " | .243 | .113 | .357 | | |
| Total | | 5.078 | 4.926 | 10.004 | | |

Legend:

H_{γ} - Energy deposited by Gammas

H_n - Energy Deposited by Neutrons

$H_{tot} = H_{\gamma} + H_n$

**Table 4.2-4: Reaction Rates for W-LiH(Nat) Shield
With and Without Temperature Feedback**

MB Temperature Feedback Included

| Zone | Material | Σ_a^{th} | Σ_T^{th} | $\phi^{\text{th}}(1)$ | $\Sigma_a\phi^{\text{th}}$ | $\Sigma_T\phi^{\text{th}}$ |
|------|----------|------------------------|------------------------|-----------------------|----------------------------|----------------------------|
| 1 | W | 6.21-1 | 9.02-1 | 2.547+12 | 1.58+12 | 2.36+12 |
| 2 | " | 6.44-1 | 9.25-1 | 6.373+12 | 4.10+12 | 5.90+12 |
| 3 | LiH(Nat) | 2.45 | 5.02 | 5.948+13 | 1.46+14 | 2.99+14 |
| 4 | " | 2.65 | 5.28 | 5.593+13 | 1.48+14 | 2.95+14 |
| 5 | " | 2.56 | 5.17 | 2.405+12 | 6.16+12 | 1.24+13 |
| 6 | " | 2.73 | 5.37 | 3.351+13 | 9.15+13 | 1.80+14 |
| 7 | " | 2.65 | 5.28 | 1.202+11 | 3.19+11 | 6.35+11 |
| 8 | " | 2.76 | 5.42 | 4.189+13 | 1.16+14 | 2.27+14 |
| 9 | " | 2.68 | 5.31 | 2.908+11 | 7.79+11 | 1.54+12 |
| 10 | " | 2.73 | 5.38 | 4.512+12 | 1.23+13 | 2.43+13 |

Temp Feedback Removed⁽²⁾

| | | | | | | |
|----|----------|--------|-------|----------|---------|---------|
| 1 | W | 9.42-1 | 1.226 | 1.315+12 | 1.24+12 | 1.61+12 |
| 2 | " | 9.42-1 | 1.22 | 4.823+12 | 4.54+12 | 5.88+12 |
| 3 | LiH(Nat) | 3.65 | 6.21 | 4.012+13 | 1.46+14 | 2.49+14 |
| 4 | " | 3.73 | 6.36 | 3.999+13 | 1.49+14 | 2.54+14 |
| 5 | " | 3.69 | 6.30 | 1.663+12 | 6.14+12 | 1.05+13 |
| 6 | " | 3.76 | 6.40 | 2.441+13 | 9.18+13 | 1.56+14 |
| 7 | " | 3.73 | 6.36 | 8.546+10 | 3.19+11 | 5.44+11 |
| 8 | " | 3.77 | 6.42 | 3.080+13 | 1.16+14 | 1.98+14 |
| 9 | " | 3.74 | 6.37 | 2.088+11 | 7.81+11 | 1.33+12 |
| 10 | " | 3.76 | 6.40 | 3.288+12 | 1.24+13 | 2.10+13 |

Notes:

(¹) ϕ^{th} represents thermal flux ($\phi < 0.1$ ev) integrated over volume of zone.

(²) Temperature effects on number densities included, but room temperature absorption cross sections used.

Figure 4.2-4 Energy Deposited in Tungsten for W-LiH(Na)

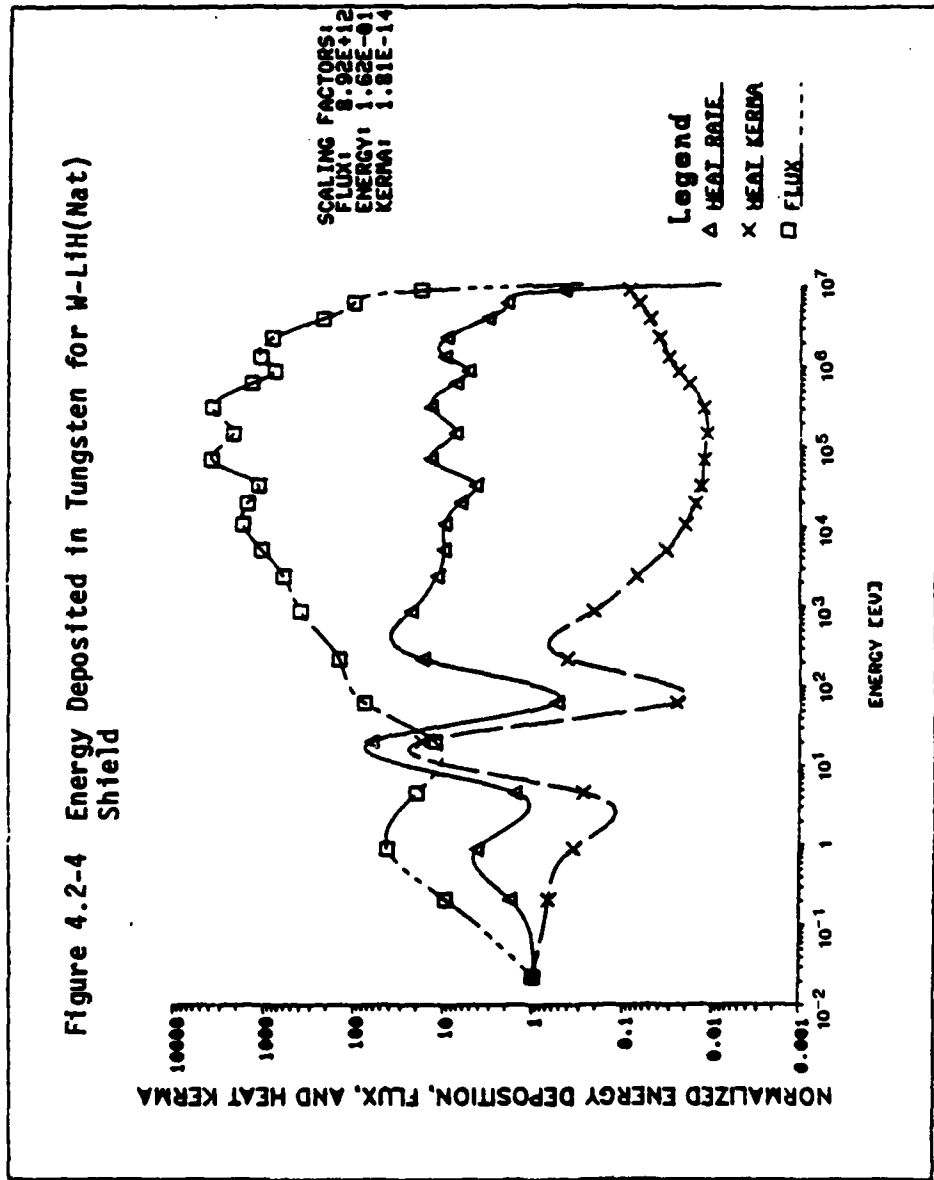


Figure 4.2-5 Energy Deposited in Inner LiH Region for W-LiH(Nat) Shield

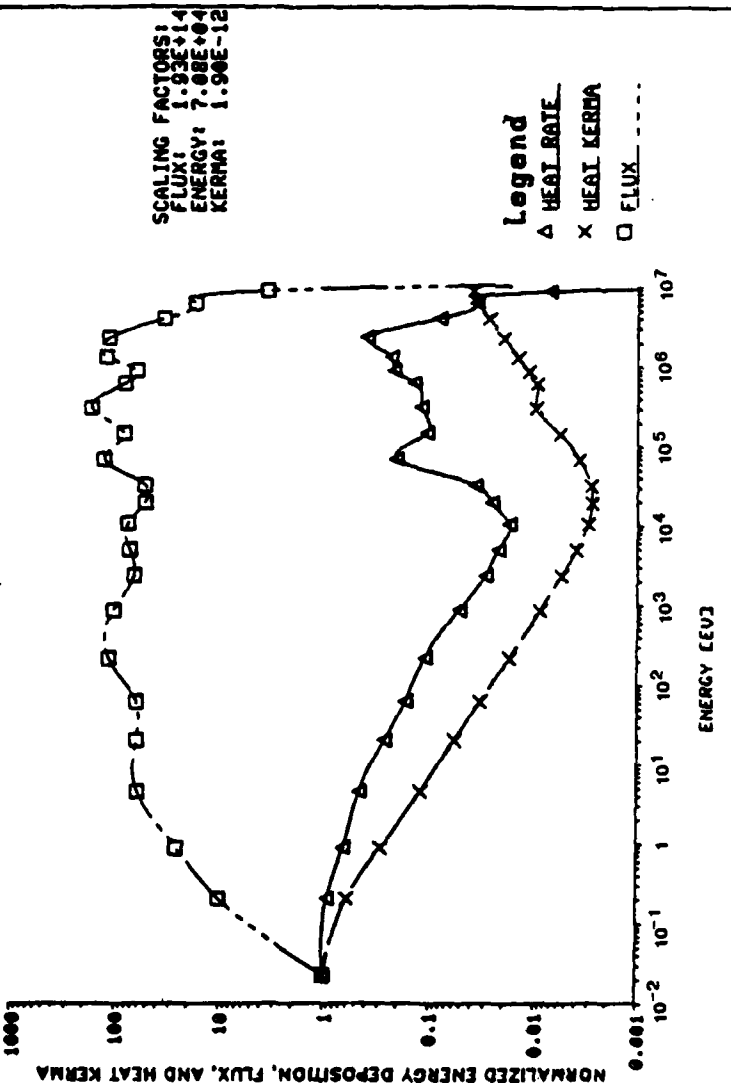


Figure 4.2-6 Energy Deposited in Outer LiH Region for W-LiH(Nat) Shield

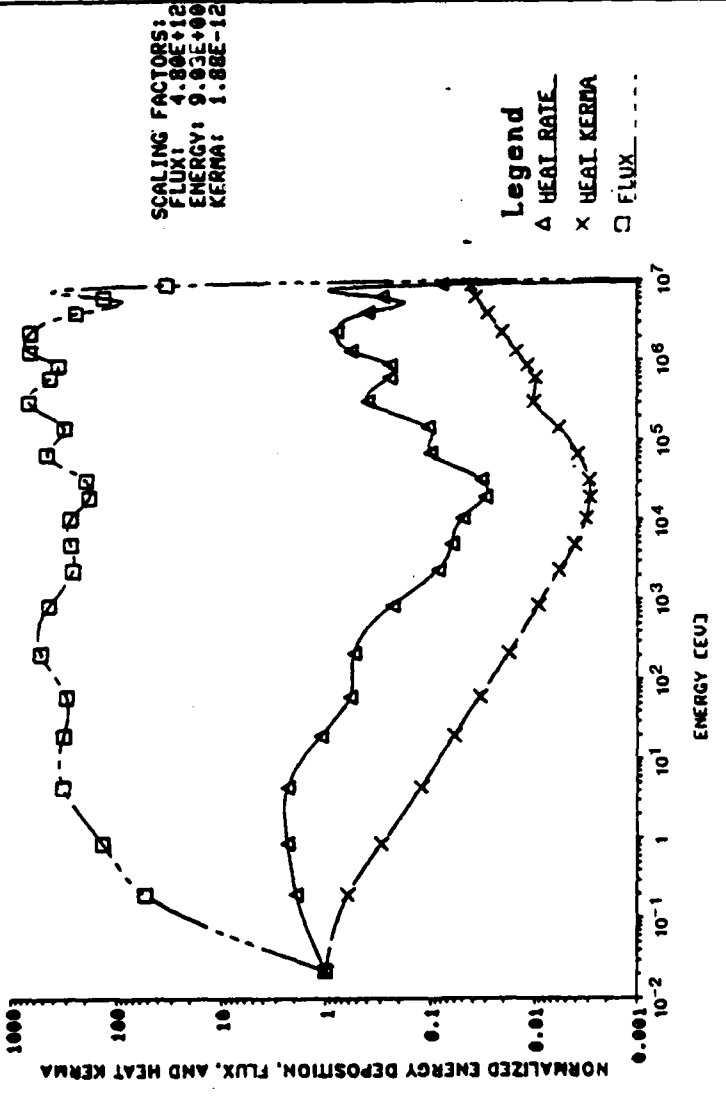


Figure 4.2-7. Flowchart of Temperature Feedback Effects Calculation Methodology for a non-Maxwell Boltzmann Flux Medium

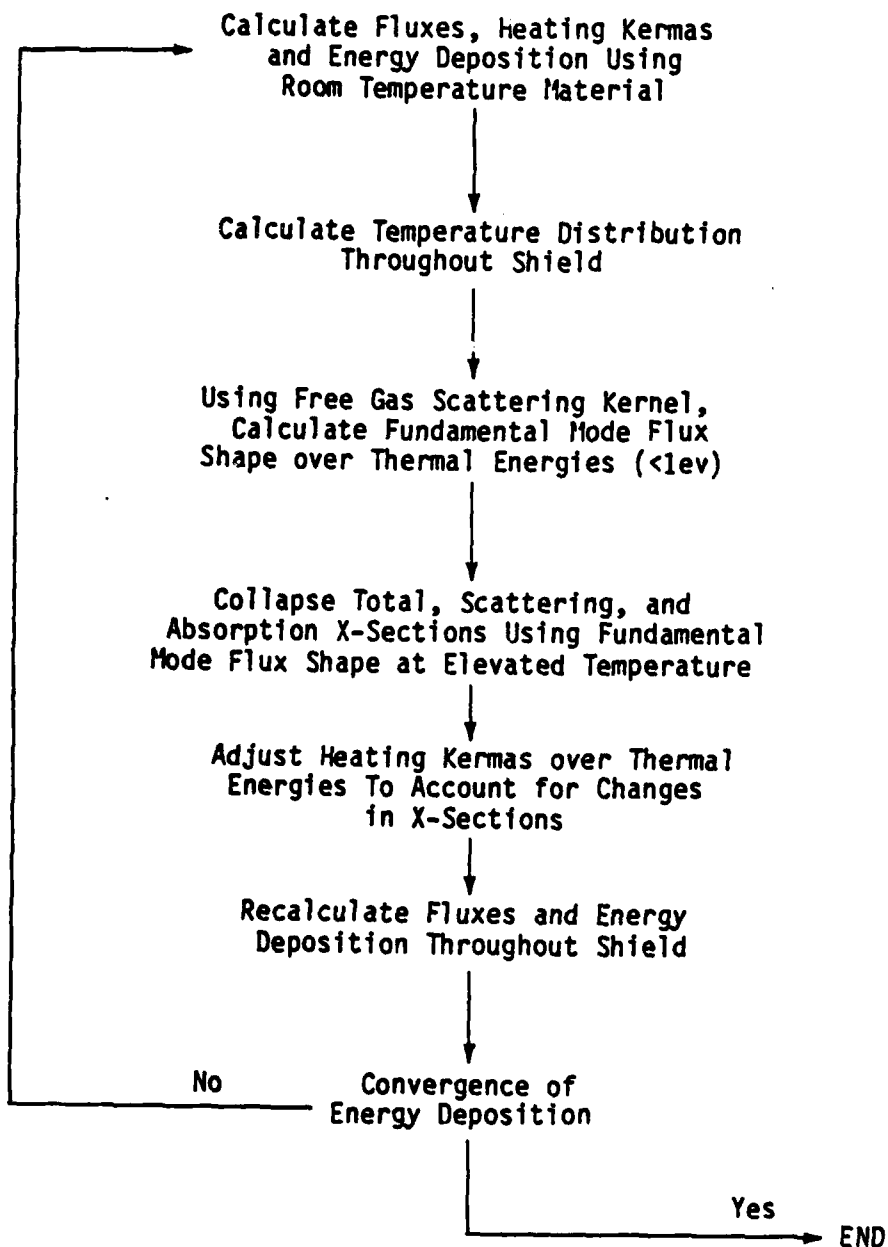


Figure 4.2-8 Flux and Source Over Thermal Energies For LiH(Nat) Temperature of 693.7 K

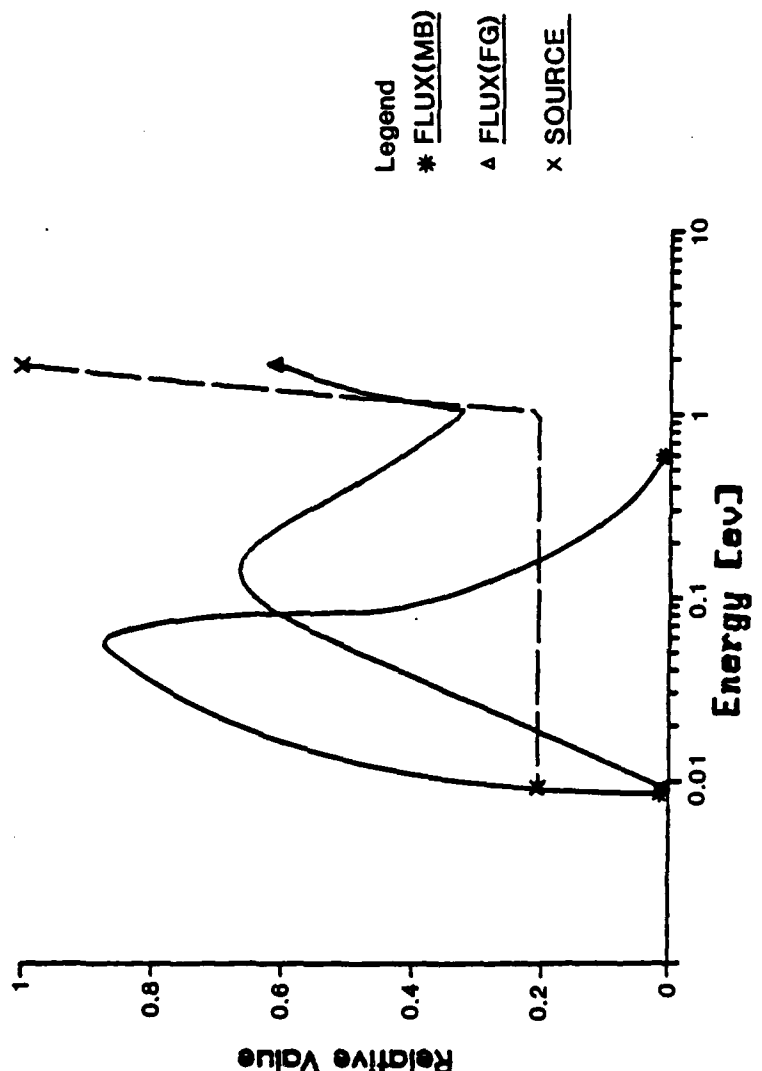


Table 4.2-8. Energy Deposited in a W-LiH(Nat) Shield With Temperature Feedback Effects Included In Cross Sections Using Free Gas Scattering Kernel

| Energy Deposited [kW] | | | | | |
|-----------------------|----------|--------------|-------|-----------|----------------------|
| Zone | Material | H_{γ} | H_n | H_{tot} | |
| 1 | W | 1.751 | .024 | 1.776 | <u>W:</u> |
| 2 | " | 1.434 | .013 | 1.447 | $H_{\gamma} = 3.185$ |
| 3 | LiH(Nat) | .094 | 1.230 | 1.324 | $H_n = .037$ |
| 4 | " | .262 | 1.465 | 1.727 | $H_{tot} = 3.202$ |
| 5 | " | .109 | .054 | .163 | <u>LiH(Nat):</u> |
| 6 | " | .272 | .898 | 1.170 | $H_{\gamma} = 1.593$ |
| 7 | " | .115 | .004 | .119 | $H_n = 6.542$ |
| 8 | " | .416 | 1.160 | 1.576 | $H_{tot} = 6.542$ |
| 9 | " | .127 | .008 | .135 | |
| 10 | " | .208 | .121 | .329 | |
| Total | | 4.778 | 4.977 | 9.765 | |

Legend:

H_{γ} - Energy Deposited by Gammas

H_n - Energy Deposited by Neutrons

$H_{tot} = H_{\gamma} + H_n$

Table 4.2-7. Energy Deposited in a W-LiH(Nat) Shield Using Room Temperature Material and Nuclear Properties

| Energy Deposited [kW] | | | | | |
|-----------------------|----------|--------------|-------|-----------|----------------------|
| Zone | Material | H_{γ} | H_n | H_{tot} | Summary |
| 1 | W | 1.745 | .025 | 1.770 | <u>W:</u> |
| 2 | " | 1.427 | .013 | 1.440 | $H_{\gamma} = 3.172$ |
| 3 | LiH(Nat) | .112 | 1.238 | 1.350 | $H_n = .038$ |
| 4 | " | .312 | 1.478 | 1.790 | $H_{tot} = 3.210$ |
| 5 | " | .129 | .040 | .170 | <u>LiH(Nat):</u> |
| 6 | " | .322 | .887 | 1.209 | $H_{\gamma} = 1.88$ |
| 7 | " | .135 | .003 | .138 | $H_n = 4.911$ |
| 8 | " | .490 | 1.146 | 1.636 | $H_{tot} = 6.797$ |
| 9 | " | .146 | .007 | .153 | |
| 10 | " | .240 | .112 | .352 | |
| Total | | 5.058 | 4.949 | 10.007 | |

Legend:

H_{γ} - Energy deposited by Gammas

H_n - Energy deposited by Neutrons

$$H_{tot} = H_{\gamma} + H_n$$

Table 4.2-6. Upscatter Cross Sections for a LiH(Nat) Medium
at Elevated Temperature Using Free Gas
Scattering Kernel

| Temp[K] | Upscatter Cross Section [cm ⁻¹] | | |
|---------|---|-----------------------|-----------------------|
| | Σ_s^{2+1} | Σ_s^{3+1} | Σ_s^{3+2} |
| 748.3 | 6.08×10^{-4} | 6.67×10^{-5} | 3.33×10^{-2} |
| 693.7 | 5.21×10^{-4} | 4.22×10^{-5} | 3.04×10^{-2} |
| 652.7 | 4.60×10^{-4} | 2.85×10^{-5} | 2.81×10^{-2} |
| 619.7 | 4.13×10^{-4} | 2.01×10^{-5} | 2.62×10^{-2} |
| 605.9 | 3.95×10^{-4} | 1.71×10^{-5} | 2.55×10^{-2} |

Legend:

Σ_s^1 ranges from 1.855 to 0.411 ev

Σ_s^2 ranges from 0.411 to 0.10 ev

Σ_s^3 ranges from 0.10 to 0.00001 ev

to determine the collapsed group differential scattering cross sections. Of particular importance were the upscattering cross sections which are not included in the BUGLE cross section library. Selected values of upscattering cross sections for the LiH(Nat) medium are included in Table 4.2-6. These upscatter cross sections were included in the radiation transport calculation to determine the new energy deposition throughout the shield with temperature feedback effects included in the input. In comparing the differential scatterings of Table 4.2-6 with the cross sections of Figures 4.2-9 through 4.2-11, one observes that the largest upscatter cross section is about two orders of magnitude less than the absorption and scattering cross sections for LiH at thermal energies. Hence, upscattering effects would not be expected to be significant.

Using both room temperature and temperature adjusted nuclide densities, cross sections and heating kermas, the new energy deposition values were generated with the radiation transport code using the coarse mesh core / fine mesh shield model. The energy deposition throughout the shield by zone are included in Table 4.2-7 for room temperature properties and in Table 4.2-8 for elevated temperatures using the free gas scattering model. In comparing the results of Tables 4.2-7 and 4.2-8, it is somewhat surprising that the room temperature case has only .13 kW less energy deposited than the elevated temperature case, for a difference of 1.3%. This was a relatively insignificant difference when one considers how thermal absorption cross sections were shown to decrease with temperature anywhere from 3.7 to 41% (see Table 4.2-5), and all cross sections (total, scattering, and absorption) decreased over all energy due to a decrease

the neutron energy increased to the thermal energy threshold (~1 ev), the opposite was true and the temperature effect on absorption was more pronounced for the non-M-B medium. The decrease in absorption in the MB medium above 0.1 ev was due to density decreases in the LiH as the temperature increased. Thus, for the temperature range of 600 K to 750 K, a decrease in absorption of about 3.7% to 6.8% was due to temperature effects on material density for LiH. Any additional changes in group cross sections above the 3.7% to 6.8% in the thermal energy range was attributable to the shift in the fundamental mode flux shape over energy at the higher temperatures from the original flux shape used in the original group collapse of the cross section library.

Recall that the original 59 BUGLE cross section set was reduced to 38 groups with a weighting based on the average flux shape. The flux weighting spectrum was determined from the criticality calculation of the core and reflector system (fine group core) without the shield. Therefore, the further decrease in absorption cross sections at thermal energies above those due to density decreases, occurred because of spectral hardening resulting from the large absorption of Li-6. Without the presence of Li-6, some spectral softening will occur which reduces the temperature effect on absorption. This, in turn, leads to the well known conclusion that in a medium in which scattering effects far exceed absorption, the effect of temperature on cross section will be 2nd order (at most) and have negligible impact on the cross section magnitudes.

In addition to the temperature dependent absorption scattering, and total cross sections, the free gas scattering kernel was also used

Table 4.2-5. Comparison of Differences in Collapsed Group Absorption Cross Section of LiH(Nat) Based on Free Gas Scattering Kernel and Maxwell Boltzmann Model at Elevated Temperatures

| Temp[k] | Zone | Eg = 1.855 to 0.411ev | | | | | | Eg = 0.411ev to 0.10ev | | | | | | Eg = 0.10ev to 0.00001ev | | | | | |
|---------|------|-----------------------|-----------------|--------|-----------------|--------|-----------------|------------------------|--------|-----------------|--------|-----------------|-----------------|--------------------------|-----------------|--------|-----------------|-----------------|--------|
| | | Σ_a^{RT} | Σ_a^{FG} | % Diff | Σ_a^{MB} | % Diff | Σ_a^{RT} | Σ_a^{FG} | % Diff | Σ_a^{MB} | % Diff | Σ_a^{RT} | Σ_a^{FG} | % Diff | Σ_a^{MB} | % Diff | Σ_a^{RT} | Σ_a^{FG} | % Diff |
| 748.3 | 3 | .7108 | .6041 | -15.0 | .6626 | -6.8 | 1.549 | 1.293 | -16.5 | 1.444 | -6.8 | 4.177 | 2.888 | -30.9 | 2.452 | -41.3 | | | |
| 693.7 | 5 | .7108 | .6116 | -14.0 | .6712 | -5.6 | 1.549 | 1.311 | -15.6 | 1.463 | -5.6 | 4.177 | 2.938 | -29.4 | 2.563 | -38.6 | | | |
| 652.7 | 7 | .7108 | .6172 | -13.2 | .6776 | -4.7 | 1.549 | 1.324 | -14.5 | 1.477 | -4.7 | 4.177 | 2.976 | -29.7 | 2.653 | -36.5 | | | |
| 650.1 | 4 | .7108 | .6172 | -13.2 | .6776 | -4.7 | 1.549 | 1.324 | -14.5 | 1.477 | -4.7 | 4.177 | 2.976 | -28.7 | 2.653 | -36.5 | | | |
| 640.3 | 9 | .7108 | .6187 | -13.0 | .6794 | -4.4 | 1.549 | 1.328 | -14.3 | 1.481 | -4.4 | 4.177 | 2.988 | -28.5 | 2.679 | -35.9 | | | |
| 619.7 | 6 | .7108 | .6215 | -12.6 | .6826 | -4.0 | 1.549 | 1.334 | -13.9 | 1.488 | -4.0 | 4.177 | 3.008 | -28.0 | 2.726 | -34.7 | | | |
| 617.4 | 10 | .7108 | .6218 | -12.5 | .6829 | -3.9 | 1.549 | 1.335 | -13.8 | 1.488 | -3.9 | 4.177 | 3.010 | -27.9 | 2.731 | -34.6 | | | |
| 605.9 | 8 | .7108 | .6235 | -12.3 | .6848 | -3.7 | 1.549 | 1.339 | -13.6 | 1.493 | -3.7 | 4.177 | 3.022 | -27.7 | 2.761 | -33.9 | | | |

Legend

Σ_a^{RT} : LiH(Nat) Group Absorption Cross Section at Room Temperature, cm^{-1}

Σ_a^{FG} : LiH(Nat) Group Absorption Cross Section at Elevated Temperature Using Free Gas Scattering Kernel (for non-MB medium), cm^{-1}

Σ_a^{MB} : LiH(Nat) Group Absorption Cross Section at Elevated Temperature Using Maxwell Boltzmann Model (for MB medium), cm^{-1}

% difference based on percent change from group cross section at room temperature

The flux shape in Figure 4.2-8 is quite interesting. In solving for the flux from the radiation transport code, FEMP2D, the three group fluxes below 1.855 ev showed only a monotonic decrease in magnitude with decreasing energy. This behavior was seen in Figures 4.2-5 and 4.2-6 for LiH(Nat). However, as the resolution of the solution over energy was increased dramatically from 3 groups to 100 groups, one actually observed a Maxwellian type peak in the flux at very low energy. In comparing the non-M-B flux for LiH(Nat) with a pure M-B flux shape, we see an expected strong shift toward higher energy. The M-B flux at a temperature of 693.7 K peaks at 0.06 ev and effectively decreases to zero by 0.45 ev; whereas, the free gas derived thermal flux peaks at a slightly higher 0.105 ev, with a relative magnitude weighted heavily toward the upper part of the thermal energy range.

With a stronger shift toward higher energy for the thermal flux, one might expect significantly different group averaged cross sections at elevated temperatures than the M-B temperature feedback equation provided. Figures 4.2-9, 10 and 11 plot the group collapsed absorption, scattering, and total cross sections for LiH(Nat) using the free gas scattering kernel. To gain an understanding of how temperature affects cross section of the non-M-B medium, Table 4.2-5 compares the differences in absorption cross sections of the LiH(Nat) medium using the free gas scattering kernel and the Maxwell Boltzman model at elevated temperature with the absorption cross section at room temperature.

From Table 4.2-5, one observes that the reduction in absorption cross section caused by elevated temperature was less in a non-M-B medium at very low energies (<0.1 ev) than in a M-B medium. However,

Figure 4.2-11 Effect of Temperature on Cross Sections of LiH(Nat) Using Free Gas Scattering Kernel for Energy Range of 0.1113 ev to 0.00001 ev

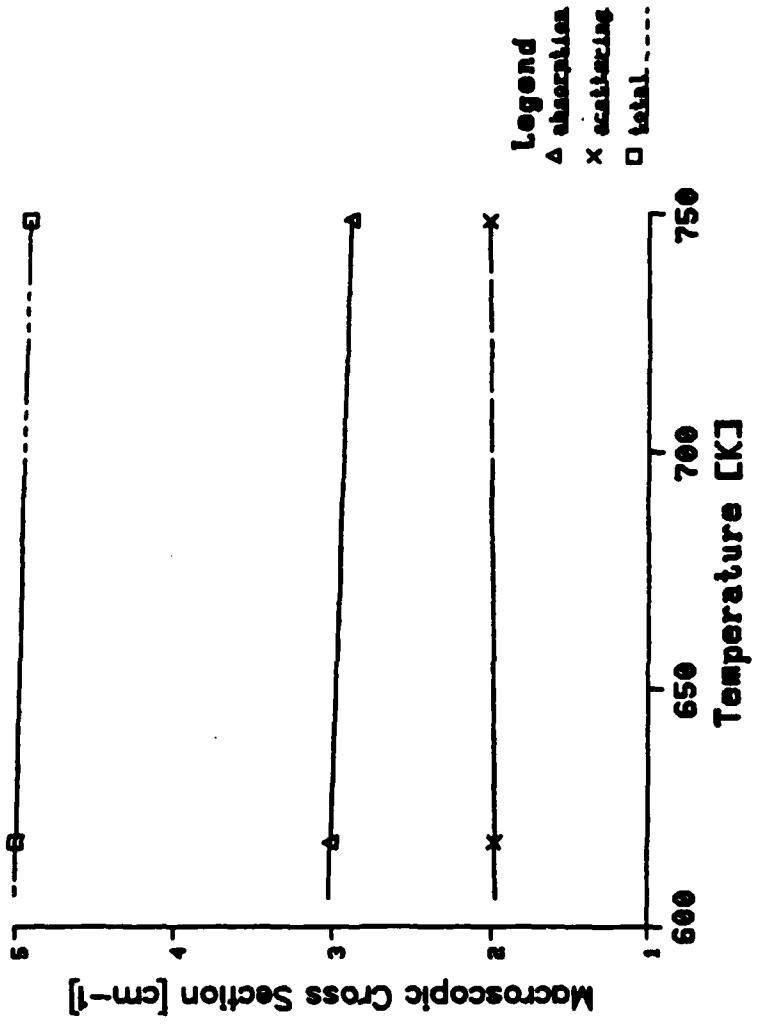


Figure 4.2-10 Effect of Temperature on Cross Sections of LiH(Nat) Using Free Gas Scattering Kernel for Energy Range of 0.411 ev to 0.1113 ev

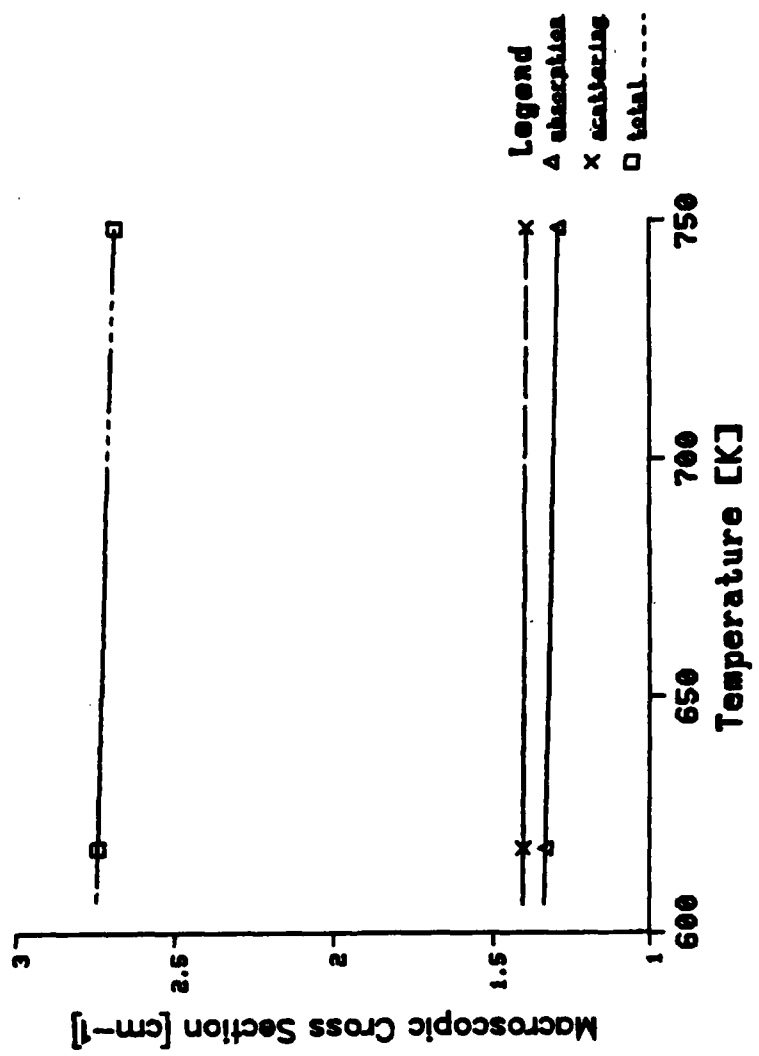
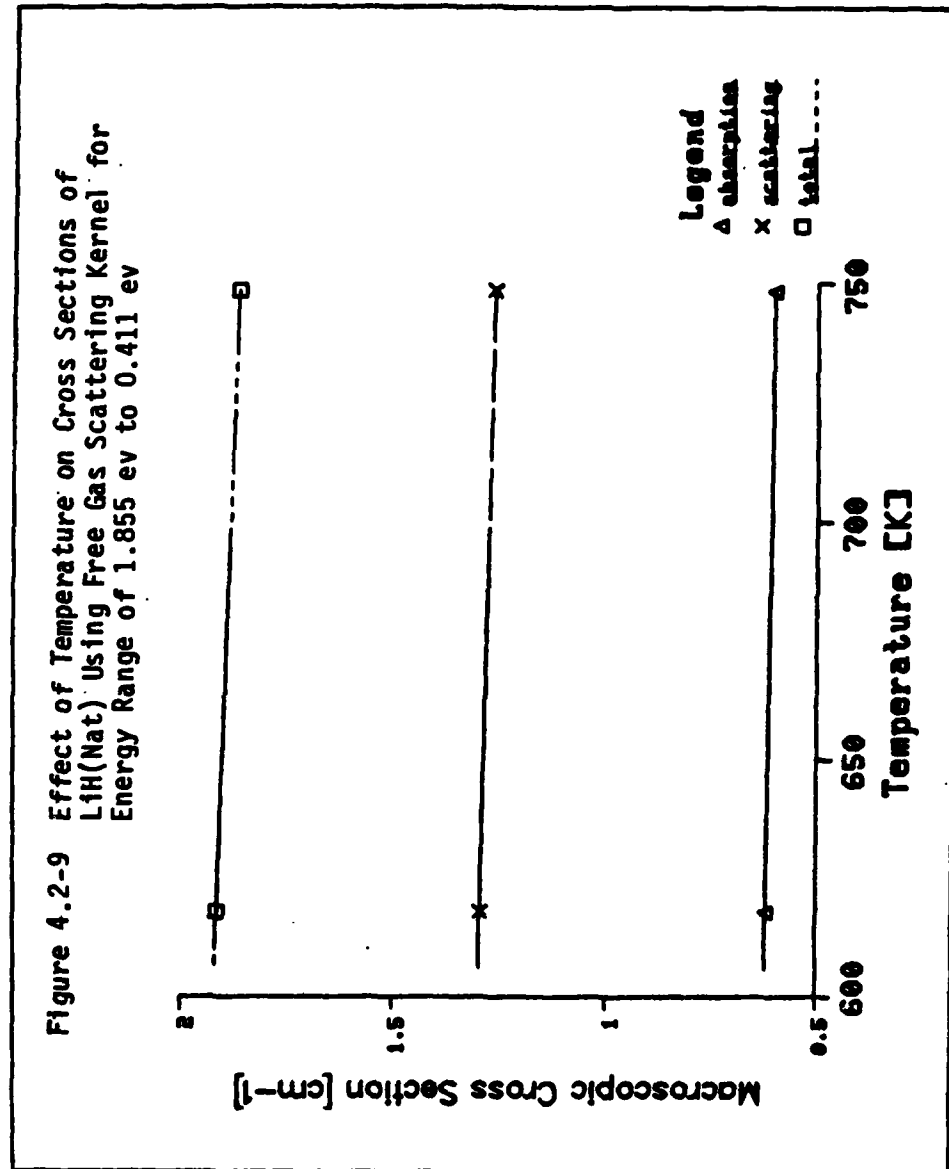


Figure 4.2-9 Effect of Temperature on Cross Sections of LiH(Nat) Using Free Gas Scattering Kernel for Energy Range of 1.855 ev to 0.411 ev



medium. For a non-M-B medium, the simple, analytic expression of Equation 3.3-22 is not appropriate for determining elevated temperature cross sections. Instead, the temperature dependent flux shape over thermal energies (< 1 ev) must be calculated and used as the weighting function in the collapse of multi-group cross sections for use in the radiation transport calculation. Figure 4.2-7 flowcharts the method of analysis used to evaluate the non-M-B medium.

The 24 neutron group cross section library used in the radiation transport calculation has three energy groups below 1.855 ev, which served as the thermal energy threshold throughout this analysis. The lowest bound energy in the BUGLE library is 10^{-5} ev. Using the free gas model, the thermal flux shape was determined based on a 100 group subdivision over the range of 1.855 ev to 10^{-5} ev. The non-symmetric system of equations as identified by Equations 3.3-43 was solved for each zone of Figure 4.2-2 containing LiH(Nat) using an average temperature, determined by a spatial weighting of all elemental temperatures for a given zone.

An example of the temperature dependent zone flux and source is plotted in Figure 4.2-8. The source curve vividly shows the effects of neutron downscatter from higher energies by the heavier lithium atoms and the lighter hydrogen atoms. From Equation 3.3-40, below an energy of $\alpha_{Li-6} E_{th}$ (where α is the collision parameter for Li-6) the only source of neutrons from higher energies is due to downscattering by hydrogen. Because the collision parameter for hydrogen is zero, the source term below $\alpha_{Li-6} E_{th}$ is a constant.

and lithium atoms. The net result was that the relative contribution of thermal energy neutrons to total energy deposition was reduced in the outer regions of the shield. Thus, temperature effects on energy deposition were not felt even close to the edge of the shield (where leakage effects come into play).

In conclusion, the decrease in absorption cross section as temperature increases for a $1/v$ medium characterized by a Maxwell Boltzmann neutron flux shape was accompanied by an increase in flux of the same proportion. The net result was that the absorption reaction rate remained constant at elevated temperature. This, in turn, resulted in a total decoupling of the internal heat generation and temperature feedback for a $1/v$ medium in which absorption is the dominant mechanism for energy deposition.

4.2.3 Temperature Effects on Energy Deposition in a Non-M-B Medium. In a strongly absorbing medium, the departure of the flux from a M-B shape can be extreme. For such a medium, the conclusions of the previous section may not be valid. The theoretical framework necessary to examine the temperature effect on energy deposition of a non-M-B medium was discussed in detail in Section 3.1. The free gas scattering kernel was used to generate energy transfer cross sections for determining temperature feedback effects. This section presents the results of applying the free gas kernel to the sample shield consisting of W-LiH(Nat) to quantify the effects of temperature on energy deposition.

The methodology required to examine temperature feedback in a non-MB medium differs from that presented in Figure 4.2-3 for a M-B

energy deposition due to neutron interactions occur. The outer LiH region of Figure 4.2-6 includes zones 9 and 10, or a final 29 cm of the shield. The values for all three figures have been normalized to the respective figures lowest energy group value.

From Figure 4.2-4, the hardness of the neutron spectrum is readily apparent, with the neutron flux almost four orders of magnitude less in the thermal energy range than in the Mev range. The resonance peak in tungsten at about 20 ev is also quite obvious from this plot. While the cross sections were not processed for doppler broadening in this analysis, the contributions to energy deposition from neutron interactions below 41 ev were less than 2% of the neutron heating in the tungsten. Thus, the consequences of not processing this resonance to account for self shielding effects were negligible.

Shifting one's focus to Figure 4.2-5, one immediately observes the expected softening of the flux in the hydride material. While the neutron flux remains relatively hard (2 orders of magnitude larger flux at 1 Mev than at thermal energy), the contribution to energy deposition from thermal energy neutrons was significantly increased due to the higher heating kerma at low energies caused by the Li-6 absorption effect. While thermal energy deposition was significant in this region, we have already seen that the absorption reaction rate remains constant due to the $1/v$ cross section and the short neutron mean free path resulting from Li-6 presence.

The outer LiH region of Figure 4.2-6 showed a hardening of the neutron spectrum farther into the LiH. This occurred because the slower neutrons had been absorbed early into the LiH at a rate higher than the thermalization caused by elastic scatterings from the hydrogen

To better understand why temperature had no effect on energy deposition in the M-B medium, the reaction rates for each zone are included in Table 4.2-4. From this data, one sees that as the thermal absorption cross section decreased at elevated temperatures, the flux experienced a corresponding increase in magnitude. Summing over the entire LiH portion of the shield, the absorption reaction rate changed by only 0.26% with the temperature effect on thermal absorption included. Since the thermal group ($\phi < 0.1\text{ev}$) accounted for only 10% of the total energy deposited in the shield, the temperature effect on energy deposition proved to be negligible.

Worthy of note is the fact that absorption reaction rate changed considerably in the tungsten at elevated temperatures, with an increase of 27% in the hotter portion (zone 1) and a decrease of 10% in the cooler, outer portion (zone 2) of the shield. This effect is attributable to the substantially larger mean free path of the thermal neutron in tungsten (1.11 cm) than in the LiH (0.128 cm). With a total thickness of 4 cm, leakage became a factor in the W which was not accounted for in the infinite medium M-B calculation of Equation 3.3-22. However, as noted earlier, the energy deposition due to neutron interactions in the tungsten is so small (and this was over all neutron energies) that the temperature effect on total energy deposition is not felt at all.

To put the contribution of neutron interactions at thermal energies into a clearer perspective, Figures 4.2-4 through 4.2-6 plot the flux, heat rate, and heating kerma for selected regions of the shield. The tungsten of Figure 4.2-4 includes zones 1 and 2. The inner LiH region of Figure 4.2-5 includes zones 3 through 8, where 90% of the

Table 4.2-9. Effects of Elevated Temperature on Energy Deposition for W-LiH (Nat) Shield

| Volumetric Heat Generation (W/cm ³) | | | | |
|---|--------------|-------------------------------|----------------------|---------------------------------|
| <u>z, cm</u> | <u>r, cm</u> | <u>q''', Room Temperature</u> | <u>q''', Density</u> | <u>q''', Density/X-sections</u> |
| 51.0 (Core-W Interface) | 0.0 | 1.023 | 1.023 | 1.024 |
| | 9.0 | .0796 | .0796 | .0797 |
| | 18.3 | .0467 | .0467 | .0467 |
| | 27.5 | .0157 | .0157 | .0157 |
| 55.0 (W-LiH Interface) | 0.0 | .1333 | .1188 | .1222 |
| | 9.0 | .1210 | .1077 | .1106 |
| | 18.3 | .0700 | .0625 | .0641 |
| | 27.5 | .0261 | .0236 | .0245 |
| 65.9 (10.9 cm into LiH) | 0.0 | .0143 | .0157 | .0166 |
| | 9.0 | .0131 | .0142 | .0151 |
| | 18.3 | .0096 | .0100 | .0106 |
| | 27.5 | .0074 | .0072 | .0074 |

Legend:

q''', Room temperature - No temperature feedback effects considered on densities or cross sections

q''', Density - Only temperature feedback effects on densities considered

q''', Density/X-section - Temperature feedback effects on densities and cross sections considered

in nuclide density at higher temperature. (The decrease in material density of LiH from 293 K to 650 K is about 5.8%) The comparison of total energy deposition might lead one to conclude that the maximum and minimum temperatures of the LiH were not significantly in error by neglecting temperature effects on material and nuclear properties. However, before making such bold assertions additional data must be presented.

Volumetric heating rates as a function of radial position are given in Table 4.2-9 for the core-W boundary, the W-LiH boundary, and for 10.9 cm into the LiH. From this table, the three sets of internal heat generation represent varying approximations in considering temperature feedback effects on energy deposition. The q''' , Room Temp data set represents heating rates calculated with room temperature properties, in which no temperature feedback on either material densities or thermal cross sections were considered. The q''' , Density heating rates were calculated with temperature dependent number densities. Again, no temperature effects on thermal microscopic cross sections were included. The final set of heating rates, q''' , Density/X-Sections were calculated with temperature feedback effects on both density and thermal microscopic cross sections.

From Table 4.2-9, neglecting all temperature effects on energy deposition results in an overestimation of internal heat generation ranging from 8.7% to 6.1% along the radial plane of the shield at the W-LiH interface. Approximately 11 cm into the LiH portion of the shield, neglecting temperature effects results in an underestimation of the heat generation ranging from 16.3 % to 0 % as the shield radius increases. However, because the magnitude of the energy deposition had

decreased by almost an order of magnitude within this first 11 cm of the LiH, the differences in energy deposition at a relatively short distance into the shield were not significant.

From the comparison of q''' , Density and q''' , Density/X-Sections data sets of Table 4.2-9, it is seen that neglecting temperature effects on thermal microscopic cross sections results in an underestimation of energy deposition throughout the shield. While the differences are not great, ranging from -2.8% to -3.7% (at the W-LiH boundary) and -5.4% to -2.7% (at 11 cm into the shield), the increase in energy deposition due to temperature effects on thermal cross sections is not intuitively obvious. However, recalling from Table 4.2-5, the lowest group ($E_n < .1$ ev) absorption cross section had a smaller decrease from room temperature using the free gas model (for a non-M-B medium) than the M-B medium. Since the absorption reaction rate for an M-B medium was not affected by temperature, it is obvious that the temperature absorption reaction rate for the non M-B medium will be higher when temperature effects on cross section are considered. To reinforce this effect, the two higher thermal energy groups (.1.855 to 0.411 ev and .411 to .1 ev) also experienced a larger reduction in absorption cross section with elevated temperature. Thus, more neutrons escape this energy range and become available for capture in the lowest group, where the larger heating kerma results in more energy deposition. This effect was verified with the larger absorption reaction rate observed for the radiation transport results with complete temperature feedback, when compared with results from temperature effects on number densities-only run.

When spatial dependence was removed by integrating the volumetric heat generation over the shield's volume, the results already presented in Tables 4.2-7 and 4.2-8 were obtained. Using the energy deposition represented by the data of these tables, the effect of neglecting temperature feedback effects on material and nuclear properties resulted in an overestimation of maximum temperature of 15 K, or ~2.2% of the local temperature value. The minimum temperature of the shield was overestimated by ~11 K, or ~2.5% of the local temperature value. When including temperature effects on the nuclide density but neglecting cross section temperature feedback (on both heating kerma and radiation transport), the energy deposition throughout the shield varied by only 0.4%. This difference resulted in only ~3 K (0.2%) overestimation of maximum and minimum temperature of the shield. Thus, we move a bit closer to concluding that there is a weak coupling between temperature and energy deposition in an SP-100 baseline design radiation shield.

To gain a better understanding of why the temperature effect on energy deposition was so slight, the energy deposited by neutrons throughout the LiH is recorded in Table 4.2-10. The flux, heating kermas, and energy deposited for the 24 neutron groups are listed for each group's average energy value. The % TOT column represents the contribution of the group's energy deposition to the total energy deposition for all neutrons. The CUM % represents the cumulative total of energy deposited, starting with the highest energy group. All fluxes, kermas, and energy deposition values are normalized to their respective lowest energy group value ($E < 0.1$ ev). From Table 4.2-10, one observes that over half the energy deposited by neutrons occurred at energies less than ~40 ev and one-quarter of the neutron energy occurred below

TABLE 4.2-10: Fluxes, Heating Kerma and Energy Deposition for Neutrons in the LiH(Nat) Portion of a W-LiH(Nat) Shield (All Values Normalized to Repetitive Lowest Energy Group)

| GROUP | AVERAGE GROUP | | ENERGY DEPT | %TUT | CUM % |
|-------|------------------|------------|-------------|------------|-----------|
| | ENERGY | FLUX | | | |
| 1 | 0.1316E+08 | 0.3356E-06 | 0.3818E-01 | 0.3673E-08 | 0.0 0.0 |
| 2 | 0.8607E+07 | 0.3114E+01 | 0.3512E-01 | 0.3135E-01 | 0.3 0.3 |
| 3 | 0.6065E+07 | 0.1527E+02 | 0.3258E-01 | 0.1426E+00 | 1.4 1.7 |
| 4 | 0.3867E+07 | 0.3036E+02 | 0.2493E-01 | 0.2169E+00 | 2.1 3.8 |
| 5 | 0.2231E+07 | 0.1012E+03 | 0.1804E-01 | 0.5230E+00 | 5.1 9.0 |
| 6 | 0.1287E+07 | 0.1075E+03 | 0.1325E-01 | 0.4083E+00 | 4.0 13.0 |
| 7 | 0.8627E+06 | 0.5524E+02 | 0.1038E-01 | 0.1644E+00 | 1.6 14.6 |
| 8 | 0.6080E+06 | 0.7113E+02 | 0.8708E-02 | 0.1775E+00 | 1.7 16.4 |
| 9 | 0.3019E+06 | 0.1492E+03 | 0.8900E-02 | 0.3805E+00 | 3.7 20.1 |
| 10 | 0.1426E+06 | 0.7270E+02 | 0.5215E-02 | 0.1087E+00 | 1.1 21.2 |
| 11 | 0.6735E+05 | 0.1125E+03 | 0.3373E-02 | 0.1088E+00 | 1.1 22.3 |
| 12 | 0.3143E+05 | 0.4592E+02 | 0.2603E-02 | 0.3426E-01 | 0.3 22.6 |
| 13 | 0.1906E+05 | 0.4537E+02 | 0.2536E-02 | 0.3298E-01 | 0.3 22.9 |
| 14 | 0.1033E+05 | 0.6701E+02 | 0.2789E-02 | 0.5358E-01 | 0.5 23.5 |
| 15 | 0.4880E+04 | 0.6358E+02 | 0.3569E-02 | 0.6506E-01 | 0.6 24.1 |
| 16 | 0.2305E+04 | 0.5778E+02 | 0.5024E-02 | 0.8320E-01 | 0.8 24.9 |
| 17 | 0.8480E+03 | 0.9062E+02 | 0.8134E-02 | 0.2113E+00 | 2.1 27.0 |
| 18 | 0.2144E+03 | 0.1007E+03 | 0.1574E-01 | 0.4542E+00 | 4.5 31.5 |
| 19 | 0.6144E+02 | 0.5499E+02 | 0.2995E-01 | 0.4721E+00 | 4.6 36.1 |
| 20 | 0.1994E+02 | 0.5511E+02 | 0.5263E-01 | 0.8313E+00 | 8.2 44.3 |
| 21 | 0.4449E+01 | 0.5417E+02 | 0.1091E+00 | 0.1694E+01 | 16.7 61.0 |
| 22 | 0.8762E+00 | 0.2294E+02 | 0.2344E+00 | 0.1541E+01 | 15.2 76.1 |
| 23 | 0.2034E+00 | 0.1039E+02 | 0.4785E+00 | 0.1425E+01 | 14.0 90.2 |
| 24 | 0.2250E-01 | 0.1000E+01 | 0.1000E+01 | 0.1000E+01 | 9.8 100.0 |

the thermal threshold (1.855 ev). While the lowest energy group flux was over two orders of magnitude less than the 673 Kev group flux and less than one-third of the 8.6 Mev group flux, almost 10% of the energy deposition occurred within this group (<.1 ev). The strong contribution of the $1/v$ absorption cross section of Li-6 accounted for this result.

As shown earlier, energy deposition in LiH(Nat) at low energies is dominated by the (n, α) reaction in Li-6. Furthermore, the effect of temperature on microscopic neutron cross sections was felt only by cross sections below the thermal threshold energy (1.855 ev for the present neutron cross section library). The other effect of temperature was the decrease in nuclide densities due to the decrease in material density of the LiH, as temperature increases. These two effects on energy deposition can be expressed analytically as:

$$\% \Delta H_{\text{tot}} = \% \Delta H_{\text{tot}}^N = \% \Delta H_{\text{tot}}^D \quad (4.2-1)$$

where:

$\% \Delta H_{\text{tot}}$ = % change in total energy deposited due to all temperature effects

$$= (H_{\text{tot}}^T - H_{\text{tot}}^{RT}) / H_{\text{tot}}^T \times 100\%$$

$\% \Delta H_{\text{tot}}^N$ = % change in $\% \Delta H_{\text{tot}}$ due to temperature effects on thermal neutron cross sections

$$= (H_{\text{tot}}^T - H_{\text{tot}}^D) / H_{\text{tot}}^T \times 100\%$$

$\% \Delta H_{\text{tot}}^D$ = % change in $\% \Delta H_{\text{tot}}$ due to temperature effects on number densities

$$= (H_{\text{tot}}^D - H_{\text{tot}}^{RT}) / H_{\text{tot}}^D \times 100\%$$

H_{tot}^{RT} = total energy deposited [kW] using room temperature properties

H_{tot}^D = total energy deposited [kW] using elevated temperature number densities, but neglecting temperature effects on cross sections

H_{tot}^T = total energy deposited [kW] including temperature effects on number densities and cross sections.

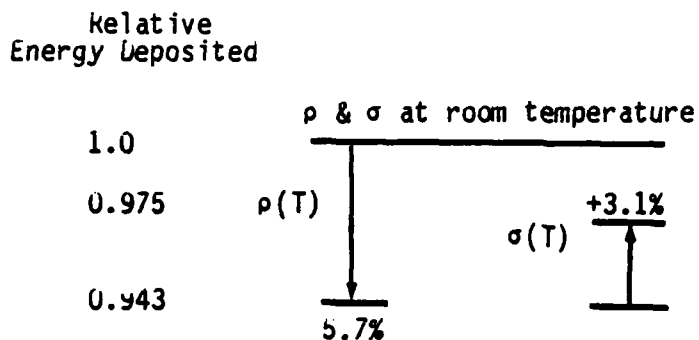
The difference of 2.48% between total energies deposited of Tables 4.2-7 and 4.2-8 represents the complete temperature effect on energy deposition for a W- LiH(Nat) shield. To quantify the portion of this difference due to temperature effects on cross sections (% ΔH_{tot}^N of Equation 4.2-1), the radiation transport calculation was also run with temperature dependent number densities, but no temperature feedback effects on cross sections. The total energy deposited was 9.474 kW, or a decrease of 3.0% from the full temperature effect deposition value of 9.765 kW. These results are summarized in Table 4.2-11 and Figure 4.2-12.

Table 4.2-11: Results of Temperature Effects on Energy Deposition for a W-LiH(Nat) Shield

| Total Energy deposited [kW] | | | %Change | | |
|-----------------------------|-------------|-------------|----------------------|----------------------|--------------------|
| H_{tot}^{RT} | H_{tot}^D | H_{tot}^T | % ΔH_{tot}^N | % ΔH_{tot}^D | % ΔH_{tot} |
| 10.006 | 9.474 | 9.765 | +3.22 | -5.69 | -2.48 |

From Table 4.2-11 and Figure 4.2-12, several important conclusions can be derived. The temperature effects on energy deposition due to density decreases were more significant than those due to decreases in thermal microscopic cross sections in LiH(Nat) for the temperature range of an SP-100 shield. Considering only temperature feedback

Figure 4.2-12 Results of Temperature Feedback Effects on Energy Deposition in a W-LiH(Nat) Shield



Legend:

$\rho(T)$ ≡ Temperature Dependent Density
 $\sigma(T)$ ≡ Temperature Dependent Cross Sections

effects on number densities results in an underestimation of the total energy deposition. The effect of temperature feedback on thermal microscopic cross sections was to increase the energy deposition due to the increase in the absorption reaction rates. This effect somewhat offsets the decrease in total energy deposition due to density decreases.

The net result is that the total energy deposited in an W-LiH(Nat) shield for an SP-100 type reactor is decreased by only a few percent due to temperature feedback effects on number densities and thermal neutron microscopic cross sections. For a shield in which the total energy deposited is on the order of 10 kW, the 2-3% change in energy deposition in the shield will not appreciably change the temperature distribution. However, for a reactor operating in the multi-megawatt range, a 2-3% change in energy deposition could possibly result in a

significant temperature change in the shield. (Energy deposition is roughly 6% of the total reactor thermal power.) Although, the temperature feedback effects on energy deposition have been shown not to be a major design consideration in engineering analysis of an SP-100 reactor shield, these results should not be taken as universally applicable to any shield design.

5.0 APPLICATION TO SP-100 SHIELD DESIGN

Having shown the limited effect of temperature on energy deposition in a shield comprised of tungsten and lithium hydride at SP-100 power levels ($\sim 1.66 \text{MW}_{\text{th}}$), the coupling of radiation transport and temperature was investigated. The need for layering the shield at high core power level was recorded in the later design of the SNAP program. However, these optimizations were based on radiation dosage requirements without regard to thermal considerations. The results of this section are intended to address this gap in our understanding of the space reactor shield design.

The earlier results regarding temperature effects on energy deposition can be considered as microscopic phenomenological coupling; whereas, the coupling effects due to the layering configuration presented in this section may be considered as macroscopic feedback effects. To examine the macroscopic effects, several different shield configurations were analyzed. The details of each configuration are included in Table 5.1-1. The thickness of tungsten is decreased somewhat as the gamma layer is moved back into the shield in order to maintain the same mass of tungsten for all configurations.

The key geometric parameters for shield configurations 1 and 2 (W located at front of shield) were already presented in Figure 4.2-2. The only difference between these designs was the substitution of LiH (Depl) for LiH(Nat) in the region extending from the W-LiH interface to the back portion of the shield which faces the thermoelectric conversion panels ($z=97.67 \text{ cm}$). The most important geometric parameters for shield configurations 3 and 4 (W located 13.4 cm into shield) are included in Figure 4.1-1.

Table 5.1-1: Shield Configurations Used in Analysis of Layering Effects on Radiation Transport-Temperature Distribution

| # | <u>Configurations</u> | Shield Centerline Thickness, cm | | |
|---|-----------------------|---------------------------------|------------------|---------------------------|
| | | <u>W⁽¹⁾</u> | <u>LiH(Dep1)</u> | <u>LiH(Nat)</u> |
| 1 | W-LiH(Nat) | 4.0 | --- | 71.0 |
| 2 | W-LiH(Dep1)-LiH Nat) | 4.0 | 42.7 | 28.3 |
| 3 | LiH(Nat)-W-LiH(Nat) | 3.86 | --- | 13.4/57.74 ⁽²⁾ |
| 4 | LiH(Dep1)-W-LiH(Nat) | 3.86 | 13.4 | 57.74 |

Notes:

1. All W thicknesses tapered to 2 cm at the radiative surface of the shield.
2. Thickness before/after the W layer.

In analyzing the shield configurations of Table 5.1-1, the complete radiation transport temperature feedback effects (densities and thermal cross sections) for the non- M-B LiH(Nat) portion of each shield were incorporated into these results. In addition, a 1-D transport calculation of the reactor and shield assembly was performed to estimate the neutron and gamma fluences at the 25 meter dose plane. After the final temperature distribution was determined, the thermal stresses and strains were calculated for the most promising shield design. These results are presented in the following sections.

5.1 Neutron and Gamma Fluences at 25 m Dose Plane. To gain an understanding of the effectiveness of the shield configurations on dosage, a P_{15} transport calculation was performed using the 1-D version of FEMP. The higher order Legendre terms in the expansion of the flux

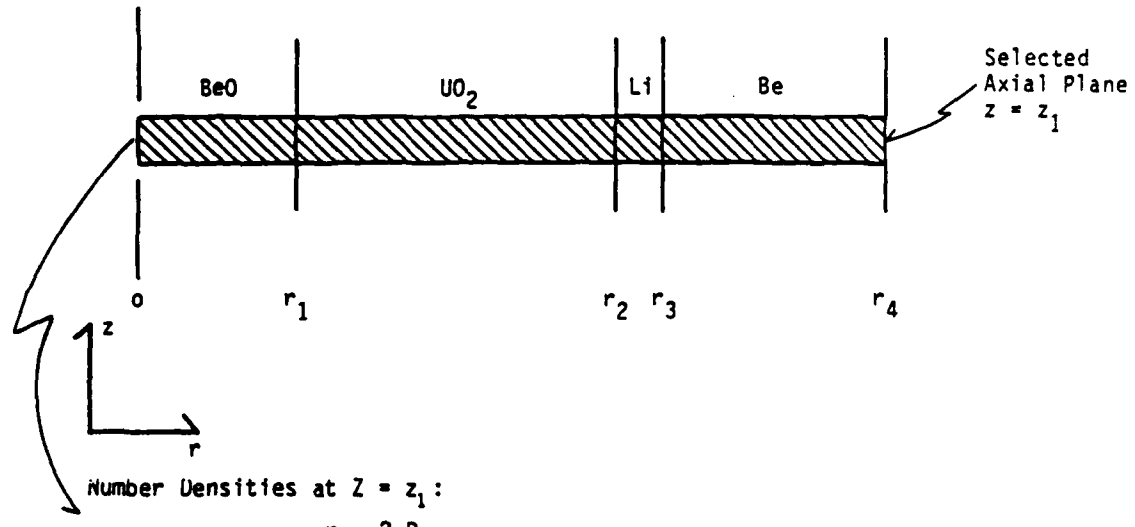
are particularly important for a deep penetration calculation in a fast reactor shield, as the scattering is highly anisotropic in the LiH region.

The number densities for the 1-D calculation were obtained by weighting the 2-D number densities by the respective volume ratio over the entire radius of the system for a given axial plane. This approach is shown in Figure 5.1-1. The accuracy of this volume weighted approach should be higher for a fast reactor than for an equivalent thermal reactor (for same power level) because the volume of the first is much smaller. Therefore, the homogenized number densities have less of an impact on dosage calculations at the 25 m axial dose plane.

The number densities used for the dosage calculations were based on the volume fractions shown earlier. The one exception to this rule was the region which included the B_4C control drums, outside the radial core reflectors. Because of the high enrichment of B-10 (80 atom %) in the B_4C and its extremely large absorption cross section (3837 barns at 0.025ev), the smearing of B_4C for a given axial plane would appreciably alter the neutron spectrum throughout the core. Hence, as shown in Figure 5.1-1 the B_4C was not included in the homogenized 1-D number densities for the axial regions subtended by the core. The effect of leaving out the B_4C was a slightly super critical core ($k_{eff} \sim 1.07$) and resulting fluences would be slightly higher than exact values.

Leakage out radial surfaces was incorporated into the 1-D calculations with transverse buckling. The 2-D shadow shield geometry does not lend itself to an exact 1-D equivalent modelling. Instead, the slightly different geometry as shown in Figure 5.1-2 was used. The two

Figure 5.1-1 Example of Collapse of 2-D to 1-D Densities for
 P_N Transport Calculation



Number Densities at $Z = z_1$:

$$N_u^{1-D} = \frac{\int_{r_1}^{r_2} N_u^{2-D} r dr}{\int_{r_0}^{r_4} r dr}$$

$$N_{Li}^{1-D} = \frac{\int_{r_2}^{r_3} N_{Li}^{2-D} r dr}{\int_{r_0}^{r_4} r dr}$$

Figure 5.1-2 Shield Geometry Modelled in 1-D Fluence Calculations

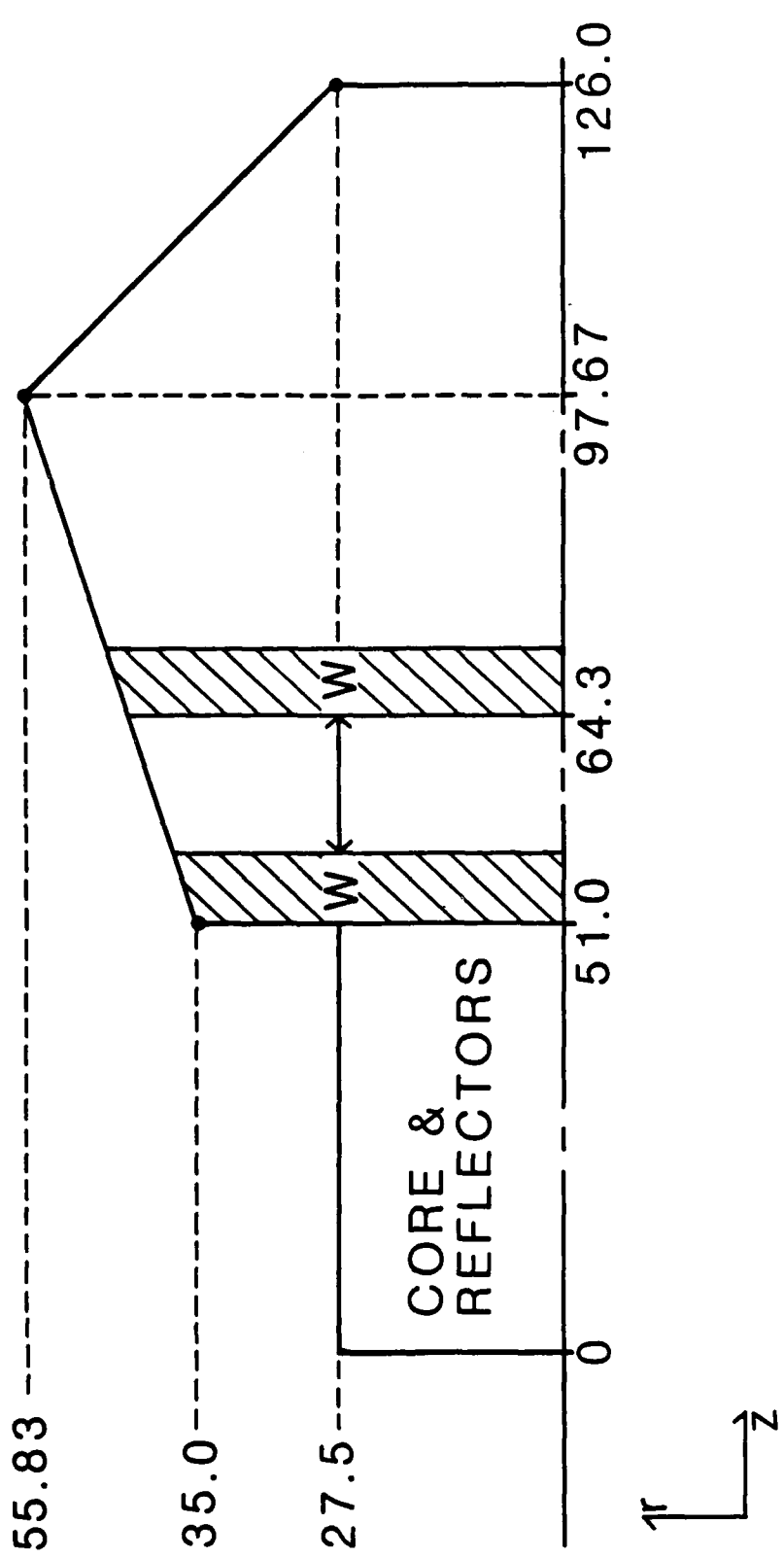


Table 5.2-3: Energy Deposition Throughout a Shield Consisting of LiH(Depl)-W-LiH(Nat) for an SP-100 Reactor Operating at 1.66 MW_{th}

| Energy Deposited [kW] | | | | | |
|-----------------------|-----------|----------------|----------------|------------------|--|
| Zone | Material | H _Y | H _n | H _{tot} | Summary |
| 1 | LiH(Depl) | .097 | .299 | .397 | <u>LiH(Depl):</u> |
| 2 | " | .050 | .107 | .157 | H _Y = .498 |
| 3 | " | .193 | .241 | .434 | H _n = .875 |
| 4 | " | .158 | .228 | .386 | H _{tot} = 1.373 |
| 5 | W | .922 | .013 | .935 | <u>W:</u> |
| 6 | " | 1.436 | .015 | 1.451 | H _Y = 2.358 |
| 7 | LiH(Nat) | .161 | .028 | .189 | H _n = .028 |
| 8 | " | .492 | 1.521 | 2.013 | H _{tot} = 2.386 |
| 9 | " | .127 | .008 | .136 | <u>LiH(Nat):</u> |
| 10 | " | .539 | 1.246 | 1.785 | H _Y = 1.319 H _n = 2.803 H _{tot} = 4.122 |
| Total | | 4.175 | 3.706 | 7.881 | |

Legend:

- H_Y - Energy deposited by Gammas
- H_n - Energy deposited by Neutrons
- H_{tot} = H_Y + H_n

Table 5.2-2: Energy Deposition Throughout a Shield Consisting of LiH(Nat)-W-LiH(Nat) for an SP-100 Reactor Operating at 1.66 MW_{th}

| Energy Deposited [kW] | | | | | |
|-----------------------|----------|----------------|----------------|------------------|--|
| Zone | Material | H _γ | H _n | H _{tot} | Summary |
| 1 | LiH(Nat) | .081 | 1.747 | 1.828 | <u>LiH(Nat):</u> |
| 2 | " | .053 | .406 | .459 | H _γ = .434 |
| 3 | " | .143 | .991 | 1.134 | H _n = 4.005 |
| 4 | " | .157 | .861 | 1.018 | H _{tot} = 4.439 |
| 5 | W | .505 | .000 | .505 | <u>W:</u> |
| 6 | " | 1.134 | .005 | 1.139 | H _γ = 1.639 |
| 7 | LiH(Nat) | .169 | .021 | .190 | H _n = .005 |
| 8 | " | .539 | 1.459 | 1.998 | H _{tot} = 1.644 |
| 9 | " | .136 | .008 | .144 | <u>LiH(Nat):</u> |
| 10 | " | .590 | 1.216 | 1.806 | H _γ = 1.434 H _n = 2.704 H _{tot} = 4.138 |
| Total | | 3.507 | 6.714 | 10.221 | |

Legend:

- H_γ - Energy deposited by Gammas
- H_n - Energy deposited by Neutrons
- H_{tot} = H_γ + H_n

Table 5.2-1: Energy Deposition Throughout a Shield
Consisting of W-LiH(Dep1)-LiH(Nat) for
an SP-100 Reactor Operating at 1.66 MW_{th}

| Energy Deposited [kW] | | | | | |
|-----------------------|-----------|----------------|----------------|------------------|--------------------------|
| Zone | Material | H _γ | H _n | H _{tot} | Summary |
| 1 | W | 2.220 | .039 | 2.259 | <u>W:</u> |
| 2 | " | 1.657 | .017 | 1.674 | H _γ = 3.877 |
| 3 | LiH(Dep1) | .189 | .209 | .398 | H _n = .056 |
| 4 | " | .383 | .394 | .777 | H _{tot} = 3.933 |
| 5 | " | .196 | .015 | .211 | <u>LiH(Dep1):</u> |
| 6 | " | .394 | .227 | .621 | H _γ = 1.923 |
| 7 | " | .183 | .001 | .184 | H _n = 1.131 |
| 8 | " | 578 | .285 | .863 | H _{tot} = 3.054 |
| 9 | LiH(Nat) | .185 | .009 | .194 | <u>LiH(Nat):</u> |
| 10 | " | .310 | .208 | .518 | H _γ = .495 |
| | | | | | H _n = .217 |
| | | | | | H _{tot} = .712 |
| Total | | 6.295 | 1.404 | 7.699 | |

Legend:

- H_γ - Energy deposited by Gammas
- H_n - Energy deposited by Neutrons
- H_{tot} = H_γ + H_n

with the remaining energy deposition occurring in the W. Furthermore, the 6.274 kW of energy deposited in zones 1 through 4 (shield center-line thickness of ~15 cm) accounted for 64% of the total energy deposited.

With the W-LiH(Depl)-LiH(Nat) shield configuration, gamma heating accounted for 6.295 kW of the 7.699 kW deposited, for an 82% fraction. The gamma heating in the tungsten rose by 0.69 kW to 3.877 kW. What occurred was an increase in scattering of lower energy neutrons into the tungsten due to the absence of the Li-6 nuclide (which reduces backscattering into the W). The slow neutrons then were absorbed by the W-184 and W-184 nuclides which produced low Mev gammas. Many of the gammas were then absorbed by the high-Z tungsten, resulting in an increase in gamma heating. The thermal neutrons which did not re-enter the W were available for radiative capture in the Li-7 and H. Many of these gammas subsequently escaped from the low Z LiH, resulting in a higher gamma fluence for the W-LiH(Depl)-LiH(Nat) configuration.

The LiH(Depl) and LiH(Nat) accounted for 3.766 kW of the 7.699 kW deposited, or a 49% fraction. Thus, we found that not only was there a reduction in total energy deposited, but a greater percentage of the heating occurred in the highly thermally conductive material, tungsten. Furthermore, the 5.108 kW of energy deposited in zones 1 through 4 represented a decrease of over 1 kW of heating in the front portion of the shield with the substitution of LiH(Depl).

Thus, we found some marked advantages from a thermal transport standpoint in replacing the highly absorbent LiH(Nat) in the front portion of the shield. The total energy deposition was reduced, a greater portion of the energy deposition occurred in the tungsten, and

the prioritized list of shield configurations will be substantially different which, in turn, requires trade-offs between radiation transport and thermal management of the shield.

5.2.1 Energy Deposition Results. Tables 5.2-1 through 5.2-3 include the energy deposition for each zone of shield configurations 2, 3 and 4 of Table 5.1-1. The energy deposition for shield configuration 1 (Table 4.2-8) was presented in Section 4.2. With the tungsten moved into the shield, the zoning of shield configuration numbers 3 and 4 do not correspond directly to the zoning configuration numbers 1 and 2. Thus, a direct comparison of zone heating between tungsten at the front and tungsten moved into the shield, is not valid.

To understand the importance of shield configuration to total deposition, the effects of replacing LiH(Nat) with LiH(Depl) for a given location of W were examined, then the effects of moving the W into the shield were analyzed, as well. With a good understanding of the relationship between shield configuration and energy deposition, the resulting temperature profile for each shield will follow in the next section.

A comparison of Tables 4.2-8 and 5.2-1 shows changes in total heating with replacement of the first 42 cm of LiH(Nat) with LiH(Depl), when the W was at the front of the shield. The total energy deposition was decreased by slightly more than 2 kW, or 21%. However, the % contribution to total energy deposition by gamma interaction changed substantially. For the shield comprised of all natural LiH, gamma heating accounted for 4.778 kW of the 9.765 kW deposited for a 49% fraction. Of this total heating value, the LiH accounted for 6.542 kW, or 67%,

absorption of thermal neutrons by Li-6 eliminates any chance of secondary gamma generation from radiative capture reactions in the W and LiH with these slow neutrons. The optimum design is shield configuration 3 from the Table 5.1-1 based on radiation transport considerations. However, substitution of LiH(Nat) with LiH(Depl) before the W still meets the fluence requirements of the SP-100 program.⁴

Thirdly, the rate of gamma attenuation with increased shield thickness is much less than the equivalent rate of neutron attenuation. With the stringent weight and volume constraints associated with reactors deployed in space, optimization of the shield configuration will result in significant improvements in the gamma attenuating capabilities of the shield.

With a basic understanding of the radiation transport performance of the SP-100 reactor shield, the next section shall present the results of the thermal performance of these same shielding configurations. Should there be a change in preference of order of shield configuration based on Figure 5.1-5, then thermal design considerations must become an integral part of the design process in space reactor radiation shielding.

5.2 Results of Shield Configuration Effects. In the last section, a layered shield consisting of LiH(Nat)-W-LiH(Nat) was shown to be the optimum design of the four shields analyzed based only on radiation protection performance. In this section, the optimum configuration in terms of thermal performance is identified. As shall be shown,

⁴ At the start of this work, the gamma fluence was 1 MRAD at the 25 meter dose plane. This requirement has recently been changed to 0.5 MRAD for the SP-100 Program, which can be met by an additional 1 cm of W. Even with the extra W, the relative position of the shield configurations of Figure 5.1-5 remains the same.

damage response functions below \sim 10 KeV threshold cause no damage to silicon [Bendel, 1977]. Since the configurations of Table 5.1-1 differ predominately from the standpoint of removing thermal neutrons (and secondary gammas), the impact on NVT fluence is minimal.

Another conclusion one may draw from Figure 5.1-4 is that the application of a removal cross section for determining fast neutron attenuation is quite reasonable. The linearity of this curve on a semi-log scale is indicative of the exponential attenuation of fast neutrons throughout the shield.

The radiation transport consequence of changing the shield configuration is vividly seen in Figure 5.1-5. The effect of moving tungsten 13.4 cm into the shield is readily apparent by the lower gamma fluence of shield configurations 3 and 4. The physics of why the gamma fluence is dramatically reduced with W moved into the shield is based on changes in radiative capture (low energy) and inelastic scattering (high energy) of neutrons in Li-7, radiative capture (low energy) of neutrons and gamma removal in W, thermal neutron absorption in Li-6 and radiative capture in hydrogen. While 1-D results should be used only for a conceptual understanding of the shield, these results agree well with more detailed 2-D Monte Carlo calculations performed at Los Alamos National Laboratory (Carlson, 1985).

Several general conclusions can be made based on the results of Figure 5.1-5. Firstly, there is a decrease by a factor of 3-5 times in the gamma fluence with the movement of the W into the shield. In fact, the SP-100 gamma fluence requirements may not be met for shield configurations 1 and 2 with for a 75 cm thick shield.

Secondly, the use of LiH(Depl) in place of LiH(Nat) results in a decrease in the radiation protection performance of the shield. The

Figure 5.1-5 7 Year Gamma Fluences of SP-100 Reactor at 25 meter Dose Plane for Several W-LiH Configurations

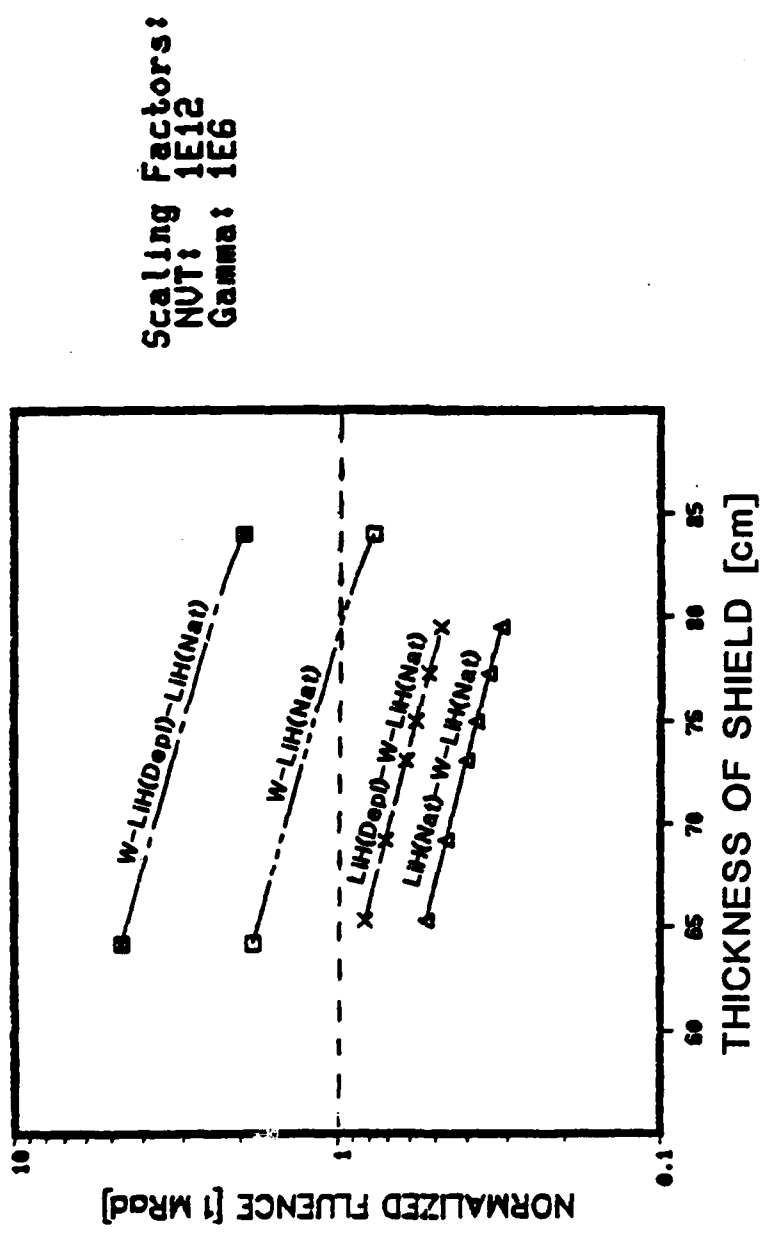
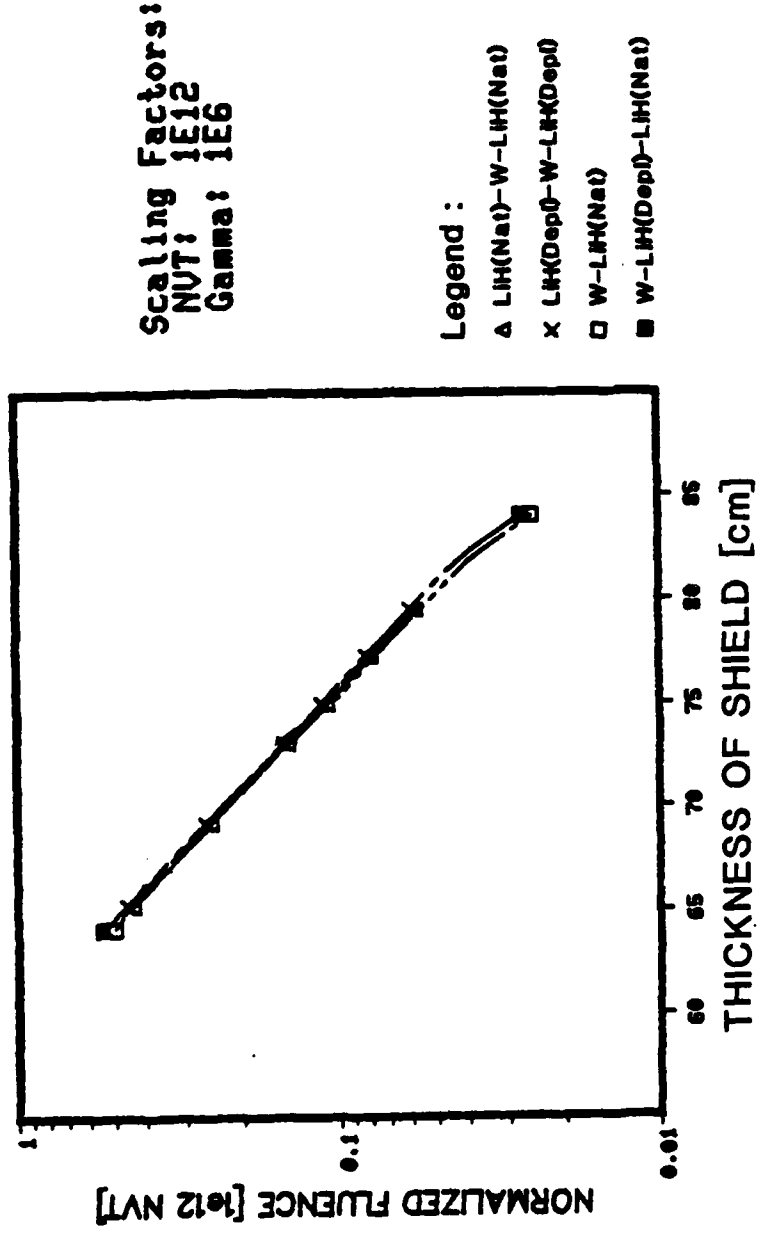


Figure 5.1-4 7 Year NVT Fluences of SP-100 Reactor at 25 meter Dose Plane for Several W-LIH Configurations



The variable θ , D_b , and x are identified in Figure 5.1-3. The scaling factor (SF) for extrapolating the 1-D fluence from the back of the shield to the dose plane follows from Equation 5.1-10 as:

$$SF = \frac{1}{32} \frac{\cos\theta}{x^2} D_b^2 \quad (5.1-11)$$

The value of D_b for the SP-100 reactor shield would be 27.5 cm if no neutrons or gammas reached point P from the rear angled surfaces of shield (Surfaces AB and CD in Figure 5.1-3). For the sake of conservatism, let's assume that all gammas and neutrons leaving these surfaces and subtended by the solid angle ω also reach point P. Since the distance from the center of the core to the back of the shield is very close to 100 cm, the value of x (back of shield to dose plane) is 2400 cm. The value of $\cos\theta$ (cosine of radius of shield to distance from back of shield to dose plane) is very nearly one. The scaling factor then becomes:

$$SF = \frac{1}{32} \frac{(2 \times 55.83 \text{ cm})^2}{(2400 \text{ cm})^2} = 6.76 \times 10^{-5}$$

With this scaling factor, the P_{15} neutron and gamma fluences at the 25 meter dose plane are included in Figures 5.1-4 and 5.1-5 for the four shield configurations being considered.

The first observation one can make from the NVT fluences of Figure 5.1-4 is that for the baseline design shield thickness of 75 cm, neutron dosage is well below the SP-100 requirement of 10^{12} NVT [JPL, 1982]. Another less obvious result is that the particular configuration of W and LiH has little effect on NVT, as long as the total mass of the gamma and neutron attenuating materials remains constant. The reason for this result lies in the fact that the magnitude of the

Substituting Equation 5.1-2 into Equation 5.1-3 and carrying out integration results in:

$$\phi_1(E, z_b) = \frac{\phi_0(E, z_b)}{2} \quad (5.1-4)$$

Recalling that the ϕ_1 component of the flux represents the current, the portion of flux exiting the shield, ϕ_n , is:

$$\phi_n(E, z_b) = \frac{1}{8\pi} \phi_0(E, z_b) \quad (5.1-5)$$

Since fluence is calculated from the ϕ_0 component of flux, the ϕ_1 portion of fluence at the back surface follows directly from Equation 5.1-5:

$$F_n(E, z_b) = \frac{1}{8\pi} F_0(E, z_b) \quad (5.1-6)$$

The fluence at point P can be determined by substituting Equation 5.1-6 into Equation 5.1-1, resulting in:

$$F_{DP} = \int_E \int_S \int_{\omega} F_n(E, z_b) d\omega dS dE$$

$$F_{DP} = \int_E \int_S \int_{\omega} \frac{1}{8\pi} F_0(E, z_b) d\omega dS dE \quad (5.1-7)$$

$$= \int_E \frac{1}{8\pi} F_0(E, z_b) \frac{\cos\theta}{x^2} \frac{\pi D_b^2}{4} dE \quad (5.1-8)$$

The multi-grouping of energies in the radiation transport calculation leads to the following relationship for fluence:

$$F_{DP} = \frac{1}{32} \frac{\cos\theta}{x^2} D_b^2 \Delta F_0(E_g, z_b) \quad (5.1-9)$$

$$F_{DP} = \frac{1}{32} \frac{\cos\theta}{x^2} D_b^2 F_0(z_b) \quad (5.1-10)$$

fluence on the 25 meter dose plane (Point P on this figure). Mathematically, the 25m maximum fluence was obtained from:

$$F_{DP} = \int_E \int_S \int_\omega F_n(E, z_b) \cdot d\omega dS dE \quad (5.1-1)$$

where:

F_n = Component of fluence at back surface exiting shield

F_{DP} = Fluence at dose plane

z_b = Distance from axial mid-plane of core to shield back surface

S = Surface area at back surface

ω = Solid angle from point P to Surface S

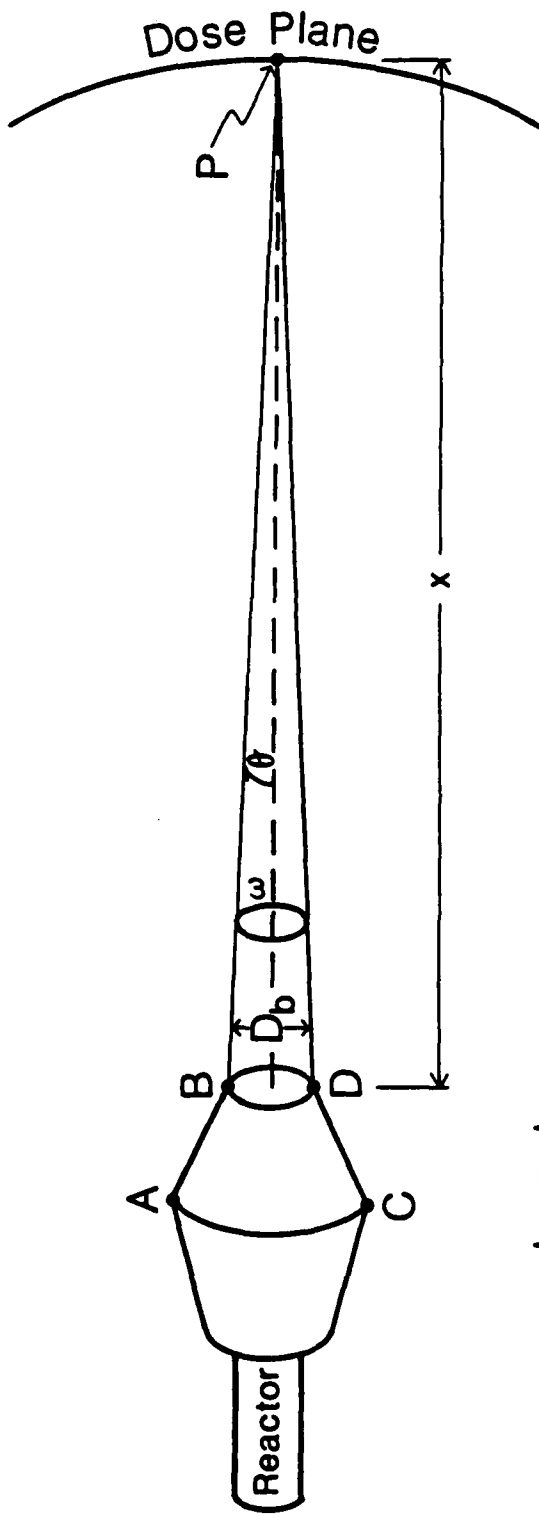
Since the fluence calculated at the back surface was based on the flux at each radial position along this surface, the directional component of the flux toward point P must be separated out. This was accomplished by assuming that the directional dependence of the flux (from the back surface to the point P) is linearly anisotropic and can be approximated by the first two terms of expansion using Legendre Polynomials, or:

$$\phi(E, z, \mu) = \frac{1}{4\pi} [\phi_0(E, z) P_0(\mu) + 3\phi_1(E, z)P_1(\mu)] \quad (5.1-2)$$

The component of flux leaving the shield from the back vertical surface then corresponds to any neutron or gamma with an angular cosine greater than zero. Using a Marshak boundary condition, the current leaving the back surface toward the dose plane is determined from [Bell and Glasstone, 1970]:

$$\int_{-1}^0 \phi(E, z_b, \mu) \mu d\mu = 0 \quad (5.1-3)$$

Figure 5.1-3 Geometric Relationship of Sources Exiting Back of Radiation Shield to Point of Maximum Dosage on 25 m Dose Plane



Legend

- P = Point on Dose Plane of Maximum Fluence
- D_b = Diameter of Back Surface
- ω = Solid Angle Subtended by Point of Maximum Fluence on Dose Plane to Back Surface of Shield
- θ = Angle from Shield Centerline to Outer Radius from Point P
- X = Distance from Back of Shield to Point P

tungsten locations correspond to either shield configurations 1 and 2 , or 3 and 4. The shield was then subdivided into zones corresponding to the 2-D centerline zones, and temperature dependent number densities from the 2-D problem were used for 1-D calculations. The radius used to calculate the transverse buckling for each zone was based on the average outer radius of each zone, with an extrapolation length based on diffusion theory added.

The dosage calculations were made with a criticality determination of the combined reactor and shield system, with the FEMPI0 transport code. The fluxes at each axial position were then used to calculate the neutron and gamma fluences, respectively. For neutron and gamma doses, the silicon damage response functions of Bendel (1977) were used. The neutron damage effects (due to both ionization and displacement) are normalized to a 1 Mev equivalent dosage [Namenson and Wolicki, 1982].

The gamma and neutron fluences were calculated for each axial position throughout the shield. The specific values corresponding to the back of the shield must then be extrapolated to the 25 meter dose plane to compare the fluences for a given shield thickness with the prescribed dosages for the SP-100 reactor system. By considering each neutron and gamma ray exiting the shield at its back surface as a point source, the dose plane fluence can be determined by integrating the individual point sources over the entire back surface and subtend the solid angle to the point on the 25 meter dose plane experiencing the largest fluence. Figure 5.1-3 diagrams the geometric relationship of the radiation sources at the back of the shield to the point of maximum

less energy was required to be removed from the hot part of the low conductivity LiH. The question as to whether the same thermal advantages apply to the configurations with W moved into the shield was the next issue to be addressed.

With the tungsten moved 13.4 cm into the shield, the gamma flu-ences were shown to decrease comfortably below the 1 MRAD requirement for the 75 cm thick shield baseline design. The energy deposited for the two configurations analyzed with the tungsten moved-in were recorded in Tables 5.2-2 and 5.2-3. The effects of replacing the first 13.4 cm of LiH(Nat) with LiH(Depl) will now be discussed.

The neutron spectrum entering the shield is quite hard, with some thermalization occurring in the beryllium and beryllium oxide reflectors. Much of the spectrum softening which occurs in the reflectors is offset by the absorption of thermal neutrons by the lithium coolant in heavy concentration in the upper plenum located between the core and the shield. Therefore, differences in energy deposition between configura-tions 3 and 4 must be due primarily to spectrum softening occur-ring within the first 13.4 cm of the shield.

From Table 5.2-2, the total energy deposited in the LiH(Nat)-W-LiH(Nat) shield is 10.221 kW, with 4.439 kW (~43%) occurring in zones 1 through 4. From Table 5.2-3, the total energy deposited in the LiH(Depl)-W-LiH(Nat) shield is 7.881 kW with 1.373 kW (~17%) occurring in zones 1 through 4. The heating in the W increased by 0.742 kW for the shield with the LiH(Depl). This increase in heating, due to the higher thermal neutron flux entering the W, when combined with the net

decrease of 3.066 kW between the two designs for zones 1 through 4 (natural or depleted LiH), accounted for the net decrease of 2.34 kW (~23%) in total energy deposited with the substitution of LiH(Depl) for the first 13.4 cm of the shield.

Gamma heating accounted for ~34% of the total energy deposited for the LiH(Nat)-W-LiH(Nat) shield and ~53% for the LiH(Depl)-W-LiH(Nat) shield. The reason for the increase with the LiH(Depl) at the front was basically the same as discussed previously for the W-LiH shields. With less neutron absorption due to removal of the Li-6 nuclide in the front portion of the shield, there were more capture reactions occurring in the Li-7, H, and W. Thus, the net result was an increase in gamma heating. However, the relative contribution of gamma heating was significantly decreased with the movement of W into the shield. Recalling that this movement was initiated to minimize the generation of secondary gammas, this decrease in relative contribution by gammas was quite understandable.

When comparing the total energy deposition of W-LiH(Nat) with the LiH(Nat)-W-LiH(Nat) shields, it was quite remarkable how the total heating values differed by less than 0.5 kW. The difference in energy deposition between the W-LiH(Depl)-LiH(Nat) and LiH(Depl)-W-LiH(Nat) shields was less than 0.2 kW. However, the relative contributions to total heating by gamma and neutron interactions was seen to be significantly different when the tungsten was moved into the shield. Because a gamma mean free path is quite larger than the neutron mean free path in LiH, one might expect very different temperature distributions, despite these small differences in total energy deposition.

In summary, the interaction of radiation with matter is a complicated process in itself. The effects of these interactions on energy deposition are further complicated when one must consider the resulting changes on reaction rates, heating kermas, charged particle and secondary gamma generation. The net result of simultaneously applying all these effects are beyond the level of understanding provided by simple analytic expressions. Hence, one is forced to adapt the capabilities of computational analyses using complex computer codes on digital computers.

The coupling of the radiation transport to the heat transfer for the four shield configurations will be presented next. What has been shown thus far is that the radiation protection performance of the shield is strongly influenced by the relative location of the tungsten, and to a lesser degree with the substitution of LiH(Nat) with LiH(Depl) in the front portions of the shield. The effect of moving the tungsten into the shield had a slight effect on the total energy deposited, and the use of LiH(Depl) resulted in a decrease of ~23% in energy deposition for either location of tungsten. The remaining issues focus on how these energy deposition results translate into temperature distributions and whether a shield optimized for minimum fluences meet the thermal performance requirements of the tungsten and LiH/stainless steel honeycomb.

5.2.2 Temperature Distribution Results. The volumetric heating rates corresponding to the four shield configurations of Table 5.1-1 were used to generate the temperature distribution throughout the 3-D axisymmetric radiation shield. For the baseline case, the radiative

surface coating was taken as chromium oxide, which for the temperature range of interest in this analysis has a constant emissivity of 0.83 [Touloukian et al., 1972].⁵ The view factor was assumed ideal with a value of 1.0.⁶ A final assumption was that the reactor was operated in a 300 km orbit, which has an equilibrium ambient temperature of 200 K [Stevenson and Grafton, 1961]. With these operating conditions, an optimum shield design (based on radiation transport and heat transfer analyses) was selected.

At this time the effects of long term exposure at low earth orbits are not clearly understood. There is some uncertainty associated with maintaining these baseline assumptions over the seven year design lifetime of the SP-100 reactor system. For example, recent shuttle flights have experienced surface etching from oxygen atoms striking its surface [Cross and Cremers, 1985]. The effect of this etching phenomenon on the chromium oxide emissivity over the operating lifetime of the reactor remains to be determined. Because of this type of uncertainty, sensitivity analyses were performed by varying baseline values of emissivity, view factor, and equivalent ambient temperature to determine changes in maximum and minimum shield temperatures (based on the LiH temperature limits previously discussed).

⁵ Ceramic oxide coatings are favored materials for heat rejection in the space environment because of their low absorbtivity of short wavelength radiation and high emissivity at thermal radiation wavelengths [Stevenson and Grafton, 1961].

⁶ An actual shield deployed in space will have some energy exchange with surrounding celestial bodies and other objects in space. Calculation of view factors to model this exchange must include reactor orbit, orientation within an orbit, position along an orbit, and any rotational spin of the reactor system. The magnitude of this energy exchange will be small in comparison with the earth-shield heat exchange, which is incorporated in the energy balance at the radiative surface as an equivalent ambient temperature.

Figure 5.2-1 Temperature Distribution in a W-LiH(Nat) Shield
for a Fast Reactor Operating at $1.66 \text{ MW}_{\text{th}}$

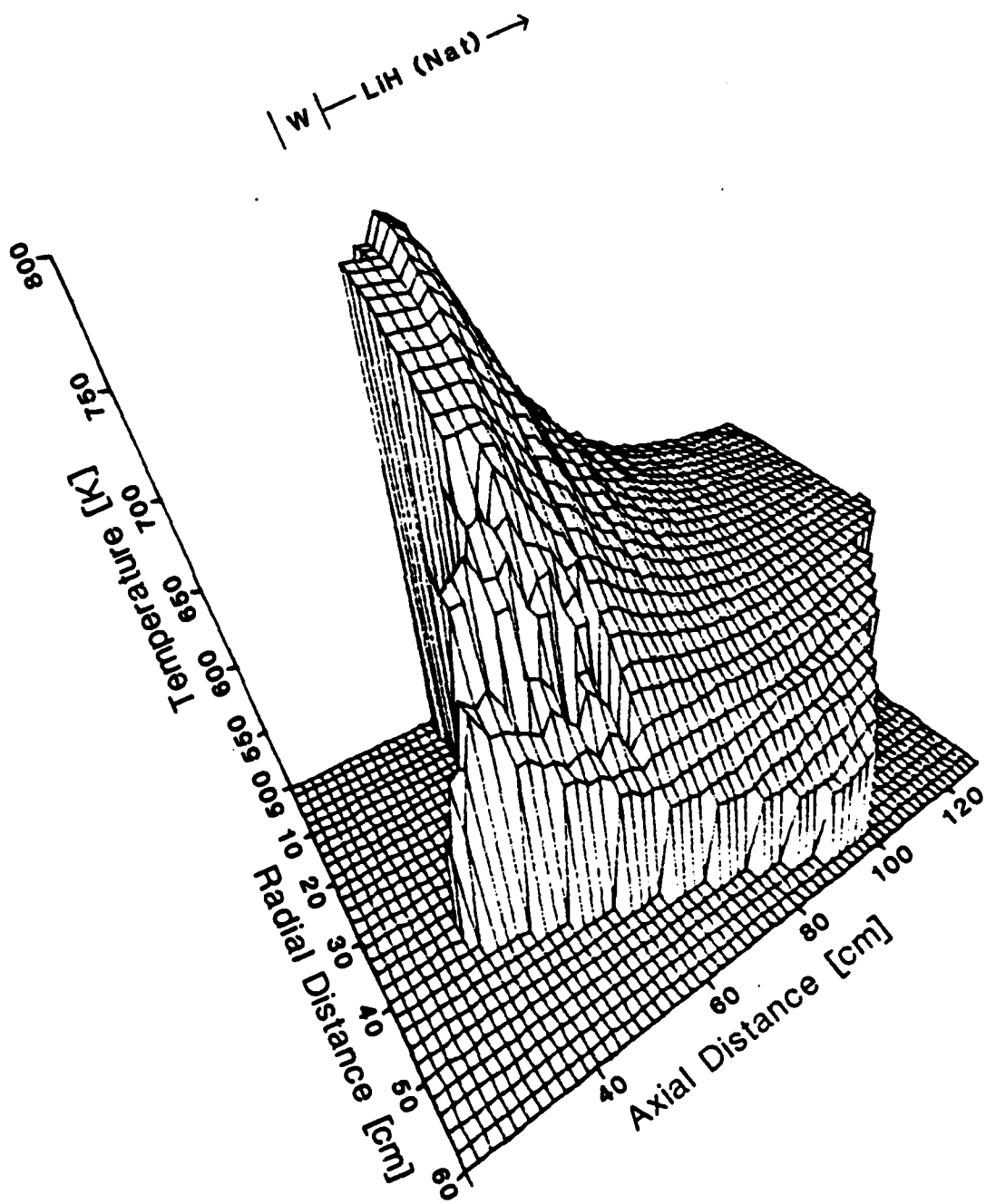


Figure 5.2-2 Temperature Distribution in a W-LiH(Degl)-LiH(Nat) Shield for a Fast Reactor Operating at $1.66 \text{ MW}_{\text{th}}$

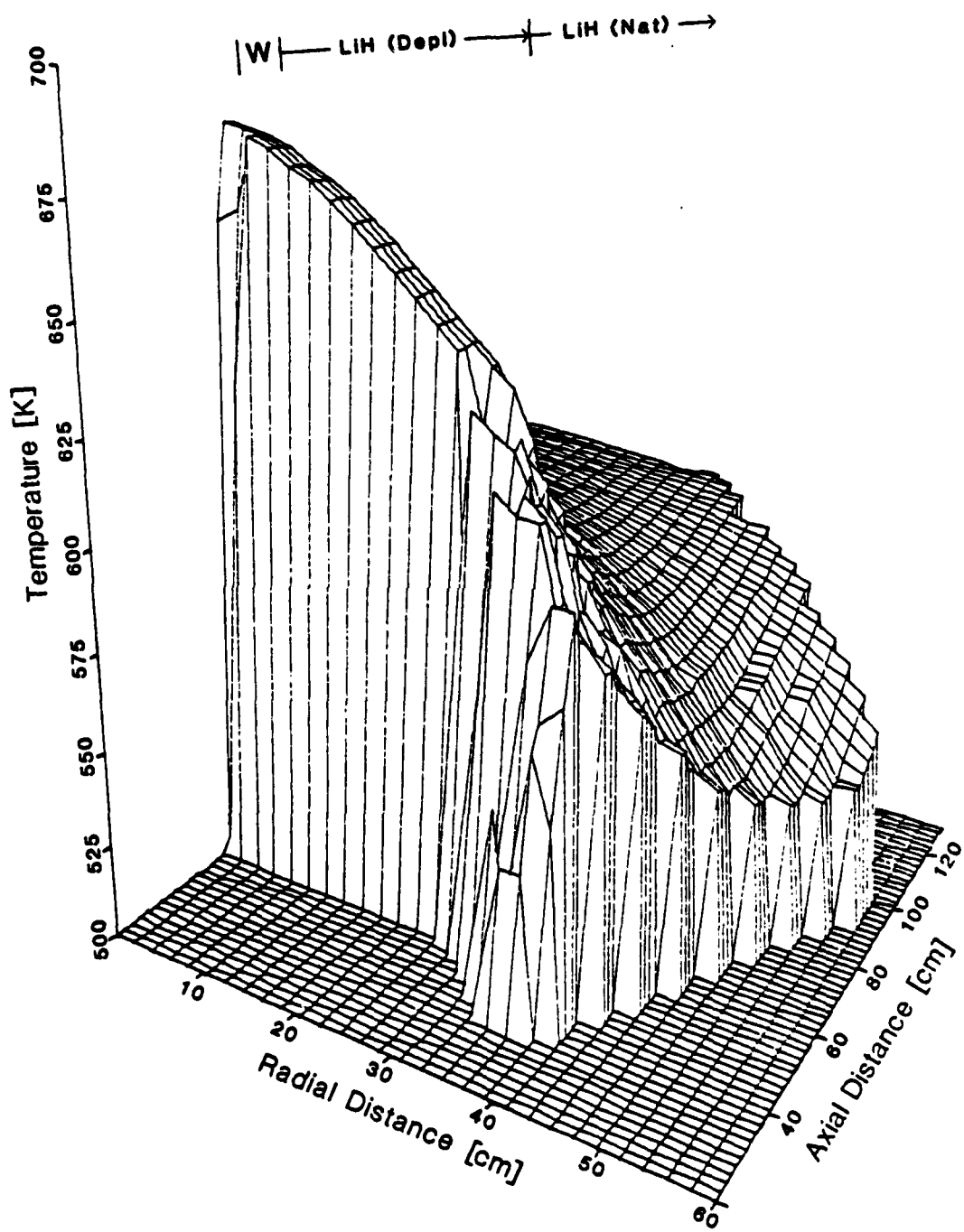


Figure 5.2-3 Temperature Distribution in a W-LiH(Nat)-W-LiH(Nat) Shield for a Fast Reactor Operating at $1.66 \text{ MW}_{\text{th}}$

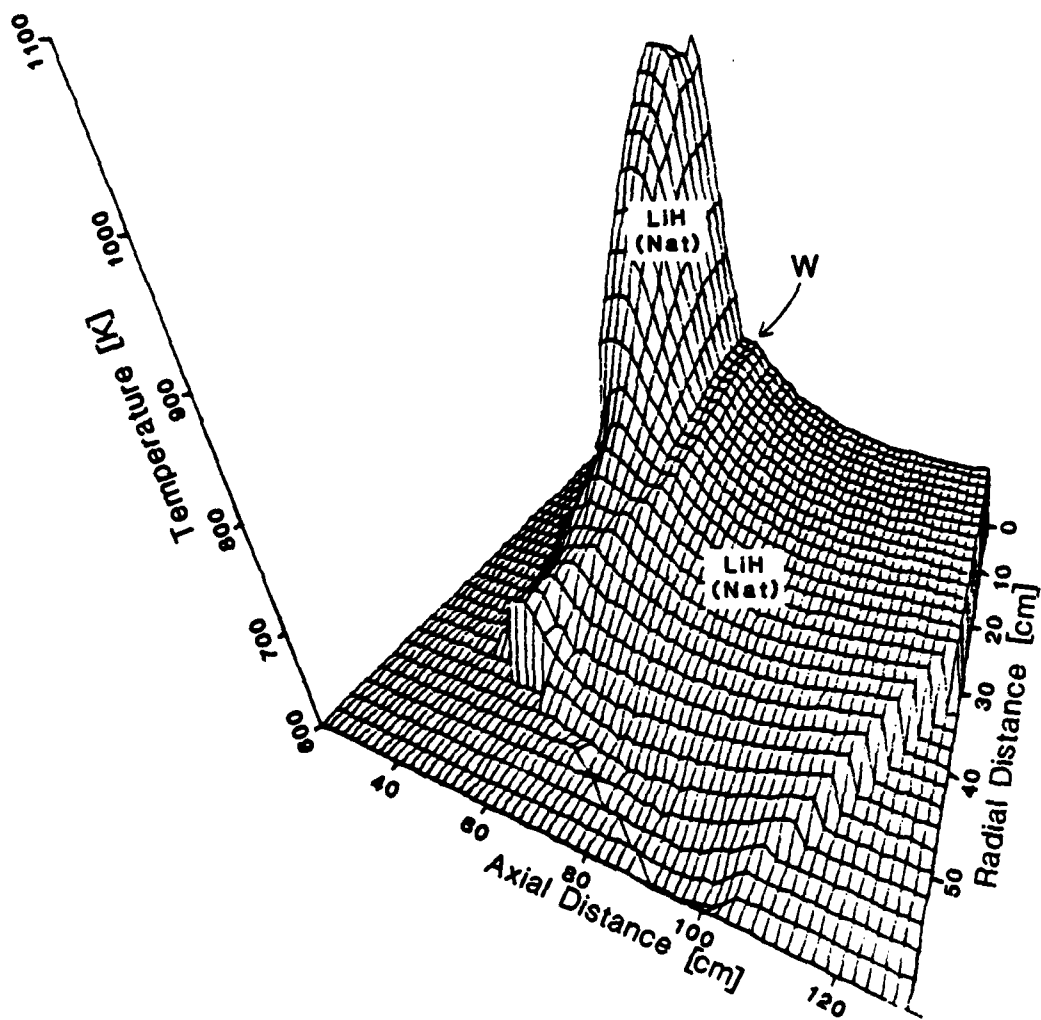
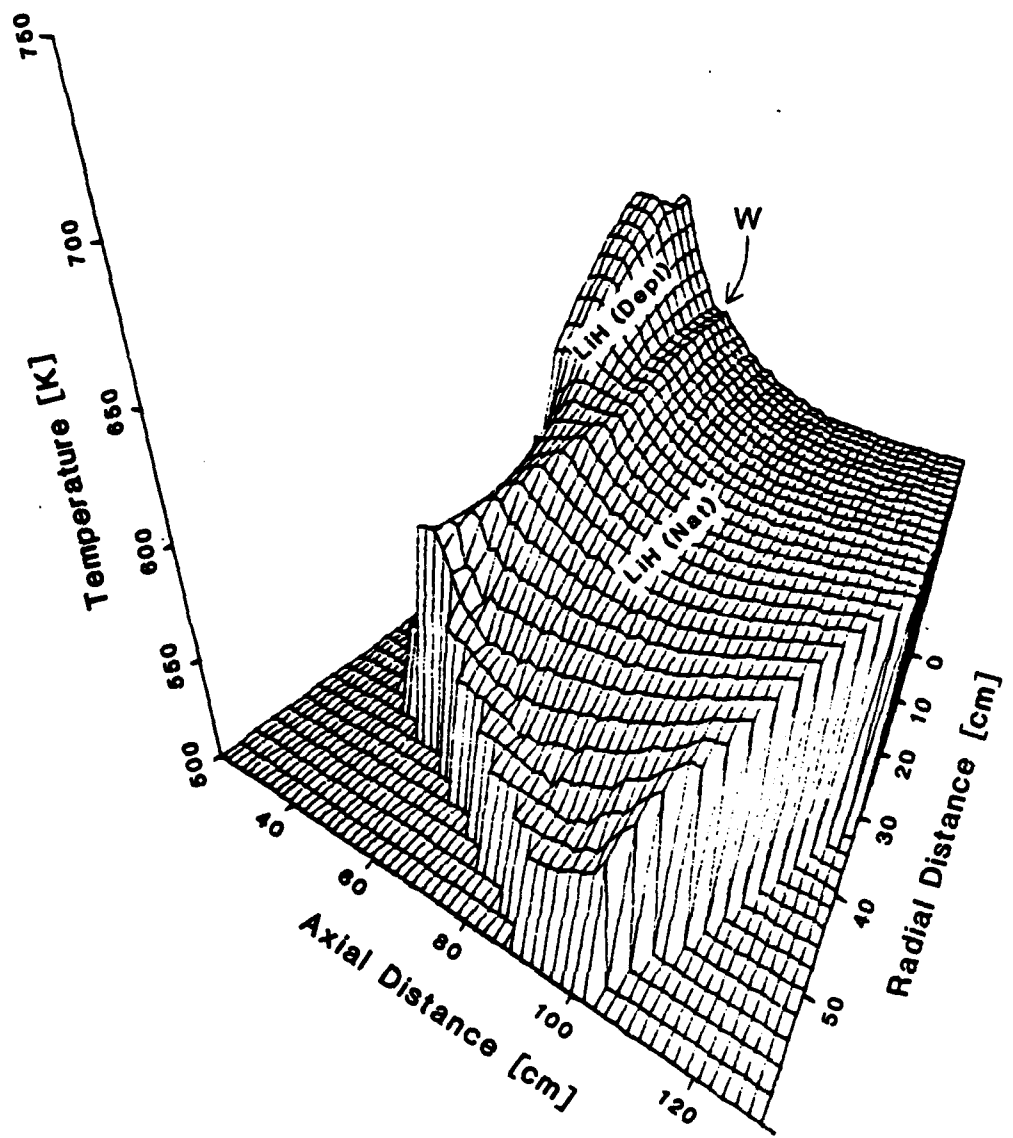


Figure 5.2-4 Temperature Distribution of a LiH(Dep1)-W-LiH(Nat) Shield for a Fast Reactor Operating at $1.66 \text{ MW}_{\text{th}}$



The front and back surfaces of the shield were adiabatic as in Figure 4.2-2 for all results presented in this section. The final temperature distributions for the four configurations of Table 5.1-1 are included in Figures 5.2-1 through 5.2-4. The 3-D plots present the steady state temperature of the shield as a function of radial and axial position. Both radial and axial coordinates are the same as identified in Figure 4.2-2.

Figures 5.2-1 and 5.2-2 present the temperature distributions for the W-LiH(Nat) and W-LiH(Depl)-LiH(Nat) shields, respectively. From Figure 5.2-1, the maximum and minimum temperatures for the all natural LiH shield were 772 K and 540 K, respectively. Recalling that ~64% of the energy deposition occurred in the first 15 cm of the shield, the large amount of internal heating in the LiH exceeds the material's ability to transport heat out, resulting in a peaking of the temperature about 2 cm into the LiH(Nat).

The maximum and minimum temperatures for the W-LiH(Depl)-LiH(Nat) shield were 680 K and 535 K, as obtained from Figure 5.2-2. The effects of 21% less energy deposited for the substitution of LiH(Depl) was readily apparent with the 92 K decrease in the maximum temperature of the LiH. The enhanced ability of this shield to transport its heat to the cooler surface was shown with the elimination of the temperature peaking inside the shield.

While neither of the W-LiH shields were attractive based on their ability to satisfy gamma fluence requirements, the W-LiH(Depl)-LiH(Nat) shield was quite acceptable based on its thermal performance. Even the W-LiH(Nat) shield could meet thermal requirements. While the maximum temperature of 772 K for the W-LiH(Nat) shield would cause some concern

regarding stainless steel-lithium interactions (and lithium-lithium nydride interactions, as well), the rapid drop in temperature that occurred beyond the 27.5 cm radial position could make this shield design (with separate inner and outer LiH canned regions) admissible from a thermal standpoint. Thus, the contribution of the highly conductive tungsten in hottest portion of the shield somewhat minimizes the benefits of the significant 21% reduction in energy deposition. The conclusion follows that the gains in thermal performance with the W-LiH(Depl)-LiH(Nat) would not be worth the sacrifice in terms of decreased radiation protection provided by the shield.

Figures 5.2-3 and 5.2-4 present the temperature distributions for the other two shield configurations with the W moved 13.4 cm into the shield. The results from these two plots were quite startling and served as the basis for making some very important conclusions regarding radiation transport-heat transfer coupling.

Focusing attention first to Figure 5.2-3, the maximum temperature for the LiH(Nat)-W-LiH(Nat) was recorded as 1074 K, and the minimum temperature as 565 K. With a melting point of 960 K for LiH, this shield was totally unacceptable based on thermal considerations. Upon melting, the LiH undergoes an expansion of ~24% in volume. This magnitude of increase in occupied space could lead to structural damage. Thus, without even considering the chemistry kinetics that would occur in the shield above 800 K, the concept of a molten shield remains unacceptable to the system designer for the SP-100 reactor system.

Returning to Figure 5.2-3, the region of difficulty was confined to a small area within the LiH at the very front portion of the shield.

Recalling that the energy deposition for this configuration was dominated by neutron interactions (with its small mean free path), one can conclude that thermal hot spots are more likely to occur in shields in which the major mechanism for energy deposition is neutron interactions. Beyond this confined region of intense thermal spiking, the temperature distribution was quite uniform. Thus, the LiH(Nat)-W-LiH(Nat) shield design was the optimal from a radiation performance viewpoint, but worst from a thermal performance viewpoint.

Transferring focus to Figure 5.2-4, a remarkable engineering feat had occurred. By substituting the first 13.4 cm of LiH(Nat) with LiH(Depl), the maximum temperature was reduced to 715 K, a decrease of 359 K. The basis for this dramatic decrease was due to radiation transport considerations. The energy deposited in the front portion of the shield was reduced from 4.439 kW to 1.373 kW. This energy decrease was attributable directly to fewer neutron interactions, meaning that the thermal spiking source was reduced significantly. Specifically, the elimination of the (n, α) reaction in Li-6 accounted for this effect.

The highly thermally conductive tungsten was moved out of the hottest region of the shield. Thus, the effectiveness of the reduction in energy deposition in this region was significantly enhanced. This point is very important and unique to shields for space reactors. Because of the concern for minimizing weight, the metal hydrides (and in particular, LiH) have been shown to be the optimum choice for the neutron attenuation portion of the space reactor shield. Despite its low thermal conductivity, LiH will remain the favored shielding

material for the next generation of space reactors, and the highly conductive tungsten will remain the favored gamma attenuation material.

Besides serving an important radiation protection function, the location of the tungsten has been demonstrated to provide an important thermal transport function, as well. When this 'thermal fin' was moved from the hottest portion of the shield to a cooler location 13.4 cm back, the coupling between neutronics performance and thermal management of the shield became even more critical. Any decrease in energy deposition assumed greater importance with the removal of the tungsten from the front of the shield. This was the reason why the substitution of LiH(Nat) with LiH(Degl) over the first 13.4 cm of the shield resulted in a decrease of 348 K in maximum temperature when comparing configurations 3 and 4; whereas, the replacement of 42 cm of LiH(Nat) with LiH(Degl) at the back region of the shield resulted in a decrease of only 92 K in maximum temperature when comparing configurations 1 and 2.

To gain more insight into the effects of removing the W from the front of the shield, Figures 5.2-5 and 5.2-6 plot the axial temperature for selected radial positions of the W-LiH(Nat) and the LiH(Nat)-W-LiH(Nat) shields. The upper two curves of each figure correspond to the shield centerline and the 14 cm radial position throughout the shield. The effect of tungsten moved into the shield is most evident from these upper curves. From Figure 5.2-6, the heat removal capacity of W is simply not 'felt' by the LiH at the insulated front surface of the shield, resulting in the extremely high temperatures at the core-shield interface. The effects of the back insulated surface are

Figure 5.2-5 Axial Temperatures in a Shield Comprised of W-LiH(Nat) for Selected Radial Positions

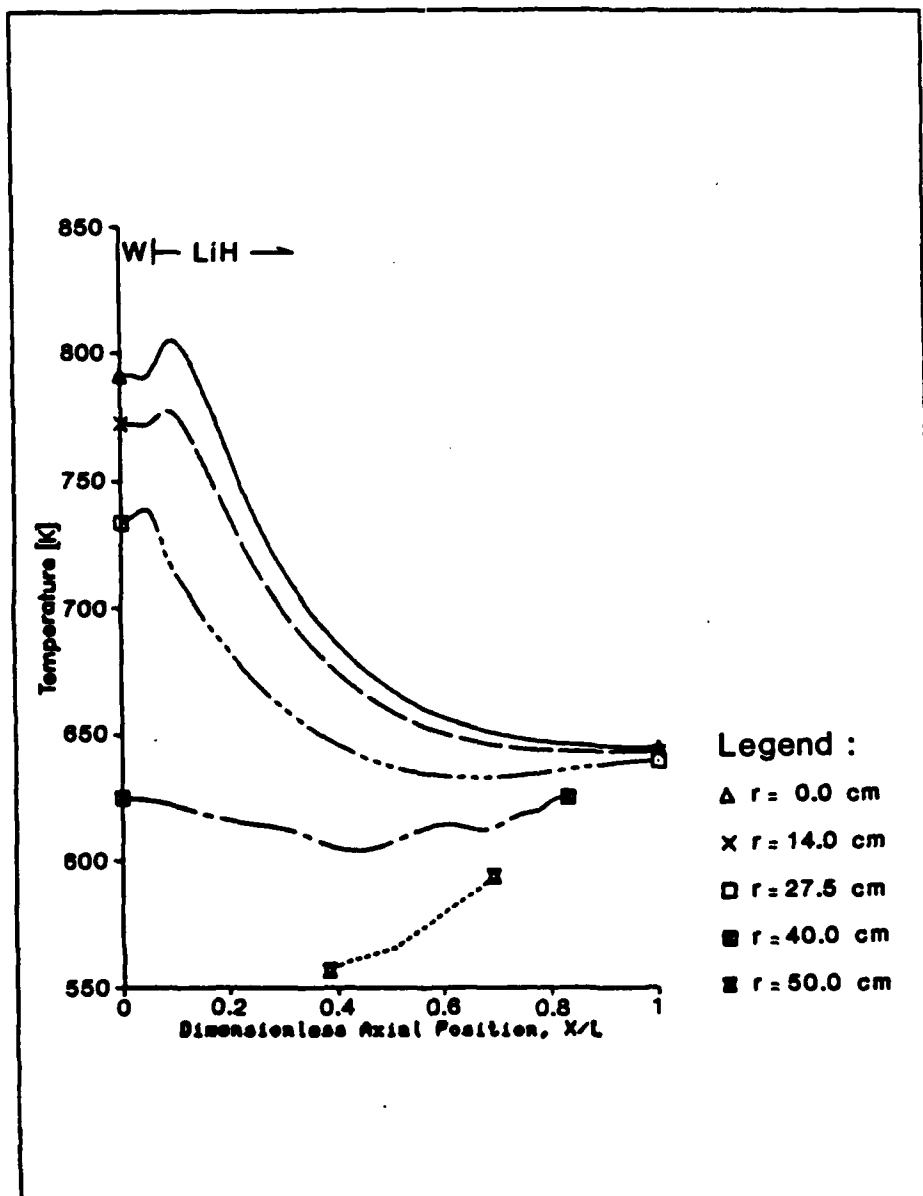


Figure 5.2-6 Axial Temperatures in a Shield Comprised of LiH(Nat)-W-LiH(Nat) for Selected Radial Positions

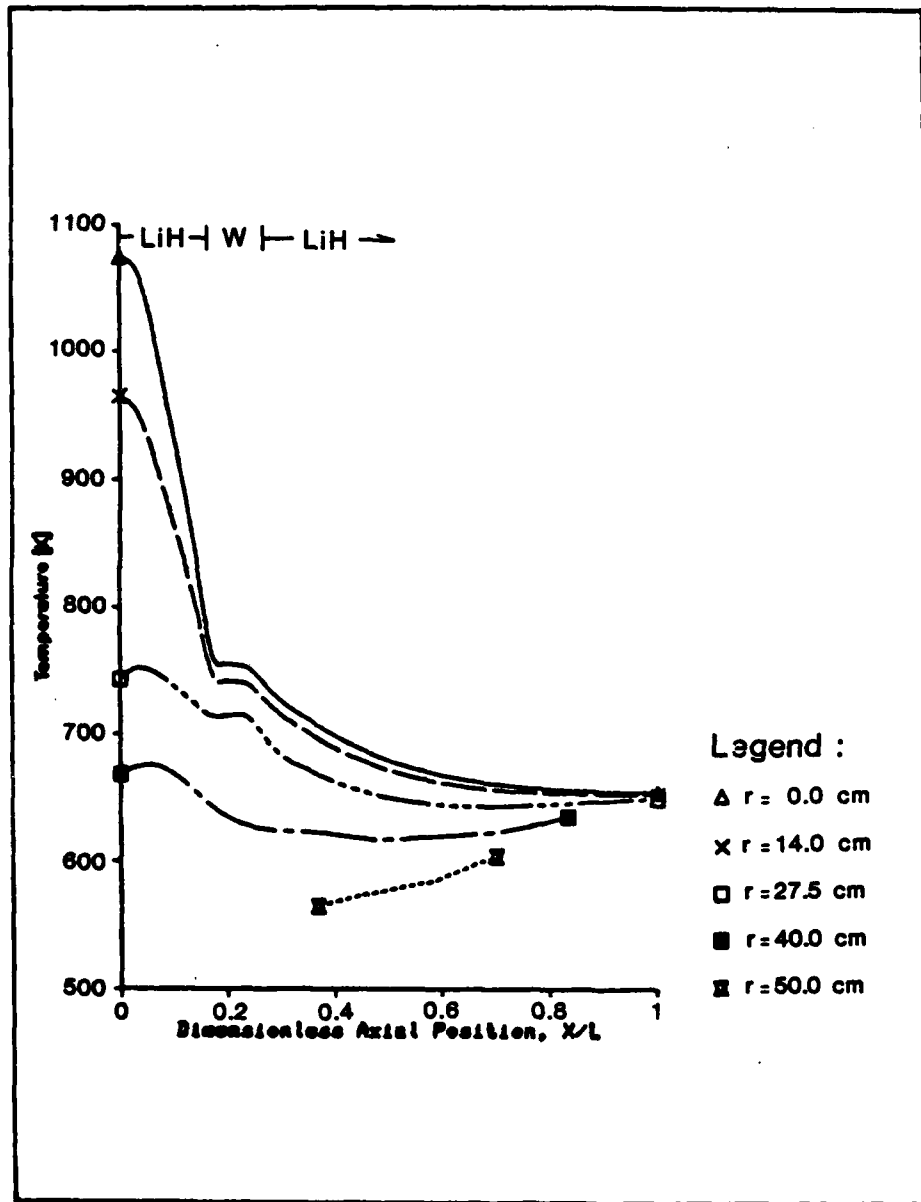
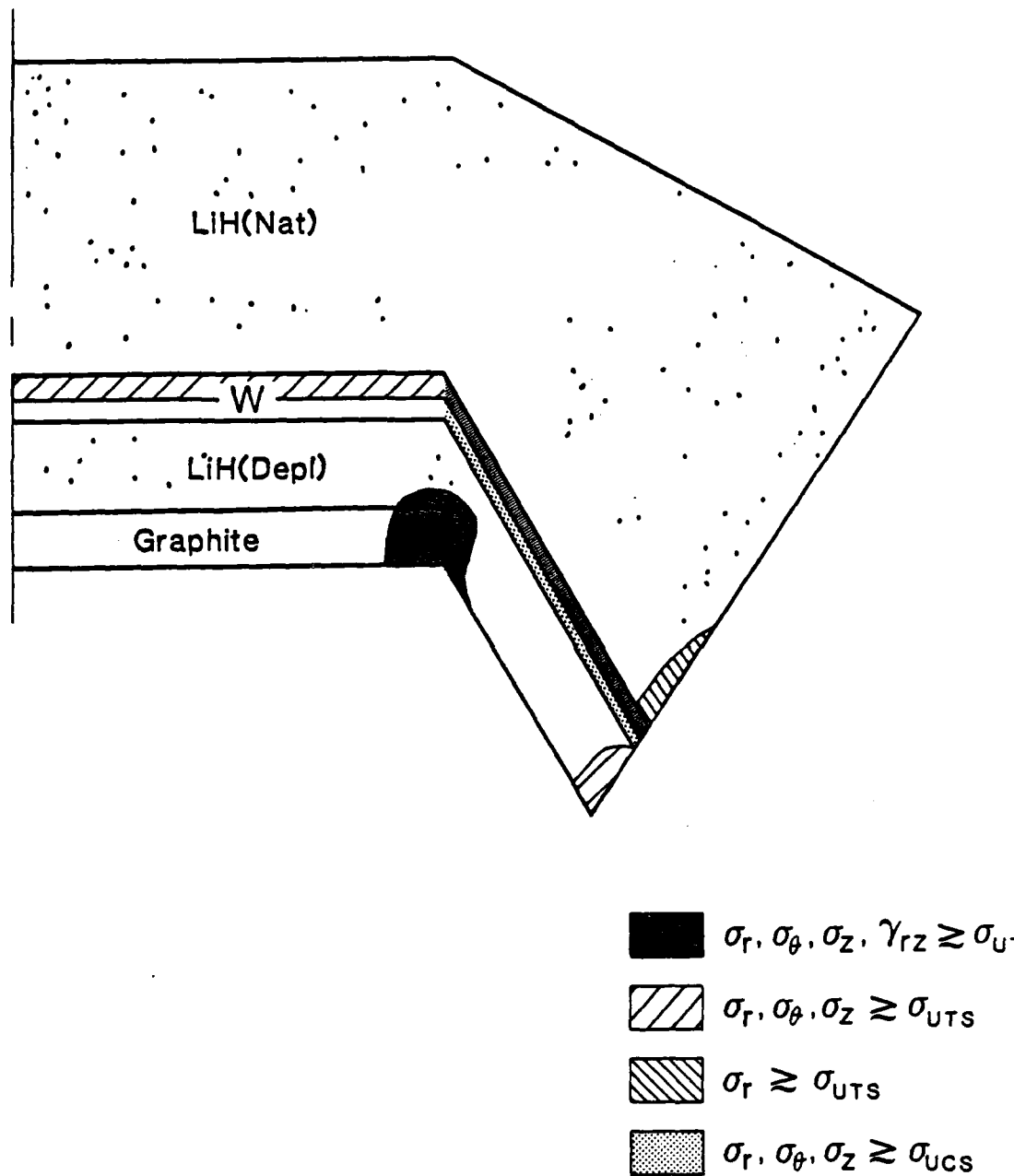


Figure 5.2-12 Regions of Concern of the Optimized Shield
from Stress Analysis with Outer Radial Surface
Free to Expand



radial surface pinned. The shield was discretized into 1288 elements and 1330 degrees of freedom. Because the purpose of this phase of the research was intended only to point out potential structural problem areas of the shield, the results are presented as shown in Figures 5.2-12 and 5.2-13.

The regions of high tensile and high compressive stressing are recorded on each figure. A stress was defined as high when its magnitude exceeded the ultimate stress for the respective stress state. The general sparseness of shading on either of the figures was the most immediate reaction to these results.

The case in which the radial surface was free to expand was intended to model the LiH not in contact with its outer casing. The radial surface region of LiH(Depl) before the W, experienced very

Table 5.2-5: Material Properties of Homogenized LiH-SS Honeycomb Matrix (99.5% LiH) Used in SHLDSTR Analysis

| <u>Property</u> | <u>Tension</u> | <u>Compression</u> |
|---------------------------------|---------------------|---------------------|
| $E_{rr} [\text{N/cm}^2]$ | 4.656×10^4 | 3.820×10^4 |
| $E_{zz} [\text{N/cm}^2]$ | 4.077×10^4 | 3.230×10^4 |
| $\epsilon_{zr} [\text{N/cm}^2]$ | 1.713×10^4 | 1.361×10^4 |
| v_{zr} | 0.183 | 0.179 |
| v_{rz} | 0.211 | 0.214 |

**Figure 5.2-11 Displacement Conditions for SP-100 Shield
for Stress Analysis**

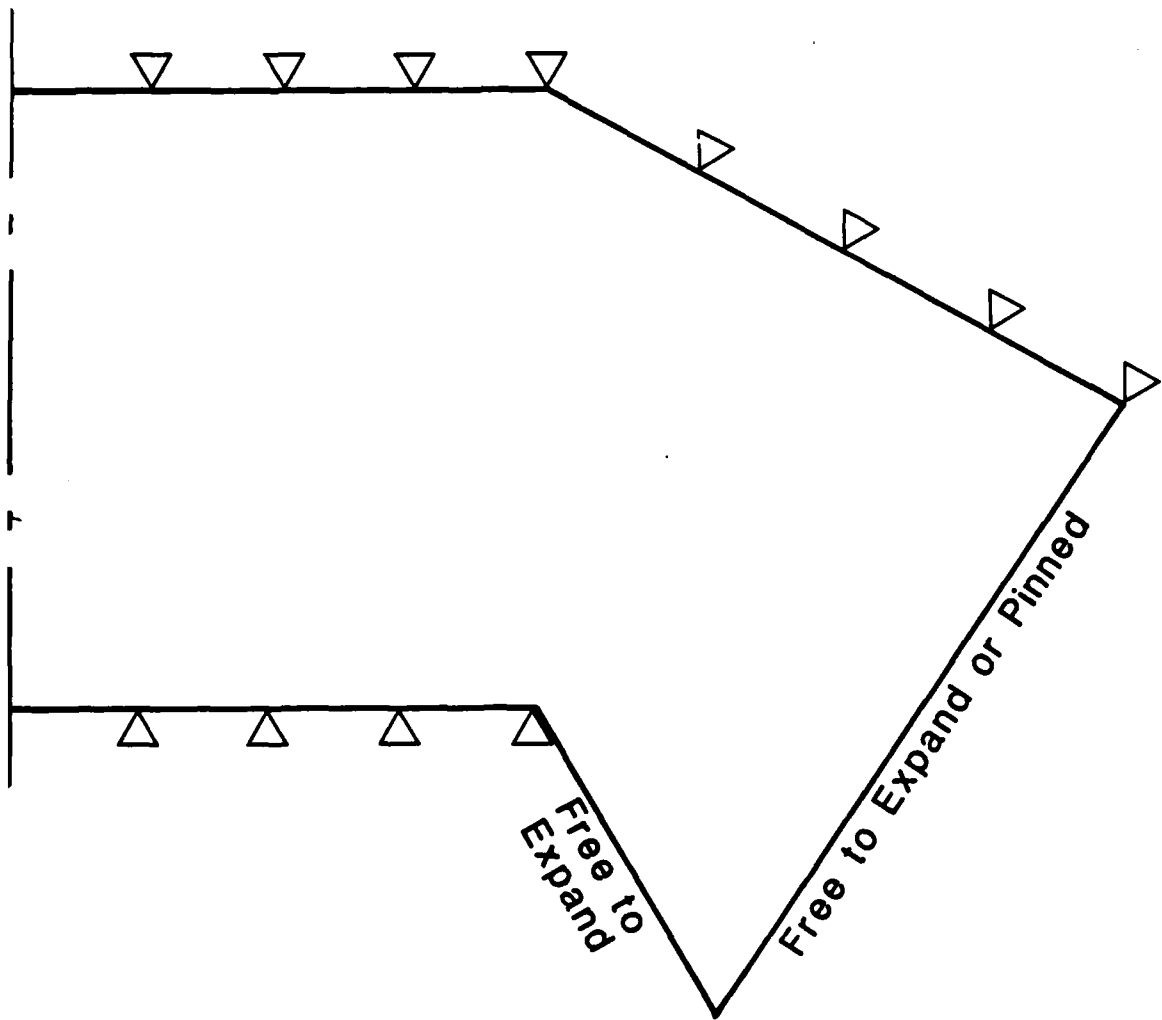


Table 5.2-4: Material Properties for SP-100 Shield
as Function of Temperature

| Material ⁽¹⁾ , ⁽²⁾ | Temperature | | | |
|---|-----------------------|-----------------------|-----------------------|-----------------------|
| | 293K | 339K | 539K | 689K |
| <u>LIN (Compression)</u> | | | | |
| $E_c^{(3)}$ | | 562,000 | 29,200 | 1f,700 |
| $\epsilon_{yp}^{(4)}$ | | 2,764 | | 4,830 |
| UTS | | 9,800 | 3,220 | 1,810 |
| $\alpha_T^{(5)}$ | 1.26×10^{-6} | 1.26×10^{-6} | 1.26×10^{-6} | 1.26×10^{-6} |
| $v^{(6)}$ | .106 | | .20 | |
| <u>LIN (Tension)</u> | | | | |
| $E_T^{(7)}$, ⁽⁸⁾ | 724,000 | | 37,600 | 21,500 |
| $\epsilon_{yp}^{(4)}$ | 663 | | | |
| UTS | 1836 | | 1347-1834 | 506-810 |
| $\alpha_T^{(5)}$ | 1.26×10^{-6} | 1.26×10^{-6} | 1.26×10^{-6} | 1.26×10^{-6} |
| $v^{(6)}$ | .106 | | .20 | |
| <u>SS-316</u> | | | | |
| $E_c, E_T^{(7)}$ | 1.90×10^6 | | 1.81×10^6 | 1.75×10^6 |
| $\epsilon_{yp}^{(4)}$ | 31,400 | | | 20,000 |
| UTS, UCS ⁽⁹⁾ | 62,100 | | | 47,600 |
| $\alpha_T^{(5)}$ | | $.304 \times 10^{-6}$ | $.912 \times 10^{-6}$ | 1.07×10^{-6} |
| $v^{(6)}$ | .306 | .306 | .306 | .306 |
| <u>Graphite.</u> | | | | |
| <u>Commercial Electrodes⁽¹⁰⁾</u> | | | | |
| E_c, E_T (// to axis) | | 276,000 | 277,000 | |
| E_c, E_T (L to axis) | | 704,000 | 830,000 | |
| ϵ_{yp} (// to axis) | | 102,000 | 105,000 | |
| UTS | | 1,650-2,520 | 1,650-2,600 | |
| α_T | | 7.0×10^{-6} | 7.2×10^{-6} | |
| v | | .25 | .25 | |
| <u>Tungsten</u> | | | | |
| E_c, E_T | | 39.6×10^6 | 39.3×10^6 | |
| ϵ_{yp} | | 18,000 | 13,500 | |
| UTS | | 37,500 | 35,000 | |
| α_T | | 4.44×10^{-6} | 4.44×10^{-6} | |
| v | | .204 | .206 | |

Notes:

- (1) All moduli and strengths given in [N/cm²].
- (2) All linear expansion coefficients given in [$\mu\text{L/L-K}$].
- (3) Lundberg, 1962.
- (4) Welch, 1967c.
- (5) E_T for LIN at elevated temperature based on
 $E_T^T = E_T^{293\text{K}} (E_C^T/E_C^{293\text{K}})$.
- (6) Reactor Handbook, Volume I, for v at 239 K; Estimated for v at 539 K.
- (7) Marks Handbook, 8th Edition.
- (8) Touloukian et al, Volume 12, 1975.
- (9) All Graphite data from Reactor Handbook, Volume I, 1960.
- (10) All Tungsten data from Metals Handbook, 9th Edition.

The boundary conditions for the shield are documented in Figure 5.2-11. The front and back surfaces of the shield were pinned, and the front angled surface was free to expand. The radiative heat transfer surface was run with either a pinned or free to expand boundary condition. These initial displacement conditions were based on the proximity of other reactor subsystems to the shield, and to gain an understanding of the significance of the boundary conditions at the radiative surface.

The material data used in this analysis are included in Table 5.2-4. There are many data gaps in the open literature for LiH. For example, experimental values for LiH elevated temperature tensile moduli, yield and ultimate tensile strength were not found, and engineering estimates based on compressive properties were constructed. For shield designs with temperatures exceeding the high 600 K range, neither tensile nor compressive data was found. Because of the uncertainty in the material data inputted to SHLDSTR, the effort required to incorporate the temperature dependent moduli and Poisson ratio's was deemed unproductive, and stress analyses were conducted with the 539 K data of Table 5.2-4.

Using the composite cylinders model and the transformation from local to global coordinates, the LiH and SS-316 data of Table 5.2-4 were homogenized with a 99.5% volume fraction of LiH. The weighted material properties for the LiH-SS matrix are included in Table 5.2-5 for the bilinear, orthotropic material (using 539 K data).

Using the temperature distribution for the graphite shield and the 539 K materials properties of Table 5.2-4, the stress distribution was determined for conditions of the radial surface free to expand and the

(Barattino et al., 1984), and the tensile and compressive material properties are not the same. Furthermore, the availability of elevated temperature properties in the open literature is severely limited for this weapons grade material.

Given the assumptions and limitations just mentioned, a first order analysis was made to determine the stress distribution in the SP-100 reactor shield based on the temperature results of the previous section. The tungsten was treated as an isotropic material, while the graphite and lithium hydride were considered orthotropic. For the graphite, the material direction parallel to the extrusion axis was coincident to the axial direction. Development of the LiH directional properties from composite theory was shown in Table 3.5-10.

However, these results were of significance from the standpoint of gaining an initial understanding of the regions of the shield where stressing may cause major problems. The simplification of the LiH - honeycomb matrix was done in a manner that would provide conservative results. The maintenance of axisymmetry implied an LiH channel (of the LiH-SS unit cell) running in each radial direction. Since the LiH is the weakest of the shielding materials, this simplification should provide a "worst case" analysis (in the sense of more yielding), as compared with the actual honeycomb structure. Also, the use of a constant moduli for a given stress state would produce larger stresses for a given displacement than the non-linear moduli would yield. Hence, the results to be presented might be considered as an upper bound to the final stress distribution throughout the shield.

from 502 K to 579 K as the product of (emissivity X view factor) decreased from 0.9 to 0.5. As with the maximum temperature, the sensitivity of T_{min} increased dramatically below a product of 0.7.

What these last figures have shown is that the shield design will have to be tailored somewhat to the environment in which it will be operated, based on thermal design constraints. Reactor shields that have been designed for low earth orbits cannot be operated in geo-synchronous orbits with the same thermal performance. While this finding is not particularly surprising to a thermal engineer, it is important that this message not be overlooked in the excitement of the moment when the next major space reactor program moves into full swing.

5.2.4 Stress Analysis Results. As mentioned earlier, the stress results presented as part of this research are based on a simplified approach of an extremely complicated problem. The constitutive equations of the LiH cast or cold-pressed into a stainless steel honeycomb matrix would be a complicated computational challenge for even a 3-D analysis. The need to maintain an axisymmetric geometric representation was the first approximation in these results. The homogenization of the LiH and stainless steel material properties using composite cylinders models represented another approximation. The requirement to map the homogenized properties from a local cartesian to a local cylindrical coordinate system, then to a different axisymmetric cylindrical system undoubtedly introduced another level of uncertainty.

To complicate matters a bit more, LiH has been shown to exhibit some creep behavior at the elevated temperatures of the shield

Figure 5.2-10 Sensitivity of Minimum Temperature with Variations in the Ambient Temperature, Emissivity, and View Factor for a Graphite-LiH(Depl)-W-LiH(Nat) Shield

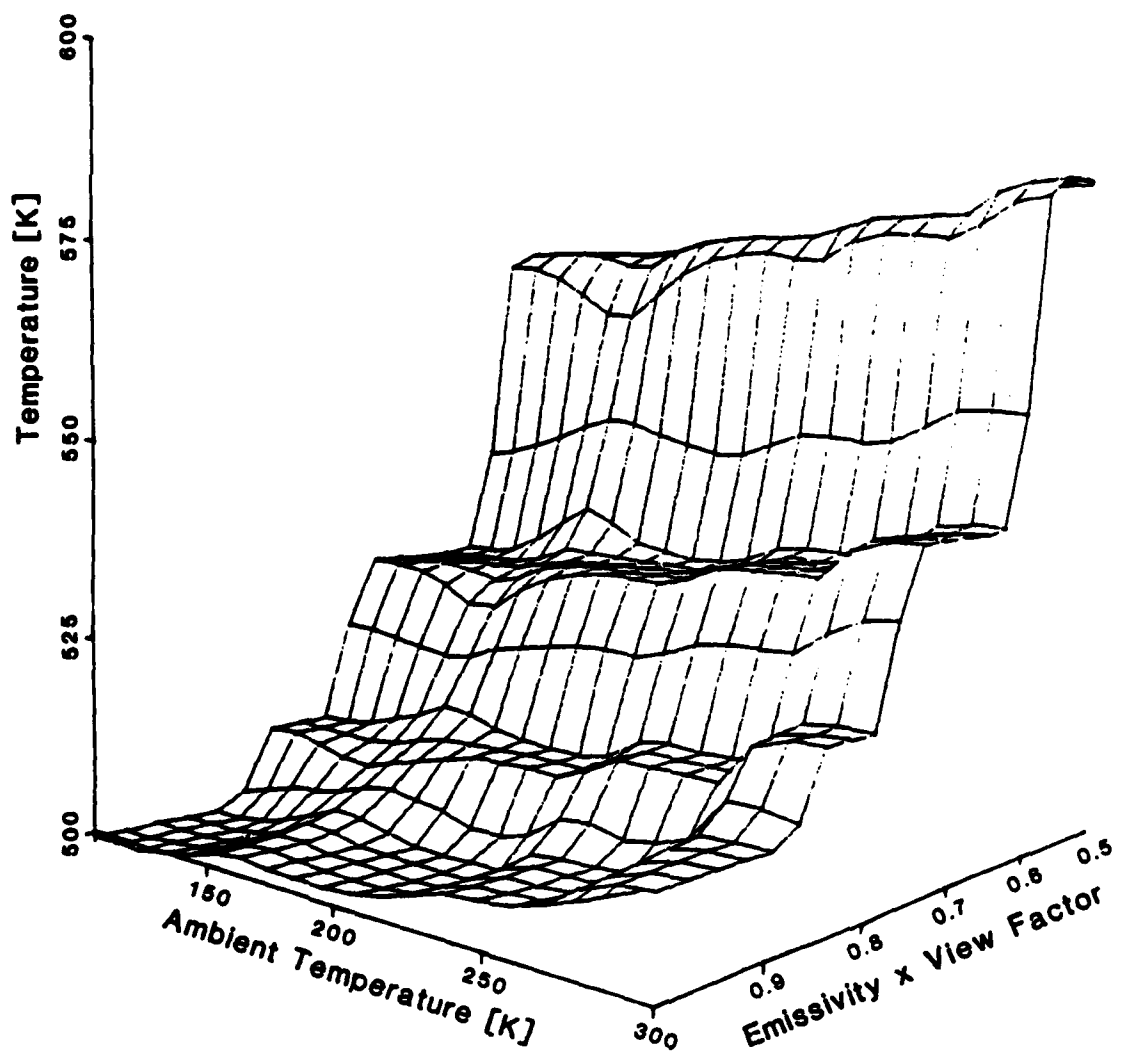


Figure 5.2-9 Sensitivity of Maximum Temperature with Variations in the Ambient Temperature, Emissivity, and View Factor for a Graphite-LiH(Depl)-W-LiH(Nat) Shield

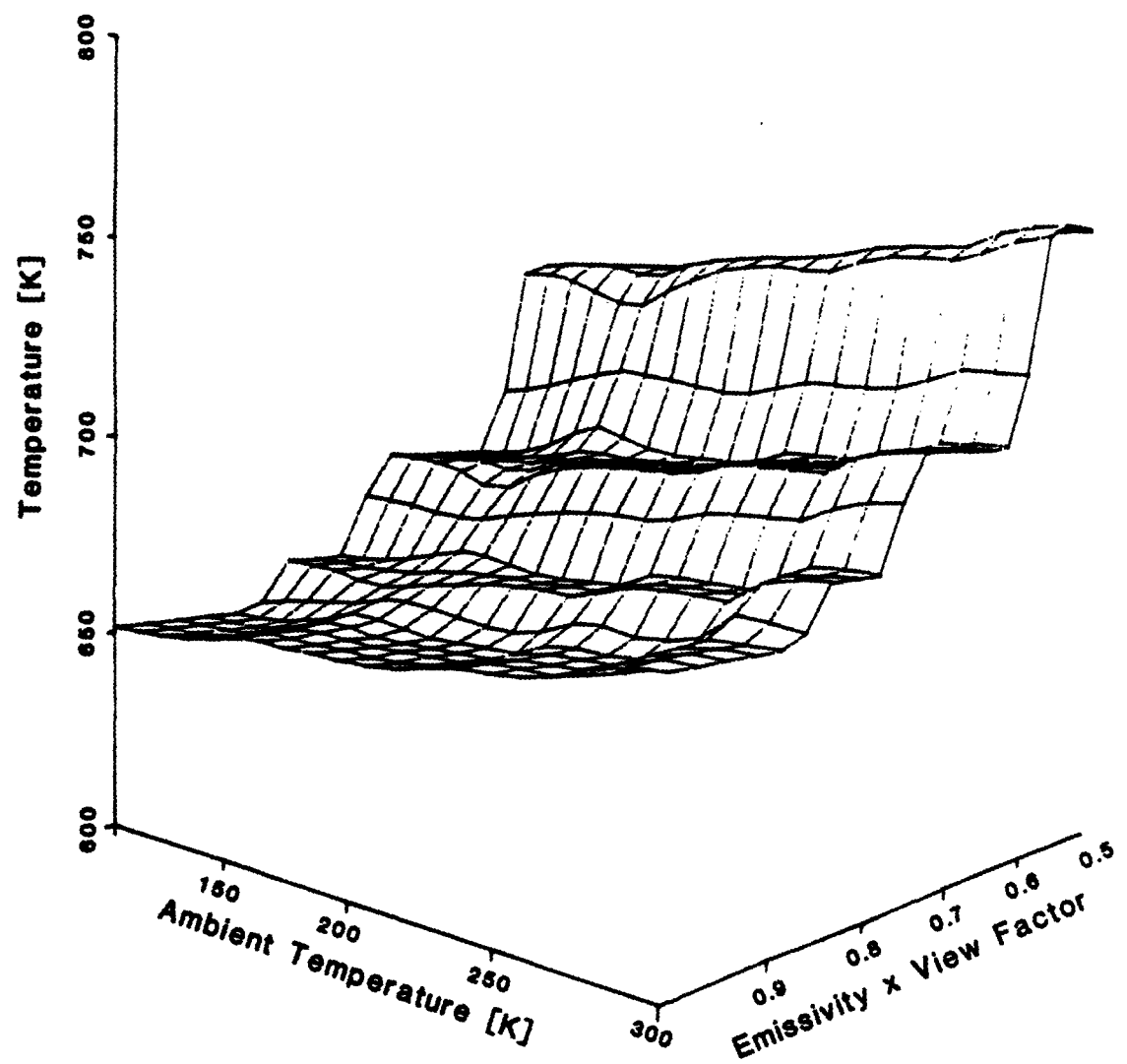
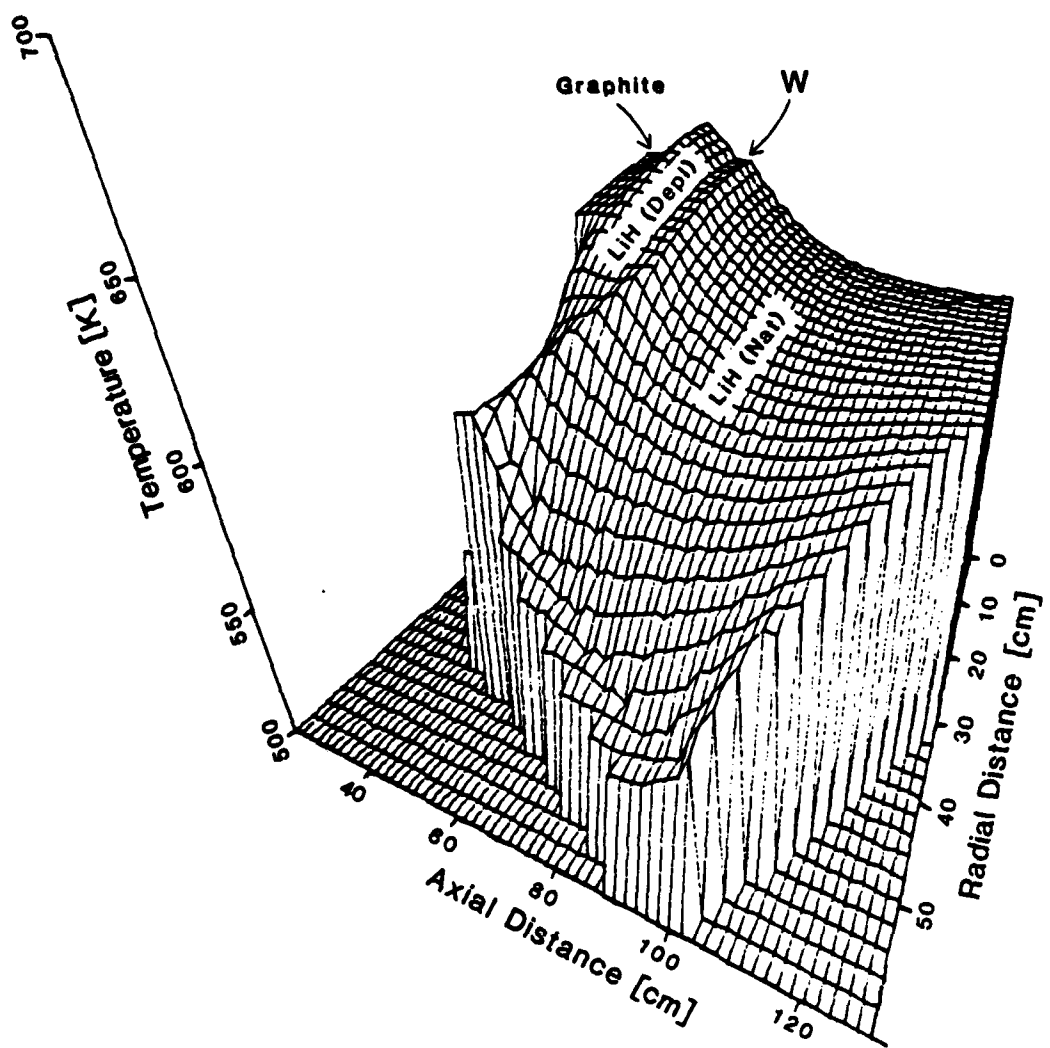


Figure 5.2-8 Temperature Distribution of a Graphite-LiH(Depl)-W-LiH(Nat) Shield for an SP-100 Reactor Operating at 1.66 MW_{th}

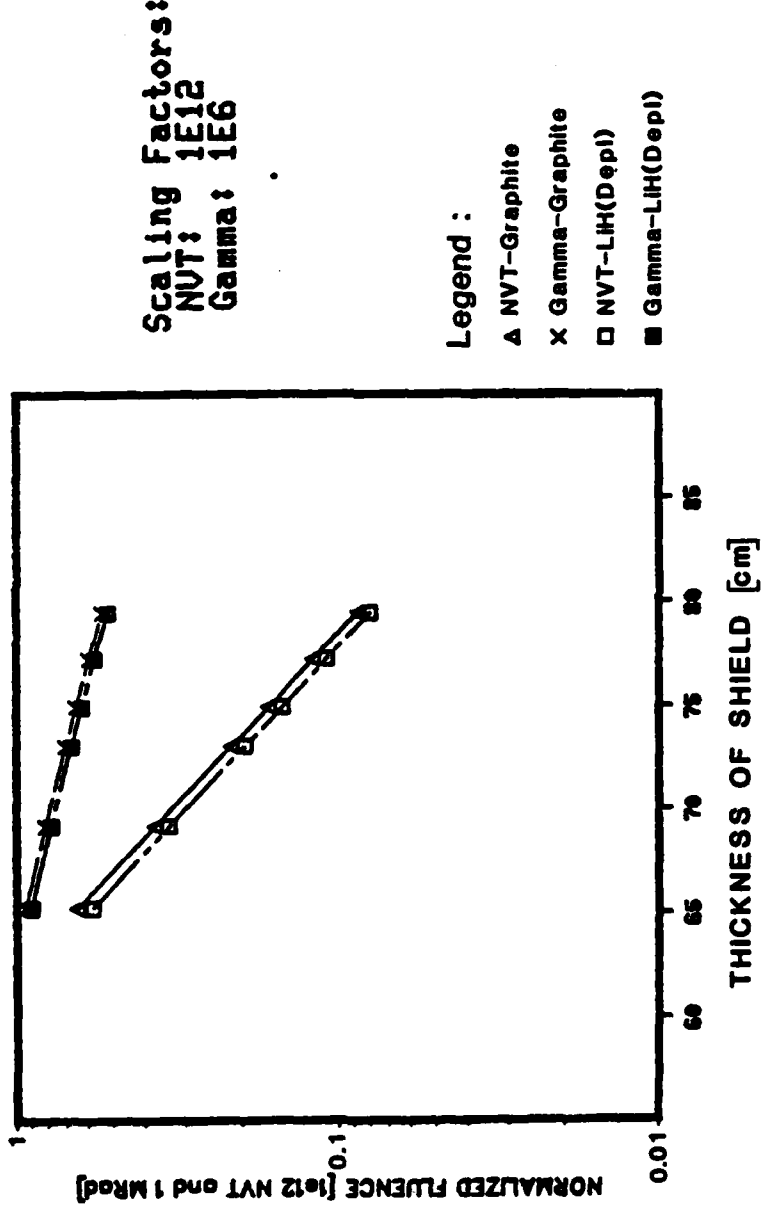


Similarly, the total energy deposited in the shield increased only slightly to 7.955 kW (from 7.881 kW) with the graphite disk included. This insignificant increase of .074 kW was attributable to the gamma activity of the carbon. The net result of this improved shield design is reflected in the temperature distribution of Figure 5.2-8. The maximum temperature of the LiH was reduced to 658 K, for a reactor operating at $1.66 \text{ MW}_{\text{th}}$. This shield design is now well below the acceptable upper temperature bound of 680 K for LiH throughout the entire shield.

The sensitivity of maximum and minimum temperatures of the LiH was investigated with respect to variations in ambient temperature, emissivity, and view factor. The results are included in Figures 5.2-9 and 5.2-10. From Figure 5.2-9, one observed that the ambient temperature had very little effect on the maximum temperature of the shield. The largest change in T_{\max} was 11 K when T_{ambient} varied from 100 K to 300 K (for emissivity X view factor = 0.83). The sensitivity of T_{\max} to the product of (emissivity X view factor) was much greater, particularly below 0.7. The swing in maximum temperature was actually quite significant, as with an increase of ~100 K (from 654 K to 753 K) as (emissivity X view factor) decreased from 0.9 to 0.5. While this range may be unrealistically large for a 300 km orbit, the design engineer must nevertheless be aware of this uncertainty, particularly if the reactor is to be considered for a power upgrade.

The sensitivity of minimum LiH temperature to variations in these same parameters is included in Figure 5.2-10. Generally, the same trends apply to minimum temperature as discussed for maximum temperature sensitivities. For an ambient temperature of 200 K, T_{\min} increased

Figure 5.2-7 7 Year Fluences of SP-100 Reactor at 25 m
Dose Plane with LiH(Depl)-W-LiH(Nat) and
Graphite-LiH(Depl)-W-LiH(Nat) Shields



optimization required that the tungsten be located 13.4 cm into the shield to minimize the effects of secondary gammas emerging from the shield. Heat transfer optimization required the highly conductive material to be located in the front portion of the shield to keep LiH temperatures within tolerable limits. Without increasing the weight or volume of the shield, a material with the neutronic characteristics of LiH(Depl) and thermal characteristics of W, added to the front of the shield could fill this need.

A candidate material selected for further investigation was graphite. With a theoretical density only twice that of LiH, replacing the first 2 cm of LiH(Depl) from the shield centerline to the 27.5 cm radius would increase the shield mass by 3.94 kg, or 0.65% of the total shield mass. (Of course, this amount of mass could be saved by reducing the LiH(Nat) thickness by 2.3 cm - still satisfying fluence requirements). The inclusion of a graphite disk at the front of the shield, with a thermal conductivity slightly greater than that of tungsten, should result in further reduction of the maximum LiH temperature below the earlier recorded value of 715 K.

Both carbon-12 (atom % 98.9) and carbon-13 (atom % 1.1) have small radiative capture cross sections (on the order of milli-barns), which result in mev gammas. However, because the cross section is so low and the tungsten follows the graphite, one would not expect any appreciable effect by the carbon on dose plane fluences. This expectation is verified in Figure 5.2-7. The fluences with and without the graphite disk are plotted for the LiH(Depl)-W-LiH(Nat) shield. From this figure, it is seen that the fluences at the dose plane remain below SP-100 requirements for both gammas and neutrons.

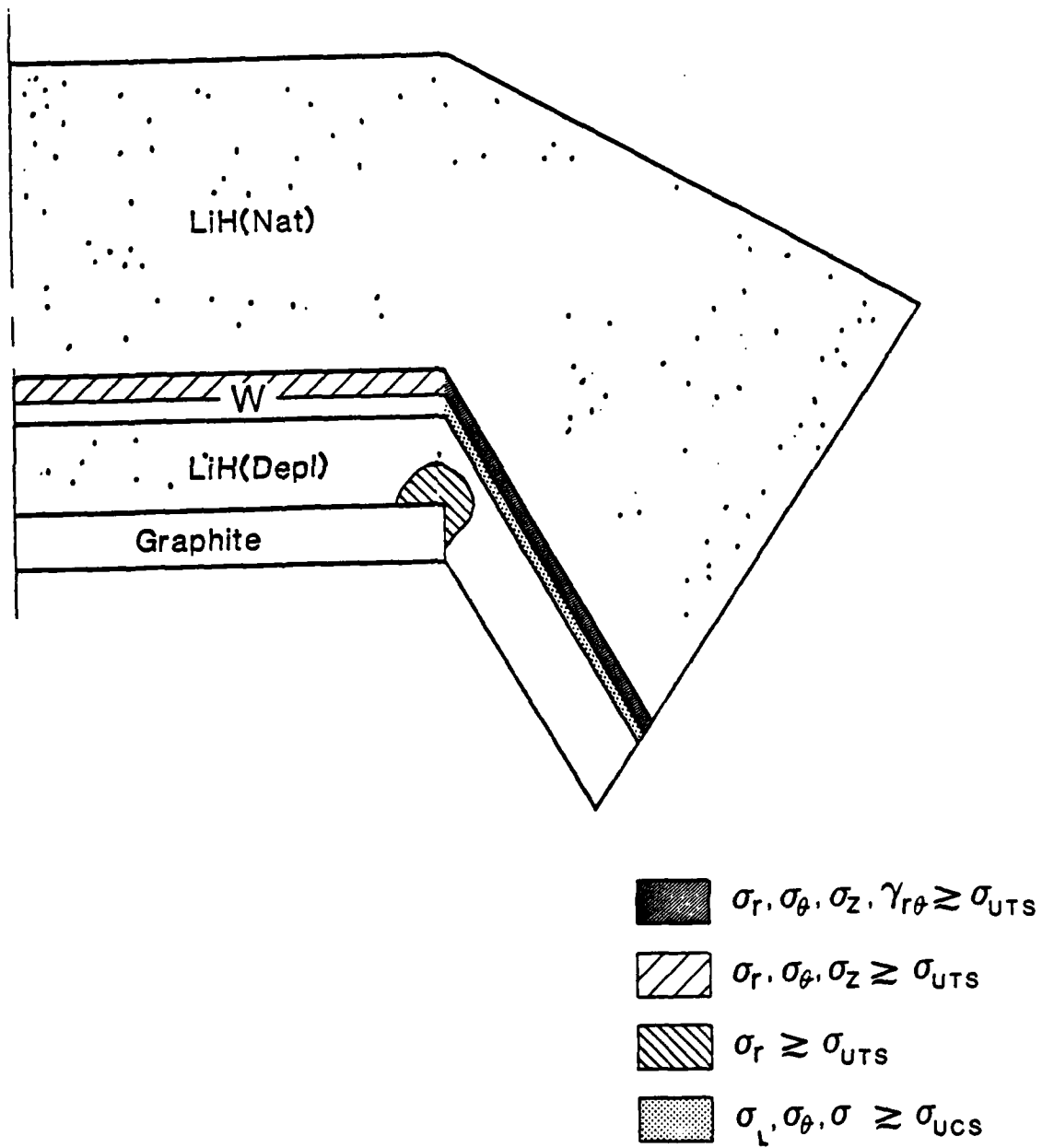
also reflected by the increase in temperatures for each radial position as one moves beyond the axial midpoint of the shield. However, these effects are quite small, as the respective neutron and gamma fluxes have been reduced by at least several orders of magnitude.

Thus, it has been shown that the optimal shield for radiation protection was the worst from the thermal performance standpoint. However, by making minor concessions in radiation protection (but still remaining below tolerable fluence limits), a passively cooled shield can be designed by paying close attention to the coupling of radiation transport, energy deposition, and heat transfer characteristics of the shielding materials. While the LiH(Depl)-W-LiH(Nat) proved to be an excellent candidate shield design for this reactor, the next section shall present a slightly modified design that provided even greater improvements on the thermal performance, without degrading the radiation protection performance of the shield.

5.2.3 Improved SP-100 Shield Design. With the knowledge obtained from the previous discussions, some fine tuning of the SP-100 shield was made to demonstrate a practical application of our enhanced understanding of space reactor shield design. Having presented in detail the four configurations of Table 5.1-1, the LiH(Depl)-W-LiH(Nat) shield was shown to be the best selection when considering both radiation protection and maximum temperature constraints. However, an improved version of this design could be designed, which will have a lower maximum temperature and a smaller temperature range throughout the shield.

The importance of the tungsten location was seen from both a radiation transport and thermal transport perspective. Radiation transport

Figure 5.2-13 Regions of Concern of the Optimized Shield
from Stress Analysis with Outer Radial Surface
Pinned

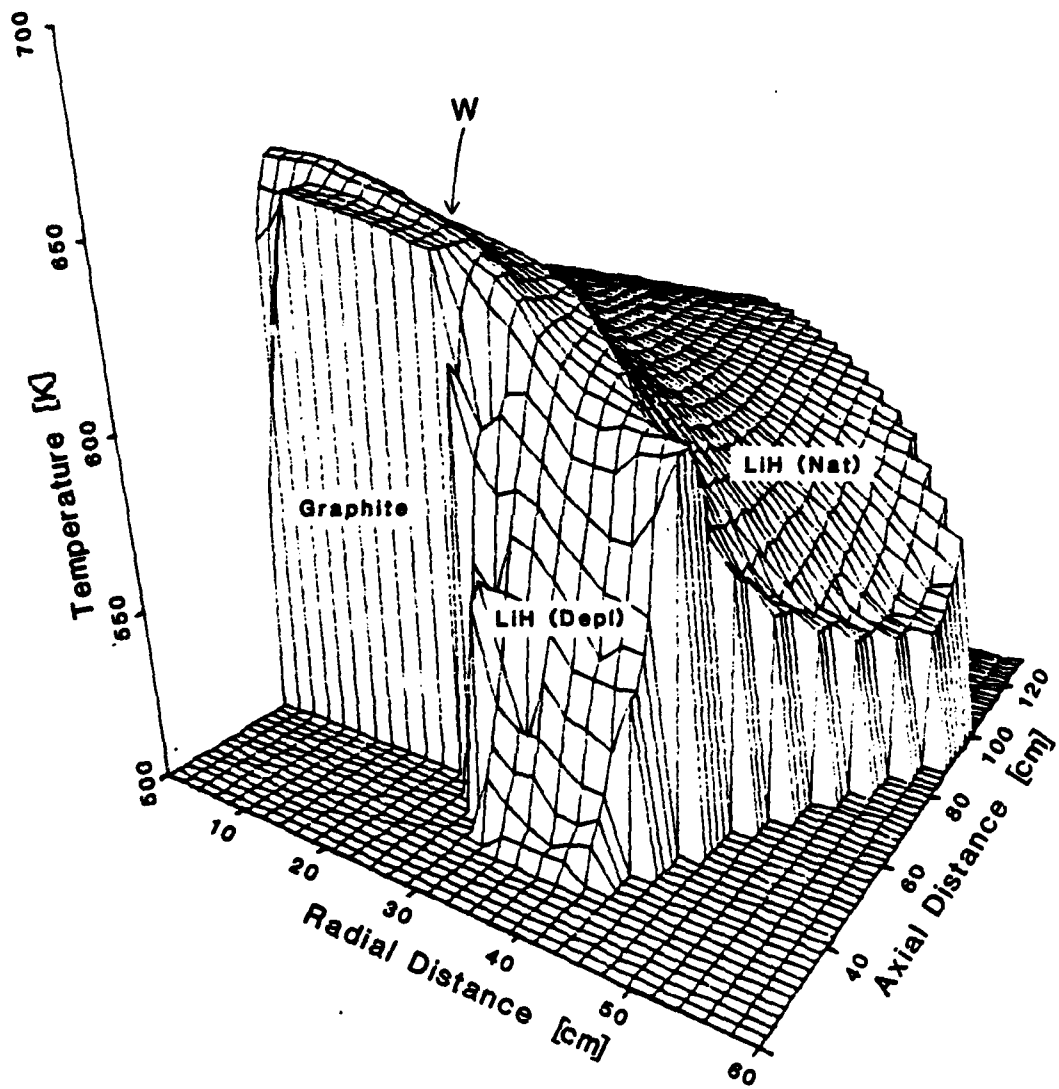


large principle direction stresses, and excessive LiH cracking would be a major concern in this region. The LiH(Nat) region behind the W, experienced large radial stresses also, but significantly smaller hoop, axial and shear stresses. The final region of concern for the LiH was at the outer disk of the graphite. With the sharp elbow of the front shield surface ($r=27.5$ cm) which is free to expand, the possibility of excessive localized stresses at the Graphite-LiH interface is an engineering concern that should be addressed in a detailed shield design.

Figure 5.2-14 is a front view of the temperature distribution for the optimized shield. Examination of this figure reveals why the stresses at the outer surface before the W and at the graphite-LiH interface were so large. The temperature gradients in these regions were rather dramatic as seen in this figure. The large temperature drop at the graphite-LiH interface was due to the significant decrease in energy deposition with a radial distance beyond the radial reflector of the core. However, the unanticipated "hump" in temperature at the radiative surface was caused by the combination of heat transferred from the graphite into this region and the relative location of the high conductivity tungsten, further into the shield. Such a result might be discouraging from the standpoint that after meeting fluence and temperature requirements, the shield would fail to maintain its structural integrity.

This concern was remedied by the results of Figure 5.2-13. By insuring very good contact of the LiH with its outer casing, the large tensile stresses at the radial surface have been eliminated. The compressive stresses generated throughout the shield were well below the ultimate compressive stress at elevated temperature. While knowing

Figure 5.2-14 Temperature Distribution of a Graphite-LiH(Depl)-W-LiH(Nat) Shield (View from Front Surface)



from practical experience that some localized cracking in the LiH will occur, we at least have a better understanding of the importance of limiting the movement of LiH at the radial surface.

For either radial surface displacement condition, the stresses in the tungsten were quite large. However, the magnitude of stresses were attributable to the linear elastic approximation used in this analysis. For unalloyed tungsten, the ductile - brittle transition temperature (DBTT) is ~450 K. By alloying the tungsten with only 3% rhenium, the DBTT is reduced to less than 100 K (Klopp, 1984). Hence, the tungsten at the operating temperature of the shield will have exceeded its DBTT. While little creep is expected in W below 100°C temperature (Hoffman, 1984), the plasticity of the W is quite evident from the stress-strain curves at elevated temperatures (Metals Handbook, 1975). Hence, the magnitude of stresses was greatly overestimated using linear analysis. Again, from practical experience, the tungsten will have no trouble maintaining its structural integrity at the shield operating temperatures.

The limitations of this first attempt (ever) at an analytic stress analysis of the shield have been discussed in detail. Furthermore, the time dependent effects of radiation embrittlement and thermal annealing were not discussed [Ma, 1983]. Nevertheless, the results of this upper bounding analysis of the thermally induced stresses in the radiation shield were encouraging. The displacement conditions of the free surface were shown to require special design attention. Also, the introduction of a graphite disk for enhanced heat removal at the front of the shield created some extra design considerations at the Graphite-LiH boundary. Of course, localized design concerns can be handled for a

shield meeting the radiation fluence and thermal transport limitations associated with the SP-100 reactor and the LiH shield.

5.3 Uncertainty Estimates.

The results provided in Sections 5.1 and 5.2 represent most probable estimates of the energy deposition, temperatures, and stresses that physically could be expected in the shield during steady-state operation. As with any analyses, the actual values were calculated with data and numerical methods in which some uncertainties are inherently present. In this section, reasonable estimates for the error bounds will be presented for the energy deposition, temperature distribution and stress results.

Uncertainty analysis for each of the technical areas ultimately translates into error introduced by input data, accuracy of the governing equation in representing the physical situation, uncertainties in material data, and numerical errors. The numerical errors result from discretization error and round-off error. The sum of these two errors is often referred to as solution errors. The discretization error is due to the approximation introduced in the expansion of the state variable by a finite series of unknown quantities (ie. nodal fluxes, temperatures or displacements). Round-off error is simply that error resulting from the finite word length associated with a digital machine, and corresponds to errors introduced with the method used to solve the algebraic system of equations (ie. Gaussian elimination or iterative solvers). With regard to numerical uncertainties, one must be aware that the state-of-the art for finite element error analysis is

still at the stage where the uncertainty analysis is uncertain, particularly for analyses over highly irregular meshes [Utku and Melosh, 1984].

The heat generation was shown earlier to be a function of the reaction rate times the energy released per reaction. Upper and lower bounds on the energy deposition can be estimated by the product of the uncertainties associated with each of the variables. Applying the uncertainty estimate method of Kline and McClintock, the uncertainty in volumetric heat generation is determined from [Holman, 1971]:

$$U_H = \left[\left(\frac{\partial H}{\partial N} U_N \right)^2 + \left(\frac{\partial H}{\partial \sigma} U_\sigma \right)^2 + \left(\frac{\partial H}{\partial \Phi} U_\Phi \right)^2 + \left(\frac{\partial H}{\partial \bar{E}} U_{\bar{E}} \right)^2 + \left(\frac{\partial H}{\partial NEH} U_{NEH} \right)^2 \right]^{1/2} / H$$
(5.3-1)

where:

U_i = Uncertainty of the i -th variable

H = Volumetric heating rate $\sim N \sigma \bar{E}$

N = Number density

σ = Microscopic cross section

Φ = Neutron or gamma flux

\bar{E} = Energy released per reaction

NEH = Numerical error in heating rates

A complete uncertainty analysis for heat generation would require a summation of individual uncertainties over each nuclide, type of reaction, and energy group. However, by inspection of Equation 5.3-1, one sees that the large uncertainty terms will dominate the total uncertainty. Hence, knowing that the uncertainties associated with

lithium are the major contributors, Equation 5.3-1 can be used to focus-in on the Li-6 and Li-7 nuclides, and the resulting uncertainty will be a conservative estimate. With this simplification, Equation 5.3-1 takes the form:

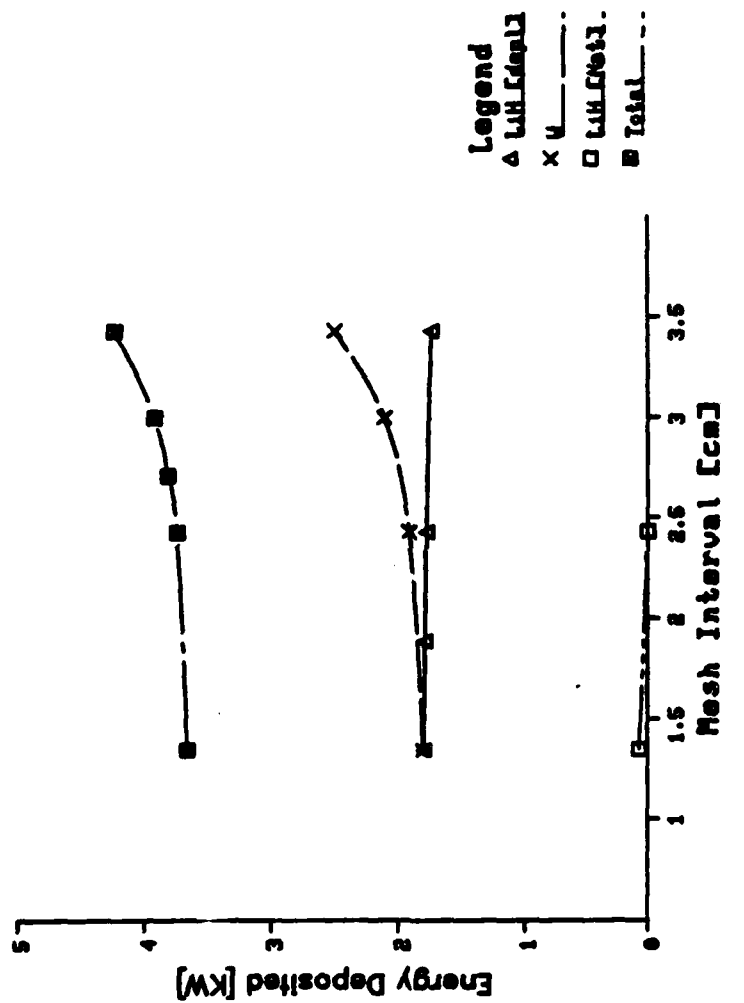
$$U_H = [U_N^2 + U_\sigma^2 + U_\phi^2 + xU^2 + (1-x)U^2 + U^2]^{1/2} \quad (5.3-2)$$
$$\bar{E}_{Li6} \quad \bar{E}_{Li7} \quad NEH$$

where x is the fraction of heating due to Li-6, and $(1-x)$ represents heating due to other nuclides. Recalling that ~39% of heating occurs below 1 ev, and the (n,α) reaction of Li-6 dominates at thermal energy, the value of x is taken as 0.39.

An additional term has been added to Equation 5.3-1, U_{NEH} , to account for the numerical error in heating rates associated with the mesh interval. For the elliptic boundary value problem, it has been shown that the numerical error using bilinear elements will be proportional to h^2 , where h is the mesh interval (Bramble and Zlamal, 1970). However, this relative measure of error does not give the engineer a proper perspective in terms of the proportion of numerical error to input data error. This topic is currently under research, with error bounds based on the governing equation and energy norms being considered within the structural community (Zienkiewicz and Morgan, 1983).

Nevertheless, the numerical uncertainty was quantified by repeated calculations of energy deposition in the shield for varying mesh intervals. For the SP-100 reactor with an LiH(Depl)-W-LiH(Nat) shield, the effects of mesh interval on total energy deposited are included in Figure 5.3-1. For these calculations, the W is 13.4 cm into the shield and the shadow shield geometry was simplified to a 40 cm cylinder

Figure 5.3-1 Change in Energy Deposited with Mesh Spacing for LiH(Dep1)-H-LiH(Nat) Shield from FEMP2D



shield. The average mesh spacing was determined by a volume weighting of each radial mesh interval, then arithmetic averaging with the axial mesh interval.

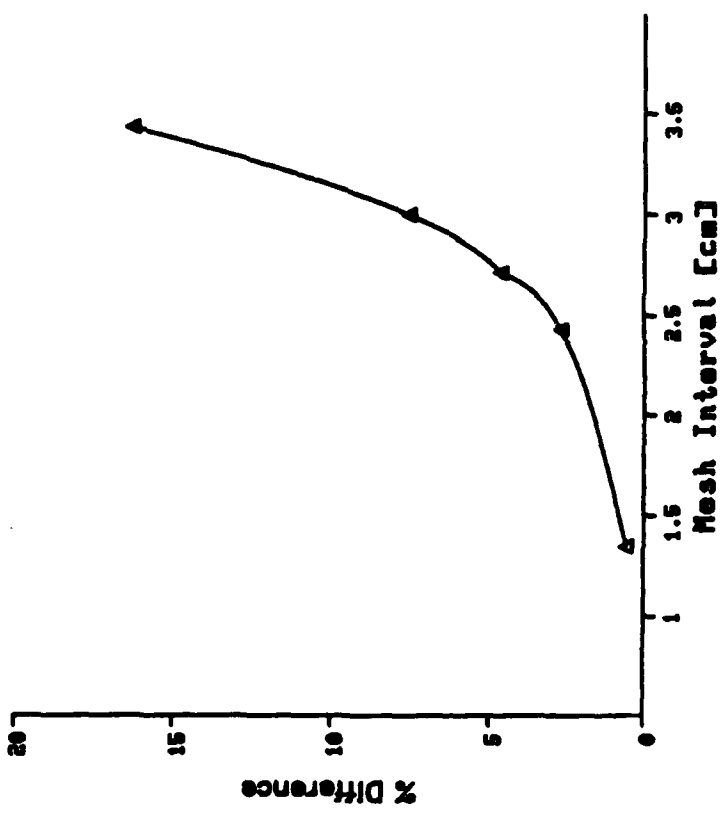
From Figure 5.3-1, we see that energy deposition in W is fairly sensitive to mesh interval. The effect is much greater in the LiH(Nat) although unnoticeable because of the small amount of heating in this region. This sensitivity is based on the large absorption cross sections at thermal energies for W and LiH(Nat). In fact, the solution provided negative heating rates throughout the LiH(Nat) for mesh intervals >2.5 cm.

Using the total energy deposition curve of Figure 5.3.1, the exact energy deposition was determined by projecting the curve to the y-axis and using the y-intercept (3.64 kW), corresponding to a zero mesh interval. With this result, the error as a function of mesh interval was calculated, and is included as Figure 5.3-2. At a mesh interval of 1.4 cm, the error was ~0.6%, and at 3.4 cm the error was 16.3%.

Thus, one readily sees the sensitivity of energy deposition to mesh spacing, and the need to 'pay the price' in terms of computational complexity when performing radiation transport calculations for SP-100 shielding calculations. For all calculations presented earlier, the mesh spacing was ~0.9 cm. Hence, we conclude that the numerical uncertainty associated with the energy deposition results presented in this research was less than $\pm 0.5\%$.

Table 5.3-1 lists the uncertainty for the major variables from each technical area. The uncertainty associated with the flux is based on the use of P_1 approximation in the 2-D radiation transport calculation. The flux uncertainty of Table 5.3-1 is based on a 1-D calculation using the SP-100 reactor system to determine the difference in the

Figure 5.3-2 Uncertainty in Energy Deposited with Mesh Spacing
for LiH(Depl)-W-LiH(Nat) Shield from FEMP2D



total heat deposited in the shield for a P_1 flux expansion compared to a P_{15} flux expansion. Any numerical error built into these results, would be included in both P_1 and P_{15} results. The flux uncertainty represents the error in heating rates in modelling the angular component of flux.

The data of Table 5.3-1 was inserted into Equation 5.3-2 to obtain $U_H = 5.9\%$. Thus, the uncertainty associated with the energy deposition was estimated as $\pm 5.9\%$. As a matter of interest, the two major sources of uncertainty are the P_1 approximation in the flux expansion and the energy release per reaction for the Li-7 nuclide. Even if a higher order flux was used, the high uncertainty in heating kermas from MACK IV would result in no gain in confidence in the energy deposition.

The temperature calculations were based on the heating rates determined from the radiation transport phase of this project. Thus, the temperature uncertainty must include uncertainties due to thermal heat transfer data, numerical error, and that already determined for the energy deposition.

In an analysis analogous to that of the volumetric heat generation, the temperature uncertainty can be determined from:

$$U_T = \left[\left(\frac{\partial T}{\partial H} U_H \right)^2 + \left(\frac{\partial T}{\partial k} U_k \right)^2 + \left(\frac{\partial T}{\partial \epsilon VF} \frac{U}{\epsilon VF} \right)^2 + \left(\frac{\partial T}{\partial T^o} U_{T^o} \right)^2 + \left(\frac{\partial T}{\partial NET} U_{NET} \right)^2 \right]^{1/2} / T \quad (5.3-3)$$

where:

H = Heating rate

k = Thermal conductivity

Table 5.3-1: Uncertainty Error Estimates For Major Variables Involved in This Research

| <u>Variable</u> | <u>Source</u> | <u>% Uncertainty</u> |
|---|--|-----------------------------|
| Density ⁽¹⁾ | Tufts Univ (Messer, 1960) | .90 |
| Microscopic ⁽²⁾ Cross section | NASA TM X-483 (Smith and Miser, 1963) | 1.4 |
| Flux | P ₁ vs P _{1,5} Calculation with FEMP1D | 2.4 |
| Energy Deposited per reaction | Nucl, Sci, & Engi. 56, 360-380 (1975) (Abdou and Maynard, 1975) | 0.023 (Li-6) 4.41 (Li-7) |
| Thermal Conductivity | Thermophysical Properties of Matter Vol. 1 (Touloukian et al., 1970) | 2.0 (W) 10.8 (LiH) |
| Emissivity | Thermophysical Properties of Matter, Vol. 9 (Touloukian, et al., 1972) | 2.5 |
| Elastic Moduli ⁽¹⁾ | Atomics International (Lundberg, 1962) | 8.5 |
| Thermal Expansion ⁽¹⁾ Coefficient | Atomics International (Welch, 1967c) | 10.0 |
| Poisson's Ratio ⁽¹⁾ | Atomics International (Welch, 1967a) | 11.3 |

Notes:

(¹) Based on LiH Data

(²) Based on Li Absorption cross section

$\overline{\epsilon VF}$ = Emissivity x view factor

T^* = Ambient temperature

NET = Numerical error for temperature

From Figures 4.2-15 and 4.2-16 there was very little effect on the maximum and minimum temperature of the shield due to changes in ambient temperature. Hence, the ambient temperature term of Equation 4.3-3 can be neglected.

While an analytic solution for the temperature obviously is not available, we nevertheless know that the temperature is directly proportional to heat generation and indirectly proportional to emissivity, view factor, and thermal conductivity. This is expressed as:

$$T \sim \frac{q''' L}{k \overline{\epsilon VF}} \quad (5.3-4)$$

For the moment, let's consider only uncertainties dealing with input data. The numerical error will be discussed shortly. From Equation 5.3-4, the temperature uncertainty can be expressed as:

$$U_T = L \left(\frac{1}{k \overline{\epsilon VF}} U_H \right)^2 + \left(\frac{q'''}{k^2 \overline{\epsilon VF}} U_k \right)^2 + \left(\frac{q'''}{k \overline{\epsilon VF}^2} U_{\overline{\epsilon VF}} \right)^2]^{1/2} / \frac{q'''}{k \overline{\epsilon VF}} \quad (5.3-5)$$

From Equation 5.3-5, we see that the largest uncertainty in temperature will occur at the hottest portion at the front of the shield, where q''' is largest and k is smallest. The characteristic length of Equation 5.3-4 does not appear in Equation 5.3-5 since this uncertainty is zero.

Substituting the appropriate data of Table 5.3-1 and using actual values in Equation 5.3-5 for the hottest LiH nodal temperature, the

certainty in temperature is determined as $U_T = 12.4\%$. Hence, the uncertainty in temperature due to input data was $\pm 12.4\%$, with the thermal conductivity of LiH accounting for most of this value.

As an alternative to the results of Equation 5.3-5, bounds on temperature due to uncertainties in input data were calculated by simultaneously considering extrema in energy deposition, emissivity, and thermal conductivity. For the graphite-LiH(Depl)-W-LiH(Nat) shield, this meant varying the internal heat generation values by $\pm 5.9\%$, varying thermal conductivity by $\pm 10.8\%$, and varying emissivity by $\pm 2.0\%$.

With these uncertainties included, the temperature distribution throughout the shield was recalculated. The maximum change in any nodal temperature from the baseline case for the optimized shield was taken to be the temperature uncertainty. For the case of increased heat generation, and decreased thermal conductivity and emissivity (Case I), the maximum temperature changed from 664 K to 697 K; the minimum temperature changed from 511 K to 515 K; and the maximum percent change in any nodal temperature was +5.0%. For the case of reduced heat generation and increased thermal conductivity and emissivity (Case II), the maximum temperature changed from 664 K to 637 K; the minimum temperature changed from 511 K to 506 K; and the maximum percent change in any nodal value was -4.5%. Thus, the maximum uncertainty in temperature from these calculated values was about $\pm 5.0\%$.

The difference between the temperature uncertainty calculated by analytic versus numerical methods was a substantial 7.4%. The basis for this difference lies in the non-linearity of the problem. As heat

AD-A158 188

COUPLED RADIATION TRANSPORT/THERMAL ANALYSIS OF THE
RADIATION SHIELD FOR A. (U) AIR FORCE INST OF TECH
WRIGHT-PATTERSON AFB OH W J BARATTINO JUL 85

4/4

UNCLASSIFIED

AFIT/CI/NR-85-53D

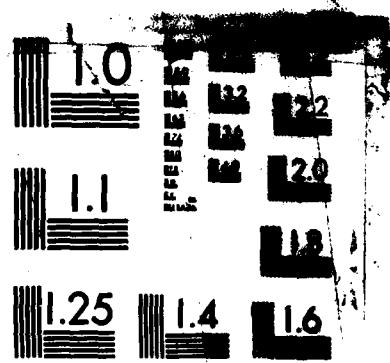
F/G 18/6

NL

END

FILMED

DTIC



MICROCOPY RESOLUTION TEST CHART
NATIONAL BUREAU OF STANDARDS-1963-A

rejection conditions worsen (ie. Case I conditions), the radiative heat transfer mechanism becomes more effective in rejecting heat. Thus, the linear effects of Equation 5.3-5 do not accurately predict the non-linear temperature effects of either case I or case II perturbations. For this reason, the temperature uncertainty value of $\pm 5.0\%$ due to input data is considered more accurate.

The numerical error was shown to consist of discretization error, and round-off error. However, J.Roy (1971) showed that when working in double precision throughout the entire problem, from matrix generation to equation solution, the effects of round-off errors will be negligible as compared to discretization error. Since SHLDTEMP and SHLDSTR were both written in double precision, discretization error will be the only numerical uncertainty considered. If there were no discretization error, the exact and approximate solutions would be the same (in the absence of all other errors). This would manifest itself in an energy balance of $q_{in} = q_{out}$. When the energy balance is not exact, the difference can be related to discretization effects.

Using the same simplified shield geometry in determining numerical error for radiation transport, the temperature analysis was performed for the 40 cm LiH(Depl)-W-LiH(Nat) shield using the fine mesh heating rates from the FEMP2D calculations. The mesh interval⁷ was varied and the relative difference between the total energy deposited and energy radiated from the shield was calculated, after the final temperature distribution was solved for. These results are included in

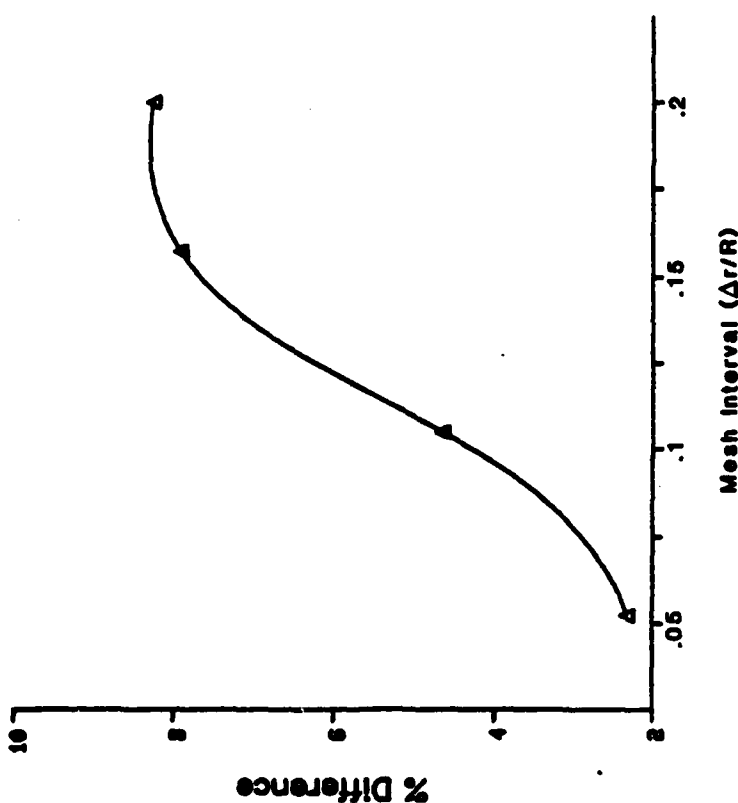
⁷ Mesh interval here represents the distance between nodes to the total length (ie. $\Delta r/R$).

Figure 5.3-3. From this figure, a mesh interval of .05 resulted in a temperature uncertainty of 2.3%, and an interval of 0.1 resulted in 4.7% uncertainty. The average mesh interval was ~0.06 for the graphite shield.

Returning to the graphite shield, the total energy deposited was 7.955 kW as calculated in FEMP2D. The 3 node triangular mesh of SHLDTEMP was overlayed onto the 4 quadrilateral mesh of FEMP2D, and the heating rates were interpolated to the temperature nodal coordinates. The total energy deposition in the shield calculated with the triangular mesh was 8.253 kW. Thus, an error in energy deposition of 3.7% was incurred in the interpolation process.

After the final temperature distribution was determined, the net energy flow out of the shield was determined as 7.879 kW. Hence, the numerical error was estimated by the relative difference of 8.253 kW and 7.879 kW, or 4.5%. However, a comparison of the energy deposition from FEMP2D and the final heat flow out of the shield resulted in an error of only 1.0%. Furthermore, of the 7.879 kW flow out of the shield, all but 1.7% of this value occurred at the radiative heat transfer surface. Since all other surfaces were supposedly insulated, the 1.7% is additive with the 4.5% resulting in a gross numerical error of 6.2%. But, because of the cancelling effects of the error components, the overall net numerical error is estimated as 2.7% (sum of additive errors of 1.0% and 1.7%). The sum of error components appear to be somewhat self-compensating, thus providing results that are well within tolerable error bounds.

Figure 5.3-3 Difference Between Energy Deposited and Energy Radiated for L1H(Dep1)-W-L1H(Nat) Shield with Mesh Interval from Temperature Analysis



Regardless of which error value one selects as the net numerical error, the value is on the order of the input data error estimated earlier as $\pm 5.0\%$. Combining the input data error with the 2.7% numerical error, the total uncertainty in temperatures will be bounded by a range of $\pm 5.7\%$.

The uncertainty in stresses due to data input can also be estimated with Equation 5.3-1. As with temperature, a closed form solution for the stresses is not available. However, from the simple analytic solution we know the functional dependence of stress on the input variables as [Burgreen, 1971]:

$$\sigma \sim \frac{E\alpha_T}{(1-v)} \quad (5.3-6)$$

From which the uncertainty can be expressed as:

$$U_\sigma = \left[\left(\frac{\alpha_T}{(1-v)} U_E \right)^2 + \left(\frac{E}{(1-v)} U_{\alpha_T} \right)^2 + \left(\frac{E\alpha_T}{(1-v)^2} U_v \right)^2 \right]^{1/2} / \sigma \quad (5.3-7)$$

Substituting the appropriate baseline values from Table 5.3-5 and the uncertainties of Table 5.3-1, the uncertainty in stress due to data input was $\pm 17.3\%$.

The uncertainty in the linear elastic formulation for the W and LiH-SS honeycomb matrix will be the dominant error source for this phase of the research. Because of the expectedly large magnitude of this uncertainty, the stress results were used only as a guideline in gaining an understanding of where the structure problem areas of the shield would be encountered.

6.0 NUMERICAL INSTABILITIES

As any numerical analyst comes to appreciate, most problems worth solving are accompanied by an array of instabilities. While some of the typical instabilities, encountered in time dependent analyses using explicit integrator schemes are well understood, non-linear analyses seem to invariably uncover instabilities not documented in the literature, and which may well be problem type or machine specific.

Numerical instabilities were encountered throughout each phase of this research. The stability of the radiation transport calculation was strongly influenced by the nuclide density used to model the vacuum conditions of outer space. Oscillatory behavior was seen at the radiative heat transfer boundary for high internal heating rates during the heat transfer analysis. Not to be left out, the stress analysis exhibited diverging behavior for the bilinear constitutive equations using a full Newton-Raphson iteration scheme.

The instabilities just mentioned had to be overcome in order to achieve the results obtained in this research. Since the scope of this research was applied engineering and not theoretical computational analysis, in-depth phase plane and modal decomposition analyses were not conducted with regard to each instability. However, in the interest of assisting those who follow in this type of research, each problem area, as well as the method with which the problem was overcome will be presented.

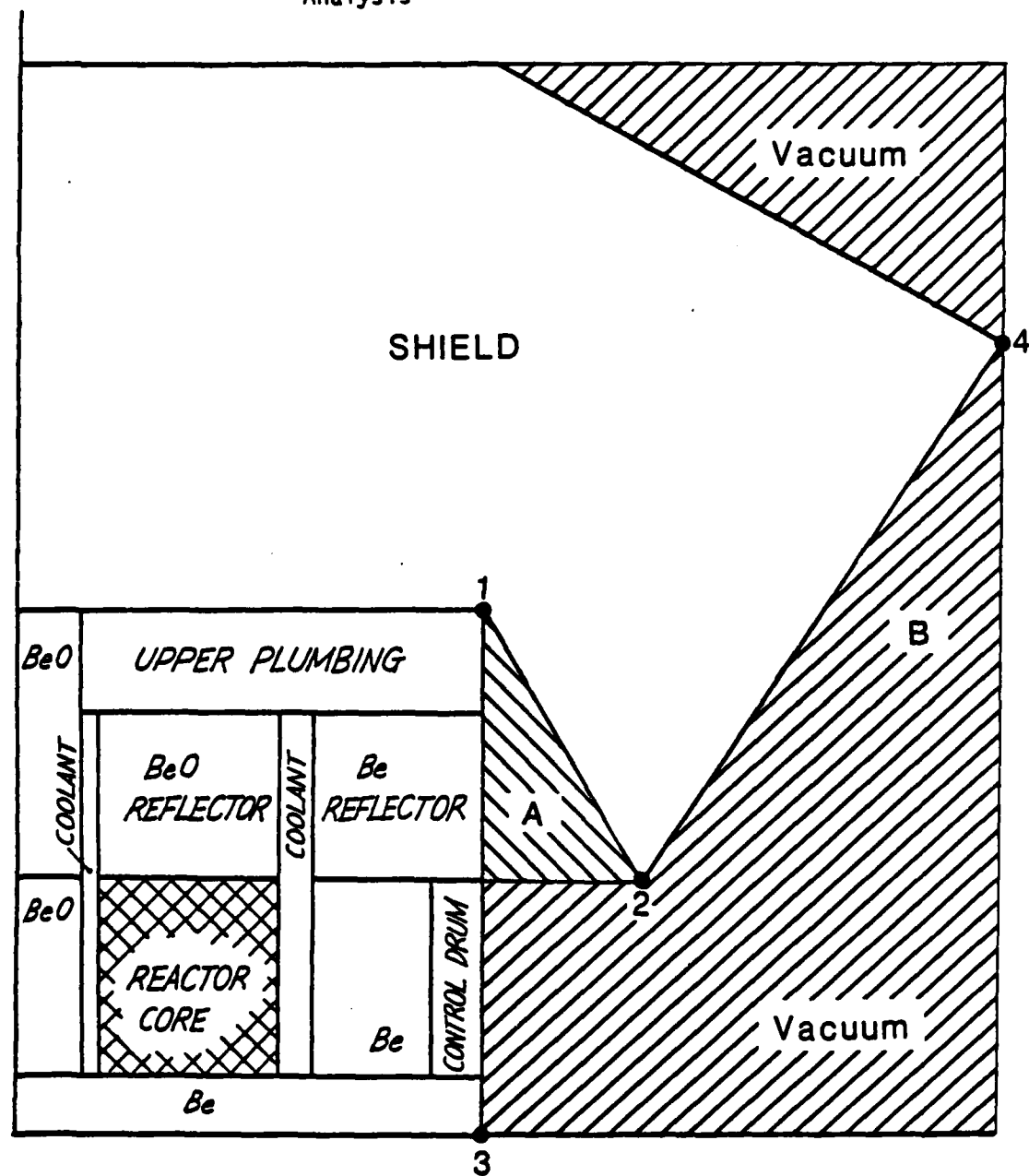
6.1 Numerical Instabilities Encountered During Radiation Transport.

In performing the 2-D radiation transport calculations required to determine the energy deposition in the shield, the vacuum environment of free space had to be modelled in the numerical grid. Figure 6.1-1 shows the regions of void to which this section is referring.

In a computational code, the vacuum is modelled with a low nuclide density of some inert gas. Since the gas was not physically present in the problem, the smallest density possible was desirable to minimize the effect of the gas on computational results. The area of most difficulty is listed in Figure 6.1-1 as region A, the region between the core axial reflector and the extruding portion at the front of the shield. Within a radial distance of approximately 10 cm, the properties of BeO, vacuum of free space, and LiH or W (depending on shield configuration) must be included in the system of equations used to solve for the neutron and gamma fluxes.

The inert gas used in the vacuum regions was nitrogen. The convergence of the system was sensitive to the number density of the nitrogen (100 atom % N-14). Table 6.1-1 lists the smallest mean free path (mfp) for N-14 over the 24 neutron groups and 14 gamma groups as a function of nuclide number. From Figure 6.1-1, for a neutron or gamma in region A, the maximum distance the radiation can travel before encountering a material is ~19 cm (Pt.1 to Pt.2). In region B, the maximum distance increases to ~102 cm. Thus, from Table 6.1-1, we see that for nuclide densities less than 10^{-5} atoms/barn-cm the nitrogen atoms are relatively transparent to the neutrons and gammas rays. For

Figure 6.1-1 Regions of Vacuum Modelled in Radiation Transport Analysis



Legend :

Region A Vacuum

Region B Vacuum

Table 6.1-1: Smallest Mean Free Path for Neutron and Gamma Interactions (over 24 Neutron and 14 Gamma Groups) for Nitrogen-14 for Varying Nuclide Densities

| Mean Free Path (cm) | N-14 Nuclide Density (atoms/barn-cm) | | | |
|---------------------|--------------------------------------|-----------|-----------|-----------|
| | 10^{-3} | 10^{-4} | 10^{-5} | 10^{-6} |
| Neutron | 85.35 | 853.5 | 8,535 | 85,350 |
| Gamma | 68.11 | 681.1 | 6,811 | 68,110 |

larger densities, the mfp is ~3.6 to 4.5 times the maximum path length in region A for a number density of 10^{-3} atoms/barn-cm; the mfp is ~6.7 to 8.4 times the maximum path length in region B for a number density of 10^{-4} atoms/barn-cm.

Sample results of several combinations of N-14 densities in regions A and B are recorded in Table 6.1-2. From this data, several observations can be made. The use of a very low number density for the void filler gas ($\sim 10^{-6}$ atoms/barn-cm) anywhere in the system produced a stiff system of equations that did not converge. The use of a high number density for N-14 (10^{-3} atoms/barn-cm), resulted in a convergent solution, with good conditioning and fast convergence. However, the high number density was shown in Table 6.1-1 to produce mfp's less than the largest possible path length of both neutrons and gammas. This means that the nitrogen presence, required only for numerical reasons, could influence the energy deposition results in the shield. (This influence is seen by comparing the total energy deposited for cases #3 and 4 of Table 6.1-2.)

As the nuclide density of N-14 is decreased, the condition number for the system is increased. Thus, a trade-off between the physical influence of the filler gas and the numerical accuracy of calculations must be made. The results of case #4 show how this trade-off was made for this research. The use of number densities of 10^{-3} atoms/barn-cm in region A and 10^{-3} atoms/barn-cm in region B was shown to limit the effects of the gas, based on mean free path considerations. However, decreasing the density in region B an order of magnitude resulted in an increase in maximum condition number by an order of magnitude.

Fortunately, the stiffest equations occurred in energy groups which did not appreciably contribute to heating for both neutrons and gammas. As the number of outer iterations is increased, the group condition number as well as the number of inner iterations required for group convergence decreased. As shown earlier, the energy deposition changed less than .1% for the coarse mesh core/fine mesh shield procedure used in this research. Thus, one gains more confidence that the benefits of case #4 in decreasing the influence of the filler gas outweighs the effects of increased condition number. As long as the number densities in the vacuum are kept constant when analyzing shield configurations, the numerical and physical inaccuracies introduced by the filler gas will not influence the comparative results of one shield versus another.

A final comment to be made is that the convergence of the system is sometimes difficult to verify for a system of equations solved iteratively. For the radiation transport problem, the analyst must understand the importance of changes with outer iteration in balance tables,

Table 6.1-2: Sensitivity of Convergence on Number Density of Nitrogen-14 Used to Model Vacuum

| <u>Case #</u> | <u>n_{N-14}^1</u> | <u>H_T^2</u> | <u># Inners³</u> | <u>Cond No.⁴</u> | | <u>Conver-</u> | | |
|---------------|--------------------------------|---------------------------|-----------------------------|-----------------------------|------------|--------------------|--------------------|---------------|
| | | | | <u>Max</u> | <u>Min</u> | <u>Max</u> | <u>Min</u> | <u>gence?</u> |
| 1 | 10^{-6} | 10^{-6} | 9.69 | 1500 | 226 | 2.89×10^6 | 1.25×10^6 | No |
| 2 | 10^{-3} | 10^{-6} | -113.58 | 2500 | 12 | 3.42×10^6 | 2.22 | No |
| 3 | 10^{-3} | 10^{-3} | 7.71 | 205 | 11 | 5.92×10^3 | 2.47 | Yes |
| 4 | 10^{-3} | 10^{-4} | 7.93 | 327 | 11 | 5.58×10^4 | 2.41 | Yes |

Notes:

1. Number densities of N-14 for regions identified in figure 5.1-1.
2. Total energy deposited in shield after 1 outer iteration.
3. Maximum and minimum # of iterations over 38 neutron and gamma groups with a convergence criteria of 10^{-4} .
4. maximum and minimum group condition number over 38 groups.

criticality, condition number, and number of iterations for group flux convergence. With this arsenal of computational flags, estimates can be made regarding the validity of results. For example, the energy deposition of case #1 of Table 6.1-2 might seem reasonable without extensive evaluation of the flags mentioned above. The validity of radiation transport results requires a very critical eye and a lot of practice on the part of the analyst in accepting the numerical results.

The information presented in this section was intended to assist others to be aware of the significance of a seemingly harmless decision to be made such as selection of a number density for the filler gas. The next instability to be discussed was encountered during the heat transfer analysis of the radiation shield.

6.2 Numerical Instability Encountered During Heat Transfer Analyses.

When validating the code SHLDTEMP with the 1-D, radiative heat transfer problem presented earlier, oscillatory behavior originating at the radiative boundary was continually encountered for high values of internal heat generation. Because the solution of the temperature distribution was such a fundamental need for this research, a fair degree of effort was spent on analyzing this instability and a means for overcoming the oscillatory behavior.

A sample problem was set-up to examine the instability in greater detail. The basic Newton-Raphson iteration method was used to solve the temperature distribution throughout the shield. Recalling from Section 3.4, the equations to be solved were:

$$\underline{\underline{K}}^i \Delta \underline{\underline{T}}^i = \underline{\underline{K}}^i - \underline{\underline{K}}^{i-1} \underline{\underline{T}}^{i-1} \quad (6.2-1)$$

- Then,

$$\underline{\underline{T}}^i = \underline{\underline{T}}^{i-1} + \Delta \underline{\underline{T}}^i \quad (6.2-2)$$

With each iteration, the matrices and vectors were updated to account for the new radiative heat transfer coefficient, calculated from:

$$k^i(T) = \sigma \epsilon F_{i+j} (T^{s(i-1)^2} + T^\infty) (T^{s(i-1)} + T^\infty) \quad (6.2-3)$$

The flowchart of Figure 3.4-3 describes this method in detail. For the sample problem, the thermal conductivities were kept constant in an effort to focus more easily on the instability problem. (As will be shown later, the thermal conductivity had no bearing on the oscillatory behavior of the numerical solution.)

6.2.1 Test Case Results. The solution of the set of algebraic equations resulting from Equation 6.2-1 is straight forward with either direct elimination or iterative solvers. Using an LDL^t factorization and back-substitution, the sample problem of Figure 6.2-1 was solved for a thick walled infinite cylinder comprised of two different materials (W and LiH), with an insulated inner surface, and a radiatively cooled outer surface.

The excellent agreement in Figure 6.2-1 between the exact and FEM solutions was for a constant internal heat generation of 0.0072 W/cm^3 . When the heat generation increased an order of magnitude to 0.072 W/cm^3 , the numerical solution of the problem did not converge, and the temperature at the radiative outer surface oscillated between

Based on these results, a "worst case" run was made to see if a combination of the previously mentioned parameters would result in a bifurcation solution for the entire range of relaxation values. The worst case included high internal heating, low surface emissivity, low ambient temperature, and a thick shield with a large void radius. The results presented in Figure 6.2-11 indicate that even for such a worst case, convergence was still attained, but at higher relaxation values.

Table 6.2-1 is a summary of the results just discussed. From these results, the following observations were made for the infinite circular cylinder with a radiative heat transfer outer radial surface:

- Thermal conductivity and the initial radiative-heat transfer coefficient have no effect on ω_{crit} or ω_{opt} .
- Variations in the inner void radius and shield thickness have negligible effects on ω_{opt} . However, these variables have a minor influence on ω_{crit} .
- Surface emissivities have a negligible effect on ω_{opt} , but a significant influence on ω_{crit} .
- The magnitude of internal heat generation and ambient temperature at the radiative surface have significant effects on both ω_{opt} and ω_{crit} .

Based on these results, it is concluded that any parameter (or combination of parameters) which contributes to increasing the internal heat generated, and/or decreasing the amount of heat radiated, would require a larger value of ω_{crit} for the numerical solution to converge to the correct solution.

Table 6.2-1. Qualitative Effects on Relaxation Parameters
with Changes in Key Variables

| Variable | Change | Effect on: | |
|---|--------|-----------------|----------------|
| | | ω_{crit} | ω_{opt} |
| Internal heat rate | + | +/M | +/m |
| Ambient Temperature | + | -/M | -/M |
| Surface Emissivity | + | -/M | NC |
| Shield Thickness | + | +/m | NC |
| Void Radius | + | +/m | NC |
| Initial Radiative Heat Transfer Coefficient | + | NC | NC |
| Thermal Conductivity | + | NC | NC |

Legend:

+ Increase

- Decrease

M Major Effect

m Minor Effect

NC No Change

Figure 6.2-9 Effects of Varying Shield Thickness on Critical and Optimal Relaxation Parameters

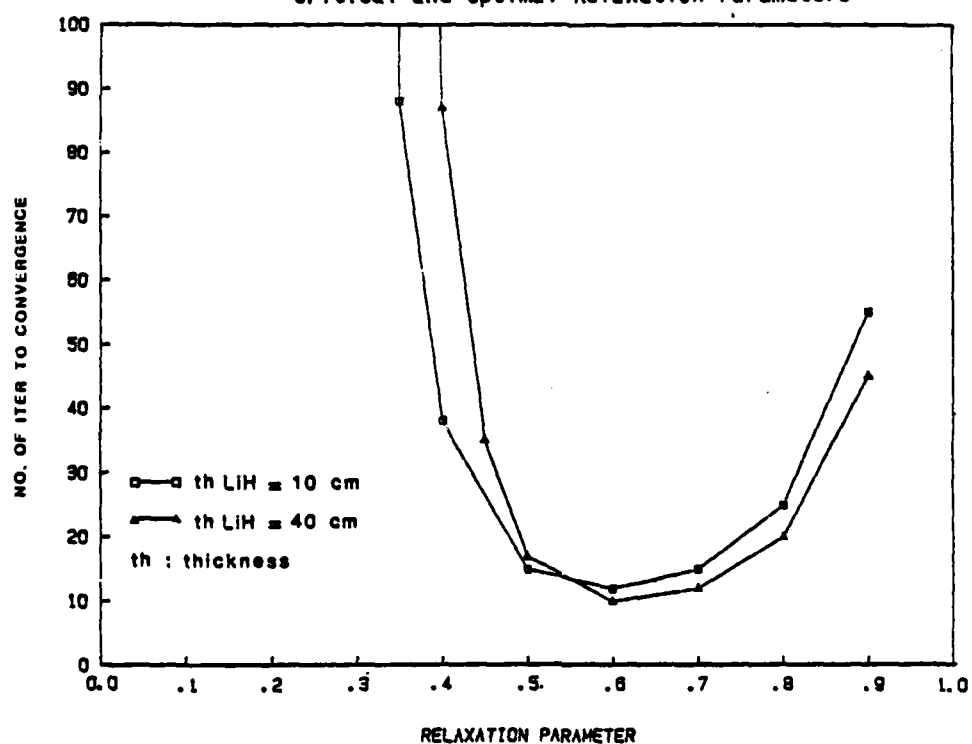


Figure 6.2-10 Effects of Varying Inner Radius on Critical and Optimal Relaxation Parameters

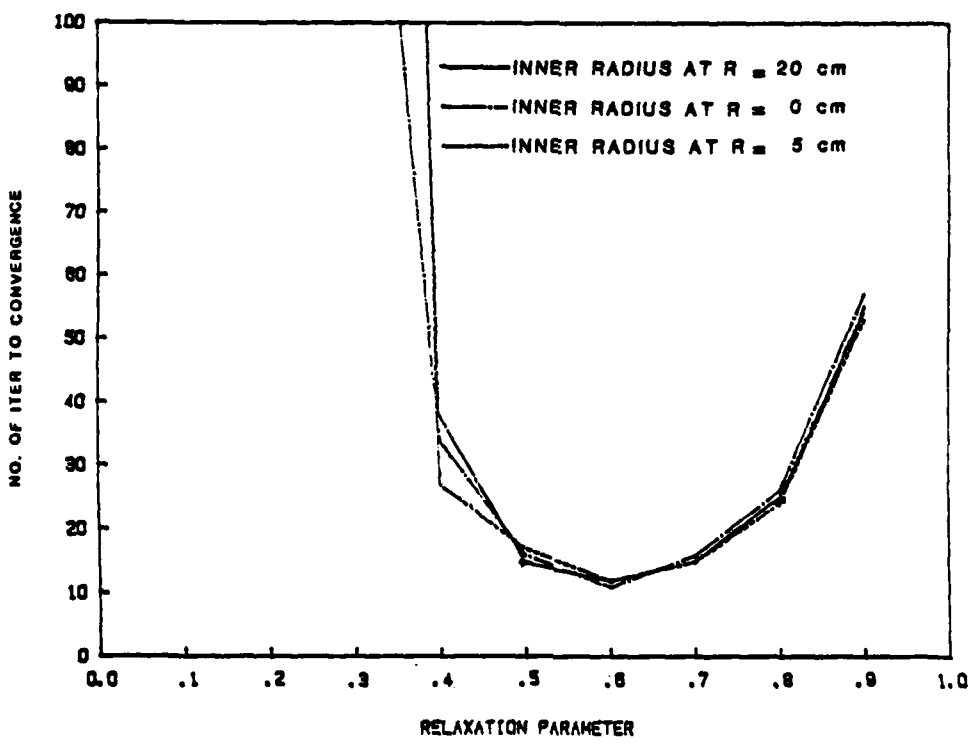


Figure 6.2-7 Effects of Thermal Conductivity on Critical and Optimal Relaxation Parameters

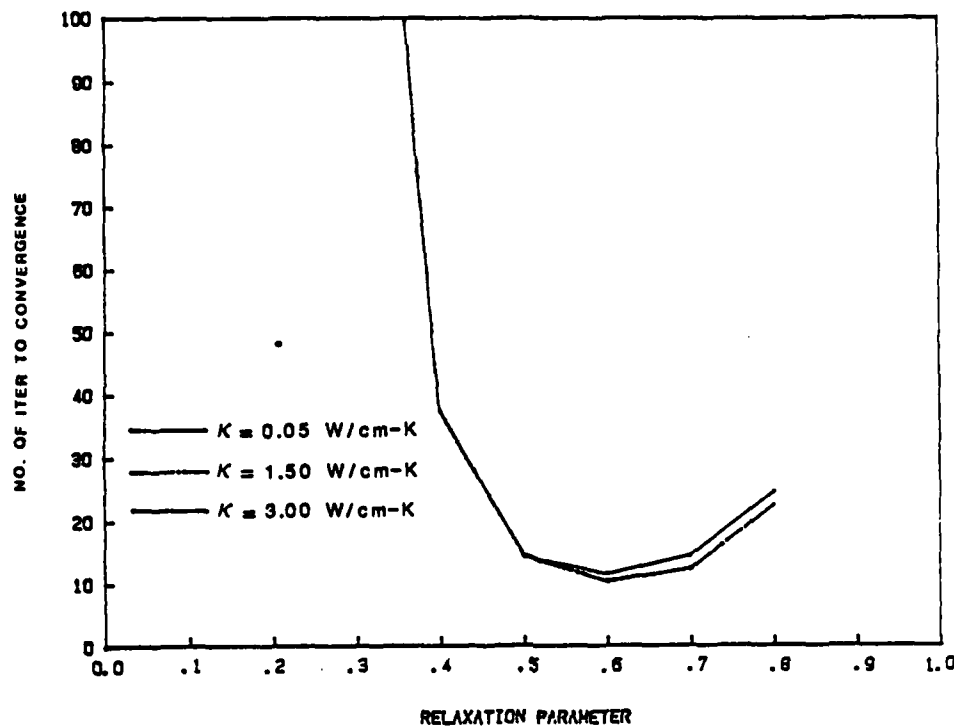


Figure 6.2-8 Effects of Varying Ambient Temperature on Critical and Optimal Relaxation Parameters

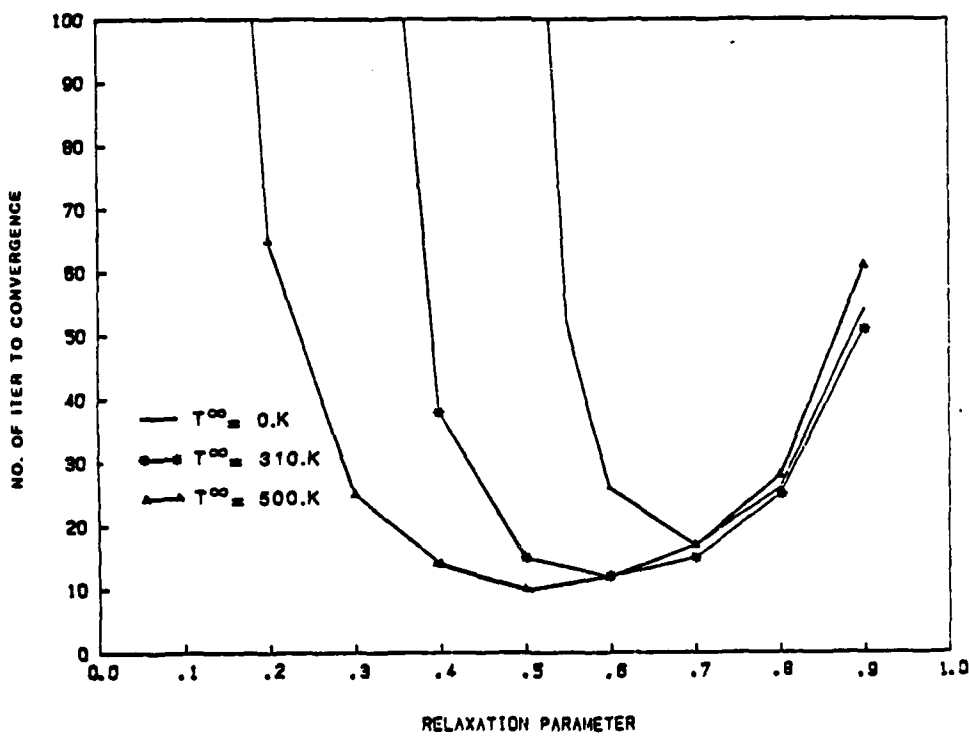


Figure 6.2-5 Effects of Initial Value of Radiative Heat Transfer Coefficient on Critical and Optimal Relaxation Parameters

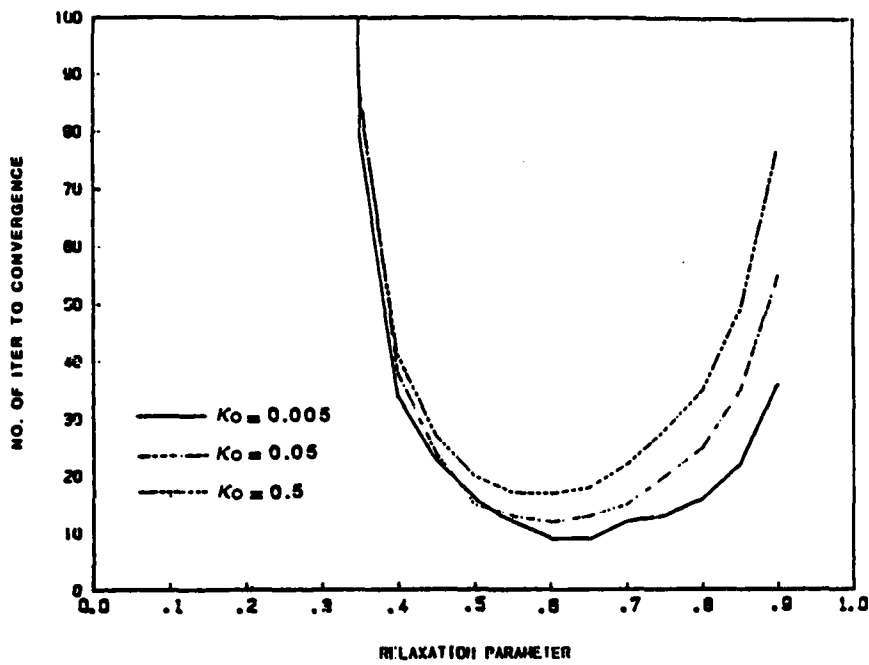


Figure 6.2-6 Effects of Varying Surface Emissivity on Critical and Optimal Relaxation Parameters

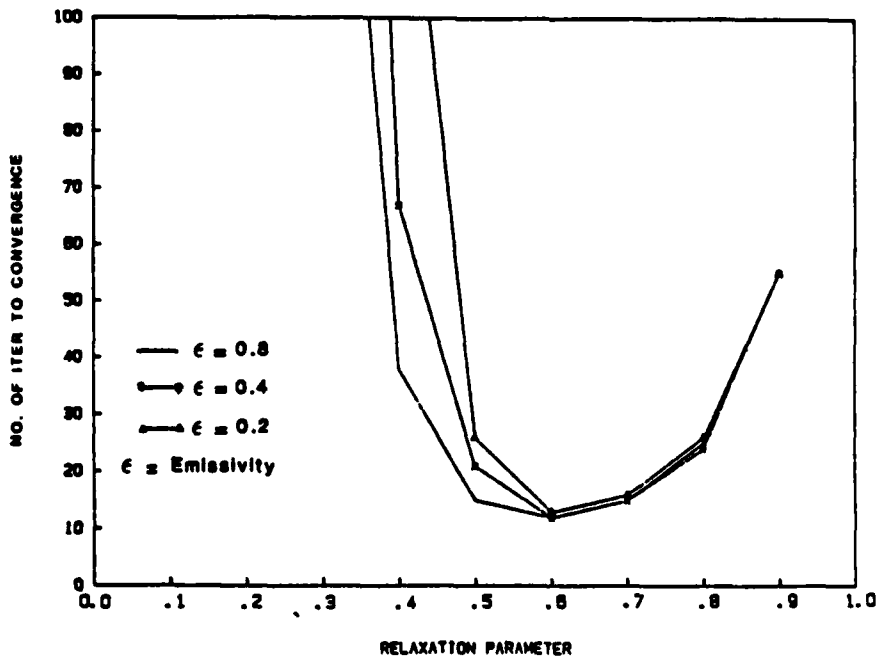


Figure 6.2-8 records the influence of ambient temperature on numerical instability; ω_{crit} decreased substantially as the ambient temperature increased. The reason for this effect is based on numerical observation, rather than physical intuition. In formulating Equation 6.2-1, the magnitude of the load vector, \underline{R} , was proportional to $(T^{\omega_4} - T^{S^4})$. Thus, as the difference between ambient temperature and surface temperature decreased, the problem became more linear. Conversely, as the differences increased, the non-linearity was increased, resulting in higher ω_{crit} .

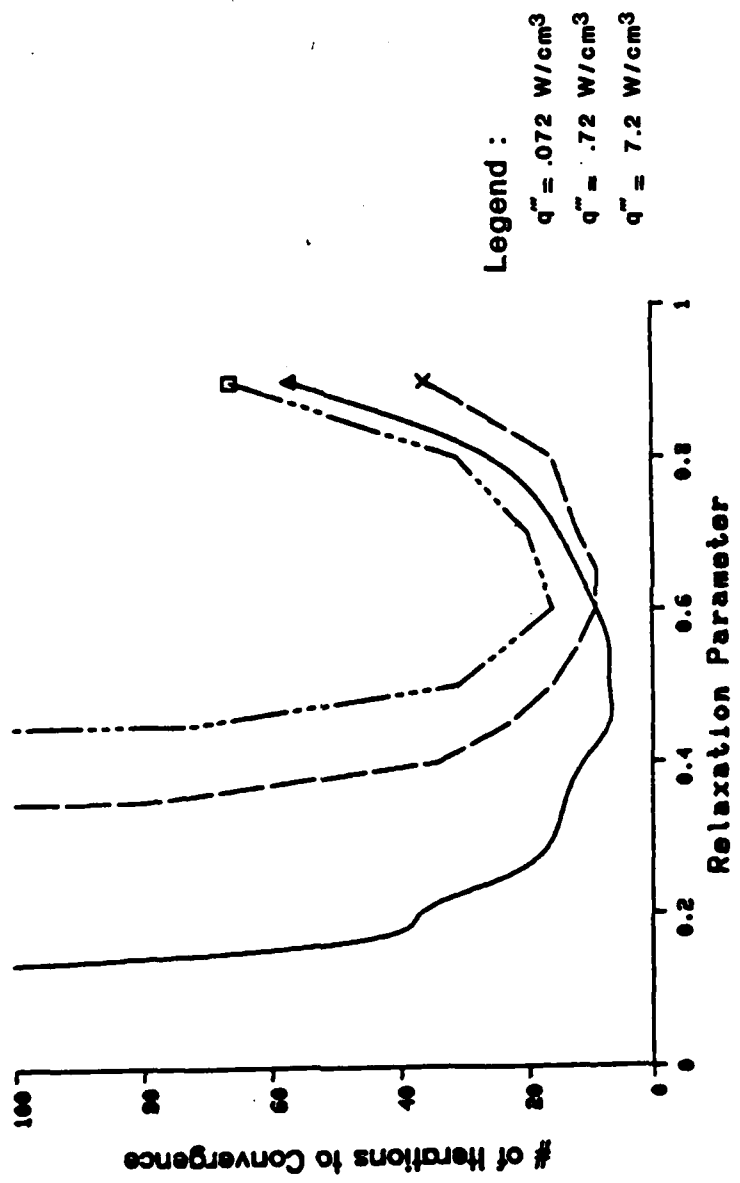
Figures 6.2-9 and 6.2-10 show the effects on ω_{crit} and ω_{opt} of shield thickness and void radius. Both variables affected ω_{crit} to some degree by changing both the total amount of internal heat generated and the total amount of heat to be radiated out. As the total heat generated increased due to a geometric increase, ω_{crit} increased. This occurred because increasing the dimensions of the shield decreased the specific surface area, while increasing the total amount of internal heat generation.

Figures 6.2-6 through 6.2-10 reflect the sensitivity of ω_{crit} and ω_{opt} to changes in the remaining variables listed above. The qualitative effects of these parameters are recorded in Table 6.2-1.

Figure 6.2-6 shows the effect of varying the emissivity of the radiative surface on the relaxation parameters, ω_{crit} and ω_{opt} . While emissivity had no effect on ω_{opt} , the value of ω_{crit} was very sensitive to the value of the surface emissivity. Such sensitivity was due to the fact that increasing the surface emissivity increased the coupling between the heat radiated and the internal heat generation in the shield, thus requiring a larger value of ω_{crit} to achieve convergence. In Figure 6.1-4, the coupling between the internal heat generation and the radiated heat was weakened when the q''' value was reduced, thus resulting in a small value of ω_{crit} . Therefore, it was concluded that strengthening or weakening the coupling between internal heat generation and radiated heat (via varying any of the above parameters) would decrease or increase ω_{crit} , respectively. This coupling effect has a direct linkage with the magnitude of the amplitude function, which will be examined analytically in the next sub section.

Figure 6.2-7 shows that thermal conductivity had no effect on the numerical stability of this problem. Thermal conductivity only affects the temperature distribution in the cylinder rather than the energy balance or thermal coupling between the internal heat generation and the radiated heat. This was also seen to be true from the analytic solution, in which the thermal conductivity was not included in the determination of the radiative surface temperature (for an adiabatic front).

Figure 6.2-4 Effects of Varying Internal Heat Generation on Critical and Optimal Relaxation Parameters



- Internal Heating Rate
- Surface Emissivity
- Thermal Conductivities
- Ambient Temperature
- Material Thicknesses
- Inner Void Radius

In Figure 6.2-4, the number of iterations required for convergence was plotted against the value of this relaxation parameter, ω , for several values of internal heat generation. In this figure, as the internal heating rate, q''' , increased, the value of ω_{crit} also increased. The explanation lies in the fact that the higher heating rate corresponds to an increase in the amplitude function; thus, more damping was required which resulted in higher ω_{crit} . Once ω_{crit} was obtained, increasing ω beyond the value of ω_{crit} did not affect the accuracy of the final temperature distribution, but changed the number of iterations required to converge to the exact solution.

Initially, the temperature at the outer radiative surface may not be well known; hence, the initial value for the radiative-heat transfer coefficient, $\kappa_0(T)$, may be badly over/under-estimated. As shown in Figure 6.2-5, the intitial estimate of $\kappa_0(T)$ did not affect the value of ω_{crit} . However, the number of iterations required for convergence increased as the initial value of $\kappa_0(T)$ became higher than the exact value. For a moderate internal heat rate ($\sim 0.072 \text{ W/cm}^3$), the effect of the initial estimate of $\kappa_0(T)$ was minimal. For the higher internal heating rate ($\sim 0.72 \text{ W/cm}^3$), the effect on the number of iterations for convergence of $\kappa_0(T)$ was more pronounced, but the solution still converged to the correct solution for any ω , provided $\omega > \omega_{crit}$.

To achieve this effect, a new radiative heat transfer coefficient, $\bar{\kappa}(T)$, was defined by combining part of the last iteration's $\bar{\kappa}(T)$ with the recently calculated $\kappa(T)$. Mathematically,

$$\bar{\kappa}^i(T) = (1 - \omega) \kappa^i(T) + \omega \bar{\kappa}^{i-1}(T) \quad (6.2-5)$$

$$= \omega \kappa_0 + \sum_{i=1}^{N-1} \omega^{N-i-1} (1-\omega) \kappa^i \quad (6.2-6)$$

Intuitively, Equation 6.2-5 represents an effort to "smooth" the value of $\kappa(T)$ for the next iteration based on the previous value for $\kappa(T)$. However, this simple explanation was not adequate to explain the bifurcation phenomenon, as an initial guess of $\kappa(T)$ based on the exact solution still resulted in oscillatory behavior when $\omega = 0$.

With the new weighted radiative heat transfer coefficient now being used, the sample problem was re-run for the internal generation values of Figures 6.2-2 and 6.2-3, which previously resulted in oscillatory behavior. For both cases, the numerical solution converged to the exact solution (within reasonable numerical error limits) above some value of ω .

The smallest value of ω which completely damped the oscillatory behavior was defined as ω_{crit} . For any value of ω above ω_{crit} , the solution continued to converge to the exact solution. However, as ω varied (above ω_{crit}), the number of iterations required for a prescribed convergence tolerance also varied. There always existed a value of ω between ω_{crit} and 1.0 which minimized the number of iterations required for convergence. This value was defined as ω_{opt} .

For the sample problem, the values and sensitivity of ω_{crit} and ω_{opt} were examined by varying the following parameters:

Figure 6.2-3 Oscillatory Behavior of Surface Temperature
for $q''' = 0.72 \text{ W/cm}^3$

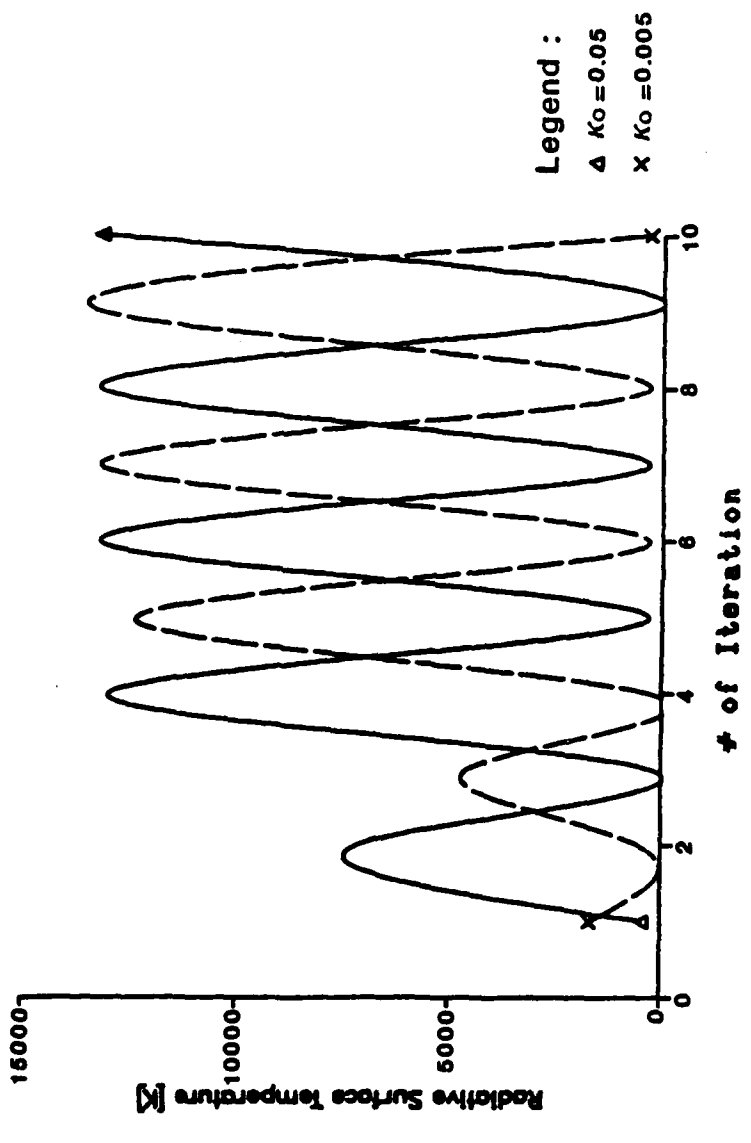
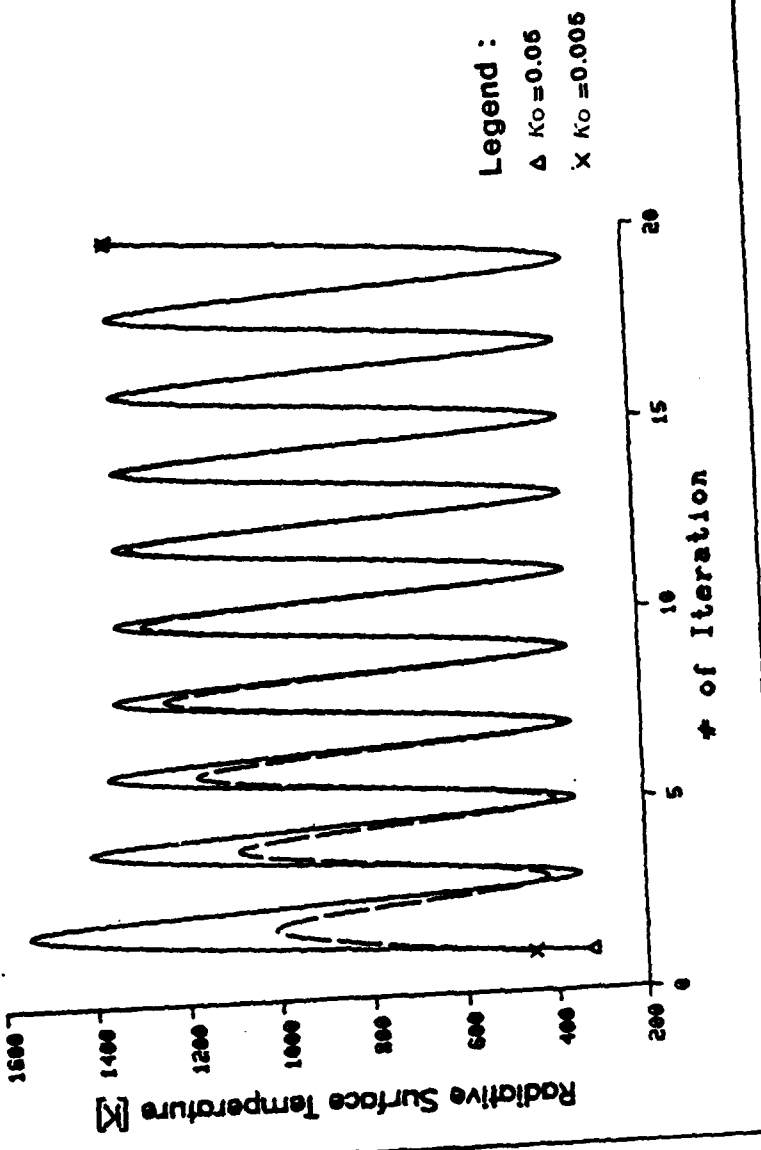


Figure 6.2-2 Oscillatory Behavior of Surface Temperature
for $q_{\text{in}} = 0.072 \text{ W/cm}^2$



very high and very low values. Figure 6.2-2 shows the calculated surface temperatures as a function of number of iteration for a variety of initial values of $\kappa(T)$. The oscillatory behavior was even more pronounced in Figure 6.2-3 as the internal heating was increased another decade to 0.72 W/cm^3 .

The results presented in Figures 6.2-2 and 6.2-3, clearly indicate that the oscillatory behavior of the surface temperature (as the # of iterations, N , approaches infinity) occurring above some critical value of internal heat generation was periodic and of constant amplitude. To eliminate this oscillatory behavior, some damping function had to be introduced which would cause the oscillations to die out as N increased. Since the surface temperature is directly coupled to the radiative heat transfer coefficient, the desired damping effect could be represented by:

$$\left(\frac{\bar{\kappa}_i - \bar{\kappa}_{i-1}}{\bar{\kappa}_i} \right) < A(q''', q_r) \phi(\omega, N) \quad (6.2-4)$$

where $\bar{\kappa}_i$ is the new radiative heat transfer coefficient (to be defined shortly). Based on Figures 6.2-2 and 6.2-3, the amplitude of the oscillations appeared to be some function of both the internal heat generated and the heat radiated from the surface to the surrounding medium. This amplitude was symbolically represented as $A(q''', q_r)$. It logically followed that the damping effect, $\phi(\omega, N)$, should be a function of some relaxation parameter, ω , and the iteration number, N . Thus, for some value of ω , we would hope for the amplitude (corresponding to oscillatory behavior) to converge to a point value as the number of iterations increases.

Figure 6.2-1 Comparison of FEM with Exact Solution
for $q_{\text{in}} = 0.0072 \text{ W/cm}^3$

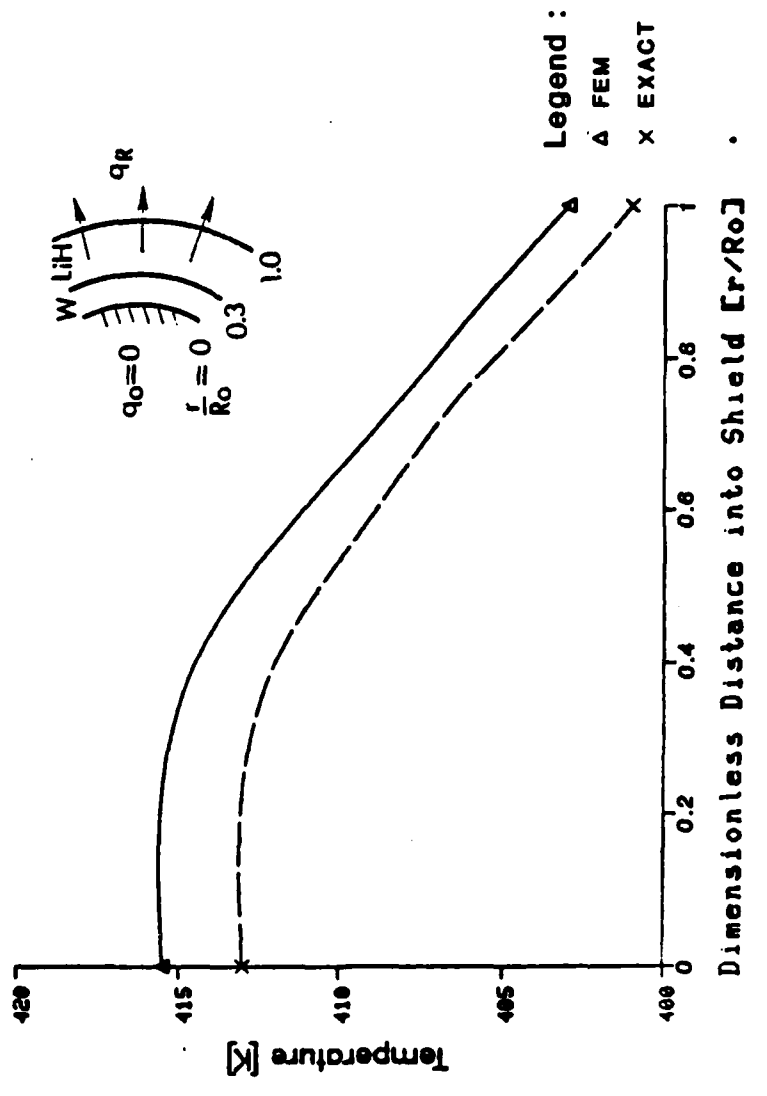
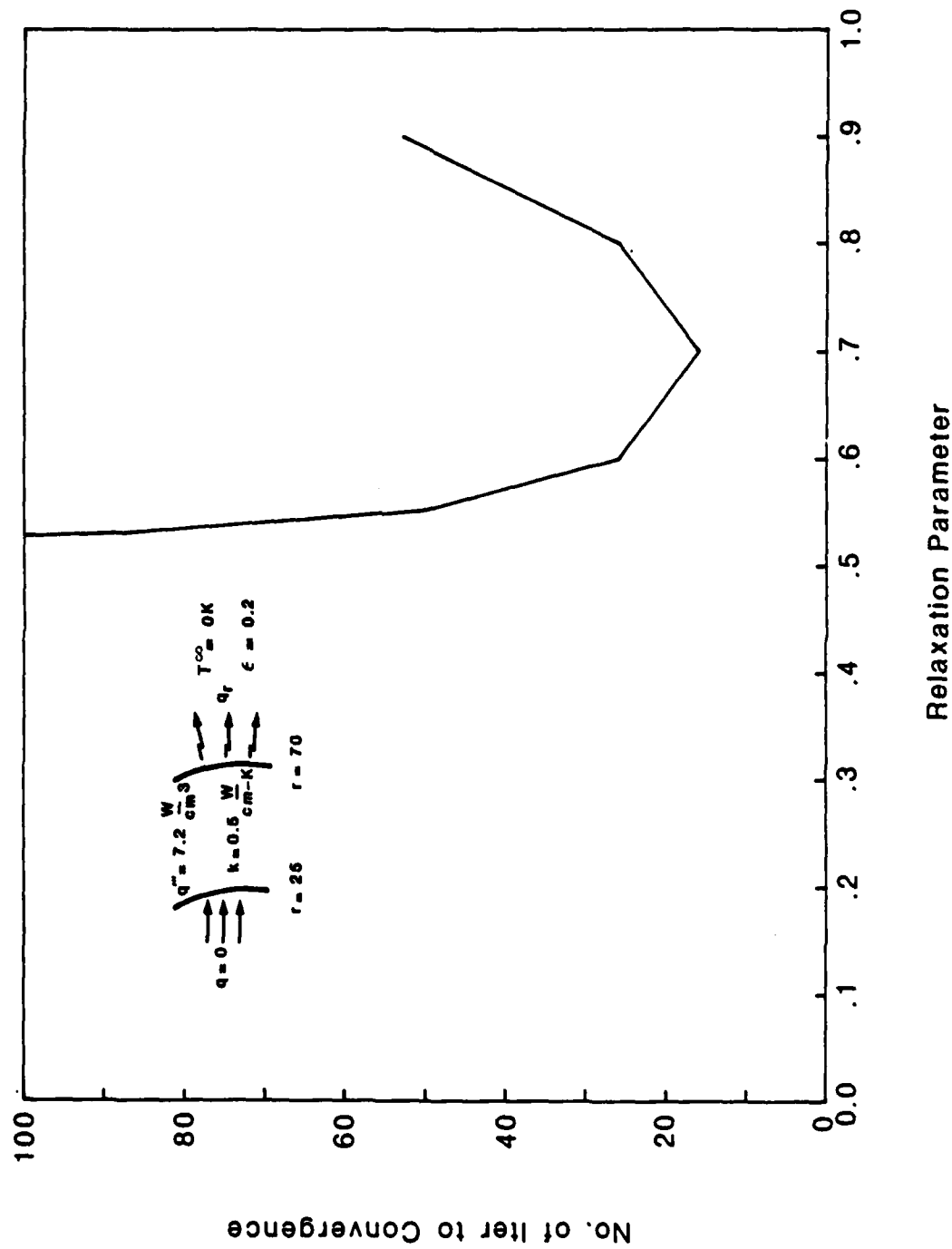


Figure 6.2-11 Results of Worst Case Run



For the wide variety of examples analyzed, ω_{crit} ranged between 0.1 and 0.52; ω_{opt} ranged between 0.5 and 0.7. Since prior knowledge of ω_{opt} is generally not known when analyzing a new problem, some estimate of this parameter is required. Based on these results, a value of 0.60 to 0.70 is recommended for the relaxation parameter to ensure convergence to the correct solution for steady-state radiative heat transfer problems using Newton-Raphson iteration.

6.2.2 Theoretical Analysis of Thermal Instability. To examine the theoretical basis for the numerical instability encountered herein, the basic Newton-Raphson algorithm was analyzed with a modal decomposition of the i th iterations \mathbf{K} matrix. We began by pre and post multiplying the basic N-R system of equations by the i th iterations eigenvectors. The result was:

$$\underset{\sim}{\psi}_m^t \underset{\sim}{\mathbf{K}}^i \underset{\sim}{\Delta T}^i \underset{\sim}{\psi}_k^t = \underset{\sim}{\psi}_m^t \underset{\sim}{R}^i \underset{\sim}{\psi}_k^t - \underset{\sim}{\psi}_m^t \underset{\sim}{\mathbf{K}}^{i-1} \underset{\sim}{T}^{i-1} \underset{\sim}{\psi}_k^t \quad (6.2-7)$$

From linear algebra, we recall that [Noble, 1969]:

$$AB = B^t A^t \quad (6.2-8)$$

From which, Equation 6.2-7 can be rewritten as:

$$\underset{\sim}{\psi}_m^t \underset{\sim}{\mathbf{K}}^i \underset{\sim}{\psi}_k^t \underset{\sim}{\Delta T}^i = \underset{\sim}{\psi}_m^t \underset{\sim}{\psi}_k^t \underset{\sim}{R}^i - \underset{\sim}{\psi}_m^t \underset{\sim}{\psi}_k^t (\underset{\sim}{\mathbf{K}}^{i-1} \underset{\sim}{T}^{i-1})^t \quad (6.2-9)$$

From orthonormality, it can be shown that [Belytschko and Hughes, 1983]:

$$\underset{\sim}{\psi}_m^t \underset{\sim}{\mathbf{K}}_1 \underset{\sim}{\psi}_k^t = \lambda_1 \delta_{mk} \quad (6.2-10)$$

where δ_{mk} is the kronecker delta.

Using this result in Equation 6.2-9:

$$\underset{\sim}{\Delta T}^i = \frac{1}{\lambda_1} (\underset{\sim}{R}^i - \underset{\sim}{\mathbf{K}}^{i-1} \underset{\sim}{T}^{i-1}) \quad (6.2-11)$$

To examine the stability of the system of equations, let's recall the oscillatory behavior of Figures 6.2-2 and 6.2-3. For dampening of the oscillatory behavior, the temperature increment for the i -th iteration, ΔT^i , must be less than the temperature increment for the $i-2$ iteration, ΔT^{i-2} . This situation is shown in Figure 6.2-12.

Defining the convergence criterion, n , as the ratio of ΔT^i to ΔT^{i-2} , this criterion takes the form:

$$n = \frac{\|\Delta T^i\|}{\|\Delta T^{i-2}\|} \quad (6.2-12)$$

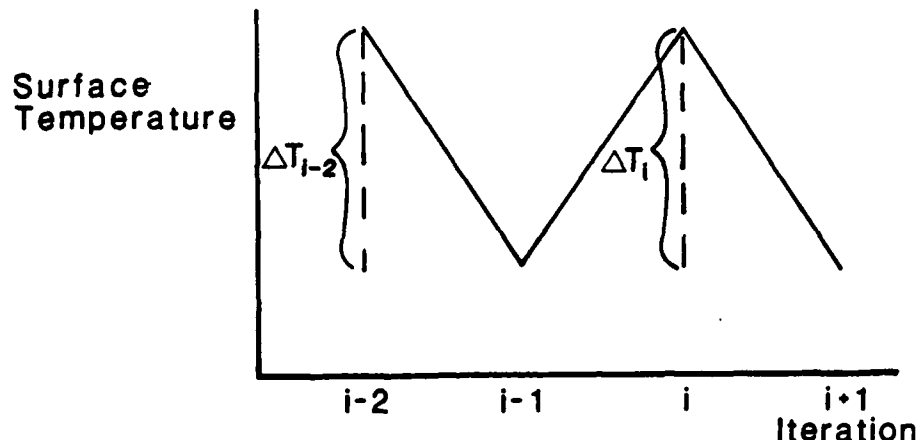
where some arbitrary norm is used to reduce the vectors to a scalar quantity. The convergence of a system can be determined from the value of n as:

| <u>Value of n</u> | <u>Convergence Condition</u> |
|--------------------------------|------------------------------|
| >1 | Divergence |
| 1 | Oscillatory |
| <1 | Convergence |

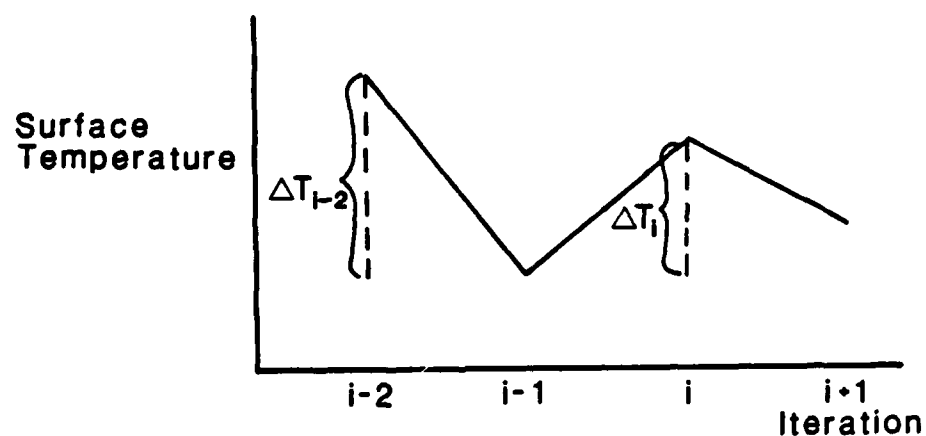
6.2.2.1 Convergence Criteria Without Relaxation. Using the newly defined convergence criteria, we can examine the condition for which oscillatory behavior would occur using the basic NR method with the relaxation parameter of Equation 6.2-5. Substituting Equation 6.2-11 into Equation 6.2-12 results in:

$$n = \frac{\frac{1}{\lambda_1} (R^i - K^{i-1} T^{i-1})}{\frac{1}{\lambda_{i-2}} (R^{i-2} - K^{i-3} T^{i-3})} \quad (6.2-13)$$

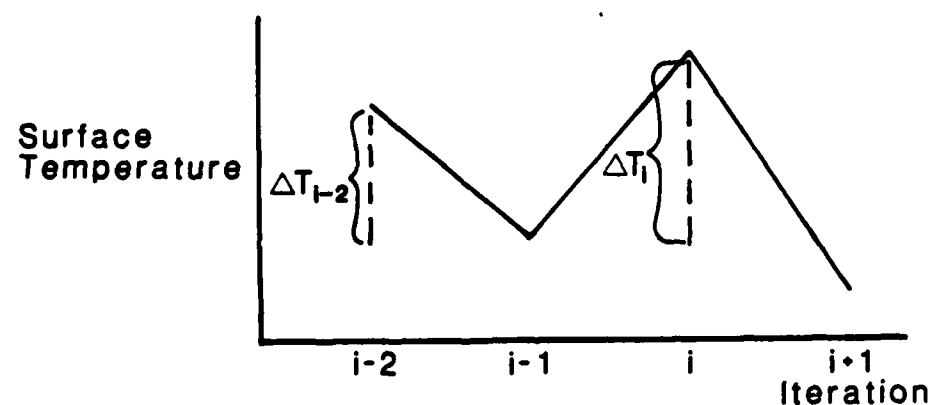
Figure 6.2-12 Convergence Criteria for Dampening of Oscillatory Behavior



a. Oscillatory Behavior [$\Delta T_{i-2} = \Delta T_i$]



b. Converging System [$\Delta T_{i-2} > \Delta T_i$]



c. Diverging System [$\Delta T_{i-2} < \Delta T_i$]

Substituting into Equation 6.2-13 the respective terms derived in Equation 3.4-22, results in:

$$n = \frac{\frac{1}{\lambda_1} (R_q^{...} - K^{i-1} T^{i-1} - R_k^i)}{\frac{1}{\lambda_{i-2}} (R_q^{...} - K^{i-3} T^{i-3} - R_k^{i-3})} \quad (6.2-14)$$

Of course, the R_k vector will assume non-zero values only for surface elements. From Equation 6.2-14, we immediately observe that when the heat generation becomes large enough, the following condition will exist:

$$\|R_q^{...}\| > \|K T - R_k\| \quad (6.2-15)$$

When this condition exists, the convergence criteria reduces to:

$$n = \frac{\frac{1}{\lambda_1} R_q^{...}}{\frac{1}{\lambda_{i-2}} R_q^{...}} \quad (6.2-16)$$

For the pure oscillatory system, K^i and K^{i-2} will be similar matrices which means

$$\lambda_1 = \lambda_{i-2} \quad (6.2-17)$$

and the convergence criterion reduces to:

$$n = 1 \quad (6.2-18)$$

or, oscillatory behavior.

6.2.2.2 Convergence Criteria With Relaxation. To examine the damping effect of the relaxation factor on the oscillations, the weighted radiation heat transfer coefficient of Equation 6.2-6 was substituted into the stability Equation 6.2-14. Inserting the respective integral forms for each term into the convergence criterion results in:

$$n = \frac{\frac{1}{\lambda_i} \left(\int_V (N_i q_i''' - \frac{k^{i-1}}{s} T^{i-1}) dV \right)}{\frac{1}{\lambda_{i-2}} \left(\int_V (N_i q_i''' - \frac{k^{i-3}}{s} T^{i-3}) dV \right) - \int_s^{\infty} \sum_{k=1}^{i-1} \omega^{i-k-1} (1-\omega) N_i N_j \kappa^k (T^{s(i-1)} - T^\infty) dS - \int_s^{\infty} \sum_{k=1}^{i-3} \omega^{i-k-1} (1-\omega) N_i N_j \kappa^k (T^{s(i-1)} - T^\infty) dS} \quad (6.2-19)$$

where N_i , N_j are the element shape functions and the subscript is used to denote summation over element nodes. The superscript still refers to the iteration number.

The key difference between Equations 6.2-14 and 6.2-19 lies in the last term of numerator and denominator. With the series summation introduced with the relaxation factor, the dissipative effects of the last term in countering the contribution of heat generation, $R_{q''''}$, are increased. Furthermore, because the summation in the numerator occurs over more terms than the mirror term in the denominator ($i-1$ compared with $i-3$), the numerator dissipation is greater than denominator dissipation. This results in a ratio that is less than unity, or a converging system.

Thus, in a somewhat generic manner we can understand how the relaxation parameter serves as a dissipative factor in dampening the oscillatory behavior of a system characterized by large internal heat generation rate.

6.2.2.3 Determination of ω_{opt} . The convergence criteria could provide some vital assistance in the determination of the relaxation parameter. As just seen, the extra dissipative terms in the numerator of Equation 6.2-19 means that selection of ω to minimize ΔT^i will not simultaneously minimize ΔT^{i-2} , which would result in an indeterminate convergence criteria. Thus, a value of ω which sets the convergence criteria to zero would ensure convergence and minimize the number of iterations needed for convergence.

For interior elements, the dissipative factor which results from the radiation heat transfer boundary contribution to the system of equations, is not present. Hence, a convergence criteria less than one will be determined by the individual surface element convergence criteria. The condition to be met now takes the form:

$$\begin{aligned} \varrho = \frac{1}{\lambda_i} \int_V (\mathbf{q}^i \cdot \mathbf{N}^i - \kappa^i T^{i-1}) dV \\ - \sum_{j=1}^{N-1} \omega^j (1-\omega) \kappa^j N^j \int_S (T^{s(i-1)} - T^\infty) ds \end{aligned} \quad (6.2-20)$$

This result is quite interesting from the standpoint that the spectral radius at the i th iteration, λ_i , will not affect the determination of ω . Another consequence of Equation 6.2-20 is that the value of ω that satisfies this criterion is to minimize the energy balance at the i -th iteration. Hence, ω_{opt} is the optimum relaxation value based on the convergence rate over energy. A final observation is that ω_{opt} will vary with each iteration.

$$\begin{bmatrix} 0 \\ 0 \\ 0 \end{bmatrix} = -\frac{\Delta}{60} \begin{bmatrix} 6r_1 + 2r_2 + 2r_3 & 2r_1 + 2r_2 + r_3 & 2r_1 + r_2 + 2r_3 \\ 2r_1 + 6r_2 + 2r_3 & r_1 + 2r_2 + 2r_3 & r_1 + 2r_2 + r_3 \\ 2r_1 + 2r_2 + 6r_3 & r_1 + 2r_2 + r_3 & r_1 + r_2 + r_3 \end{bmatrix} \begin{bmatrix} q_1^{i-1} \\ q_2^{i-1} \\ q_3^{i-1} \end{bmatrix} - \frac{k}{12A} \begin{bmatrix} h_1^2 + c_1^2 & h_1 h_2 + c_1 c_2 & h_1 h_3 + c_1 c_3 \\ h_2^2 + c_2^2 & h_2 h_3 + c_2 c_3 & h_2 h_1 + c_2 c_1 \\ h_3^2 + c_3^2 & h_3 h_1 + c_3 c_1 & h_3 h_2 + c_3 c_2 \end{bmatrix} \begin{bmatrix} T_1^{i-1} \\ T_2^{i-1} \\ T_3^{i-1} \end{bmatrix}$$

$$-\omega^0 (1-\omega) k^{i-1} (T^{i-1}) \frac{1}{12} \begin{bmatrix} 3r_1 + r_2 & r_1 + r_2 & 0 \\ r_1 + r_2 & r_1 + 3r_3 & 0 \\ 0 & 0 & 0 \end{bmatrix} \begin{bmatrix} T_1^{i-1} - T^0 \\ T_2^{i-1} - T^0 \\ 0 \end{bmatrix}$$

$$-\omega (1-\omega) k^{i-1} (T^{i-2}) \frac{1}{12} \begin{bmatrix} 3r_1 + r_2 & r_1 + r_2 & 0 \\ r_1 + r_1 & r_1 + 3r_2 & 0 \\ 0 & 0 & 0 \end{bmatrix} \begin{bmatrix} T_1^{i-1} - T^0 \\ T_2^{i-1} - T^0 \\ 0 \end{bmatrix}$$

$$-\omega^2 (1-\omega) k^{i-2} (T^{i-3}) \frac{1}{12} \begin{bmatrix} 3r_1 + r_2 & r_1 + r_2 & 0 \\ r_1 + r_1 & r_1 + 3r_2 & 0 \\ 0 & 0 & 0 \end{bmatrix} \begin{bmatrix} T_1^{i-1} - T^0 \\ T_2^{i-1} - T^0 \\ 0 \end{bmatrix}$$

(6.2-21)

Substitution of the respective nodal values into Equation 6.2-20 and carrying out the integrations, results in the system of Equations of 6.2-21 for each surface element (nodes 1 & 2 on boundary).

Examination of the Equations 6.2-21 shows that the first two equations are generated from the surface boundary nodes, and the third equation accounts for the interior node. As the mesh interval becomes small, the following simplifications into Equation 6.2-21 can be introduced for each surface element:

$$\begin{aligned} r_1^1 &= r_2 \\ \dots &\quad \dots \\ q_1^1 &= q_2 \\ T_1^{i-1} &= T_2^{i-1} = T^{s(i-1)} \end{aligned} \tag{6.2-22}$$

Substituting these simplifications results in the same equation for the radiative boundary nodes of the surface element. Focusing attention to a single equation and isolating the relaxation parameter results in:

$$\begin{aligned} &(1-\omega)\kappa^i + \omega(1-\omega)\kappa^{i-1} + \omega^2(1-\omega)\kappa^{i-2} + \omega^3(1-\omega)\kappa^{i-3} + \dots \\ &= \frac{2}{\epsilon_{12} r_1 (T_1^{i-1} - T^*)} \left[\frac{\Delta}{60} [(12r_1 + 3r_3)q_1''' + (3r_1 + 2r_3)q_3'''] \right. \\ &\quad - \frac{k}{12\Delta} (2r_1 + r_3) [(b_1^2 + c_1^2 + b_1 b_2 + c_1 c_2) T_1^{i-1} \\ &\quad \left. + (b_1 b_3 + c_1 c_3) T_3^{i-1}] \right] \end{aligned} \tag{6.2-23}$$

For pure oscillatory behavior, we know that:

$$\begin{aligned}\kappa^{i-1} &= \kappa^{i-3} = \kappa^{i-5} = \kappa^{i-\text{odd}} \\ \kappa^i &= \kappa^{i-2} = \kappa^{i-4} = \kappa^{i-\text{even}}\end{aligned}\quad (6.2-24)$$

Substituting these relationships into Equation 6.2-23 results in:

$$\begin{aligned}(1-\omega) [1+\omega^2 + \omega^4 + \omega^6 + \dots] \kappa_i &+ (\omega + \omega^3 + \omega^5 + \omega^7 + \dots) \kappa_{i-1}] \\ &= \frac{c_1 - c_2}{c_3}\end{aligned}\quad (6.2-25)$$

where:

$$\begin{aligned}c_1 &= \frac{\Delta}{60} [(12r_1 + 3r_3)q_1''' + (3r_1 + 2r_3)q_3'''] \\ c_2 &= \frac{k}{12\Delta} (2r_1 + r_3) [(b_1^2 + c_1^2 + b_1b_2 + c_1c_2)T_1^{i-1} \\ &\quad + (b_1b_3 + c_1c_3)T_3^{i-1}] \\ c_3 &= \frac{b_{12}r_1}{2} (T_1^{i-1} - T'')\end{aligned}$$

The expression for ω can be simplified using the binomial expansion:

$$(1 \pm x)^{-1} = 1 \mp x \pm x^2 \mp x^3 \dots \quad (x^2 < 1) \quad (6.2-26)$$

Using this expansion, Equation 6.2-25 can be re-written as:

$$[\frac{1}{1-\omega} - 2]\kappa^i - [\frac{1}{1-\omega} - 1]\kappa^{i-1} = -\frac{c_1 - c_2}{c_3} \quad (6.2-27)$$

Isolating ω :

$$\omega_{\text{opt}} = \frac{1 - EB}{2 - \kappa^{i-1}/\kappa^i - EB} \quad (6.2-28)$$

where:

$$EB = \frac{c_1 - c_2}{c_3 \kappa^i}$$

After each iteration, two conditions can exist, either $\kappa^i > \kappa^{i-1}$ or $\kappa^i < \kappa^{i-1}$. Since κ^i is proportional to T^3 , it is reasonable to make the following assertions once oscillatory behavior has begun:

$$\kappa^i > > \kappa^{i-1}$$

or,

$$\kappa^i < < \kappa^{i-1}$$

A value for ω can now be determined for either condition.

Condition I: $\kappa^i > > \kappa^{i-1}$

Neglecting κ^{i-1} in Equation 6.2-28 results in:

$$\omega_{\text{opt}} = \frac{\kappa^i - \frac{c_1 - c_2}{c_3}}{2\kappa^i - \frac{c_1 - c_2}{c_3}}$$

Simplifying,

$$\omega_{\text{opt}} = 1 - \frac{1}{2c_4} \quad \text{for } \kappa^i > > \kappa^{i-1} \quad (6.2-29)$$

where:

$$c_4 = \frac{c_1 - c_2}{\kappa^i c_3}$$

What c_4 physically represents is an energy balance of surface elements in which the numerator is comprised of the total heat generated in the element c_1 , and heat conducted into the element, $-c_2$; and the denominator, $\kappa^i c_3$, is the heat radiated from the surface boundary of the element.

Thus,

$$c_4 = \frac{\text{Heat Generation Within Element} + \text{Heat Conducted Into Element}}{\text{Heat Radiated From Surface of Element}} \quad (6.2-30)$$

We now understand the significance of ω . It is simply a value to force an energy balance at the radiative surface; in effect, a method for determining the radiative heat transfer coefficient necessary for convergence over energy. When $\kappa^i > > \kappa^{i-1}$, this means $T^{s(i-1)} > > T^{s(i-2)} = T^{s(i)}$. The condition means that the energy radiated at the surface is greater than the energy available for rejection. Hence, c_4 will be less than one. As convergence is approached, c_4 approaches one and ω_{opt} goes to zero.

Equation 6.2-29 also places bounds on the initial value of the radiative heat transfer coefficient.

Since,

$$0 < \omega_{\text{opt}} < 1$$

From this condition, we find that κ_0 has only a lower bound.

Specifically,

$$\frac{c_1 - c_2}{c_3} < \kappa_0 \quad (6.2-31)$$

Condition II: $\kappa^i < < \kappa^{i-1}$

Neglecting κ^i in Equation 6.2-28 results in:

$$\omega_{\text{opt}} = \frac{\frac{c_1 - c_2}{c^3}}{\frac{c_1 - c_2}{c_3} + \kappa^{i-1}}$$

Simplifying,

$$\omega_{opt} = 1 - \frac{1}{1+c_5} \text{ for } \kappa^i < < \kappa^{i-1} \quad (6.2-32)$$

where:

$$c_5 = \frac{c_1 - c_2}{\kappa^{i-1} c_3}$$

Because κ^{i-1} is always positive, there is no upper or lower bound on κ_0 for this condition.

Since the expressions for determining ω_{opt} were based on asymptotic limits ($\kappa^i > > \kappa^{i-1}$ or visa versa), the next concern is to find the value that ω should assume as convergence is approached ($\kappa^i = \kappa^{i-1}$). Returning to Equation 6.2-23, the left hand side can be factored into the following form:

$$\begin{aligned} \kappa^i + (\kappa^{i-1} - \kappa^i) \omega + (\kappa^{i-2} - \kappa^{i-1}) \omega^2 + (\kappa^{i-3} - \kappa^{i-2}) \omega^3 \\ + \dots (\kappa^{N-i-1} - \kappa^{N-i}) \omega^{N-1} \end{aligned} \quad (6.2-33)$$

From this equation, we see that as κ^i approaches κ^{i-1} the contribution of ω to stability becomes negligible. In the limit as $\kappa^i = \kappa^{i-1}$, ω can assume any value without affecting the energy balance of the surface elements. Hence, we do not need an explicit form for determining ω near convergence and the previous expressions for ω_{opt} can be used.

The expression for ω_{opt} of Equation 6.2-28 was programmed into SHLDTEMP. The test case was recalculated with these expressions and, for the improved graphite shield, rapid convergence was achieved. An additional advantage of using these results was realized by monitoring the value of energy balance for the surface elements given by the variable c_4 of Equation 6.2-29. It was found in some test case runs that

using only temperature convergence criteria can sometimes result in artificial convergence, in which the radiative surface temperature had converged but the inner temperatures had not. This false convergence condition was readily observable by a value of c_4 much different than 1.0(~ 1.5).

6.2.3 Thermal Instability Summary. In performing non-linear temperature analysis using Newton-Raphson iterations and simplex, finite elements, oscillatory behavior was encountered as the internal heat generation rate was increased above some threshold value. As the heat generation rate was further increased, the range of the oscillations increased, as well. Applying an extrapolation concept to the N-R method, a relaxation parameter was introduced to operate on the non-linear portion of the surface elements stiffness and load vector. For a wide variety of test cases, the use of this relaxation parameter, when higher than a threshold value, ω_{crit} , resulted in elimination of the oscillatory behavior and convergence to the correct solution. An analytic expression for determining ω_{opt} for each surface element which varies with each iteration, was developed by performing a nodal decomposition on the basic N-R method.

6.3 Numerical Instabilities Encountered During Stress Analyses.

The LiH cast or cold-pressed into a stainless steel honeycomb matrix was shown to be characterized by bilinear, orthotropic constitutive equations. Since the elements which are in tension and compression were not known apriori, the system of equations must initially be solved for the displacements using either the tensile or compressive

limitation became apparent. The figure providing volume expansion of LiH as a function of temperature and fast neutron fluence, was shown in the historical review to be based on an incomplete data base at the time of its origination. As any good engineer would do, conservative swelling estimates at high fluences ($>10^{17}$ NVT) and low temperatures (<600 K) were made because of these data gaps. While a passively cooled shield can be designed for a specific reactor and power level, the flexibility of ramping the core to several thermal outputs during its lifetime may be an attractive user option, particularly for some military applications. For this reason, a shield design for a steady operating power level may not be desirable for a dual mode operation of the system. Hence, the conservatism of the LiH temperature limit of 600 K at the outer surface may well be a self-inflicted design limitation which does not merit adherence to.

To maintain the LiH temperature within acceptable temperature limits for a given power level, this research has shown that shield configuration and thermal boundary conditions can be adjusted to meet these goals. Another means of fine tuning the final temperature distribution might be the proper usage of selective coatings on the radiative heat transfer surfaces. A precise definition of the external heat flux on this surface for a given orbit and orientation may result in optimal heat rejection based on spectral matching/mismatching of the coating. For example, a surface coating material with high effective emissivity at higher surface temperatures and lower emissivity at lower temperatures would be highly desirable.

Exact deployment schemes for an SP-100 reactor have not been addressed at this time. Hence, addressing specific design considerations such as view factors of the shielding surface was premature, and

temperature feedback effects on energy deposition in the shield for epithermal and thermal reactors should be explored. The trade-offs here are that a greater percentage of energy deposition will occur below thermal threshold energies due to the softer flux spectrum; however, this effect will be offset by the low specific surface area for the large core, resulting in less radiation leakage into the shield.

As shown in the uncertainty analysis, the gains in accuracy due to a higher flux expansions are offset by the current uncertainty of the heating kerma of MACK IV. Improvements in heating kerma uncertainty may not require much effort if the updates are limited to the nuclides expected to be found in a space reactor shield. This improvement will be essential when multi-megawatt reactors are to be developed for future space applications. For such reactors, the current 3-4% errors in energy deposition in the shield will result in uncertainties in heat generation in the shield on the order of kilowatts (instead of tenths of kilowatts for the SP-100).

With the results of this research, it is recommended that the radiation transport community include the constraints of energy deposition, in addition to dosages, in shield optimization codes. As was shown here, the thermal limitations of the space reactor shield design cannot be treated as an afterthought in the design of the shield.

Moving to the thermal analyses, several research areas are ripe for investigation. The maintenance of the LiH temperature above 600 K near outer regions of the shield most definitely requires additional investigation. During this research, the conservation of this design

8.0 AREAS FOR FUTURE RESEARCH

As with many research projects, the questions resolved with the current results gave rise to many additional ones. This section briefly outlines possible areas for future research dealing with the space reactor shield.

In the subject area of radiation transport, several follow-on topics come to mind. With the axisymmetric FEMP2D extended to solve for the arbitrary order flux, a comparison of the 2-D with 1-D energy deposition rates would provide the transport community with valuable design information. It has already been shown that 2-D temperature results differ greatly from the equivalent 1-D temperature calculations because of the additional heat rejection surface (Barattino and El-Genk, 1984.) However, if the 2-D heating rates could be determined with a 1-D calculation (with transverse leakage), the 2-D temperature analysis could then readily be performed with significant computational cost savings. The effects of shadow shield angle, shielding configuration, and relative dimensions of the shield would be important parameters in the 1-D equivalency verification.

With regard to temperature feedback effects, the free gas scattering kernel was used in this research. Other scattering kernels have appeared in the literature such as the harmonic oscillator, the phonon expansion, and the heavy gas models (Williams, 1966). While each of these kernels have been applied to specific experimental data other than LiH, a comparison of temperature dependent thermal neutron cross sections would be of interest, probably more to the nuclear science community than to thermal engineers. Additionally, the

designing a shield for radiation transport, with afterthought given to extraneous subjects such as thermal design, are no longer acceptable for designing space reactor shields.

front of the shield resulted in a reduction in the maximum shield temperature of ~350 K. This significant decrease in temperature was due to a combination of neutronic and thermal effects based on LiH and W properties.

A final shield design consisting of Graphite-LiH(Depl)-W-LiH(Nat) was shown to possess temperatures below maximum temperature requirements of LiH (~680 K) for an SP-100 reactor operating at $1.66 \text{ MW}_{\text{th}}$. The final temperature distribution was used to calculate the thermally induced stresses and strains throughout the shield. Using bilinear, orthotropic constitutive equations with homogenized material properties based on the composite cylinders models, large tensile stresses were found along the W-LiH(Nat) interface at the outer radial position of the graphite where its meets the LiH(Depl), and at the radiation heat transfer surface when this outer surface was free to expand.

Finally, numerical instabilities were encountered during each phase of this research. A discussion of these instabilities, as well as the techniques used to overcome them, was included.

In conclusion, the coupling between radiation transport and temperature distribution was strongly influenced by the shield configuration. A shield optimized for radiation protection was found to be totally unacceptable based on maximum temperature limitations of the LiH. However, by making minor trade-offs in the radiation protection performance of the shield, a shield which satisfied thermal limitations with passive cooling could be designed. The need to give equal design emphasis to both radiation and thermal considerations of the space shield was found to be an essential requirement of any reactor system operating at mega-watt thermal power levels. Past design procedures of

**Table 7.1-1: Summary of Varying H-LiH Configuration for SP-100 Reactor
Operating at 1.66 MW_{th}**

| Shield Configuration | Energy deposited ¹ [kW] | n ² [kW] | Total [kW] | Max Temp ³ , ⁴ [K] | Min Temp ² , ⁴ [K] | Comments |
|---------------------------------------|---------------------------------------|------------------------|---------------|---|---|---|
| 1. H-LiH(Nat) | 4.78 | 4.98 | 9.76 | 772.4 | 540.1 | 4 cm H 71 cm LiH |
| 2. H-LiH(Dep1)-LiH(Nat) | 6.30 | 1.40 | 7.70 | 680.5 | 535.1 | 4 cm H 42.7 cm LiH(Dep1) 28.3 cm LiH(Nat) |
| 3. LiH(Nat)-H-LiH(Nat) | 3.51 | 6.71 | 10.22 | 1074.0 | 564.5 | 13 cm LiH(Nat) 3.83 cm H 52.7 cm LiH(Nat) |
| 4. LiH(Dep1)-H-LiH(Nat) | 4.17 | 3.71 | 7.88 | 715.0 | 512.3 | 13.3 cm LiH(Dep1) 3.83 cm H 57.2 cm LiH(Nat) |
| 5. Graphite-LiH (Dep1)- H-LiH(Nat) | 4.28 | 3.68 | 7.96 | 665.0 | 511.5 | 2 cm Graphite 11.3 cm H-LiH(Dep1) 3.83 cm H 57.2 cm LiH(Nat) |

Notes:

1. Error Bound for Energy Deposition is $\pm 5.91\%$
2. Based on: Ambient Temperature = 200 K
Emissivity x View Factor = 0.83
3. Error Bound for Max Temperature is $\pm 5.0\%$
4. Error Bound for Min Temperature is $\pm 1.1\%$

2.5% less than that calculated at room temperature. For an SP-100 shield with 10 kW or less of total heat generated, the 2.5% decrease translates into ~250 watts. This change in energy deposition results in a maximum change in temperature on the order of 1.5%. Thus, it was concluded that temperature feedback has minor effect on energy deposition and on temperature distribution in typical SP-100 shield.

The second part of this research examined the effects of shield configuration on temperature distribution of the shield. Four shield configurations were analyzed: two with tungsten at the front of the shield and two with the tungsten moved 13.4 cm into the shield. The 13.4 cm distance, based on Monte Carlo calculations performed at Los Alamos National Laboratory (Carlson, 1985), was found to produce the minimum fluence at the dose plane. For both tungsten locations, the effect on the temperature distribution and the gamma fluence of layering the LiH with LiH(Depl) followed by LiH(Nat) were considered.

The total energy deposition in the shield was reduced with the tungsten moved into the shield due to the reduction of secondary gammas caused by neutron capture in Li-7 and H. Table 7.1-1 is a summary of the results of the four basic configurations and an improved shield design with a layer of graphite at the front of the shield.

The importance of LiH(Depl) was strongly effected by the location of the tungsten. With W at the front, the use of ~42 cm of LiH(Depl) resulted in a decrease of ~100 K in maximum temperature of the LiH. With the W moved 13.4 cm into the shield, the use of LiH(Depl) at the

of technical disciplines. This research represents the first documented application of FEM in solving the coupled radiation transport, temperature, and stress analysis of a space reactor radiation shield.

The numerical code developed during this research was employed in analyzing the SP-100 shield, coupled to a 1.66 MW_{th} fast reactor. Specifically, the radiation tranport-temperature coupling was used to examine two important issues. The first was the determination of temperature feedback effects on energy deposition in the non-Maxwellian LiH. The second issue evaluated was the relationship between the layered (W-LiH) shield configuration and the temperature distribution in the shield to examine whetner an optimized shield for radiation protection would be acceptable from a thermal performance perspective.

In determining the temperature effects on energy deposition, a W-LiH(Nat) shield was used as representative of an upper limit for any effects. Using the free gas scattering model to generate temperature dependent differential scattering and total neutron cross sections in the LiH, a thermal neutron flux spectrum was calculated and used as a weighting function in the generation of multi-group neutron cross sections (to include thermal upscatter cross sections). Energy deposition was recalculated from radiation transport calculations with the temperature dependent cross section and number densities. The result of considering temperature effect on number densities only (using room temperature cross sections) was a decrease of 5.9% in the total energy deposition in the shield (as compared with room temperature conditions). When temperature effects on both number densities and cross sections were included, the decrease in energy deposition was only

7.0 CONCLUSIONS

The availability of large power systems in space will open a new frontier for mankind. The SP-100 reactor is the first major step in our permanent occupation and utilization of space. However, because the costs of transporting man and material into this new environment are so high, the ingenuity of design engineers will be taxed in meeting the constraints of weight and volume requirements. With the shield accounting for 20-30% of the total system weight, the selection of materials is important to the design process of this subsystem.

Extensive experimental testing of candidate shielding materials was conducted during the SNAP program. As discussed in the historical review, tungsten and lithium hydride were the most commonly used materials for gamma and neutron attenuation, respectively. The shield consisting of tungsten-lithium hydride (in stainless steel honeycomb) was selected for its superior radiation protection characteristics per unit weight. At the lower power levels of the SNAP reactors, the thermal performance of the shield was not a major design limitation. Although at the close of the SNAP program, emerging concerns regarding temperatures and stresses throughout the shield remained unanswered.

During the time of SNAP program closeout in 1973 and the start of today SP-100 program (in 1983), major advances have been made in the computational tools available to the design engineer. The finite element method has proven to be a remarkably versatile numerical method in the spatial discretization of the governing equation for a variety

Figure 6.3-2 Resultant Stress State for Bilinear, Orthotropic Material Using Full Newton-Raphson Iteration

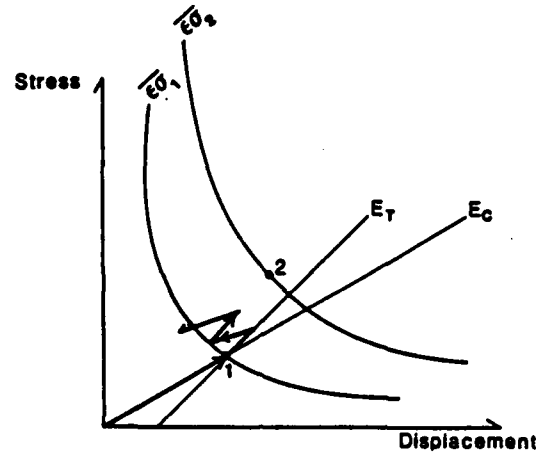
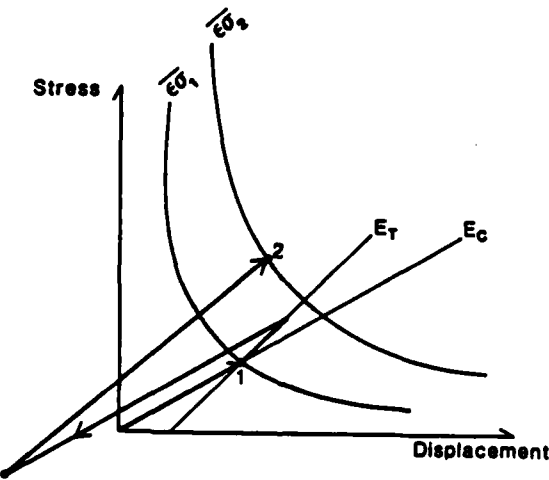


Figure 6.3-3 Resultant Stress State for Bilinear, Orthotropic Material Using Modified Newton-Raphson Iteration



and compressive moduli of the material, the rather obtuse path through the $-\sigma$, $-\epsilon$ quadrant was required to arrive at point 2.

Unfortunately, the concept of strain energy isotherms opens up the difficult issue of whether the resultant stress state is unique. Until uniqueness is proven, the resultant stress state represents an estimation of the "most likely" equilibrium condition of the shield during steady state operation.

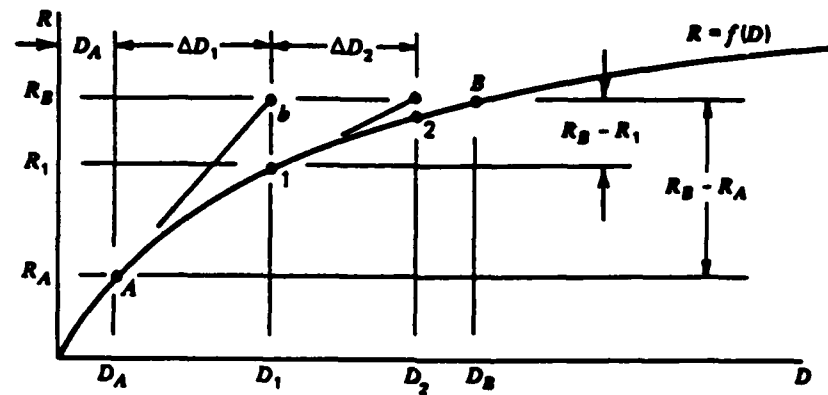
In conclusion, the use of a full Newton-Raphson iteration for the bilinear orthotropic shield produced a stress state which failed to converge to the energy criteria. The adaptation of a modified N-R iteration, with the inner loop converging on displacement criteria and the outer loop converging on energy criteria, resulted in a stress state which met all convergence criteria. While the stresses appear reasonable based on engineering judgement, the uniqueness of the solution remains an open issue from a theoretical viewpoint.

which failed to converge over energy. Figure 6.3-2 is a visualization of the result. While the stress distribution varied slightly from one iteration to the next, the strain energy of the shield (measured by \underline{U} , \underline{R}) remained relatively constant, regardless of the number of iterations. The force difference criteria (measured by $\|\underline{R} - \underline{K}\underline{U}\|_2/\|\underline{R}\|_2$) remained constant with iteration, failing to meet convergence criteria of 10^{-6} . From Figure 6.3-2, point 1 represents the initial stress state after the 1st iteration, using only compressive properties. With each iteration, a slightly modified stress state was obtained but always along the constant strain energy isotherm, $\overline{\epsilon\sigma}_1$. The correct stress state is identified on Figure 6.3-2 as point 2, which is at a different strain energy isotherm, $\overline{\epsilon\sigma}_2$. This resultant stress state was never achievable with the full-N-R iteration, and instead, produced stresses which were quite unrealistic (ie. negligible compressive, radial stresses and huge, compressive hoop stresses at the radiative heat transfer surface which was free to expand).

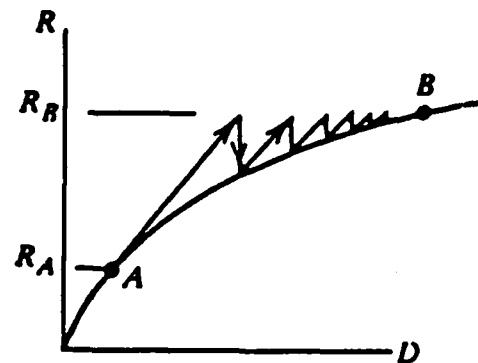
The modified N-R iteration method produced stress states which converged over displacement and applied energy criteria.

Figure 6.3-3 is a conceptualization of how this occurred using the solution method of Figure 3.5-10. The change in stress and displacement with each iteration shown in this figure are representative of a single node in the discretized shield. Allowing the displacements to converge before updating the stiffness matrix, resulted in a transfer from one energy isotherm to another. What was rather fascinating from Figure 6.3-3 was the manner in which the transfer from $\overline{\epsilon\sigma}_1$, to $\overline{\epsilon\sigma}_2$ occurred. Since a direct transfer was not feasible given the tensile

Figure 6.3-1 Full and Modified Newton-Raphson Iteration Methods



a. Full (Standard) Newton-Raphson Iteration
for a Single Degree of Freedom



b. Modified Newton-Raphson Iteration
for a Single Degree of Freedom

Source: Cook, 1981

properties throughout the shield.⁸ After each iteration, the directional moduli corresponding to the stress state for the previous iteration were then used in the reformulation of stiffness matrix and load vector. This process is repeated until convergence criteria were met.

The method just described constitutes a full Newton-Raphson iteration, with updated equations after each iteration. In the interest of reducing costs, the literature abounds with modified N-R algorithms in which the stiffness matrix is updated only periodically to minimize the computational efforts associated with the reformulation. The difference between full and modified N-R methods in arriving at the final solution for a single-degree-of-freedom is shown in Figure 6.3-1. In the modified N-R method, the stiffness matrix is not updated after each iteration, resulting in less computational time for matrix formulation. The trade-off lies in the fact that more iterations are required for convergence using modified N-R. The advantage of full N-R versus modified N-R method thus becomes problem specific [Bathe, 1982]. The key point here is that either method should result in the same set of stresses for a given problem.

After the final temperature distribution was determined for a specific shield design, the thermal stresses were calculated. Using a full Newton-Raphson iteration for the bilinear, orthotropic material resulted in a stress-strain distribution throughout the shield

⁸ A mix of tensile and compressive elements based on some initial guess is possible, but not considered generic enough for coding into SHLDSTR.

handled better with a general sensitivity analysis as shown earlier. However, general view factor programs already exist and may be added to this code package to allow for more specificity in future analyses.

Additionally, it was shown that the error in the LiH thermal conductivities is about $\pm 11\%$, and this large uncertainty dominates the resulting uncertainty in final temperatures. More reliable thermal conductivity data for LiH will decrease the error in the calculated temperatures for a given confidence level. Hence, more accurate thermal data could be experimentally derived, especially for the directional properties of the LiH-SS honeycomb matrix in both cast and cold-pressed form.

The area of stress analysis provides many opportunities for further research. The bilinear orthotropic treatment of the LiH-SS matrix was a first cut at a stress analysis of this complex structure. Future work should include the creep of the LiH and the non-linearity of the tungsten at elevated temperatures.

The accuracy of the composite cylinders models for material properties of the "homogenized" LiH-SS matrix should be validated experimentally at elevated temperatures. If substitute materials are used in the experiment, the crystal structure of the LiH substitute (fiber) should closely resemble that of the face centered cube of LiH. The temperature of the experiment should be at $\sim 2/3$ the melting point of the fiber material, and $\sim 1/2$ the melting point of the stainless steel substitute. Furthermore, the ratio of uni-axial material properties (E , G , ν) of the fiber and matrix at experimental temperatures, should closely approximate those of LiH and SS at shield operating temperatures.

The cracking in the LiH will be due primarily to the heating-freezing cycling during the formation of the LiH-SS matrix. Hence, a thoroughly accurate modelling of the stresses during steady state operation should begin with the transient cycling of the materials, followed by simulation of external loading during launch into space. This, in turn, would include a transient thermal and stress analysis, and a understanding of the sequence of operations used during the casting or pressing process of the LiH shield. Of course, such a research project implies the tacit assumption that material properties of the LiH at elevated temperatures are either known or would become available to the analyst. Without such data, the large uncertainty in results would render the value of this recommendation highly questionable.

An obvious extension of this work is to use the codes to evaluate other candidate shielding materials. For example, alternatives to LiH include yttrium hydride, zirconium hydride and even boron carbide. While each of these candidates have higher thermal conductivities and melting points than LiH, they also have higher densities and fewer hydrogen atoms per unit volume. Furthermore, the application of composite materials opens a news list of options to be studied.

A less obvious extension to this research is the radiation and thermal response of the shield during pulsing mode operation. The concept of a dual mode reactor which operates at a kilowatt level steady state power rating, and can also be pulsed to provide propulsion to some payload, is an application that has merit in both military and civilian circles.

A dual mode functional requirement for an LiH shield may cause some difficulties as LiH has high heat capacity, but low thermal conductivity. While the dual mode reactor may be a number of years away, it offers an exciting challenge for the shield designer.

A final area that is rich in potential future research topics relates to the computational aspects of this work. The instabilities discussed in Section 6.0 were obstacles which had to be overcome in order to conduct the engineering analyses of the shield, which was the primary focus throughout this research. What serves as an obstacle to the engineer represents an opportunity to the mathematician. Why the non-linear radiation heat transfer showed oscillatory behavior and how the use of a relaxation parameter damped this behavior is a topic worthy of vigorous mathematical investigation. The convergence of a non-linear governing equation with linear boundary conditions was proved by Oden (1973). However, the non-linear governing equation with non-linear boundary conditions is a problem currently under research.

The quest for more computationally efficient algorithms to solve non-linear systems could be directed to this subject area. For example, the Newton-Raphson method described in the theory section is but one method of solving the non-linear problem. Schreyer (1980) showed the merit of a modified secant iterative solution technique for solving a transient, non-linear heat transfer problem using finite elements in one dimension. In validating SHLDTEMP, this author found that a secant method for finding the temperature at the radiative surface and formulating the radiation heat transfer coefficient from this value, resulted in a convergence rate ~25% faster than the Newton-Raphson method provided. This observation, in turn, gives rise to the question as to

whether the improved convergence rate was dependent on the order of the bilinear trial function. The purpose of these examples is to emphasize that a host of computational issues usually accompanies any new code development, and it seems that rarely does one find his particular problem covered in the literature. This is not surprising when one recalls that widespread use of finite element method is still in its infancy, relative to analytic solution methods that have ancestral roots covering hundreds of years.

As mentioned at the outset of this section, the results of this research have seemingly given rise to a number of research topics worthy of follow-on efforts. The subject of radiation shielding analyses for space reactors is experiencing a re-birth that should result in some exciting research for a number of years to come.

APPENDIX 1

ANALYTICAL SOLUTION FOR 1-D, W-LIH SLAB SHIELD WITH RADIATIVE BACK SURFACE AND EITHER ADIABATIC OR ISOTHERMAL FRONT SURFACE.

The accuracy of the finite element method to determine the temperature distribution of the shield was validated by comparing the numerical results with 1-D closed form analytical solution. Figure 3.4-6 includes a schematic of the problem setup used for the comparison. The input data used in the test cases of Section 3.4 is included in Table A1 of this appendix.

The governing equations and boundary conditions for this problem during steady-state operation are as follows:

(A) Tungsten [$0 \leq x \leq a$]:

$$\nabla \cdot [k_w(T) \nabla T_w(x)] + B_w(\mu_w, x) q_{0\gamma} e^{-\mu_w x} + q_{0n} e^{-\Sigma_{R_w} x} = 0 \quad (A1-1)$$

with:

$$T_w(x=0) = T_0 \quad (\text{constant front surface temp})$$

or,

$$-k_w T_w(x=0),_x = 0 \quad (\text{adiabatic front surface}) \quad (A1-2)$$

and,

$$T_w(x=a) = T_{int} \quad (A1-3)$$

(B) Lithium Hydride [$a \leq x \leq b$]:

$$\nabla \cdot [k_L(T) \nabla T_L(x)] + B_L(\mu_L, x) q_{L\gamma} e^{-\mu_L(x-a)} + q_n e^{-\Sigma_{R_L}(x-a)} = 0 \quad (A1-4)$$

with:

$$T_L(x=a) = T_{int} \quad (A1-5)$$

and,

$$T_L(x=b) = T_b \quad (A1-6)$$

$(B_L q_{L_Y})$ and q_{L_n} are determined through the use of the following relations:

$$B_L(\mu_L, x) q_{L_Y} = B_w(\mu_w, x) e^{-\mu_w a} \quad (A1-7)$$

$$q_n = q_{0n} e^{-\sum R_w a} \quad (A1-8)$$

It is assumed that heating in the shield will occur as a result of gamma and neutron interactions in the shield. The gamma heating results from the heat generated due to photoelectric absorption, Compton scattering, and pair production. The gamma buildup factor is an empirical value which accounts for the heating effects of secondary radiations. The value of the buildup factor is based on the gamma energy, attenuation coefficient, and shield geometry. For a multi-layered shield, when the thickness of the outermost layer of the shield (i.e., LiH) exceeds 2-3 mean free paths, the buildup factor of the outermost layer is generally used for shield design (but based on the total number of mean free paths along the line of sight through all the materials). Because the buildup factor was assumed to be constant within a particular material region, it is mathematically equivalent to consider the initial gamma heating rate to be the product of $(B_w \cdot q_{0w})$ and neglect mention of buildup. For this reason buildup was not discussed in the main text for the 1-D problem. It is used in this Appendix for the purpose of completeness.

Analytical Solution:

Assuming constant thermal conductivities and buildup factors throughout the tungsten and lithium hydride, the analytical solutions for each region during steady-state operation are obtained as follows:

(A) W: Region: ($0 \leq x \leq a$)

i. Adiabatic Front Surface:

$$T_w(x) = T_{int} + B_w \frac{q_0 \gamma}{k_w \mu_w^2} [e^{-\mu_w a} - e^{-\mu_w x} + \mu_w(a-x)] + \frac{q_0 n}{k_w \Sigma_R^2} [e^{-\Sigma_R a} - e^{-\Sigma_R x} + \Sigma_R(a-x)] \quad (A1-9)$$

ii. Constant Temperature Front Surface

$$T_w(x) = T_0 + B_w \frac{q_0 \gamma}{k_w \mu_w^2} (1 - e^{-\mu_w x}) + \frac{q_0 n}{k_w \Sigma_R^2 r_w} (1 - e^{-\Sigma_R w x}) + \frac{x}{a} [(T_{int} - T_0) + B_w \frac{q_0 \gamma}{k_w \mu_w^2} (e^{-\mu_w a} - 1)] + \frac{q_0 n}{k_w \Sigma_R^2 r_w} (e^{-\Sigma_R w a} - 1) \quad (A1-10)$$

(B) LiH Region ($a < x < b$)

i. Adiabatic Front Surface

$$T_L(x) = \left[\frac{x-a}{b-a} \right] T_b - \left[\frac{x-b}{b-a} \right] T_{int}$$

$$+ \frac{B_L q_L \gamma}{k_L \mu_L^2} [e^{-\mu_L(b-a)} \left[\frac{x-a}{b-a} \right] - \left[\frac{x-b}{b-a} \right] - e^{-\mu_L(x-a)}]$$

$$+ \frac{q_L n}{k_L \Sigma^2 R_L} [e^{-\Sigma R_L(b-a)} \left[\frac{x-a}{b-a} \right] - \left[\frac{x-b}{b-a} \right] - e^{-\Sigma L(x-a)}] \quad (A1-11)$$

ii. Constant Temperature Front Surface

$$T_L(x) = T_b + \frac{B_L q_L \gamma}{k_L \mu_L^2} [e^{-\mu_L(b-a)} - e^{-\mu_L(x-a)}]$$

$$+ \frac{q_L n}{k_L \Sigma^2 R_L} [e^{-\Sigma R_L(b-a)} - e^{-\Sigma R_L(x-a)}]$$

$$+ \left[\frac{x-b}{b-a} \right] [(T_b - T_{int}) + \frac{q_L \gamma}{k_L \mu_L^2} (e^{-\mu_L(b-a)} - 1)]$$

$$+ \frac{q_L n}{k_L \Sigma^2 R_L} (e^{-\Sigma R_L(b-a)} - 1)] \quad (A1-12)$$

Determination of T_{int} and T_b

To determine the W-LiH interface temperature, T_{int} , and the back surface temperature, T_b , energy balances at each surface are used. For T_{int} , the following balance is made:

$$-k_w T_{w,x} = k_L T_{L,x} \text{ (at } x = a) \quad (A1-13)$$

The following expressions for the interface temperature are obtained:

1. Adiabatic Front Surface

$$\begin{aligned} T_{int} &= T_b + \frac{B_L q_{LY}}{k_L^2 \mu_L^2} e^{-\mu_L(b-a)} + [(b-a)\mu_L - 1] \\ &+ \frac{q_L n}{k_L \sum R_L^2} [e^{-\sum R_L(b-a)} + (b-a)\sum R_L - 1] \\ &+ B_W \frac{q_0 Y}{\mu_W} \frac{(b-a)}{k_L} [1 - e^{\mu_W a}] \\ &+ \frac{q_0 n}{\sum R_W} \frac{(b-a)}{k_L} [1 - e^{-\sum R_W a}] \end{aligned} \quad (A1-14)$$

ii. Constant Temperature Front Surface

$$\begin{aligned}
 \left[\frac{k_w}{a} + \frac{k_L}{b-a} \right] T_{int} &= \left[\frac{k_w}{a} \right] T_0 + \left[\frac{k_L}{b-a} \right] T_b \\
 &+ \frac{B_L q_L Y}{\mu_L^2} \left[\mu_L + \frac{1}{b-a} (e^{-\mu_L(b-a)} - 1) \right] \\
 &+ \frac{q_{L_n}}{\Sigma_{R_L}^2} \left[\Sigma_{R_L} + \frac{1}{b-a} (e^{-\Sigma_L(b-a)} - 1) \right] \\
 &+ \frac{B_W q_0 Y}{\mu_W^2} \left[\frac{1}{a} (1 - e^{\mu_W a}) - \mu_W e^{-\mu_W a} \right] \\
 &+ \frac{q_{0_n}}{\Sigma_{R_W}^2} \left[\frac{1}{a} (1 - e^{-\Sigma_{R_W} a}) - \Sigma_{R_W} e^{-\Sigma_{R_W} a} \right]
 \end{aligned}$$

(A1-15)

To determine the back surface temperature, T_b , the following energy balance is made:

$$-k_L T_{L,x} = \epsilon \sigma F_{fj} (T_b^4 - T_\infty^4) \text{ at } x=b \quad (\text{A1-16})$$

When the view factor at the back surface is taken as unity, the following expressions for T_b are obtained:

i. For Adiabatic Front Surface

$$\begin{aligned}
 T_b = \sqrt[4]{T_a^4 + \frac{B_W q_0 Y}{\mu_W \epsilon \sigma} (1 - e^{-\mu_W a}) + \frac{q_{0_n}}{\Sigma_W \epsilon \sigma} (1 - e^{\Sigma_W a})} \\
 + \frac{B_L q_L Y}{\mu_L \epsilon \sigma} (1 - e^{-\mu_L(b-a)}) + \frac{q_{L_n}}{\Sigma_L \epsilon \sigma} (1 - e^{-\Sigma_L(b-a)})
 \end{aligned}$$

(A1-17)

ii. For Constant Temperature Front Surface:

$$\begin{aligned}
 \varepsilon\sigma(T_b^4 - T_a^4) = & - \frac{\beta_L q_{L_Y}}{\mu_L} e^{-\mu_L(b-a)} + \frac{q_{L_n}}{\Sigma_{R_L}} e^{-\Sigma_{R_L}(b-a)} \\
 & + \frac{1}{(b-a)} [k_W(T_b - T_{int}) + \frac{q_{L_Y}}{\mu_L^2} (e^{-\mu_L(b-a)} - 1) \\
 & + \frac{q_{L_n}}{\Sigma_{R_L}^2} (e^{-\Sigma_{R_L}(b-a)} - 1)] \quad (A1-18)
 \end{aligned}$$

Table A1: Input Data for Test Cases
(Slab and Cylinder)

| | Slab | Cylinder* |
|-------------------------|------------------------|-----------------|
| Nuclear Data | | |
| μ_w | .667 | N/A |
| μ_L | .0444 | N/A |
| Σ_{r_w} | .2120 | N/A |
| Σ_{r_L} | .1178 | N/A |
| Thermal Data | | |
| k_w | 1.3 W/cm-K | 1.3 W/cm-K |
| k_L | .052 W/cm-K | .052 W/cm-K |
| q_{o_f} | .036 W/cm ³ | |
| q_{o_n} | .36 W/cm ³ | .72-.072 W/cm-K |
| B_w | 10.0 | N/A |
| B_L | 10.0 | N/A |
| ϵ | .8 | .8 |
| T_o | 310 K | 310 K |
| Geometric Data | | |
| a (Thickness of W) | 5.0 cm | 5.0 cm |
| b (Thickness of Shield) | 85.0 cm | 15.0 cm |
| b-a (Thickness of LiH) | 80.0 cm | 10.0 cm |

*Constant volumetric heating rate used for cylinder test case.

APPENDIX 2

ANALYTICAL SOLUTION FOR 1-D, W-LiH CYLINDER SHIELD WITH RADIATIVE OUTER SURFACE, AND CONSTANT INTERNAL HEAT GENERATION.

In Appendix 1, the 1-D analytic solution for the W-LiH slab shield was presented. In this appendix, the 1-D analytic solution for the W-LiH cylindrical shield is presented for an adiabatic inner surface, radiative heat transfer outer surface, constant heat generation and thermal conductivities. Figure 3.4-7 includes a schematic of this problem setup. The input data used in the test case of section 3.4 for the cylindrical shield is included in Table A1 of Appendix 1.

Governing Equations and Boundary Condition

The governing equations and boundary conditions for this problem during steady-state operation are as follows:

(A) Tungsten [$0 \leq r \leq a$]

$$\frac{1}{r} \frac{d}{dr} r k_w \frac{dT}{dr} + q''' = 0 \quad (A2-1)$$

$$\text{with: } \frac{dT}{dr} = 0 \text{ at } r = 0 \quad (A2-2)$$

$$T(r=a) = T_{int} \text{ at } r = a \quad (A2-3)$$

(B) Lithium Hydride [$a \leq r \leq b$]

$$\frac{1}{r} \frac{d}{dr} r k_L \frac{dT}{dr} + q''' = 0 \quad (A2-4)$$

$$\text{with: } T(r=a) = T_{int} \quad (A2-5)$$

$$T(r=b) = T_b \quad (A2-6)$$

Analytic Solutions

With an adiabatic inner surface, radiative heat transfer outer surface, constant heat generation and thermal conductivities, the analytic temperature solutions for each region of the shield are as follows:

(A) Tungsten $[0 \leq r \leq a]$

$$T_w(r) = T_{int} + \frac{q'''}{4k_w} a^2 \left(1 - \frac{r^2}{a^2}\right) \quad (A2-7)$$

(B) Lithium Hydride $[a \leq r \leq b]$

$$\begin{aligned} T_{LiH}(r) &= T_b + \frac{q'''}{4k_L} \left[\frac{\left(1 - \frac{a^2}{b^2}\right)}{\ln b/a} \ln \frac{r}{b} + \left(1 - \frac{r^2}{b^2}\right) \right] \\ &\quad + \frac{(T_{int} - T_b)}{\ln b/a} \ln \frac{r}{b} \end{aligned} \quad (A2-8)$$

Determination of T_{int} and T_b

Energy balances were made to determine the W-LiH interface temperature, T_{int} , and radiative surface temperature, T_b .

T_{int} was determined from:

$$k_w T_{w,r} = k_L T_{L,r} \quad \text{at } r=a \quad (A2-9)$$

From which:

$$T_{int} = T_b + \frac{q'''}{4k_L} b^2 \left(1 - \frac{a^2}{b^2}\right) \quad (A2-10)$$

T_b was determined from:

$$-k_L T_{L,r} = \epsilon\sigma(T_b^4 - T_\infty^4) \quad (A2-11)$$

Let

$$\text{Fun 1} = \frac{1}{b \ln a/b} [k_L(T_b - T_{int}) + \frac{q'''}{4} b^2 (1 - \frac{a^2}{b^2}) + \frac{q'''}{2} b^2 \ln \frac{a}{b}]$$

$$\text{Fun 2} = \epsilon\sigma F_{i+j} (T_b^4 - T_\infty^4) \quad (A2-12)$$

T_b could then be found directly or indirectly:

i. Direct: Substitute $(T_b - T_{int})$ from equation A2-10 into equation

A2-12 and solve for T_b :

$$T_b = \sqrt[4]{T_a^4 + \frac{1}{\epsilon\sigma F_{i+j}} \left(\frac{q'''b}{2} \right)}$$

ii. Indirect: Using a root finder routine (ie.Zero-in), the value of T_b is solved from:

$$\text{Fun 1} - \text{Fun 2} = 0$$

REFERENCES

- Abdou, M.A., Gohar, Y., and Wright, R.Q., Mack-IV, A New Version of MACK, A Program to Calculate Nuclear Response Functions from Data in ENDF/B Format, ANL/FPP-77-5, Argonne National Laboratory, Argonne, Illinois, July 1978.
- Abdou, M. A., and Maynard, C. W., "Calculational Methods for Nuclear Heating - Part 1: Theoretical and Computational Algorithms", Nuclear Science and Engineering: 56, 360-380 (1975).
- American Society for Metals, Metals Handbook, 9th Edition, Vol. 2, Metals Park, OH, 1975.
- AMPX: A Modular Code System for Generating Coupled Multi-Group Neutron-Gamma Libraries from ENDF/B. ORNL/TM-3706. Oak Ridge National Laboratory, Oak Ridge, Tenn, March 1976.
- Bailey, S., Vidyanathan, S., and VanHoomissen, J., "Liquid Metal Cooled Reactors for Space Power Applications", Space Nuclear Power Systems (Eds. M.S. El-Genk, and M.D. Hoover), Kreiger Publishing Company, Inc., 1984.
- Barattino, W.J., and El-Genk, M.S., "Thermal Analysis of Radiation Shield for Space Reactors Using Analytical and Finite Element Methods," Space Nuclear Power Systems (Eds. M.S. El-Genk and M.D. Hoover), Kreiger Publishing Company, Inc., 1984.
- Barattino, W. J., El-Genk, M.S., and McDaniel, P. J., "Thermal Analysis Considerations of a W-LiH Radiation Shield for the SP-100 Reactor", Proceedings of the 2nd Symposium on Space Nuclear Power Systems (Eds. M. S. El-Genk and M. D. Hoover), Kreiger Publishing Company, Inc., 1985.
- Barattino, W.J., El-Genk, M.S., and Voss, S.S., "Review of Previous Shield Analysis for Space Reactors", Space Nuclear Power Systems (Eds. M.S. El-Genk and M.D. Hoover), Kreiger Publishing Company, Inc., 1984.
- Bathe, Klaus-Jurgen, Finite Element Procedures in Engineering Analysis, New Jersey: Prentice Hall, Inc., 1982.
- Beckurts, K.H. and Wirtz, K. Neutron Physics. New York: Springer-Verlag, Inc., 1964.
- Beiriger, F., Jr., Thermal Analysis-Advanced ZrH₂ Reactor, TI-696-20-001. Atomics International, Canoga Park, CA, May 1968.
- Bell, George I. and Samuel Glasstone, Nuclear Reactor Theory. New York: Van Nostrand Reinhold Company, 1970.

Belytschko, Ted, and Hughes, Thomas, J. R., eds. **Computational Methods for Transient Analysis**, New York: North Holland Publishing Company, 1983.

Bendel, Warren L., "Displacement and Ionization Fractions of Fast Neutron Kerma in TLD's and Si", **IEEE Transactions on Nuclear Science**, Vol. NS-24, No. 6, December 1977.

Bergan, P.G. and Clough, R.W., "Convergence Criteria for Iterative Processes", **AIAA Journal**, Vol. 10, No. 8, 1972, pp. 1107-1108.

Bramble, James H. AND Zlamal, Milos, "Triangular Elements in the Finite Element Method", **Mathematics of Computation**, Vol. 24, No. 112, October 1970.

Burgreen, David, **Elements of Thermal Stress Analysis**. New York: C.P. Press, 1971.

Carlson, Donald E., "Minimum Mass Configurations of Tungsten and Lithium Hydride in the Shadow Shield of the SP-100 Space Reactor," **Proceedings of the 2nd Space Nuclear Power Systems Symposium**, (Eds. M. S. El-Genk and M.D. Hoover), Kreiger Publishing Company, Inc., 1985.

Christensen, R. M., **Mechanics of Composite Materials**, New York: John Wiley and Sons, Inc., 1979.

Christensen, R. M., and Lo, K. H., "Solutions for Effective Shear Properties in Three Phase Sphere and Cylinder Models," **J. Mech. Phys. Solids**, Vol. 27, 1979.

Cook, Robert D., **Concepts and Applications of Finite Element Analysis**, New York: John Wiley and Sons, Inc., 1981.

Cross, Jon B. and Cremers, David A., "Atomic Oxygen Surface Interactions-Mechanistic Study Using Ground Based Facilities", **Proceedings of the AIAA 23rd Aerospace Sciences Meeting**, Reno, Nevada, January 1985.

Duderstadt, J.J. and Hamilton, L.J. **Nuclear Reactor Analysis**. New York: John Wiley and Sons, Inc., 1976.

Eisenstat, Stanley C., **Efficient Implementation of a Class of Pre-conditioned Conjugate Gradient Methods**, Research Report #185. Department of Computer of Science, Yale University, August 1980.

Engle, W.W., Jr., R.L. Childs, F.R. Mynatt, and L.S. Abbott, Optimization of a Shield for a Heat Pipe Cooled Fast Reactor Designed as a Nuclear Electric Space Power Plant, ORNL-TM-3449. Oak Ridge National Laboratory, Oak Ridge, Tenn, June 1971.

- Finlayson, B.A. and Scriven, L.E. "The Method of Weighted Residuals - A Review", *Applied Mechanics Review*, Vol. 19, No. 9, 735-748 (1966).
- Fletcher, J.K. "The Solution of the Multigroup Neutron Transport Equation Using Spherical Harmonics", *Nuclear Science and Engineering*, 84, 33-46 (1983).
- Foderaro, Anthony, *The Elements of Neutron Interaction Theory*. Cambridge, Mass.: The MIT Press, 1971.
- Geitzen, A.J., et al., *A 40 kWe Thermionic Power System for a Manned Space Laboratory*, Gulf-GA-A10535, Gulf General Atomics, 1971.
- Glasstone, Samuel and Sesonske, Alexander, *Nuclear Reactor Engineering*, 3rd Edition. New York: Van Nostrand Reinhold Company, 1981.
- Gulf General Atomics, *A 40 kWe Thermionic Power System for a Manned Space Laboratory*, GULF-GA-A10535, 1971.
- Hageman, A.L. and Young, D.M. *Applied Iterative Methods*, New York: Academic Press, 1981.
- Hoffman, E.E. "Technology Status of Tantalum Alloys", *Space Nuclear Power Systems*, (Eds. M.S. El-Genk and M.D. Hoover), Kreiger Publishing Co., Inc., 1984.
- Holman, J. P., *Experimental Methods for Engineers*. New York: McGraw-Hill Book Company, 1971.
- Huebner, Kenneth H., and Thornton, Earl A., *The Finite Element Method for Engineers*, 2nd edition, New York: John Wiley and Sons, Inc., 1982.
- Idelsohn, S., Laschet, G., and Nyssen, C., "Pre-and-Post-Degradation Analysis of Composite Materials with Different Moduli in Tension and Compression," *Computer Methods in Applied Mechanics and Engineering*, 30 (1982) 133-149.
- Jones, Robert M., *Mechanics of Composite Materials*. Washington, D.C.: Scripta Book Company, 1975.
- Jones, Robert M., "Stress-Strain Relations for Materials with Different Moduli in Tension and Compression", *AIAA Journal*, Vol. 15, No. 1., January 1977.
- JPL, *SP-100 Conceptual Design Description No. 1*. NASA-Jet Propulsion Laboratory, Pasadena, CA, June 1982.
- Kantorovich, L. V., and Krylov, V. I., *Approximate Methods of Higher Analysis*. New York: Interscience Publishers, Inc., 1958.
- Kaszubinski, L.J., *Shield Materials Recommended for Space Power Nuclear Reactors*, NASA TM X-2835, July 1973.

- Keshishian, F., et al., **Radiation Shielding for Zirconium Hydride Reactor Systems**, AI-AEC-13081, Atomics International, Canoga Park, CA, 1973.
- Klopp, W.D. "Technology Status of Molybdenum and Tungsten Alloys", **Space Nuclear Power Systems** (Eds. M.S. El-Genk and M.D. Hoover), Kreiger Publishing Co., Inc., 1984.
- Lahti, G.P. and P.F. Herrman, **Comparison of Tungsten and Depleted Uranium in Minimum Weight Layered Shields for a Space Based Power Reactor**, NASA TM-X-1874. NASA Lewis Research Center, Cleveland, OH, September 1969.
- LANL, **SP-100 Project Semi-annual Technical Progress Review**. Los Alamos National Laboratory, Los Alamos, N.M., October 1982.
- Lundberg, L. B., **Mechanical Properties of LiH Part 1: Compression Test**. Atomics International, Canoga Park, CA, 9 November 1962.
- Ma, Benjamin M., **Nuclear Reactor Materials and Applications**, New York: Van Nostrand Reinhold Company, 1983.
- Marks' **Standard Handbook for Mechanical Engineers**, 8th Ed. Eds: T. Baumeister, E. Avallone, and T. Baumeister, New York: McGraw Hill Book Company, 1978.
- Masora, D.G., **SNAP 8 Design Description**, NAA-SR-MEMO-8740. Atomic International, Canoga Park, CA, 1973.
- Messer, Charles E., **A Survey Report on Lithium Hydride**, NYO-9470. Tufts University, October 1960.
- Mueller, William M., Blackledge, James P., and Libowitz, George G., **Metal Hydrides**. New York: Academic Press, 1968.
- Namenson, A. I., and Wolicki, E. A., "Average Silicon Neutron Displacement Kerma Factor at 1 MeV", **IEEE Proceedings**, 1982.
- Noble, B., **Applied Linear Algebra**. Englewood Cliffs, N.J: Prentice-Hall, 1969.
- Oden, J. T., **Finite Elements of NonLinear Continua**. New York: Mc Graw Hill Book Company, 1972.
- Oden, J.T., "Theory of Conjugate Projections in Finite Element Analysis", **Lectures on Finite Element Methods in Continuum Mechanics**, (Eds. J.T. Oden and E.R.A. Oliveira), The University of Alabama, 1973.
- Personal Communication with Dr. Lee Bertram, Sandia National Laboratory, Albuquerque, New Mexico (1985)
- Personal Communication with Dr. Lynn Lundberg, Los Alamos National Laboratory, Los Alamos, New Mexico (1984).

- Personal Communication with Dr. Patrick J. McDaniel, Sandia National Laboratories, Albuquerque, New Mexico (1984).
- Pian, Theodore H.H. and Tong, Pin, "Basis of Finite Element Methods for Solid Continua", International Journal for Numerical Methods in Engineering, Vol. I, 3-28 (1969).
- Reactor Handbook, Vol. I Materials, 2nd Edition, C. R. Tipton, ed. New York: Interscience Publishers, Inc, 1960.
- Rivello, Robert M., Theory and Analysis of Flight Structures. New York: McGraw Hill Book Company, 1969.
- Roy, John R., "Numerical Error in Structural Solutions", Journal of the Structural Division Proceedings of the American Society of Civil Engineers, April 1971.
- Schaeffer, N. M. (Ed.), Reactor Shielding for Nuclear Engineers, KIP-2595. U. S. Atomic Energy Commission, 1973.
- Schreyer, Howard L., Nonlinear Finite Element Heat Conduction Analysis with Direct Implicit Time Integration, ANL/RAS 80-10. Argonne National Laboratory, Argonne, Illinois, June 1980.
- Smith, Roger L. and Miser, James W., Compilation of the Properties of Lithium Hydride, NASA TMX-483. National Aeronautics and Space Administration, January 1963.
- SNAP 50/SPUR Program Summary, CNLM-5889, September 1964.
- SP-100 Conceptual Design Study, General Electric Company, Space Systems Division, Valley Forge Space Center, December 1983.
- Stevenson, J. A., and Grafton, J. C., Radiation Heat Transfer Analysis for Space Vehicles, AFASD TR 61-119. Wright Patterson AFB, December 1961.
- Thermophysical Properties of Matter, Volume 9: Thermal Radiative Properties: Coatings. (Eds. Y. S. Touloukian, D. P. DeWitt, and R. S. Hernicz), New York: IFI/Plenum Company, 1972.
- Thermophysical Properties of Matter, Volume 12: Thermal Expansion: Metallic Elements and Alloys. (Eds. Y. S. Touloukian, R. K. Kirby, R. E. Taylor, and P. D. Desai), New York: IFI/Plenum Company, 1975.
- Thompson and Schwab, Nuclear Heating in Reference ZrH₂ Shield, TI-696-23-040. Atomics International, December 1969.
- Utku, Senol, and Melosh, Robert J., "Solution Errors in Finite Element Analysis", Computers and Structures. Vol. 18, No. 3, 379-393, 1984.
- Voss, S. S. Snap Reactor Overview, AFWL-TN-84-14, Air Force Weapons Laboratory, Kirtland AFB, NM, 1984.

Welch, F. H. Lithium Hydride Technology: III. Properties of Lithium Hydride for SNAP Shielding Applications, NAA-SR-9400, Vol. III. Atomics International, Canoga Park, CA, (Referred to as 1967a).

Welch, F. H., Lithium Hydride Technology: IV. A Novel Neutron-Gamma Material for Snap Applications, NAA-SR-9400, Vol. IV. Atomics International, Canoga Park, CA, 1967. (Referred to as 1967b)

Welch, F. H., Lithium Hydride Technology: V. Testing and Examination of SNAP Shadow Shields, NAA-SR-9400, Vol. V. Atomics International, Canoga Park, CA, 1967. (Referered to as 1967c).

Wills, E. Z., A Finite Element Projection Method for the Solution of Particle Transport Problems with Anisotropic Scattering. Ph.D. Thesis, The University of New Mexico, 1984.

Wilkinson, J. H., The Algebraic Eigenvalue Problem. New York: Oxford University Press, 1965.

Williams, M. M. R., The Slowing Down and Thermalization of Neutrons. New York: John Wiley and Sons, Inc., 1966.

Wilson, Edward L., "Structural Analysis of Axisymmetric Solids", AIAA Journal, Vol. 3, No. 12, December 1965.

Zienkiewicz, O. C., and Morgan, K., Finite Elements and Approximation. New York: John Wiley and Sons, Inc., 1983.

END

FILMED

9-85

DTIC